UNIVERSITÀ DI PISA

Dipartimento di Fisica E.Fermi
Corso di Laurea Magistrale in Fisica

Multi-wavelength Spectroscopic Study of Shock Phenomena Driven by Explosive Outbursts in Symbiotic-like Recurrent Novae.

Supervisor:
Prof. Steven N. SHORE

Candidate:
Alessandra Azzollini

Anno Accademico 2020-2021

Ai nonni e a Paola

Contents

Introduction **4**

1 Shock Waves in Symbiotic-like Recurrent Novae **6**
1.1 Shock Waves . . . 6
1.2 Symbiotic-like Recurrent Novae . . . 11
1.3 Stages of the outburst . . . 13
1.4 Light curve evolution during outburst . . . 19
1.5 Spectral line evolution . . . 20
1.6 Description of the targets . . . 26
1.6.1 RS Ophiuchi . . . 27
1.6.2 V745 Scorpii . . . 27
1.6.3 V3890 Sagittarii . . . 28
1.6.4 T Coronae Borealis . . . 28
1.6.5 V407 Cygni . . . 28

2 Instruments and Datasets **30**
2.1 Swift Ultraviolet/Optical Telescope . . . 31
2.1.1 The UVOT grisms design . . . 33
2.1.2 The UV grism . . . 35
2.1.3 Wavelength calibration . . . 36
2.1.4 Flux calibration . . . 38
2.1.5 Swift UVOT/UV-grism dataset . . . 39
2.2 International Ultraviolet Explorer . . . 39
2.2.1 IUE dataset . . . 42
2.3 European Southern Observatory . . . 42
2.4 South African Astronomical Observatory . . . 43
2.5 Cerro Tololo Inter-American Observatory . . . 43
2.6 Nordic Optical Telescope . . . 43
2.7 Ondřejov Observatory . . . 43
2.8 Astronomical Ring for Access to Spectroscopy . . . 44

3 Data Analysis **45**
3.1 Data reduction . . . 45
3.1.1 Swift spectra . . . 45
3.1.2 IUE spectra . . . 48
3.1.3 ESO, SAAO, CTIO, SMARTS, NOT, OES and ARAS spectra . . . 48
3.2 Early analysis . . . 48
3.2.1 Radial velocity . . . 49
3.2.2 Measurement of the spectral lines . . . 49
3.3 Light curves . . . 50
3.4 Line profiles overview . . . 55
3.4.1 Permitted, semi-forbidden and forbidden transitions . . . 55
3.4.2 The Balmer series . . . 57

3.4.3 The Helium lines . . . 71
3.4.4 Si III and C III . . . 76
3.4.5 Multiple ionised lines . . . 80
3.4.6 Coronal lines . . . 89

4 Results and Conclusions **94**
4.1 Density determination . . . 95
4.2 Ionisation of the ambient medium . . . 98
4.3 Shock breakout . . . 102
4.4 Concluding remarks . . . 102

A Journal of observations **104**
A.1 Swift . . . 104
A.1.1 RS Oph . . . 104
A.1.2 V3890 Sgr . . . 105
A.2 IUE . . . 105
A.2.1 RS Oph - low resolution . . . 105
A.2.2 RS Oph - high resolution . . . 106
A.2.3 V745 Sco . . . 106
A.2.4 V3890 Sgr . . . 106
A.2.5 T CrB - low resolution . . . 106
A.2.6 T CrB - high resolution . . . 107
A.3 ESO . . . 107
A.3.1 V745 Sco . . . 107
A.4 SAAO . . . 108
A.4.1 V745 Sco . . . 108
A.5 SMARTS CHIRON . . . 108
A.5.1 V745 Sco . . . 108
A.6 NOT . . . 108
A.6.1 V407 Cyg . . . 108
A.6.2 V745 Sco . . . 109
A.7 Ondřejov . . . 109
A.7.1 V407 Cyg . . . 109
A.8 ARAS . . . 109
A.8.1 V3890 Sgr . . . 109
A.8.2 RS Oph - quiescence . . . 110
A.8.3 T CrB - quiescence . . . 110

Bibliography **112**

Ringraziamenti **120**

Introduction

Shock fronts are dynamical phenomena frequently encountered in astrophysical environments, which are usually responsible for the introduction of disturbances in the hydrodynamical equations describing the plasma behavior. The propagation of these discontinuous fronts resembles the evolution of acoustic waves, but with different intrinsic features, above all their supersonic characteristic speed (by definition).

The symbiotic stars are interacting binary systems with a hot white dwarf (WD) accreting mass from a more evolved companion, whose wind creates a dense nebular cloud around the system. They were first separated taxonomically by [Merrill and Humason(1932)], who used this name because their spectrum showed anomalous combinations of features. The simultaneous presence of strong absorption and emission lines was difficult to interpret at that time, but a phenomenological picture of an "odd couple" wide binary was already proposed by [Gaposchkin(1957)] in her classic monograph. The absorption and continuum spectrum is compatible with a cold late-type giant or supergiant at $T < 5000\ K$, while the strong emission lines from transitions of hydrogen, helium and higher ionisation species require either a strong heating source or hard photoionising source. Most important, the nebular forbidden lines require photoionisation beyond tens of eV. After 1978, the *International Ultraviolet Explorer (IUE)* solved the paradox, providing spectroscopy at good resolution below $3000\ \mathring{\mathrm{A}}$ and demonstrating the presence of the compact, hot component. The existence of a White Dwarf (WD) in this type of systems was further confirmed by observations in other wavelength bands, especially in the X-rays. These confirmed that the accreting component of the binary is moderately massive, $M \sim 0.6 - 1\ M_{\odot}$, embedded in the wind of the Red Giant (RG) companion and accreting enough gas to emit through an accretion disc. The WD is the remnant of a $M \sim 4 - 10\ M_{\odot}$ progenitor whose dynamical and physical traits changed due to the interaction with a wind, which stripped the envelope in the final stages of its evolution producing a circumstellar environment similar to planetary nebulae and leaving an enriched bare core.

In general, symbiotic stars are considered a subclass of Recurrent Novae (RNe), interacting binaries with a red giant closely bounded and transferring material to a massive white dwarf, which undergo multiple quasi-periodic explosions. They have longer periods than about a year with the peculiarity that the giant and WD progenitors expanded separately without previous mass exchange. The RG is sufficiently extended, its surface gravity low enough and the wind produces a circumbinary medium that is partially accreted while flowing past the WD. Mass accretion phase in Recurrent Novae resembles that of Classical Novae (CNe), in which heavy elements - C, O and Ne rather than He from CNO nuclear burning from the core and the envelope - are overabundant and, when sufficient amounts of material accumulated on the WD surface, accretion leads to the onset of a thermonuclear runaway, which powers the outburst of the system and fast ejection of almost all the accreted gas at more than several $10^3 km\ s^{-1}$, well above the escape velocity for the WD. The timescale for similar eruptive events is short compared to the radiative and sonic time for the ejecta, therefore the expulsion generates a shock wave that propagates through the surrounding medium. These systems harbor more massive degenerates, likely $M \gtrsim 1.2\ M_{\odot}$.

The key to understand Symbiotic-like Recurrent Novae (Sy-RNe) and their evolution is that the ejected material is not a passive structure, as in classical novae where the ionisation and opacity of the ejecta are governed by the originating WD. In contrast, the ejecta form a powerful shock that propagates through a dense circumstellar medium and dynamically affects the subsequent evolution of the system. Differently from CNe and other explosive events, these systems are not freely expanding, even from the first moments after the explosion. The expelled material from the WD crosses the surrounding disc and expands through the dense and extended RG wind. Unlike CNe, in which the ejecta simply cool while expanding and have constant mass, this never occurs in Sy-RNe. The emission is powered not only by the central WD, but also

from the shocked material crossed by the passing front. The resulting hard continuum is never observed in freely expanding media and lines from high ionisation collisionally excited transitions are observed within the post-shocked gas. The emission strength increases as the evolution goes on and is produced because the highly energetic pulse from the explosion increasingly ionises the wind of the companion. Lines from different types of transitions appear in the spectrum, depending on the process that created them: permitted lines are usually formed in the expelled portion of the WD envelope, emission lines from light species (H Balmer lines, He I and He II, for example), higher ionisation and intercombination lines form in the shocked ejecta as they cool by recombination or collisional excitation in extended and less dense ejecta. The compresence of a strong spectral continuum, intense emission lines and absorption features due to either the neutral or shocked and ionised giant wind profoundly affects the medium in which the shock expands and, more importantly, produces a peculiar spectroscopic evolution of the outburst, that is different from that of other systems.

The known Galactic SyRNe are a few: RS Oph, V745 Sco, V3890 Sgr, T CrB and V407 Cyg. They all have one or more registered outburst at quasi-regular intervals of a few years. This thesis aims for examining the available spectroscopic data of these binaries, most of which were collected in the modern era of CCD spectroscopy and space astronomy. The most extensively studied system is RS Oph, for which numerous but heterogeneous information is available. The most recent outbursts of this nova occurred in 1985 and 2006. In 1985, IUE and EXOSAT gathered extensive data in UV and XRs, but optical data is relatively sparse and not digital or archival for the most part. In contrast, the 2006 outburst was extensively observed in the optical and IR but not in the UV, until the present work. An ultraviolet study of RS Oph is possible because the *Swift* spacecraft had already been launched and provided extended coverage of both UV and XR regions for the system, even if at much lower resolution than the datasets from the previous event. The Swift observations of RS Oph in 2006 remained unexamined and are the main thrust for the analysis in this thesis. In addition, this work presents a spectroscopic study of the outburst of the other Galactic Sy-RNe in the optical, using data acquired with the *European Southern Observatory Ultraviolet and Visual Echelle Spectrograph* (ESO UVES), *Cerro Tololo Inter-American Observatory* (CTIO) SMARTS, Ondřejov Observatory, *Nordic Optical Telescope* (NOT) and several other instruments from the *Astronomical Ring for Access to Spectroscopy* (ARAS) archive, with a particular focus on the evolution of the shock wave during and after the explosion.

Chapter 1

Shock Waves in Symbiotic-like Recurrent Novae

1.1 Shock Waves

Shocks are discontinuous flows with greater velocity than the local speed of sound occurring due to thermal pressure, radiative acceleration or other mechanical sources in almost any physical environment, on Earth as well as in stars and more complex astrophysical contexts ([Hollenbach and Thronson(1987)]). In general ([Glass(1974)]), a shock is a very sharp and thin wave front generated when a gas (but the same could be true for liquids and solids) is subjected to a quick energy release, leading to a sudden explosion. The key is the essentially non-linear nature of the phenomenon. As a result, a volume at high pressure and temperature expands through the neighboring regions. The front alters the surrounding medium making pressure, density and temperature increase and simultaneously inducing a flow behind itself. The front progressively slows down according to the properties of the encountered medium and stalls when it reaches pressure balance with the surroundings. A shock wave is supersonic by definition, and the strength of the wave depends on the *Mach number*, defined as $M = {}^{v}/_{c_s}$, where v is the flow velocity and c_s the local speed of sound. The higher this number (or its variation across the disturbance), the stronger the shock. When a shock crosses a fluid, the overrun medium reaches higher values of density, pressure and entropy than before and such alterations of the material are more substantial for stronger shocks. In astrophysical circumstances, it is quite common that physical conditions are such that expanding shock waves are easily produced, often as consequences of high energies involved in nuclear reactions. In particular, shock phenomena occur when non-linear effects become important and flows are significantly modified ([Mihalas and Mihalas(1984)]). When generated in stellar environments, shock waves are easily discovered because they drastically alter the thermodynamic properties of the gas, especially producing prominent emission lines in the observed spectra.

Shock waves behavior can be described through distinction between two different extremes, depending on their intrinsic properties. For *adiabatic shocks*, the front suffers negligible energy losses, whereas the gas is subject to a net increase of temperature according to mass and momentum conservation laws. *Radiative shocks*, instead, arise when the timescale for radiative cooling is shorter than the dynamical one and they are characterised by energy release from the post-shock gas with resulting decrease in temperature and pressure enhancement due to compression by the front. To describe the onset and the subsequent propagation of a shock wave - for example, in Supernovae and their remnants -, the simplest possible model is a one-dimensional spherical adiabatic flow. The problem was first treated by [Sedov(1959)] and [Taylor(1950)] in the case of an explosion occurring at some point and the evolution of the system can be regarded as the time development of physical parameters as function of fluid velocity and density. If the explosion begins in $r = 0$ with sudden release of energy and then spherically propagates in a uniform medium with density ρ, the resulting shock is one-dimensional. In addition, if there is no characteristic length scale for the medium in which the ejected gas passes, the expansion is *self-similar* (structurally invariant). The blast evolves at constant density ρ_0, maintaining energy E_0 constant while having a decreasing energy density:

$$\frac{E_0}{\rho_0} = L^5 t^{-5} = dimensionless\ constant, \tag{1.1}$$

and this relation directly follows from dimensional considerations. It immediately follows that:

$$R\left(t\right) = \lambda_E \left(\frac{E_0}{\rho_0}\right)^{\frac{1}{5}} t^{\frac{2}{5}}. \tag{1.2}$$

This is the *Sedov-Taylor similarity* solution for an adiabatic blast wave, with R(t) being the time-dependent radius of the spherical shock propagating outward and $\lambda_E = constant$ accounting for the structural details. The shock velocity can be expressed as:

$$V_\Sigma = \frac{dR\left(t\right)}{dt} = \frac{2}{5}\frac{R}{t}. \tag{1.3}$$

The key of the similarity solution is that, once it has been obtained, all physical properties can be obtained in terms of the shock radius R(t) and the dynamical equations have to be solved only once. Similarity solutions can, however, be applied only if the system dynamics is determined by a set of constant properties - energy, momentum or mass through the ejecta.

When an acoustic wave turns into a shock due to a rapid variation in its properties, the front gets sharper and the physical and dynamical quantities are modified all of a sudden through a thin layer characterised by the presence of both viscosity and thermal conduction. This is the main property of shocks and the key to distinguish them from other types of propagating fronts. After its creation, a shock cannot be treated as non-dissipative and adiabatic, such that it propagates while dissipating energy and being damped by this effect, as explained later in this section. For a radiative shock, three different components are usually identified: the radiative precursor heating and partially ionising the environment through hard radiation coming from the shocked layer, the adiabatic shock front consisting of a thin layer in which dissipative processes accelerate and heat the gas, and a wider region dominated by inelastic collisions which come into play through processes of radiative cooling, emission, recombination and downstream compression. If the upstream and downstream traits of the front are fixed in space and time independent, it is referred to as a *steady shock* and the hydrodynamical equations of mass continuity and momentum-energy conservation can be used.

$$\begin{aligned}
\frac{\partial \rho}{\partial t} \ + \ \nabla \cdot \rho \mathbf{v} &= 0 \\
\frac{\partial \rho \mathbf{v}}{\partial t} \ + \ \nabla \cdot \left(p\mathbf{I} + \rho \mathbf{v}\mathbf{v}\right) &= -\rho \nabla \Phi + \eta \nabla^2 \mathbf{v} \\
\frac{\partial \epsilon}{\partial t} \ + \ \nabla \cdot \rho \mathbf{v} \left(\frac{v^2}{2} + \frac{\gamma}{\gamma - 1}\frac{p}{\rho} + \Phi\right) &= p\mathcal{L}\left(\rho, T\right)
\end{aligned} \tag{1.4}$$

where ρ is the density, $\mathbf{v}$ the velocity, $\mathbf{I}$ is the unit matrix,Φ the gravitational potential, η the viscosity, $\epsilon = \rho\left(\frac{v^2}{2} \ + \ E\right)$ the total energy density, E the internal energy, $\frac{\gamma}{\gamma-1}\frac{P}{\rho}$ the enthalpy and $\mathcal{L}$ a volumetric energy loss rate that takes into account all radiative, heating and viscous loss terms.

To determine physical quantities behind the front, shocks are conveniently treated in a reference frame in which the adiabatic front is stationary and their evolution can be described using the so-called *Rankine-Hugoniot relations*, reported in Eq.1.7. These relations ensure the conservation of physical quantities across the two sides in the reference frame of the shock, but admit a discontinuous jump of conditions across the front if seen from another frame. If $\partial_t \to 0$, then across the area A of the shock:

$$\begin{aligned} \int \hat{n}\nabla\cdot(\rho u)\ dA = 0, \\ \int \hat{n}\nabla\cdot\left(p+\rho u^2\right)\ dA = 0, \\ \int \hat{n}\nabla\cdot\left(\epsilon+\frac{p}{\rho}+\frac{u^2}{2}\right)\ dA = 0, \end{aligned} \tag{1.5}$$

so that:

$$\begin{aligned} \left[\rho u\right]_\Sigma = 0, \\ \left[p+\rho u^2\right]_\Sigma = 0, \\ \left[\epsilon+\frac{p}{\rho}+\frac{u^2}{2}\right]_\Sigma = 0, \end{aligned} \tag{1.6}$$

where $[\ ]_\Sigma$ indicates that the quantity is conserved across the front. In another form,

$$\begin{aligned} \rho_1 u_1 &= \rho_2 u_2, \\ p_1+\rho_1 u_1^2 &= p_2+\rho_2 u_2^2, \\ h_1+\frac{u_1^2}{2} &= h_2+\frac{u_2^2}{2}, \end{aligned} \tag{1.7}$$

where the subscripts indicate the two sides of the front and $h=\frac{\gamma}{\gamma-1}\frac{p}{\rho}$ is the specific enthalpy. Rankine-Hugoniot conditions can be written in another form, in terms of sound speed across the front. If $c_{s,i}^2=\frac{\gamma p_i}{\rho_i}$ where i denotes the side of the front, Eq.1.7 become:

$$\begin{aligned} \rho_1\left(u_1^2+\frac{c_{s,1}^2}{\gamma}\right) &= \rho_2\left(u_2^2+\frac{c_{s,2}^2}{\gamma}\right) \\ \frac{u_1^2}{2}+\frac{c_{s,1}^2}{\gamma-1} &= \frac{u_2^2}{2}+\frac{c_{s,2}^2}{\gamma-1}. \end{aligned} \tag{1.8}$$

In terms of upstream Mach number $M_1=\frac{u_1}{c_{s,1}}$ and using the two relations $u_2=\left(\frac{\rho_1}{\rho_2}\right)u_1$ and $\frac{M_1^2}{M_2^2}=\left(\frac{u_1 c_{s,2}}{u_2 c_{s,1}}\right)^2$, the previous conditions can be re-written in alternative form.

$$\begin{aligned} \frac{\rho_2}{\rho_1} &= \frac{(\gamma+1)\,p_1+(\gamma-1)\,p_2}{(\gamma-1)\,p_1+(\gamma+1)\,p_2}=\frac{(\gamma+1)\,M_1^2}{(\gamma-1)\,M_1^2+2}, \\ \frac{p_2}{p_1} &= \left(\frac{\rho_2 M_1}{\rho_1 M_2}\right)^2=\frac{2\gamma M_1^2-(\gamma-1)}{\gamma+1}, \\ \frac{T_2}{T_1} &= \left(\frac{c_{s,2}}{c_{s,1}}\right)^2=\frac{\left[2\gamma M_1^2-(\gamma-1)\right]\left[(\gamma-1)\,M_1^2+2\right]}{\left[(\gamma+1)\,M_1\right]^2}, \\ M_2^2 &= \frac{(\gamma-1)\,M_1^2+2}{2\gamma M_1^2-(\gamma-1)}, \end{aligned} \tag{1.9}$$

so:

$$M_2^2 \rightarrow \frac{\gamma-1}{2\gamma}\ as\ M_1 \rightarrow \infty. \tag{1.10}$$

In an ideal gas, $\gamma = {}^5/_3$ implies ${}^{\rho_2}/_{\rho_1} = 4$ in the strong shock limit $M_1 \gg 1$. The last relation of Eq.1.9 shows that the flow has a lower Mach number after the passage of a shock front.

The previous equations provide a link between the properties of the flow and the discontinuity boundary. In other words, extremely narrow discontinuities are able to provide conservation of mass, momentum and energy fluxes across themselves, without any kind of accumulation of the cited quantities ([Zel'dovich and Raizer(1967)]). In many astrophysical situations, the approximation of planar shock waves is not the best suited to describe the propagation of supersonic fronts in the system, especially when the environment for waves formation is the interstellar medium within two close stellar objects. In such cases, at least the two-dimensional description is needed. If a discontinuity wave crosses two regions that are separated by an interface and whose physical properties are such that the speed of sound changes across it, it is subject to a change of direction, but conservation and jump conditions do not vary across the front. In this case, the shock propagates with an inclination angle through the surrounding gas and consists of two different components relative to the flow velocity: the parallel front undergoes no jump and neither any alteration of physical conditions, whereas the part of the front propagating perpendicular to the flow velocity is subject to a discontinuous jump. The modified and adapted Rankine-Hugoniot relations are listed in Eq.1.11

$$\begin{aligned} \rho_1 v_1 \sin\phi &= \rho_2 v_{2,\perp}, \\ \rho_1 \left(v_1 \sin\phi\right)^2 + p_1 &= \rho_2 v_{2,\perp}^2 + p_2, \\ \frac{1}{2}\left(v_1 \sin\phi\right)^2 + \frac{\gamma}{\gamma-1}\frac{p_1}{\rho_1} &= \frac{1}{2} v_{2,\perp}^2 + \frac{\gamma}{\gamma-1}\frac{p_2}{\rho_2}, \end{aligned} \tag{1.11}$$

where 1 and 2 indicates pre-shock and post-shock quantities, γ is the ratio of specific heats (assumed to be constant) and ϕ the impact inclination angle of the front, in such a way that $v_1 \sin\phi$ and $v_1 \cos\phi$ are the velocity components. A compression front usually has $v_1 > v_2$ and is refracted away from the normal direction by an angle $\chi < \phi$, while a rarefaction shock is redirected on the opposite path. The result is that sound speed of the flow increases after the passage through the compression front. Equations 1.11 can be solved for a compression shock by using the relation $\frac{v_{2,\perp}}{v_{2,\parallel}} = \tan\chi$ and replacing the normal velocity with $v_1 \sin\phi$ on the incoming and $v_{2,\perp}$ on the outgoing side. After the passage of the shock, the conditions become:

$$\begin{aligned} \frac{v_1 \sin\phi}{v_{2,\perp}} &= \frac{(\gamma+1)\,p_2 + (\gamma-1)\,p_1}{(\gamma-1)\,p_2 + (\gamma+1)\,p_1}, \\ \frac{p_2}{p_1} &= \frac{\gamma\left[2M_1^2 \sin^2\phi - 1\right] + 1}{\gamma+1}, \\ M_2^2 &= \frac{2 + (\gamma-1)\,M_1^2}{2\gamma M_1^2 \sin^2\phi + (\gamma-1)} + \frac{2M_1^2 \cos^2\phi}{2\,(\gamma-1)\,M_1^2 \sin^2\phi}. \end{aligned} \tag{1.12}$$

If the shock is planar and incident from the normal direction, this conditions reduce to Eqs.1.9. An additional case is the impact of the gas with a shock of finite curvature radius R. The treatment is similar to that for oblique shocks, but now a finite radius of curvature creates an additional acceleration term to the transverse flow. The interaction is described by:

$$\begin{aligned} \frac{\partial \mathbf{v}}{\partial n} &= \frac{\partial v_n}{\partial n}\hat{\mathbf{n}} + \frac{\partial v_t}{\partial n}\hat{\mathbf{t}}, \\ \frac{\partial \mathbf{v}}{\partial t} &= \left(\frac{\partial v_n}{\partial t} - \frac{v_t}{R}\right)\hat{\mathbf{n}} + \left(\frac{\partial v_t}{\partial t} + \frac{v_n}{R}\right)\hat{\mathbf{t}}, \end{aligned} \tag{1.13}$$

where $\hat{n}$ and $\hat{t}$ are the unit vectors definining the two directions - normal and parallel to the front -, and v_n, v_t the corresponding shock velocity components. If the shock front has an inclination θ, the Mach number of the incident flow can be written as:

$$M^2 = \left(\frac{\gamma p}{\rho}\right)^{-1} |\mathbf{u}|^2 \cos^2\theta. \tag{1.14}$$

In real situations, the steady front is not always a good approximation and other phenomena have to be taken into account. In general, shock compression is more highly affected by viscosity than heat conduction. The viscous force is responsible for the momentum exchange in the gas and the conversion of mechanical into thermal energy, whereas conduction indirectly affects the conversion due to pressure redistribution. As in the previous discussion, viscosity can be neglected and the only dissipative process is conduction, either radiative heat transfer or electron heat conduction. In the absence of viscosity, the state of the gas changes discontinuosly according to the Rankine-Hugoniot conditions. However, when the front is strong, continuous distributions of temperature and density cannot be established if only heat conduction is occurring: a density jump appears, thus viscosity has to be present and is able to remove the strong discontinuity. In the opposite case when viscosity is acting and heat conduction neglected, the environment can be described in a similar manner to the simplest case of continuous solutions for the physical quantities on the two sides of the shock. The only difference is that entropy monotonically increases across the front. In an ionised gas, the relative motion and energy exchange between electrons and ions is important and viscous and conductive dissipation can play a role. In particular, heat conduction is usually more significant for electrons than ions, but the two processes do not considerably differ. In this case, the wave propagates through an already ionised gas and ion viscous forces act on it, converting some fractions of the gas kinetic energy into heat. The temperature of both the ions and electrons increases. This conversion is not the only responsible process: little thermal energy is transferred from the ion to the electron gas, consequently the increase in electron temperature due to viscous force is negligible. Thermal energy is transferred from the ions to the electrons and this leads to temperature equilibration over the *relaxation timescale* $\tau_{ei} \sim \frac{m}{m_e}\tau' \sim \frac{m}{m_e}\frac{1}{N\overline{v}_e\sigma}$ for the establishment of Maxwellian velocity distributions, where $\tau' \sim \frac{1}{N\overline{v}_e\sigma}$ is the collision time, N the total number of gas particles, σ the cross section for collisions between ions and electrons. Behind the compression shock, relaxation occurs in a region of finite thickness equal to many mean free paths, in which density and pressure remain constant, gradients of physical quantities are small and dissipation processes negligibly small. In this environment, dissipation, viscosity and heat conduction only play a role in the region where gradients are large for the crossing shock. In contrast, if the electrons heat conduction is included, the electrons move faster than ions, hence the gradients in the relaxation zone are not negligible anymore. Electron conduction accelerates the process of temperature equilibration, with a resulting pre-heating of the gas ahead of the viscous compression front. In fact, since their velocity is high enough, electrons overcome the shock, going forward and leaving it behind. As a result, ions temperature sharply increases because the hotter electrons transfer thermal energy to them while their own temperature remains constant. When electron conduction is included, the temperature of the electrons and behind the wave are of the same order of magnitude due to the *isoelectron-thermal* nature of the shock, therefore the pre-heating layer prior to the compression front and the relaxation region behind have thickness of the same order. This thickness is generally larger for stronger shocks, but this only holds for non-linear conduction. In contrast, for standard heat conduction with the thermal coefficient increasing for decreasing temperature, the thickness decreases for stronger fronts.

When the shock wave propagates in a stratified medium, the adiabatic approximation is no longer suitable to describe the system. If the shock propagates through a medium with $\rho \propto r^{-\alpha}$, the expansion resembles an H II region, but with a slightly different law:

$$r(t) \sim R_0 \left(\frac{t}{t_0}\right)^{\frac{4}{7-\alpha}}, \tag{1.15}$$

where R_0 is the initial distance of the shock from the central source and t_0 the starting instant of the event. The front sweeps up the surrounding material, but then it is again accelerated and reinforced by the progressively lower density of the neighboring gas; the increasing speed of the front eventually gets so high that it reaches an infinite value in a finite time scale and arrives at a stage of break-out. Treating shocks

passing through dense stratified media is more complicated due to interactions between the discontinuity and gas particles, as applies to SN, young SN remnants, leading to physical processes such as collisional ionisation and recombination, excitation, line emission cooling and even charge exchange in some cases ([Dopita(1977)], [Chevalier et al.(1980)]).

Observationally, shocks in optically thin media generate emission lines of atomic and molecular species. The shock wave can be decomposed into three regions: (a) the radiative precursor that excites and ionises the medium through UV and XR radiation emitted by the post-shocked gas; (b) an adiabatic front that accelerates and heats the shocked gas through dissipative phenomena; and (c) a region dominated by radiative cooling, collisionally excited emission and recombination. Strong intercombination and forbidden lines in wide ranges of ionisation states, as well as ultraviolet emission due to the propagation of the precursor ahead of the shock are the principal diagnostics since the temperature and density in the post-shocked gas regulate the properties of emitted radiation from the region; the *precursor* is responsible for excitation and photoionisation of the pre-shocked gas before the front arrives. This begins with a UV pulse created by the explosion, hence it is capable of ionising atoms at great distance, but this is rapidly subject to recombination because the shock is not sufficiently hot to make ionisation last yet. During violent events, soon after the start narrow emission lines and a strong continuum due to collisional excitation of resonance, intercombination and forbidden transitions of H, He and highly ionised species up to coronal lines created by ions of the iron peak appear in the spectrum. Such lines are the result of the passage of the precursor through the medium, which progressively expands and weakens, as its associated radiative emission supplies gas ionisation. After the passage of the front, the shocked gas cooles and recombines, resulting in emission of forbidden and semi-forbidden lines of heavy elements, for instance [O III] $\lambda\lambda$ 1660 Å, 4363 Å, 4959 Å, 5007 Å, [O II] $\lambda\lambda$ 3727 Å, 7319 Å, 7330 Å, C III] λ 1909 Å, [S II] $\lambda\lambda$ 4069 Å, 6716-31 Å, and C II] λ 2326 Å. Since this is effect is radiative, NLTE rather than due to local kinetic temperature, in the optical spectrum radiative shocks are considered the main source of emission from underionised species like [O I] whose creation ionisation potential is $\chi = 13.62$ eV, [O II] $\chi = 35.11$ eV or [S II] $\chi = 22.52$ eV, very intense ionisation lines at high excitation temperature - [O III] $\chi = 54.89$ eV, [Ne III] $\chi = 41.07$ eV, [Fe VI] $\chi = 72.40$ eV, [Fe XII] $\chi = 252.90$ eV and [Fe XIV] $\chi = 348.30$ eV lines, for example -, the presence of various ionisation states of single species and large intensity ratio between different emission lines ([Hollenbach and Thronson(1987)], [Shore(2002)]). In the ultraviolet, unmistakable traces of shock waves formation and propagation are strong resonance and semi-forbidden lines of ionised species, such as Si III] with ionisation potential for creation $\chi = 16.34$ eV, C III] $\chi = 24.38$ eV, O III] $\chi = 35.11$ eV, N III] $\chi = 29.59$ eV, O IV] $\chi = 54.89$ eV, C IV $\chi = 47.87$ eV and N V $\chi = 77.45$ eV, and these lines can also be employed for the determination of shocks physical parameters such as density, velocity, temperature and chemical composition. All these features are also used to distinguish dynamical structures due to fast shocks from other sources, such as H II or other photoionised regions. Shocked environments show spectral lines that are not observed in other types of photoionised and photoexcited regions, mostly because of the different instrinsic nature of density jump: it is incompressible in an HII region, on the contrary it is compressible in shocks and this makes collisionally excited ionic lines an important diagnostic tool for shock phenomena.

1.2 Symbiotic-like Recurrent Novae

Novae are binary systems with interacting components, one of which is a compact star as a white dwarf and the other a cooler object, a red dwarf or a red giant. Among the wide classification of such objects, systems like RS Ophiuchi et similia are included in the class of *Symbiotic-like Recurrent Novae (Sy-RNe)*, a peculiar category of violent bodies defined as binaries in which a massive White Dwarf *(WD)* orbits within the wind or the extended atmosphere of an evolved Red Giant *(RG)* star. In turn, Sy-RNe are part of a larger hierarchy, that of Recurrent Novae *(RNe)*, i.e. binaries with mass transfer from a late-type secondary star to a white dwarf primary that exhibit more than an observed outburst over their lifetime, with recurrence timescale $\sim 10 - 100\ yr$, much shorter than that of Classical Novae ($\sim 10^4 - 10^5\ yr$). In general, the term *symbiotic-like* is associated to interacting binaries of this type because, as observed in symbiotic stars, either cool star features, such as absorption bands, and nebular and more highly ionised emission lines appear simultaneously in the spectrum, e.g. in [Nussbaumer and Stencel(1987)].

Of the known Recurrent Novae, ten are Galactic, two are sited in the Large Magellanic Cloud and some

in M31. These systems are sub-divided into two classes, depending on their orbital period ([Jose(2016)], [Shore(2002)]). The *short period Recurrent Novae* are similar to Classical Novae *(CNe)*. They have orbital periods from a few hours to about 1.5 days and are composed of a Main Sequence or subgiant star and a WD companion. There are six known Galactic systems of this type (U Sco, V394 CrA, KT Eri, LMC1968, CI Aql, IM Nor, T Pyx). Our focus is, instead, on the *long period Recurrent Novae*, RS Oph, V745 Sco, V3890 Sgr and T CrB, whose orbital periods are more than a few hundred days and in which a hot massive white dwarf (near the Chandrasekhar limit) is bound to a cold red giant companion. Another system is now included, V407 Cyg, that was classified as a D-type symbiotic binary with long pulsation period for the Mira variable until, in 2010, it was discovered in outburst in close resemblance to the spectroscopic development of RS Oph ([Shore et al.(2011)], [Shore et al.(2012)]).

As in CNe, the vicinity and different masses of the two components throughout their evolution make such binaries the perfect sites for the occurring of continuous mass transfer from the red giant, which typically loses mass onto the companion. This process usually occurs through the low-mass component filling its own Roche surface and expelling material ($\dot{M} \sim 10^{-7} - 10^{-10} M_{\odot}\ yr^{-1}$, depending on the evolutionary stage of the companion) through the inner Lagrangian point (L_1). Because of its angular momentum, the inflowing mass spirals into the WD as an accretion disc and the build-up of hydrogen-rich material on its surface raises the temperature at the lower boundary. This occurs because, when a fraction of the ejected material from the secondary falls on the primary star, it gets progressively compressed by continuous infalling of material. The WD envelope is at least partly degenerate and the ions are increasingly heated by compression. Nuclear burning sets on, but the degeneracy prevents the envelope from dynamically re-adjusting through expansion. The nuclear energy generation rate is high enough to produce a *thermonuclear runaway (TNR)* that powers the nova eruption. Nova outbursts are, therefore, the sudden expansions of huge amounts of dense material, with disturbances in the energy balance of the star leading to the release of great energies and the propagation of a shock wave, whose main effect is to accelerate the gas layers past the sound speed until they can escape, while the front itself steadily steepens during the propagation; this stratum separates from the surface of the star and emits a gas cloud into space. In this, novae explosions in symbiotic systems resemble a miniature version of type II Supernovae, but with lower energy (the peak luminosity is $\simeq 10^5 L_{\odot}$ in Novae and $\simeq 10^{10} L_{\odot}$ in Supernovae) and ejected mass ($1.4\ M_{\odot}$ in SNe, $10^{-4} - 10^{-7}\ M_{\odot}$ in Novae) and shorter timescales for the shock evolution. For example, the overall dynamics of aspherical expansion of the ejecta after the outburst - especially in RS Oph - has been often compared to the explosion of SNII 1987A ([Wang et al.(2002)]). Differently from a Classical Nova, the shock wave propagates through the red giant wind interstellar medium, and this is, again, similar to what happens when a wave due to the core collapse of a Supernova propagates through the wind of its massive progenitor. Both Novae and Supernovae can be naturally regarded as immediate explosions originating from a central source in a spherically symmetric background, with a smaller value for the thickness of the stratum that powers eruption than for the stellar radius and the fastest material from the outburst reaching further distances in the shortest time.

The major difference is that, in CNe the white dwarf remains after the eruption and, in general, outbursts are confined to the outer accreted envelopes. The similarities in explosion features between these two systems induces resemblances in the observational counterpart, too: both SNe and RNe show spectral traces of the iron curtain and resonance lines with strong P Cygni profiles superposed, even if they begin to differ when characteristics of the initial shocks and of the overall velocity field are considered.

The conditions that lead to the onset of the thermonuclear runaway are the same for the two classes of novae, and their origin can be found in the accretion of Hydrogen-rich material from the non-degenerate star to the compact gainer.

Novae of both types require a white dwarf as the gainer. The bulk of the accreted gas is made of hydrogen and piles up until the base of the accreted layer reaches and overcomes the energy threshold for the ignition of nuclear burning. The subsequent TNR in both systems accelerates the accumulated material away from the white dwarf through an expanding shell, whose velocity is usually thousands of km/s ([Townsley(2008)], [Sekiguchi(1995)]). For this reason, Recurrent Novae expel lower masses of gas, but at higher velocities. This provokes the sudden brightening of the objects typical of such events, which generally lasts for some hours or days, after which the nova brightness begins a decline phase in the following weeks and months. In CNe, the nova ejecta contains material from the white dwarf (carbon and oxygen for CO-WD, oxygen, neon and magnesium for O-Ne-Mg-WD) and the star gets eroded after many

outburst cycles, whereas in RNe heavy elements like C, O, Ne are not enriched in the ejected gas, therefore the white dwarf is not eroded. Elemental abundances for these objects can be derived through proper modelling of spectroscopic observations and measurements. In particular, early phases are characterised by the predominance of elements around the iron peak, with UV absorptions and optical emissions; in fact, in early stages densities are large and temperatures moderate, the envelope is degenerate and the set in of nuclear reactions is such that the high involved energies cannot be transported only by radiation: convection is needed since superadiabatic gradients are present in the envelope, and this process carries Fe-peak nuclei from the deeper layers to the outer cooler regions of the envelope. On the contrary, the usual behavior of later spectra is to principally show CNO nuclei in emission, with very weak Ne and Fe lines.

Moreover, while in CNe some elements of intermediate mass are overproduced in ejecta relative to solar abundances - N, O, C, species with $A < 10$, S, Cl, Ar, Ca are some examples -, in RNe expelled material shows huge amounts of H and He but no overabundance of heavier species than Ca with respect to solar values; in addition, species like Li, O and Ne are scarcely produced, while S and Ar are slightly overabundant in RNe ejecta. After the explosion, the compact star remains intact and the accretion begins again. On the other hand, RNe are characterised by higher white dwarf masses, smaller white dwarf radii, much higher escape velocity and accretion rates, hence much shorter inter-outburst periods: the greater surface gravity of the WD requires a lower mass to ignite the eruption, while the higher rate means that material is being accumulated more rapidly, consequently the trigger value is reached sooner. Another difference is the orbital period, typically a few hundreds of days for Sy-RNe and less than one day for Classical Novae. After the explosion, differences become more evident due to the different nature of constituents of the two system; since the mass donor is a red giant instead of a less evolved star, the fast ejecta expand through the denser circumstellar matter of the red giant's wind. During quiescence, most Recurrent Novae are more luminous than Classical Novae because of the greater accretion rate and the red giant nature of the companion [Jose(2016)]. Spectroscopically, novae of either type show predominantly emission lines of various species, with broad profiles due to several different processes taking place during the event. Recurrent Novae commonly show higher velocities than CNe and this translates into greater width of line profiles.

To sum up, features that characterise Recurrent Novae are small amplitude eruption, high surface gravity, high ejecta velocity and the presence of bright accretion discs with high mass loss rates, along with long orbital periods, fast ejecta. Observationally, RNe are usually associated with bright quiescent phases in the near infrared part of the electromagnetic spectrum, the appearance of plateau in the light curve and the detection of high excitation spectral lines during explosions. The key point to understand the physical and dynamical evolution of a Recurrent Nova outburst is that the total ejected mass is finite and expanding, consequently the shell undergoes different phases and its optical depth is subjected to several changes over time. In the early phases, the ejecta are initially small, dense and optically thick in almost every spectral region, the shell expansion occurs rapidly with respect to the thermal timescale for the gas, so the adiabatic expansion quickly lowers the temperature while a huge increase in opacity occurs. The process of adiabatic cooling takes place while the central source remains at constant bolumetric luminosity, thus radiation shifts to longer wavelengths and the maximum in optical luminosity is produced by flux redistribution of ultraviolet radiation at high opacity. Soon after the peak luminosity, the ejecta become progressively thinner and the density of the shell diminishes. Then, after the rise of the shock fronts in the expanding envelope, their passage through the medium and collisions between ejecta and circumstellar material, the surrounding environment gets heated from the compressional mechanism and this increase in the temperature of the material provokes a further fall of opacity in the outer layers. Within a few years after the outburst, the ejecta can often be seen as small, nebulous shells surrounding the post-nova star.

1.3 Stages of the outburst

Even though the general mechanism for the evolution of close binary systems before and after the explosion phase is well described by the progression mass transfer - thermonuclear runaway - propagation of the shock wave and the corresponding ionisation front through the wind and circumstellar material, it is instructive to go more deeply into the single steps of such a complex turn of events ([Shore(2012)], [Shore(2014)], [Darnley and Henze(2020)], [Darnley(2021)]). The development of outburst phases is ac-

companied, as a counterpart, by the spectroscopic evolution of the systems. The first step to consider is the accretion stage on the white dwarf, induced by mass transfer from the larger companion; the actual mechanism for this to happen is still under debate ([Wynn(2008)]), but two main candidates have been brought into play and they both probably occur. The first hypothesis is that mass transfer occurs through *Roche lobe overflow (RLOF)*: the giant filling its Roche lobe. On the other hand, the white dwarf may gravitationally capture a fraction of the wind from the giant, leading to mass transfer through *stellar wind capture (SWC)*. The separation between stellar components is large enough that the wind is terminal. Therefore, if the transfer is partially or entirely due to the wind, one can consider the flow of material coming from infinity with velocity v_∞ equal to the terminal velocity of the wind. It is gravitationally deflected and begins accreting. For an accretion stream of this type, the flow goes from supersonic to subsonic creating an oblique shock wave and producing compressional heating of the gas while it falls onto the central star. The shock also dissipates kinetic energy and further refracts the flow outward. The condition for wind capture, *Bondi-Hoyle flow* ([Bondi and Hoyle(1944)]), is:

$$r_\star \simeq \frac{2Gm_{WD}}{v_\infty^2}, \tag{1.16}$$

where $r_\star$ is the critical radius. The accretion rate is lower than $\dot{M}$, the mass loss rate from the giant, since:

$$\dot{M} \simeq \rho v_\infty^2 r_\star^2, \tag{1.17}$$

so:

$$\dot{M}_\star \simeq \rho_\infty \frac{\pi G^2 M^2}{m_p v_\infty^2} \approx \left(\frac{G^2 M^2}{m_p a^2 v_\infty^4}\right)\dot{M}, \tag{1.18}$$

where m_p is the mass of the proton, ρ_∞ the outflow density from the companion at the WD and a is the separation between the components. From EXOSAT observations in the XRs, we know that, for example, the red giant in RS Oph has a mass loss rate $\geq 10^{-9}\ M_\odot\ yr^{-1}$, consistent with a recombination timescale of $\sim$ 6 months and an ambient mean density $\sim\ 10^6\ cm^{-3}$ [Shore(2008)]. The wind carries angular momentum, so direct accretion is improbable even in systems with such long orbital periods. Consequently, a disc forms around the WD, by supplying mass and transferring angular momentum from the inner to the outer parts of the white dwarf. Such an accretion disc is formed as lost material from the donor component of the binary accumulates around the white dwarf before being transported on its surface; during actual eruption phases, this disc is perturbed or disrupted, but then it appears to rapidly re-form. Since outbursts of novae similar to RS Oph are produced by thermonuclear runaways, to set up the energy loss sufficiently high amounts of mass ($\sim 4\times10^{-6}M_\odot$) have to be accreted on the white dwarf surface to ignite hydrogen burning and other nuclear reactions. In several systems, transport of mass from the giant to the dwarf is more easily promoted by the deflection of the red giant's wind towards the orbital plane due to the gravitational push from the companion and accretion through stellar wind capture seems to be more likely ([Mikolajewska(2008)]). At the current state of the art, the majority of Sy-RNe are the scenes of mass transfer via stellar wind capture, though few peculiar giants may be more probable donors of material through Roche lobe overflow.

[Springel(2005)] and [Mohamed et al.(2012)] used the *Smoothed Particle Hydrodynamics (SPH)* GADGET-2 code to model the quiescent mass loss and outburst phases of RS Oph, taking into account effects of the binary motion, stellar wind, accretion and cooling, although it does not include the internal structure of the two stars. The RG loses mass through injection of low velocity particles near the surface in such a way that material is lifted beyond the RG's Roche lobe but does not escape from the binary. From the simulation, the dense wind is confined in the orbital plane and it soon provokes the formation of two spirals. Among these structures, the first is caused by the gas that escapes from the system through the outer Lagrangian point, while the other is created when the outflow of material coming from the Roche lobe crosses the inner Lagrangian point, as Fig. 1.1 shows. During this phase, both a shock and an accretion disc are formed. The disc reaches the boundary of the Roche lobe of the WD. The wind from the RG plays an important role in the model: since the WD runs through it during this steady mass accretion process, the relative motion between the two binary components make some part of the wind fall onto the WD and

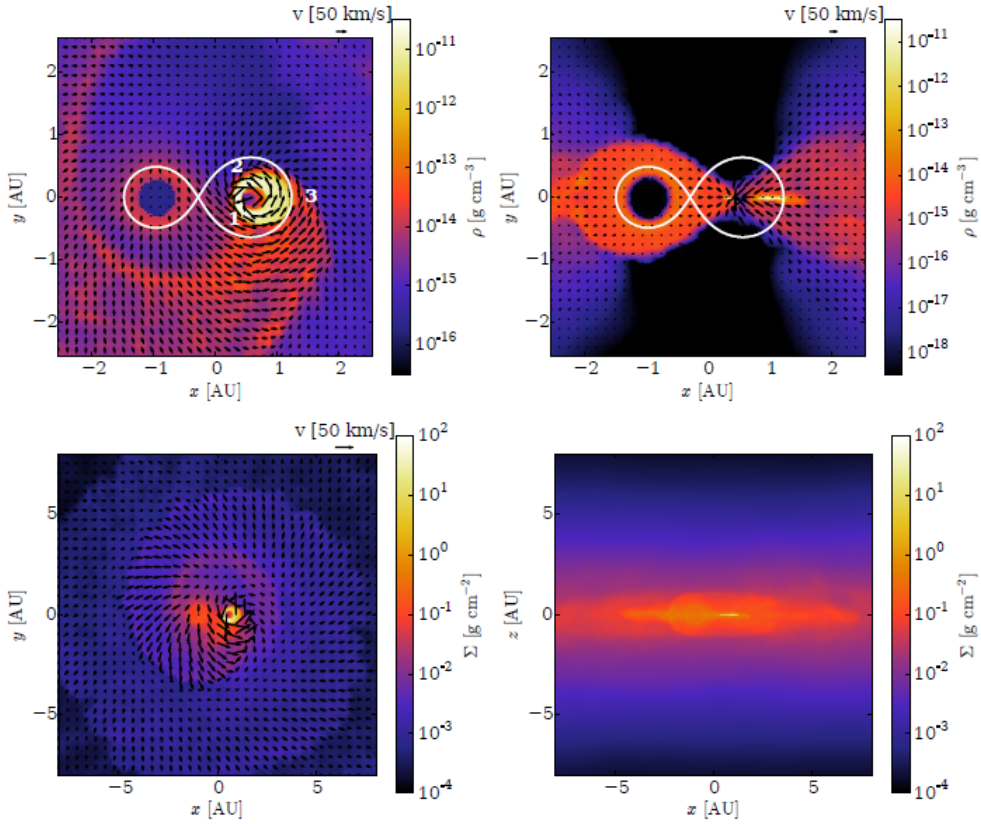

Figure 1.1: Modelling mass loss during quiescent phases of the Recurrent Nova RS Oph. The Red Giant component is the one on the left, the White Dwarf and the accretion disc on the right. In the first panel, numbers represent the overflow from the Roche lobe (whose boundary is depicted by the white solid line): (1) interacts with the wind, (2) and (3) create the two spiral structures. The lower panel displays the merging of spiral streams and the wind stratification. ([Booth et al.(2016)])

the accretion disc because it is no longer able to support itself. The WD passing through the wind of the RG also produces the formation of a polar inflow in the system, with gas falling back on the binary. The rise of this asymmetry in the simulation is consistent with what is observable from RS Oph itself. According to the simulation, the mass transfer phase in RS Oph would be conforming with this scenario and, in particular, X-ray observations could be successful in explaining emission - of $H\alpha$ line with broad wings, for instance - as the settling of shocked material from the polar inflow on the WD.

The appearance of dynamical spiral structures during mass transfer is consistent with the results of simulations performed through 3D hydrodynamical models, for example the one in [Walder et al.(2008)], who employed the code A-MAZE, an adaptive mesh refinement (AMR) hydrodynamical code that uses Cartesian meshes and a multi-dimensional high-resolution finite-volume integration scheme. In the simulation, the evolution of RS Oph from the mass accretion phase (through the RG wind only) to the subsequent explosion and post-outburst stages was modelled adopting a nearly isothermal polytropic equation of state with $\gamma = 1.1$ and a co-orbiting reference frame.

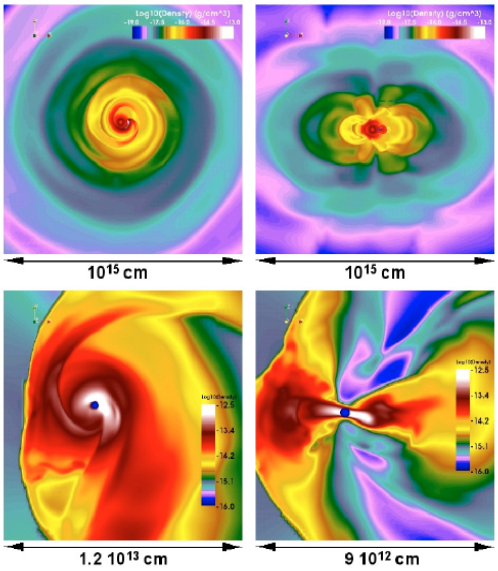

(a) Mass accretion stage. The density is displayed in logarithmic scales and gcm^{-3} units. The upper panels show the entire computational domain, with the xy-plane on the left and yz on the right, whereas the lower plots consist of a zoom around the accreting WD, in the same planes as above.

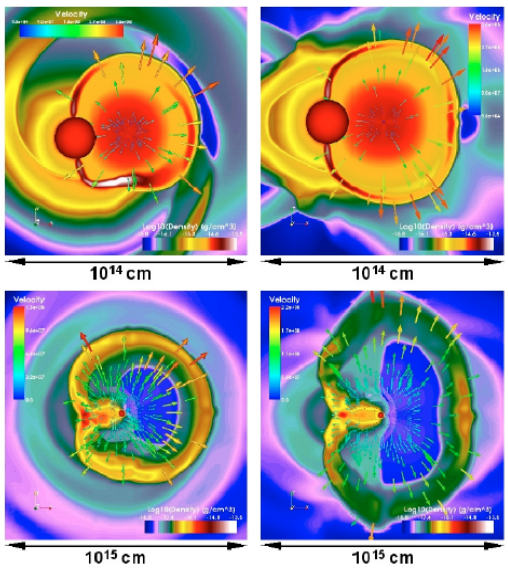

(b) Outburst phase. The density and velocity are displayed in logarithmic scales and gcm^{-3}, cms^{-1} units. The upper and lower panels show the system 29 hours and 21 days after the explosion, respectively.

Figure 1.2: Density distribution from the 3D hydrodynamical simulation of RS Ophiuchi in [Walder et al.(2008)]. The Red Giant is shown in red, the White Dwarf in blue.

The two components were simulated as spherical regions of radii $2.2 \times 10^{11}\ cm$ and $150\ R_{\odot}$, respectively, with physical conditions so that a mass accretion rate of $10^{-7} M_{\odot} yr^{-1}$ could be achieved. At first, the red giant wind entirely dominates the system, which is then relaxed over the crossing time for the evolved stellar component and momentum losses are eventually computed in such a manner that, when they become constant, the outburst was triggered in the relaxed structure. Fig.1.2(a) illustrates the resulting density structure, which is extremely dependent on the ratio between the RG wind and the orbital velocities. When $v_{RG} \gg v_{orb}$, the orbital plane shows a spiral pattern; orbital speed can be written as $v_{orb} = \frac{2\pi a}{P}$ and the assumed velocity and known orbital period are $v_{RG} = 20\ km\ s^{-1}$ and $P = 455\ days$, consequently, in RS Oph $R \equiv \frac{v_{RG}}{v_{orb}} \leq 1$ and the spiral pattern becomes self-interacting while a dense accretion disc starts forming around the WD. When the outburst is initiated, a sudden injection of energy and mass in the system produces a highly asymmetric shock. This is shown in Fig.1.2(b), where the density distribution is shown for the remnant of the outburst. The shock is more extended in the poleward directions due to the mass enhancement in the orbital plane with respect ot the poleward direction during the quiescent phase of accretion. The subsequent evolution of the remnant from the explosion is non-spherical and faster toward the poles.

In a similar way, the cited SPH simulation is useful to model the early evolution and it seemed to agree with the hypothesis of mass accretion through Roche lobe overflow, for RS Oph at least. In fact, one of the results from the simulation was that, after the accretion of mass, nova showed a highly bipolar structure: this can be only originated by a slow wind, therefore mass accretion is more likely induced by low velocity material filling the Roche lobe than by wind. UV observations of the 1985 outburst of RS Oph ([Shore(2008)], [Shore and Aufdenberg(1993)], [Shore et al.(1996)]), instead, took a slightly different stand, in better agreement with the assumption of the other 3D model. In their interpretation, the strength of wind emission features in the UV line development signaled the likely absence of Roche lobe overflow at the origin of the Nova activity. Wind and mass flow cannot simultaneously be present in the binary, so mass supply should be provided to the white dwarf by a wind. Their calculation of spectral line widths through measurement of the Full Width at Half Maximum (FWHM, in $km\ s^{-1}$) for the narrow emission component of line profiles was consistent with typical values of Red Giant winds speed, $\sim 90\ km\ s^{-1}$.

Independent of the accretion details, the white dwarf reaches a point where it can accumulate no more mass because of its degenerate nature and, as a consequence, a TNR sets up and provokes the explosion: in Classical Novae, the runaway is produced as a feedback to the ignition of nuclear reactions on the surface of the compact object because the enviroment initially cannot dynamically respond to the rapid rise in energy generation rate and the consequent heating. Material expelled from the surface of the white dwarf expands into the surrounding medium, especially through the wind of the red giant. In the first steps of this stage, the radiation pulse is highly energetic and ionises the wind. Then, this composite and hot material passes through the outer extended layers of the red giant wind and alters the shape of the shock moving outwards, which causes a decrease in the density of the expanding gas; as a consequence, ejecta becomes progressively thinner and the optically thick surface (the effective photosphere) starts moving inwards, in such a way that it becomes possible to observe more deeply in hotter and slower layers. To better visualise how the system is organised and where the different components are located, Figs. 1.3(a) and 1.3(b) show schematic representations of the binary and what is going on to the different regions of a Symbiotic Recurrent Nova during outburst.

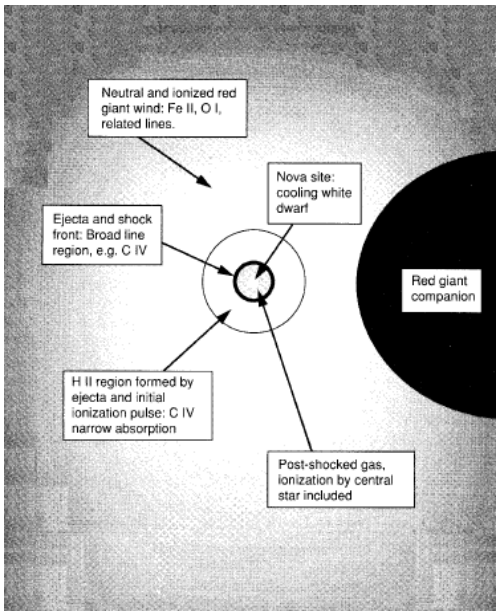

(a) [Shore(2007)]

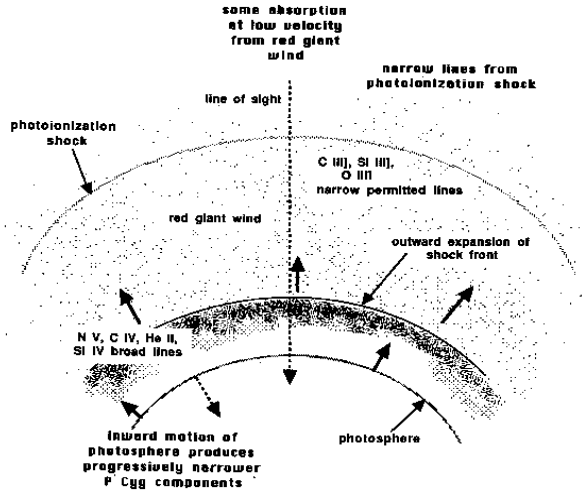

(b) [Shore et al.(1996)]

Figure 1.3: Expanding ejecta through Red Giant wind during outburst.

This scheme is consistent with the results of SPH simulations ([Booth et al.(2016)]): when nova shells are introduced in the model after the end of mass transfer, the expelled material over-runs and expels the disc. Due to the density gradient between the two regions, the higher density accretion disc deforms the ejecta from the nova making it bipolar in structure. This environment is shown in Fig.1.4: the bipolar lobes and the ring are produced by expelled material from the nova and the wind, respectively. At this time, the shock front arising from the density gradient runs in the polar direction through the equatorial ring and the accretion disc, with resulting higher temperatures and density in the whole environment.

Similar final results were presented in another 3D hydrodynamical model, FLASH ([Fryxell et al.(2010)]), based on the adaptive mesh refinement (AMR) for the 2010 eruption of V407 Cyg ([Pan et al.(2015)]). The model neglected the nuclear burning, varying mass accretion rate and time-changing wind velocity, so the calculation treated the eruption as a Sedov-like explosion centered on the white dwarf. As shown in Fig.1.5, after about one week, the forward shock front has swept up the wind from the red giant, while the reverse shock travelled back toward the white dwarf (A and B in the image, respectively). The forward front arrives at the edge of the cold stellar companion at about 15 days and triggers the onset of *Rayleigh-Taylor (R-T)* discontinuities due to the great density differences (C in figure). The shock then overruns the RG, provoking substantial heating and compression of the star, the wind and the circumbinary density en-

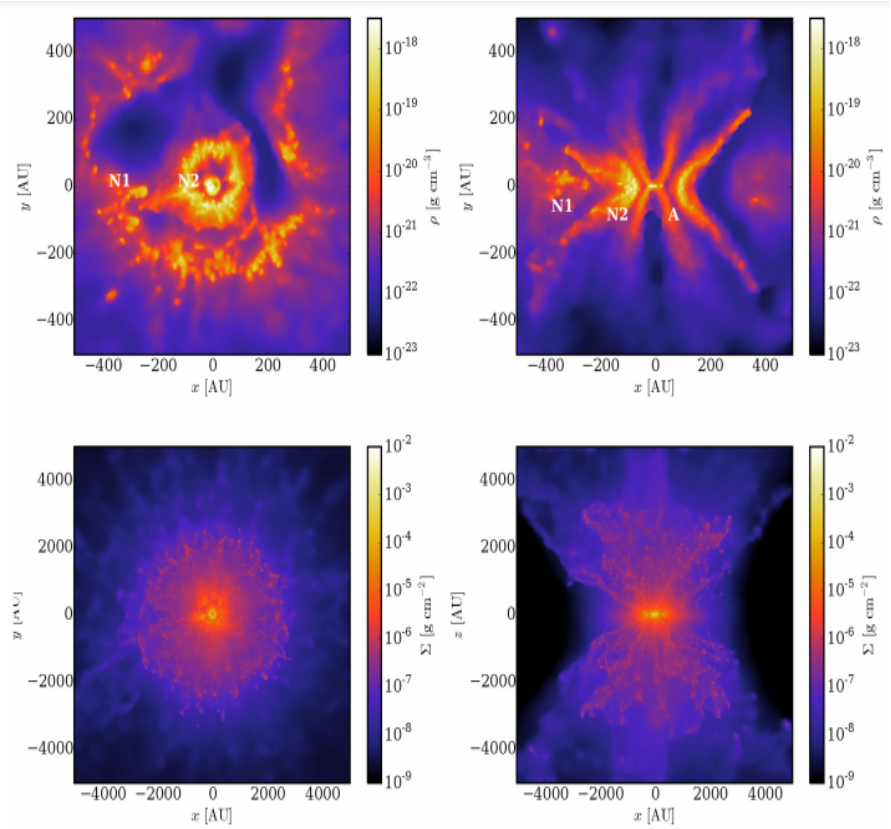

Figure 1.4: SPH simulation of the outburst of RS Oph ([Booth et al.(2016)]): in the upper panel, the equatorial ring formed by the swept-up wind material in two successive nova explosion (N1, N2) and the evaporative wind from the accretion disc (A). In the lower panel, the bipolar structure due to the interaction between the accretion disc and the wind.

hancement (CDE) around the white dwarf. At this point, the forward shock interacts with the spiral arm and more numerous reverse shock waves are created as a result. These fronts slam into each other and the outcome is the appearance of additional shocks with filamentary shape (E in the picture). These filaments are repeatedly formed and destroyed by the reverse shocks, while the spiral arm is destroyed during this stage, which occurs about 70 days after the eruption.

The two simulations show that there are actually two separate fronts propagating in the medium, the forward proceeding into the stellar wind and the reverse shock that propagates back toward the otherwise non-shocked ejecta ([Walder et al.(2008)], [Metzger et al.(2014)], [Orlando et al.(2017)]). A schematic representation of the described environment is pictured in Fig.1.6

High Mach numbers, of order $\sim 10^2$ are usually associated with the initial propagation of the forward shock, but then the value is expected to decrease over time, from about $M \geq 10$ in the first week after the eruption to $M \simeq 5$ until a few months after the establishment of R-T instabilities. The evolution shows almost freely expanding ejecta with nearly spherically symmetric shock location at the very beginning of the outburst. The propagation of the forward shock is slightly faster in the orbital plane rather in the direction of the pole. Then, the ejecta begin digging out gas: when a sufficient amount of material has been swept up, momentum conservation weakens the shock front and its velocity reduces. The rate of decline is strongly dependent on explosion energy, mass loss rate from the red giant and density of the circumbinary density enhancement around the white dwarf. Fig.1.7 displays how the system evolves as a result of four simulations with different values of these parameters, listed in Table 1.1.

As a result, the shock radius evolution can be modelled as a power law:

$$r_{shock} \propto t^{\alpha}, \tag{1.19}$$

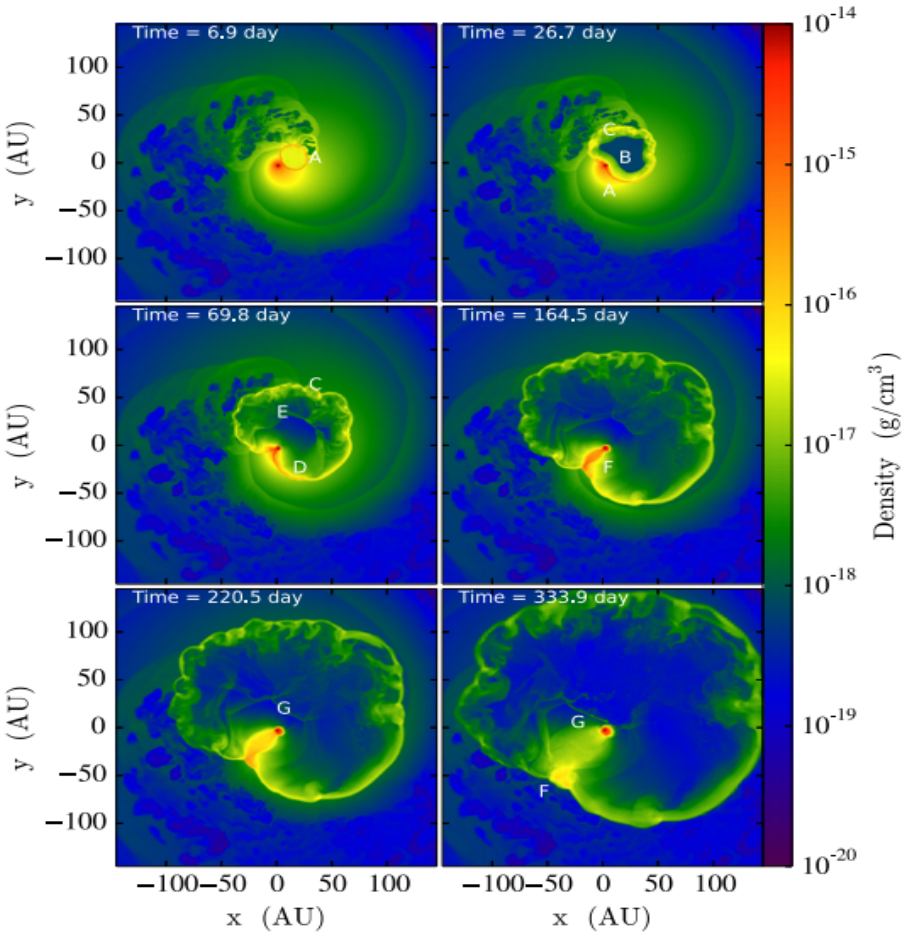

Figure 1.5: Simulation of the outburst of V407 Cyg ([Pan et al.(2015)]): schematic of a typical gas density distribution in the orbital plane after the eruption. The color scale indicates the logarithm of the gas density in $g\ cm^{-3}$. A labels the RG wind and the spiral arm, B the WD; C indicates the presence of Rayleigh-Taylor instabilities, D the passage of the shock through the RG wind, E the formation of filament-like shocks, F the high-density tail at the back side of the RG, G the interaction between many reverse shocks.

where α is a constant whose value depends on the stage of evolution. In particular, $\alpha \simeq 0.5 - 0.8$ in the first week, then it progressively decreases until 100 days after the eruption, due to the interaction between the front and the RG and the resulting decrease in the orbital plane velocity component. More than 100 days later, α increases again when the forward shock has overrun the RG. This model of shock wave evolution is in good agreement with what actually occurs during the outburst. Since most of the detected emitted radiation comes from the interaction between the RG wind, the propagating shock and the circumbinary matter, it is essential to understand how shock waves growth proceeds in order to have deeper insight of the dynamical and physical processes leading to spectral lines formation.

1.4 Light curve evolution during outburst

To distinguish between the different stages of a Recurrent Nova outburst, it can be useful to look at the differences in light intensity during the whole event. Light curve is the amount of emitted energy in a specific wavelength range of the electromagnetic spectrum per unit time and will, indeed, reflect all the changes in physical and dynamical properties of the system. As described in Section 1.3, the sequence will show common traits between various objects.

Even if Recurrent Novae have a similar cause to Classical Novae, the key features of their evolution

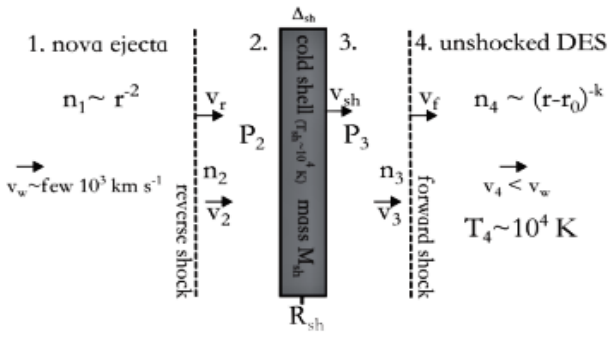

Figure 1.6: In this graphic scheme of the shock wave propagation in the surrounding medium, region 1 indicates the nova outflow, which interacts with the dense external shell (DES, region 4) through the interplay between the shocked ejecta (region 2) and shocked DES (region 3), separated by a cold neutral shell containing the swept-up mass. The forward shock is driven into the DES, while the reverse front is driven backwards into the ejecta ([Metzger et al.(2014)]).

during outburst are fundamentally different. A Classical Nova runs a gamut of stages during explosive events: they usually show an initial rapid rise until a maximum optical brightness phase is reached in $1 - 2\ days$, then after some hours or a very few days begin to drop and tend to re-establish the pre-outburst luminosity through a decline toward quiescence. During the decline phase, at first the ejecta are usually optically thick and prevent the observer to see the central source until, at about 3-4 magnitudes below the peak, they turn optically thin and the star is visible from outside. The rate at which the ejecta become optically thin depends on the expansion velocity and mass and affects the resulting evolution in brightness and its timescale. In general, the most luminous Novae are also the most rapid to fade. When quiescence is established, light comes predominantly from the accretion disc and usually show activity on short timescales, from seconds to minutes: fast flickerings briefer than minutes are typical signs of ongoing mass accretion and are formed in the impact region between the accretion flow and the disc. In contrast, the interaction between the ejecta coming from the compact WD with the dense wind flowing from the RG affects the evolution of SyRNe. After the explosion, these systems never enter a freely expanding phase and the next stages are also different, because the ejecta never simply cool and neither the accretion flow has constant mass as in CNe. Observational examples of light curves from RNe are presented later in Section 3.3 about data analysis, here some details about the general expected behavior are reported.

1.5 Spectral line evolution

As a probe of what is happening and to have an idea of the driving mechanisms, spectroscopy provides the useful tool. The spectral energy distribution (SED) and individual lines give information about what is happening in the different parts of the system. It is, therefore, important to understand where line formation takes place and follow spectral variations while physical conditions are changing over several orders of magnitude. The most important difference between the evolution of the ejecta in CNe and SyRNe is that the mass of the ejecta increases over time due to the loading of material provided by the RG wind. This changes both energy and momentum of the system and the resulting spectral development is intrinsically different. Another important point is that, unlike CNe, the upstream gas is heated and ionised by the precursor and subsequently swept up (in part) by the shock. This fundamentally alters line formation compared with freely expanding material.

Single line profiles show substantial changes over time, and the overall spectral evolution provides clues about the state of ejecta and central sources ([Shore(2013)], [Williams et al.(1991)]). In SyRNe, the slow red giant wind at $v_w \simeq (a\ few\ tens)\ km\ s^{-1}$ into which the fast ejecta at $v \simeq (a\ few\ thousand)\ km\ s^{-1}$ run generate emission lines appearing on top of a strong continuum at all wavelengths, especially in the early phases of the eruption, when forward shock is moving into a $1/r^2$ density distribution. For instance, strong coronal lines appear in optical spectra of almost all known Recurrent Novae. They are usually very similar between different outbursts and are always formed due to shock heating during the supersonic

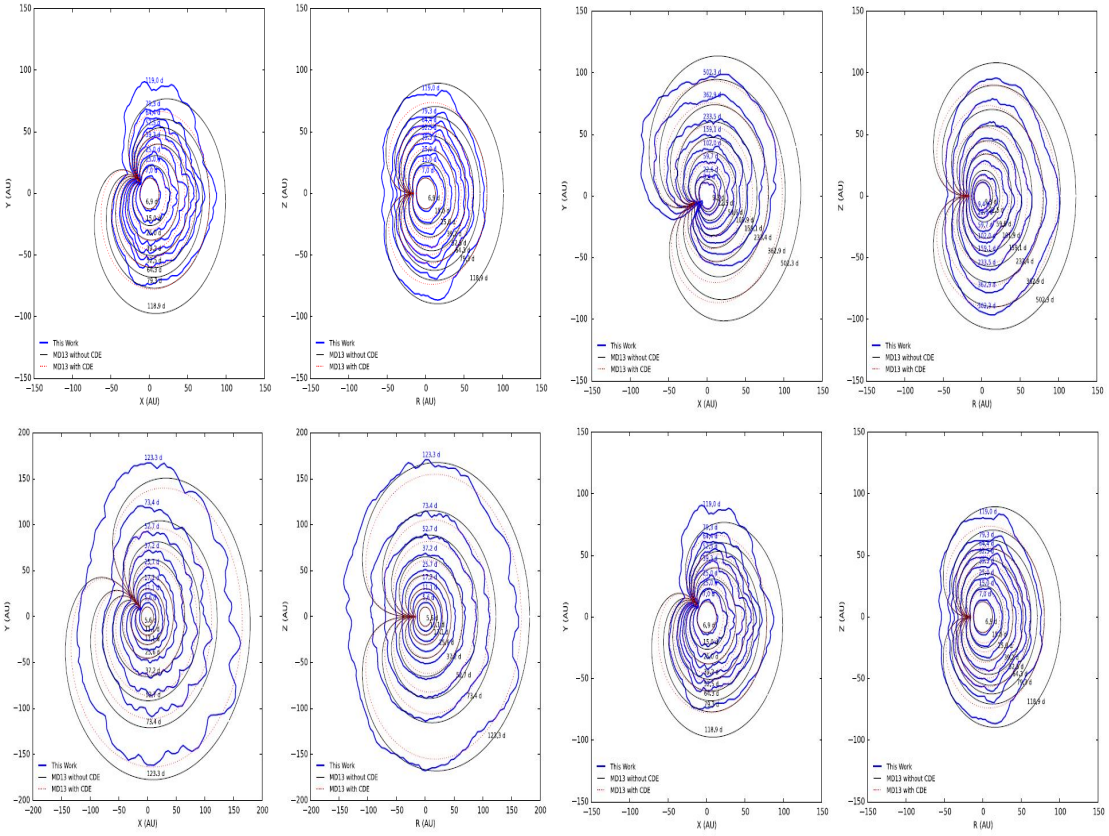

Figure 1.7: Shock waves evolution in 3D hydrodynamical simulations ([Pan et al.(2015)]). From the top left to the bottom right, four models with different values of wind mass loss rate, eruption energy and ejected mass. Blue contours indicate the shock radius evolution at different times, black contours a comparison with analytical models, red dots analytical models with circumbinary density enhancement included.

Model	$\dot{M}_{wind}(M_\odot\ yr^{-1})$	**A (A.U.)**	$v_{wind}(km\ s^{-1})$	$T_{wind}(K)$	$E_{ej}(erg)$	$M_{ej}(M_\odot)$
M6E43	10^{-6}	16	20	7000	1.2×10^{43}	10^{-7}
M6E44	10^{-6}	16	20	7000	1.2×10^{44}	10^{-6}
M7E43	10^{-7}	16	20	7000	1.2×10^{43}	10^{-7}
M7E44	10^{-7}	16	20	7000	1.2×10^{44}	10^{-6}

Table 1.1: Adopted values in 3D hydrodynamical simulations for the shock radius evolution of Fig.1.7 ([Pan et al.(2015)]). The columns contain the reference name for the simulation, RG mass loss rate, binary separation, RG wind speed, effective wind temperature, eruption energy and mass of the ejecta.

expansion of nova ejecta through circumstellar material from the wind.

With Mach numbers exceeding 50 at the start of the expansion, the post-shock gas reaches $\approx 10^7$K, and the emitted XR (> 1 keV) suffices to produce emission from [Fe X], [Fe XI], [Ar XI], [Fe XIV], [Ar X] and similar coronal during the early stages of the outburst. These are initially narrow (of the same order as the wind velocity). The excitation of these lines is by electrons, still only around 10^4K and thermalised from the precursor, also once the shock accelerates the gas the line widths suddenly increase if the density is still sufficiently low ($\leq 10^7 \mathrm{cm}^{-3}$). Other forbidden lines arise from lower ionization species, e.g., [O III]. These forbidden lines have typical critical densities of order $10^5\ cm^{-3}$ so they trace gas encountered in the wind periphery (at many system separations). The Balmer H and He I and II emission lines are also produced by both shocked and non-shocked ejected material.

The permitted spectral lines trace the expanding ejecta. The appearance of blue-shifted narrow absorption lines ([Shore et al.(2011)], [Iijima(2008)], [Iijima(2012)], [Iijima(2015)], [Iijima(2014)]) arise from the circumstellar wind from the red giant. During the quiescent mass loss phase preceding the explosion, emission comes predominantly from the region near the gainer, where material from the RG accretes on the WD companion; the ionization is limited to He^+ and O^{2+}. Absorption lines (or absorption components on emission profiles) originate in the photoionised wind close to the binary, while the outer part of the wind should create emission of neutral or singly ionised species. Orbital modulation traces the effects of the cooler wind ([Shore and Aufdenberg(1993)]).

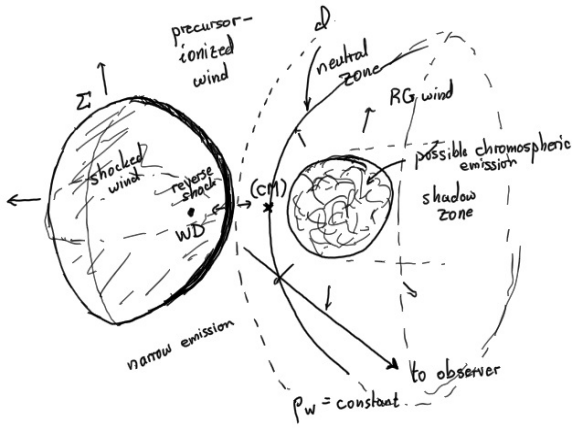

Figure 1.8: Schematic model for lines formation in a Symbiotic-like Recurrent Nova (Shore 2021, private comm.).

A cartoon of the regions where line formation occurs is shown in Fig. 1.8. The structures may persist even at the end of the mass accretion stage, hence some spectral features could still be present in the succeeding phases. Post-outburst SyRNe spectra are always dominated by emission lines and, at different stages of evolution of various binaries, spectral changes can be significant over time intervals from days to years. It is important to recall that the development of a CN spectrum is essentially different than the cases treated here. The freely expanding ejecta in the classical systems (including the short period RN), are passive converters of the illuminating continuum of the remnant WD. The spectral development follows a pattern driven by the changes in the emission from the WD but mainly caused by the density drop in the ejecta. The so-called *iron curtan* stage, which may also occur in the earliest freely expanding epoch of SyRNe, produces a rapid increase in UV line opacity when the temperature of the ejecta fall below about 20,000 K. This is only expected for the SyRN in the first week or so of the expansion, before the ejecta have appreciably increased in mass (e.g., [Walder et al.(2008)]). The higher ejection velocities seen in the recurrent systems, along with their lower mass (about 10^{-2} the mass of the non-recurrent systems) means the lines turn optically thin very rapidly and the additional heating of the post-shocked gas ensures that the ionisation never falls sufficiently to produce the curtain. Consequently, the light curve is driven by the dynamics of the ejecta, not their radiative reprocessing, and the long plateau phase seen in most classical systems does not occur. The precursor, instead, contributes to changes in the rate of decline from the post-shocked gas continuum, as the recombination driven emission lines (especially of the Balmer series) can produce several tenths of a magnitude.

However, although many features substantially change over time, the dynamical origin for some components of spectral profiles is common between distinct lines and make them detectable even when overlying and additional structures are present. In the early phases immediately after outburst, density is sufficiently high that emission lines are predominantly from permitted transitions. The encountered medium gets progressively denser but the ionisation level continuously increases and forbidden lines begin to appear in addition at later times. The reference starting point for the outburst is usually taken as the maximum in visual light of the system and steps for time (and phase) dependent analysis are calculated in days after this zero point. Within about one month later, spectra are generally dominated by strong emission lines overlapping a broad continuum due to the non-equilibrium between electrons (which originate continuum) and ions (producing lines); H Balmer and other neutral or singly-ionised lines (from He, O, N, Fe and others) are particularly strong and broad at this stage, whereas coronal lines are barely noticeable. After two months or so, lines are already narrower and show a higher degree of ionisation. Coronal lines and He II are now much more intense, doubly and higher ionised species show up, together with larger amounts of forbidden and shock-driven emission lines like Mg II, O III. At this stage, the transition from predominantly permitted to high excitation forbidden lines normally occurs in short time intervals. Another month later, excitation and intensity of the emission lines are substantially reduced, some neutral or singly ionised species like O I, He II, Fe I and N I significantly weakened and are almost invisible; a bit of absorption from the red giant begins to appear too, mostly through the appearance of TiO bands and components of red continuum from the secondary late-type companion, which progressively stengthens as continuum from nova envelope fades. More than 100 days after the beginning, a general decrease in both intensity and excitation degree of emission lines is conspicuous; coronal lines are usually still present, H, O and He lines persist even if their strength is lower. When the outburst is definitively over - one or more year after time zero -, the giant completely dominates the spectrum, with very strong and narrow Balmer lines, but also components from He, Fe and overimposed emission lines. This progression in the emergence and fading of spectral lines of different kind during and after outburst is fairly satisfied by the known members of Symbiotic-like Reccurent Nova class of objects ([Anupama and Prabhu(1989)], [Shore et al.(1996)],[Gonzalez-Riestra(1992)],[Williams et al.(1991)]).

The line profiles observed during the outburst stages of SyRNe are composite and, because the ejecta are essentially optically thin, trace the wind and shock structures separately. The appearance of forbidden lines of higher ionisation species, the *coronal stage*, is driven by the XRs and FUV. Although it is so called because one sees the same lines as those in the Solar corona, their origin is substantially different. The corona is a magnetically dominated atmosphere whose temperature is maintained by non-thermal heating mechanisms, primarily magnetic reconnection and shocks. The ionization states, such as Fe^{13+} and beyond, result from collisional ionisation equilibrium within the plasma. In contrast, the SyRN are dominated, initially, by photoionisation of the precursor, hence the ionisation equilibrium is actually never established. There is an additional radiative source, one related to the WD. The so-called *supersoft stage* (SSS) is the soft XR emission from the residual nuclear burning on the WD. This adds to the shock-generated precursor emission and dominates the wind ionisation after shock breakout. Hard XRs significantly influence the forward shocked gas ([Vaytet et al.(2011)]). Ionisation of the ejecta continues growing while opacity keeps decreasing and the source dominates the state of the expanding gas for several months. The latest and final stages of the nova evolution are characterised by narrow stellar emissions when the site of the explosion is no longer contaminated by the ejecta. It is a *dead* phase from a dynamical point of view, but it is the stage at which the different contributors of the spectrum features can actually be distinguished. The post-outburst spectrum is usually identified by the presence of strong absorption lines from the red giant and by high neutral and single-ionised metallic optical depths sufficing to hide circumstellar emission from the white dwarf. There is a progressively more relaxed behavior of the compact body and a very quick recombination of the surrounding ambient gas. At the very end of the outburst phase, the wind from the red giant has largely recombined, the white dwarf is in a renewed quiescent state at a relatively low temperature; during this quiescence, the system is usually not undergoing any eclipse and the dominant spectral component is radiation from the red giant wind.

The UV and optical line profiles show two contributions: (1) a very broad wing due to the very fast but optically thin material that has been expelled from the white dwarf and expands later on and this dominates the shape of the lines until about 60 days after the explosion, and (2) a narrow feature, whose formation occurs because the explosion generates high-energy UV photons that lasts until about 100 days

after the start of the explosion, beyond which shock wave break-out occurs and recombination processes of the previously ionised wind become the main source of emission. The breakout occurs because, during outburst, the wind from the red giant is swept up by the shock wave which, at a certain point, reaches the effective boundary of the wind (when the mass of the ejecta is approximately constant and the ejecta are cooling).

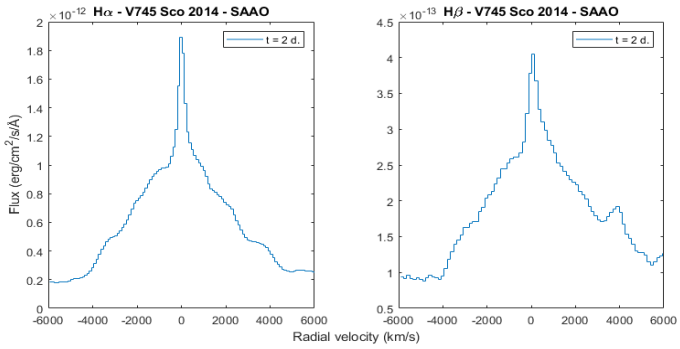

Figure 1.9: V745 Sco 2014: examples of spectral line from the dataset used in the present work. Extracted Hα 6563 Å and Hβ 4861 Å Balmer lines in observation done by the South African Astronomical Observatory on MJD 56696.1

Fig.1.9 is a representative illustration of this features of spectral profiles: the two components, the narrow and the broad one, are clearly visible in both lines. The outburst spectrum initially shows broad emission lines whose widths decrease over time as the high velocity ejecta expand with $v_{exp} \geq 4 \times 10^3\ km\ s^{-1}$ ([Anupama(2008)], [Skopal et al.(2008)]). Line profiles may even show broad wings with different components - a narrow and a broader part extending on both sides of the narrow one, and likely asymmetries in the blue and red edges of the wings depending on the environmental structure. The progressive narrowing of the early broad lines is due to the distribution of the velocity field at the moment of gas expulsion, that is the gas at higher speed will cover a greater distance in an equivalent time step. Over time, the cooling of the expanding gas proceeds along with decreasing density and emissivity of the environment, while ionisation goes up as a consequence of the activity of the hot body. These features are expected to be seen in lines profile and can be used as signals of an actual explosion rather than a mass transfer episode. Meanwhile the shock and ionisation front propagate through the red giant wind, the narrow lines showing up in the spectrum mark the appearance of the effects of the Strömgren sphere formed by the hot ionising radiation of the primary star.

Initially, only broad permitted lines dominate the spectrum, then after the luminosity peak both strong coronal and high excitation lines are visible. They usually have a narrower profile compatible with the dynamics of the processes causing their appearance. These lines disappear progressively as the nova evolves and finally vanish when it enters the nebular phase, during which new profiles show up as a consequence of the emergence of the secondary star's spectrum. During quiescence, the optical spectrum is dominated by the red giant photosphere, with emission from neutral hydrogen and helium powered by the steady emission from the WD and its disc (as in symbiotic systems), while higher ionisation states are absent. Quiescent emission profiles often show narrow central absorption very similar to what is expected to see in presence of slow dense wind. The transition of spectral lines from intense emission to absorption is a signal of the end of any interaction between ejecta and the giant's wind. The variability in shape and details of spectral lines in quiescence reflects the activity of the white dwarf embedded in the wind envelope from the companion. The line strengths change as a result of accretion rate fluctuations due to unsteady mass transfer or disc instabilities, or some components may vary according to column density changes in the absorbing envelope of the wind, which is optically thick.

In the latest stages, the red giant and its wind dominate the spectrum. During quiescence the ambient wind is at first partially ionised only in the region closest to the WD, then it gets significantly ionised all of a sudden due to the highly energetic radiation produced in the explosion and rapidly starts recombining as the nova ejecta progressively expand; fast ejected material keeps expanding through the pre-existing dense gas from the RG and is more and more decelerated until the wind almost completely stops the

expansion ([Munari(2019)]). This is the phase at which the emitted radiation from the red giant wind vastly overcomes and covers that from the white dwarf, becoming the dominant spectral component. Strong evidence of the presence of the wind is the displacement to which many lines are subjected to: relative to the corresponding rest wavelength, the vast majority of lines will show a blueshift due to the huge velocities involved and perhaps even the effects of the Strömgren sphere shape around the binary. The value of the shift is presumed to differ depending on the affected species, with the result that permitted resonance lines will be less altered than the highest ionisation ones. Another cause for the blueshift is the propagation of the shock and, in particular, the emission from post-shocked part of the wind: the gas downstream of the shock is cooling and reducing its expansion speed, consequently radiation coming from this region modifies the observed spectrum. The prediction is that different components of line profiles are due to different contributions from the wind: the steady gas in the ionised region and the inner part of the wind affect the low-velocity emission, the shock-heated layer and the outer wind prevail in the high-velocity constituent of emission profiles. Besides, transitions in the inner wind are expected to show an additional redshifted and asymmetric line component ([Nussbaumer and Vogel(1987)]). The wind does not have a well-defined boundary, but it can be ideally outlined a frontier where the shock is not able to further power the ionisation of the wind, i.e. the so called *breakout* stage. In the spectrum, the passage through this phase is marked by the predominance of narrow emission lines over resonance lines in the optical and any other emission line in the ultraviolet. After the shutdown of the ionisation source, recombination of the gas starts to predominate, neutralise the HII region and make the optical depth of the wind enhanced. As the opacity along the line of sight of the dwarf is forced to increase after the breakout, emission from the central source softens and the spectrum is dominated by the cooler components of the binary system ([Shore et al.(1996)]).

A probe of the presence of the wind is the absorption on low ionization species (e.g., Na I, Mg I/II, Ca II, Fe II (and related species), Si II, Sc II) seen against the WD and ejecta. These absorptions disappear in the first few weeks as the combined effects of precursor photoionisation and shock compression alter the density and temperature of the environment. The Balmer lines are especially important here because their absorption strength reflects the UV pumping of the $n = 2$ state by the Lyman series, powered by the explosion (these would not normally appear in such cold wind environments). The weakening of this component is mainly caused by the expansion of the shock into so large a volume that the emission overwhelms the P Cyg trough ([Shore et al.(1996)]).

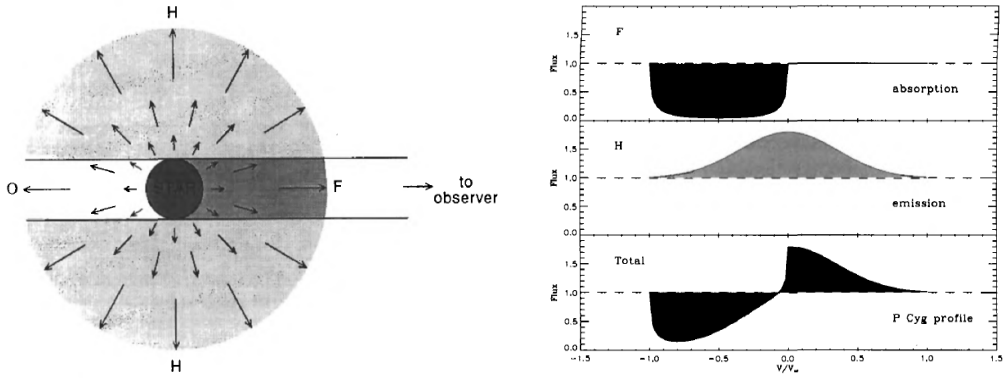

Figure 1.10: Formation of P Cygni profiles ([Lamers and Cassinelli(1999)]). S represents the star that emits a continuum, F a tube in front of the stellar disk in which the gas is moving toward the observer, O the occulted tube by the star with gas flowing away and radiation not reaching the observer, H the region that would be observed as a halo surrounding the star if the wind could be spatially resolved.

Fig. 1.10 shows a scheme of the creation of this type of profile feature, while Fig. 1.11 displays the noticeable presence of P Cyg and other absorption structures in the spectra of the nova V407 Cygni. In particular, the upper panel shows absorption components at low velocity ($v_{max} \simeq -65\ km\ s^{-1}$) on H$\alpha$ and Hβ lines from the Balmer series, which remain visible throughout the outburst, with decreasing strength and width. As shown in the lower panel, these features appear also on the other lines of the

H series and are caused by recombination in the RG wind, hence they map the structure of the wind. Additional absorption components show up on the blue wings of the strong emission lines: on Hα, they are mostly due to atmospheric water molecules, whereas lines from Y II 4855 Å , Ti II 4856 Å and Cr II 4857 Å appear on Hβ wing during the early stages of the outburst ([Shore et al.(2012)]).

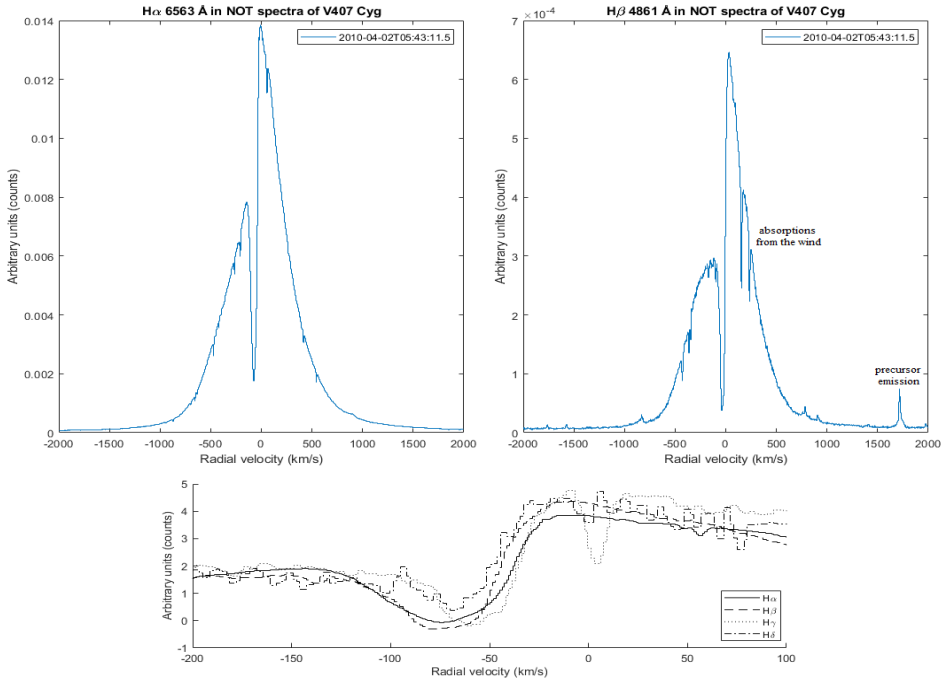

Figure 1.11: V407 Cygni 2010: extracted Hα and Hβ Balmer lines during the outburst. Observation done with the Nordic Optical Telescope on MJD 55288.2. In the lower panel, comparison between absorption components on lines of the Balmer series.

Different regions of the wind give different contributions to the rise of the profile: radiation from the central star creates the continuum with absorption lines, then this radiation is scattered by the gas in the region surrounding the star and never reaches the observer because of the presence of the wind. In addition, SyRNe also display shadowing effects and further contribution from the cromosphere and heated sub-WD side. Over timescales from one to some years, the WD changes its orbital phase relative to the RG wind and this changing position results in extinction effects similar to an atmospheric eclipse. The main outcome is that the *observed* WD continuum is altered by absorption from the wind. The scattered photons are responsible for the blue-shifted absorption component (and also produce Rayleigh scattering, as known for the symbiotics ([Skopal et al.(2008)]). Soon after the beginning of the outburst, the strongest lines are UV resonant transitions, which probe the expansion of fast ejecta and are responsible for the presence of P Cygni structures; but then the ejected material further expands and the external regions of the expanding shell get progressively more optically thin: as the very high-velocity material become less dominant in the formation of absorption components on spectral line profiles, P Cygni features become thinner as a result. Another possibility is that P Cyg traits may disappear or actually never appear if the ejection from the white dwarf is greatly asymmetric or the shell of expelled material breaks up into smaller components. For this reason, P Cyg structure are expected to fade when the nebular phase begins and Novae are more likely to show such features in optical spectra - for which resolution is sufficiently higher - than in UV observations ([Shore(2007)]).

1.6 Description of the targets

To describe the behavior of symbiotic-like recurrent novae in details, the best illustration is given by systems themselves and their peculiarities. Each known binary of this kind has specific aspects that make it

unique and different from every other even in the same categorisation, but several properties are in common and can be easily identified. Major features of the known Galactic Recurrent Novae are summarised in Table 1.2.

Star	Orbital period (days)	M_{WD} ($M_\odot$)	Recurrence time (years)	Recorded outburst
				1898, 1933, 1958
RS Oph	455	1.36	18	1967, 1985, 2006
V745 Sco	uncertain	1.35	25	1937, 1989, 2014
V3890 Sgr	519	1.30	28	1962, 1990, 2019
T CrB	228	1.37	80	1866, 1946
V407 Cyg	1.6×10^4	1.20	uncertain	1936, probably 1998, 2010

Table 1.2: Schematic summary of the main properties of long period Symbiotic-like Galactic Recurrent Novae ([Hachisu and Kato(2001)]).

In this section, a panoramic of the main characteristics of the systems is made and the general scenario is depicted.

1.6.1 RS Ophiuchi

RS Ophiuchi (RS Oph) is a Symbiotic Recurrent Nova located at a distance of $d \simeq 1.6 \pm 0.3\ kpc$ from the Sun ([Bode(2010)]), displaying an apparent magnitude of about 12.5 in the V-band during its quiescent phase and eruptions every 22 years or so, reaching values up to $\sim 5\ mag$. The known outbursts occurred in 1898, 1907, 1933, 1945, 1958, 1967, 1985, 2006. The two components of the binary are a Red Giant of type M0/2III and a White Dwarf with an orbital period of $P_{orb} \sim 455\ days$ and a separation between components $a = 2.68 \times 10^{13} cm$. The system displays very small eccentricity, inclination between $30° - 40°$ and lacks of optical eclipses ([Dobrzycka and Kenyon(1994)]). The compact star of the system is massive, having a value close to the Chandrasekhar limit $M_{WD} \simeq 1.2 M_\odot$, whereas the bigger component has a much lower mass, $M_{RG} = 0.8 M_\odot$. In the process of mass transfer, the red giant plays the role of the donor and, since its radius ($R_{RG} \sim 10^{13} cm$) seems to be lower than the Roche lobe radius (using the Eggleton relation, $R_{RL} = \frac{0.49 q^{2/3}}{0.6 q^{2/3} + \ln\left(1+q^{1/3}\right)} a \approx 9.21 \times 10^{12}\ cm$, where $q = \frac{M_1}{M_2} \simeq 0.66$), transport likely occurs via the giant wind. Estimates of the mass loss rates give $\dot{M}_{RG} = 10^{-7} M_\odot\ yr^{-1}$ ([Shore et al.(1996)]) at $v_{RG} = 20\ km\ s^{-1}$ ([Mohamed et al.(2013)]). The most recent outburst occurred in 2006, during which the system ejected about $M_{ej} \sim 1.1 \times 10^{-6} M_\odot$ at energies of $\simeq 1.1 \times 10^{43}\ erg$ ([Ness et al.(2009)], [Walder et al.(2008)], [Bode et al.(2006)]). The 2006 outburst was the first one of this Nova to be observed in wider wavelength ranges: until the previous outburst in 1985, only optical surveys were performed. It is considered the prototype for this sort of objects and it is still under debate whether it may be the progenitor of a type-Ia Supernova or not.

1.6.2 V745 Scorpii

At a distance $d = 7.8 \pm 1.2\ kpc$ the outbursts of V745 Sco occur every 25 years or so and have been registered in 1937, 1989 and 2014. The components are an M6III giant and a $M_{WD} \simeq 1.3 M_\odot$ white dwarf, with a dubious orbital period. According to different determinations, estimates through optical observations during quiescence vary from $P_{orb} \simeq 510 \pm 20\ days$ to $P_{orb} \simeq 137\ days$, $P_{orb} \simeq 77\ days$ and $P_{orb} \simeq 100\ days$ ([Page et al.(2015)], [Schaefer(2009)], [Schaefer(2010)], [Mróz et al.(2014)], [Delgado and Hernanz(2019)]). During the eruption, the apparent magnitude can increase up to $9.4\ mag$ at the maximum peak, with total energies of the order $\sim 10^{43}\ erg$ and the ejected mass is around $M_{ej} \sim 10^{-7} M_\odot$. The total lost mass is more or less one order of magnitude below the accreted mass required for the explosion to be triggered. This means that the white dwarf component is accreting mass from the companion and this makes V745 Sco an ideal candidate as a SN-Ia progenitor, because the WD mass is near the Chandrasekhar limit and, if it is made of carbon and oxygen, the C in the center can ignite, leading to the explosion as a type-Ia Supernova. The total mass loss rate before the thermonuclear runaway is estimated around $\dot{M}_{wind} = 3 \times 10^{-7} M_\odot$ and

it occurs at a velocity rate of $v_{wind} = 10\ km\ s^{-1}$. When the outburst begins, the initial expansion velocity is $v_{exp} = 3 \times 10^3\ km\ s^{-1}$, while the shock wave propagates through the medium at $v_{sh} = 4 \times 10^3\ km\ s^{-1}$ ([Drake et al.(2016)], [Page et al.(2015)]). This is a very rapid nova, it fades $2 - 3\ mag$ between $6 - 9\ days$ and, during the 2014 outburst, it reached a visual magnitude of 9. During its quiescence, the red giant shows pulsations of period 136.5 and $77.4\ days$.

1.6.3 V3890 Sagittarii

V3890 Sgr is at a distance $d = 5.2\ kpc$ from the Sun. It is usually included in the category of RS Oph-like systems, being similar in dynamical and spectroscopical evolution. The most recent photometric and spectroscopic studies of this Sy-RN during quiescence ([Mikołajewska et al.(2021)]) proved that the two components are a massive WD with $M_{WD} = 1.35 \pm 0.13\ M_\odot$ and a lighter M5III giant with $M_{RG} \simeq 1.05 \pm 0.11\ M_\odot$, that presumably fills its Roche lobe ([Anupama(2008)], [Anupama and Mikołajewska(1999)]). The inclination of the orbit is $\simeq 67 - 69°$, the orbital period is estimated by photometric observations performed through AAVSO and SMARTS data as $P_{orb} = 227.53 \pm 0.17\ days$ ([Schaefer(2010)]). The binary underwent recorded outbursts in 1962, 1990 and 2019. During the latest explosion, the luminosity increased to an apparent magnitude of about $8\ mag$ at the peak. Photometric and spectroscopic observations made during quiescence showed some continuous flickering on timescales of tens of minutes and amplitudes of $\sim 0.03\ mag$ with increasing amplitude toward the blue and also a $103.8 \pm 0.4\ days$ periodicity due to small pulsations of the red giant. The source of this activity is linked to the likely presence of an accretion disc around the WD and caused by variations in the accretion rate of the system.

1.6.4 T Coronae Borealis

T Coronae Borealis (T CrB) is often used as reference model to study the quiescence stage of symbiotics. The main reason for this is that the most recent outburst of this RN occurred 75 years ago and it was only observed in the visible wavelength range. Consequently, detailed comparisons between this and other symbiotic binaries can only be made during quiescence. Comparing the inter-outburst behavior of the other RNe and the obervation of T CrB reveals that the vast majority of novae has UV fluxes decreasing during quiet phases: since the white dwarf's activity dominates this wavelength range, the effect is due to the simultaneous effects of cooling of the white dwarf and decreased accretion rates during quiescence. Two outbursts of T CrB have been registered, in 1866 and 1946, even though the two component of the systems are always active. A mirror of this activity is the strong X-rays emission up to energies of $E_{max} \sim 100\ keV$ even during quiet stages. The White Dwarf is a massive one, $M_{WD} \simeq 1.1 M_\odot$, while the secondary object is a M3III Red Giant of lower mass, $M_{RG} \simeq 0.7 M_\odot$. It is at a distance of $d = 1.3\ kpc$, has an orbital period $P_{orb} = 227\ days$ and can reach an apparent V magnitude of $2.5\ mag$ at maximum peak during eruption. Differently from similar novae, mass transfer in T CrB is characterised by low accretion rates, $\dot{M} < 3 \times 10^{-9} M_\odot\ yr^{-1}$ and is probably due to the interference of an accretion disc surrounding the WD. This accretion disc has an optically thin boundary layer and the inner part radiates like an optically thin plasma at about $\sim 10\ keV$ ([Luna et al.(2008)]). The presence of such a boundary layer is one of the main differences between T CrB and RS Oph: the latest one shows the lack of - or, maybe, just a very low luminosity - a boundary layer during quiescence and an optically thick accretion disc. The most likely reason for this is the rapidly rotating RS Oph white dwarf, compatible with its high mass and huge amounts of accreted mass and angular momentum ([Mukai(2008)], [Szkody et al.(1991)]). Another important issue of the behavior of T CrB is orbital modulation in the fluxes of the emission lines, which is also noticeable in quiescent spectra of RS Oph. It is due to the intrusive presence of the environment, in particular of the RG wind, which produces absorption features and variations in the continuum structures that vary over time, following the orbital modulation ([Shore and Aufdenberg(1993)]).

1.6.5 V407 Cygni

V407 Cyg is a Symbiotic Recurrent Nova consisting of a massive White Dwarf and a M6III Mira-type Red Giant, i.e. a cold pulsating variable star with a long pulsation period of 763 $days$. It was discovered in outburst in 2010, when it reached a luminosity $< 8\ mag$ and is the first symbiotic nova detected

in γ-rays. The orbital period of this system is uncertain, while the orbital separation $a \simeq 16\ AU$. The distance from this binary is uncertain, but approximately in the range $d \simeq 1.7 - 2.7\ kpc$. During outburst, it ejects $M_{ej} \sim 10^{-6} M_{\odot}$ material with a speed $v_{ej} \sim 3200 \pm 345\ km\ s^{-1}$ and energy $E_{ej} \sim 10^{44}\ erg$, while the pre-TNR mass loss rate from the RG is estimated to be $\dot{M}_{wind} \sim 2 \times 10^{-6} M_{\odot}\ yr^{-1}$ at $v_{wind} = 10\ km\ s^{-1}$ ([Martin and Dubus(2013)], [Munari et al.(1990)]). Observations of the 2010 outburst ([Iijima(2012)], [Iijima(2015)], [Iijima(2014)]) were consistent with the theoretical assumptions that the cool component of the binary is a Mira variable and, moreover, that the system shows light curve variations with a period of $\simeq 750\ days$, which may be due to pulsations of the variable. The wind of the Mira is driven by radiation pressure during pulsation and the acceleration zone of this quasi-spherical outflow is comparable to the binary separation, hence mass transfer leading to violent eruption of the system is likely due to wind capture again. When thermonuclear runaway sets off, about one week after the beginning of the outburst the expanding shock wave has a velocity $v_s \simeq 800\ km\ s^{-1}$, sweeps out the Red Giant wind and creates a reverse shock propagating backwards into the ejecta and towards the White Dwarf. The main consequence of this double propagation is the sudden development of Rayleigh-Taylor instabilities on the contact surface between the two. As the evolution keeps going, the shock slows down due to momentum conservation and the velocity of the ejecta decreases too ([Pan et al.(2015)]). In the bigger picture, the explosion of V407 Cyg is not spherical, the wind is less confined toward the orbital plane and the material expulsion less collimated than other similar systems ([Shore et al.(2011)], [Shore et al.(2012)]).

Chapter 2

Instruments and Datasets

Thanks to the wide range of different physical, dynamical and chemical processes and situations that occur during the lifetime of a symbiotic system, Recurrent Novae can be studied in almost every wavelength region. In the last decades, interest has grown toward deep and *panchromatic* analysis of these kind of objects, with the purpose of a better understanding of the mechanisms and details leading to their recurrent explosions and either to predict some scenarios for their subsequent development. From a spectroscopic point of view, Recurrent Novae with symbiotic behavior portray an inestimable source of investigation of physical and dynamical processes at different orders of magnitude for what concerns the parameters into play. It is the reason why these systems have been examined in virtually all spectral regions, X-rays, radio, ultraviolet, optical and infrared. Due to involved high energies (and temperatures), the ultraviolet part of the spectrum is an ideal laboratory to inspect these violent stars, mostly because the light we see coming from such binaries is primarily emitted radiation from the white dwarf, a compact body which is usually very hot and bright. Photons coming from the White Dwarf, however, strongly interacts with the surrounding wind of the Red Giant, and this dominates the electromagnetic spectrum, because of the Strömgren sphere and absorption through the iron curtain. Ejecta flowing within the wind and the expanding H II region after the eruption produce noticeable variations in the ionisation of the circumstellar matter and, since UV region is the most strongly altered by absorption from the cool gas and emission from the ionised wind, spectra in this range are precious to study changes to the ionisation structure of the system. Plasma diagnostic in the UV part of the spectrum is fundamental for the inspection of systems of this type because the majority of suitable transitions to study the interaction between the ejecta and the wind of the RG occur in this range. Furthermore, Ultraviolet spectra probe the outermost layers of the observed stars, so they can provide useful information about element abundances and densities. As a parallel example, this wavelength range is commonly used also for type-Ia Supernovae, especially to understand characteristics of the progenitors and the details of the explosions; since symbiotic-like Recurrent Novae are considered probable progenitors of this type of supernovae, UV data can be used as a tool for this goal, too ([Pan et al.(2018)]). In other words, UV photons are powerful tools because they dominate emission from both high velocity ejecta, ionised wind flowing from the red giant and inner part of accretion disc (when present) and provide a lot of information about shock fronts evolution and interaction between shock waves and the atmosphere of the red giant.

Alongside the analysis in the ultraviolet, optical studies of symbiotic novae can provide fruitful and compelling information, too. In particular, optical spectra can be handled to follow the evolution of permitted lines, from which fundamental parameters like electron density, mass, temperature and radius of the ejecta and chemical abundances can be derived. Moreover, visible light is the optimal tool for a deep examination of what happens during the coronal phase of the outburst of a recurrent nova, during which the shock front created by the explosion heats the gas of the envelope as it expands at supersonic speed outwards through the surrounding giant's wind. Since most of coronal lines emission rises due to the cooling of the shocked ejecta, the study of these transitions and this spectroscopic phase is essential to have a better knowledge of shock propagation and the associated mechanisms ([Anupama and Prabhu(1989)]). In the archives, huge amounts of optical data are available; for the UV part of the electromagnetic spectrum, things get more complicated because the accessible instruments are only a few, hence spectra are less nu-

merous. However, the IUE and Swift archives provide a certain number of data taken during the outbursts of symbiotic recurrent novae. Galactic Symbiotic Recurrent Novae cited in Table1.2 have all been observed in outburst, providing an almost complete survey which is useful for comparison. Table 2.1 briefly lists the analysed spectra, whose journal of observations can be found in Appendix A and summarises some primary information about the instruments and wavelength ranges.

Object	Archive	Observations date	Spectral region (Å)	# spectra
RS Oph	Swift UV grism	March 2006 - May 2008	1700-7000	70
RS Oph	IUE low resolution LPW	February 1985 - March 1991	1800-3400	34
RS Oph	IUE low resolution SPW	February 1985 - September 1995	1200-2000	38
RS Oph	IUE high resolution LPW	February - April 1985	1800-4000	9
RS Oph	IUE high resolution SPW	February - April 1985	1100-2000	12
RS Oph	ARAS	March 2011 - June 2020	4000-8000	81
V745 Sco	IUE low resolution LPW	August 1989	1800-3400	7
V745 Sco	IUE low resolution SPW	August 1989	1200-2000	4
V745 Sco	SAAO	February 2014 - May 2014	3500-7000	6
V745 Sco	CTIO	August 1989 - April 1992	3000-8000	10
V745 Sco	SMARTS	February 2014	4500-9000	5
V745 Sco	NOT FIES	February 2014	500-7500	3
V745 Sco	ESO UVES	March 2014 - May 2015	3600-9500	25
V3890 Sgr	Swift UV grism	September 2019	1700-7000	26
V3890 Sgr	IUE low resolution LPW	May 1990	1800-3400	2
V3890 Sgr	IUE low resolution SPW	May - September 1990	1200-2000	5
V3890 Sgr	ARAS	August - October 2019	3500-9000	61
T CrB	IUE low resolution LPW	January 1979 - August 1990	1800-3400	35
T CrB	IUE low resolution SPW	January 1979 - August 1990	1200-2000	36
T CrB	IUE high resolution LPW	June 1980 - April 1982	1800-3400	3
T CrB	IUE high resolution SPW	June 1980 - February 1988	1100-2000	5
V407 Cyg	NOT FIES	April 2010 - October 2014	3500-7500	18
V407 Cyg	Ondřejov OES	March 2010 - April 2011	5700-6800	42

Table 2.1: Description of the datasets

The next paragraphs provide an overview of the data and the corresponding instruments description.

2.1 Swift Ultraviolet/Optical Telescope

The *Neil Gehrels Swift Observatory* - previously called *Swift Gamma Ray Burst Explorer* or, simply, *Swift* - is a flexible and rapid-response NASA satellite orbiting since November 2004 for studying γ-ray bursts (GRBs) science with multi-wavelength capability. It consists of three instruments, a wide-field-of-view Gamma-Ray Burst detector and narrow field X-ray and optical telescopes, which work together to observe GRBs in γ-rays, X-rays, ultraviolet and optical wavebands. Swift observations are primarily performed to determine the origin of GRBs, classify and determine their evolution and interaction with the surroundings, use these events to study the early Universe and perform a X-ray survey of the sky. Swift is provided with three onboard instruments, whose field of operation covers an energy range of $\simeq 0.002 - 150\ keV$: the *Burst Alert Telescope (BAT)* detects the location of GRBs to an accuracy of about 3-arcmin in the energy range $15 - 150\ keV$ with high sensitivity and a large field of view; the *X-ray Telescope (XRT)* works between $0.2 - 10\ keV$ to improve BAT's estimate of a GRB position and observe it over a very wide range of magnitudes and fluxes; in the range 170-650 nm, the Swift arrangement activates its final instrument, the *Ultraviolet and Optical Telescope (UVOT)*, a 30-cm diameter modified Ritchey-Chetrien telescope with a 45° primary mirror, which allows rapid observations of the optical counterparts and determination of the red-shift of the object.

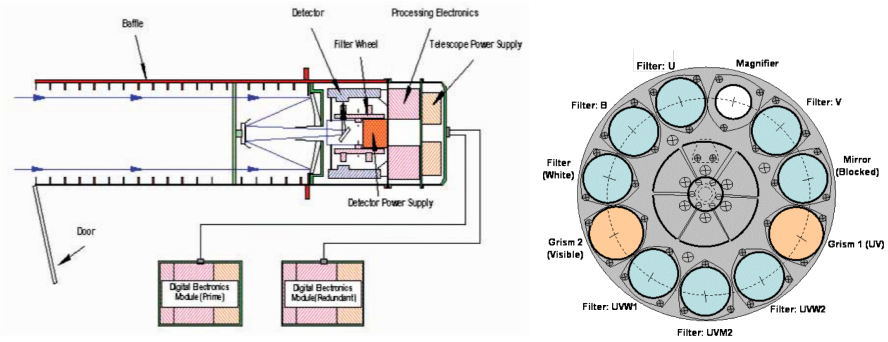

(a) The 30 cm Ritchie-Chrétien telescope in the UVOT layout. Arrows denote the path of light through the telescope.

(b) The filterwheel with the filters, grisms, a magnifier and a mirror.

Figure 2.1: Layout of the Swift Ultraviolet and Optical Telescope.

Fig. 2.1(a) displays the layout of the telescope: light enters through an open door in the baffle and is then redirected into the detector, with a simultaneous reduction of stray light background; the detector lies in front of the power supply between two filter wheels and, behind this set-up, the processing electronics is positioned and provided with two separate Digital Electronic Modules, one prime and the other redundant. In this design, the baffle also contains an inclined mirror, whose primary task is to deflect light and reflect it into the filterwheel for the next steps of the path. The UVOT filter-wheel, in Fig. 2.1(b), allows an easier selection of the desired filter (either UV, lenticular optical or clear filters, a UV or optical grism or a blocked position) with a 4-times magnifier that results in 0.13 arcsec pixels for near diffraction limited imaging; the presence of this wheel limits the capabilities of the telescope when bright sources are present in the field of view. Moreover, UVOT is able to provide spectroscopic observations, thanks to the presence of several broadband filters and 2 grisms (one optical, one UV), mounted on a wheel in front of the detector. The design for the two grisms is a Zemax optical model, which uses the set-up to predict dispersion, order overlap, point spread function (PSF) and throughput and their variation with the source position in the field of view. The grisms have two elements, the grism itself and a tilt compensator, as the schematic representation of the instrument optics in Fig.2.2 shows. The incident beam is dispersed by the grism through a prism and a transmission grating, then the focal plane is adjusted by the tilt compensator, which flattens the tilt resulting from the dispersion. The overall optics of this set-up is more complex than a simple prism, in order to optimise the first order. Five dispersion orders are created: the 0th order is extended toward the UV, the -1 order is very fuzzy, the 2nd and 3rd orders can overlap on the 1st one as in the V grism or curve away as in the UV one. The different configurations of the two grisms translates into different types of order overlap. The 2nd and 3rd order of the V grism fall on top or in line with the 1st order and their contribution can be neglected in most objects, with the exception of the bluest. For those, some 2nd order light with $\lambda > 4000$ Å may overlap with the 1st order and this can be taken into account. In contrast, spectra from the UV grism are curved because one component of the optics is slightly tilted. Consequently, 2nd and 3rd orders can be separated from the 1st order because there is a significant offset between them. When the orders overlap, contamination can be estimated and corrected. Another feature of the optical design of the instrument is that the PSF - the photons distribution over the detector -, broadens toward the red part of the UV grism. As depicted in Figs. 2.3 and 2.4, which show the variation of Swift UVOT/UV-grism point spread function as a function of wavelength, the PSF is quite large for $\lambda > 4500$ Å, making the spectrum flattened at those wavelengths, while at $\lambda < 3000$ Å the cross-widening of photons coming from the cathode dominate the distribution; the width of the PSF is typically 3 $pixels$, corresponding to about 10 Å.

The field of view for UVOT is equal to 17 arcmin square and the image is recorded on a photon-counting CCD detector, with a similar design to the two micro-channel plate intensified CCD (MIC) detectors of XMM-Newton/OM design; these are photon-counting devices suitable for the detection of low signals and faint objects. The UVOT/UV-grism provides images of modest signal-to-noise ratio in the wavelength and magnitude ranges $1700 - 2900$ Å, $11 - 15$ mag, with a resolution $R \approx 150$. The main limit to UVOT spectroscopic observations is the problem with wavelengths longer than 2900 Å: UV grism could

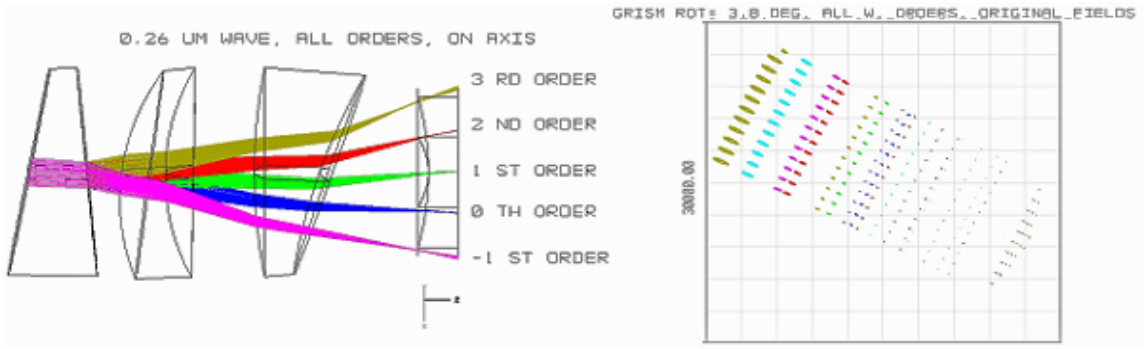

Figure 2.2: The optics design of Swift Ultraviolet and Optical Telescope. On the left, the UVOT/UV-grism with explicit illustration of the different wavelengths and orders. The beam comes from the left and is directed toward the entrance of the image intensifier on the right end of the image. On the right panel, distribution of the orders in a spot image obtained by applying the Zemax model to the field position and wavelength of any incident ray; the plot is also representative of the PSF of the system. ([Kuin et al.(2015)])

2nd order wavelength ($\mathring{A}$)	1st order wavelength ($\mathring{A}$)
1750	2902
1910	3285-3415
2143	3930
2325	4330-4360, 4335
2476-2550	4700-4780
2800	5444

Table 2.2: Peculiarities of the overlap in orders of dispersion in the Swift UVOT/UV grism. The 2nd order falls onto the 1st one and appears in its spectrum at the specified wavelengths.

actually extend longwards, but these regions suffer confusion and overlapping from second-order light. For $\lambda > 2900$ Å, in fact, the second order falls onto the first one; see Table 2.2.

In this regard, wavelength calibration of the spectra is an additional source of difficulty, due to the curvature of the images and the varying sensitivity as a function of position of the instrument. Swift is an orbiting detector, consequently a specific pointing can be replicated only in the brief arch of a few arcseconds and variations often appear even within consecutive exposures. As explained in the next sections, this limit for the calibration can be partially overcome with a careful optimisation of the objects position in the detector.

2.1.1 The UVOT grisms design

The main detector is a *Microchannel plate (MCP) Intensified Charge coupled device (CCD or MIC)* for the conversion of each incident photon on the S20 multi-alkali photocatode into an electron, itself amplified by a 3-stage MCP. When light hits the detector with a certain number of photons, the resulting electrons cloud impacts a P46 fast-phosphor screen, which is connected to a CCD in frame transfer mode. The area of each exposure would be a 256x256 CCD image, but the readout increases the resolution by 8x or so, resulting in a 2048x2048 pixels wide image. The transfer and transformation of photons into electrons and vice versa is affected by several limitation, one of which is a consequent change in the size of each 8x8 sub-pixels on the sky: the residuals from the mechanism is an unavoidable pattern - known as *modulo-8 (MOD-8)* scheme -, of dark pixels next to the spectra of bright sources on the raw image. During the post-processing phase of data analysis, it is possible to minimise the effect of such a pattern, but in some conditions it cannot be completely removed as a result of the so called *coincidence loss* effect, the registration of multiple photons during a single CCD readout interval. The problem of coincidence loss is almost impossible to entirely remove when the telescope is pointing at very bright sources. Bright objects are subjected to further losses because of other events registered in the pixels nearby, which may interfere with the detection. An

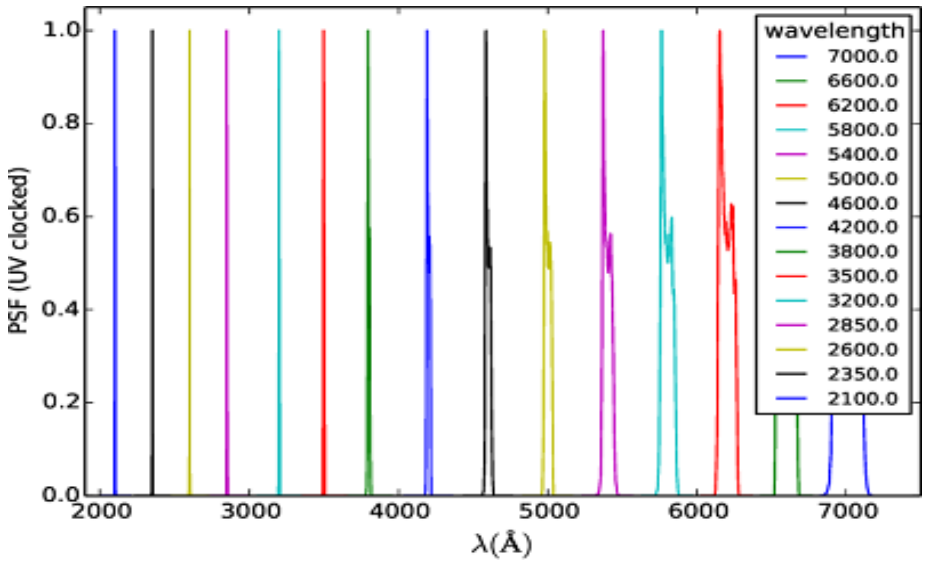

Figure 2.3: The trend of Zemax model's point spread function with wavelength in the UV grism design. The 2D-model PSF has been integrated normal to the dispersion. ([Kuin et al.(2015)])

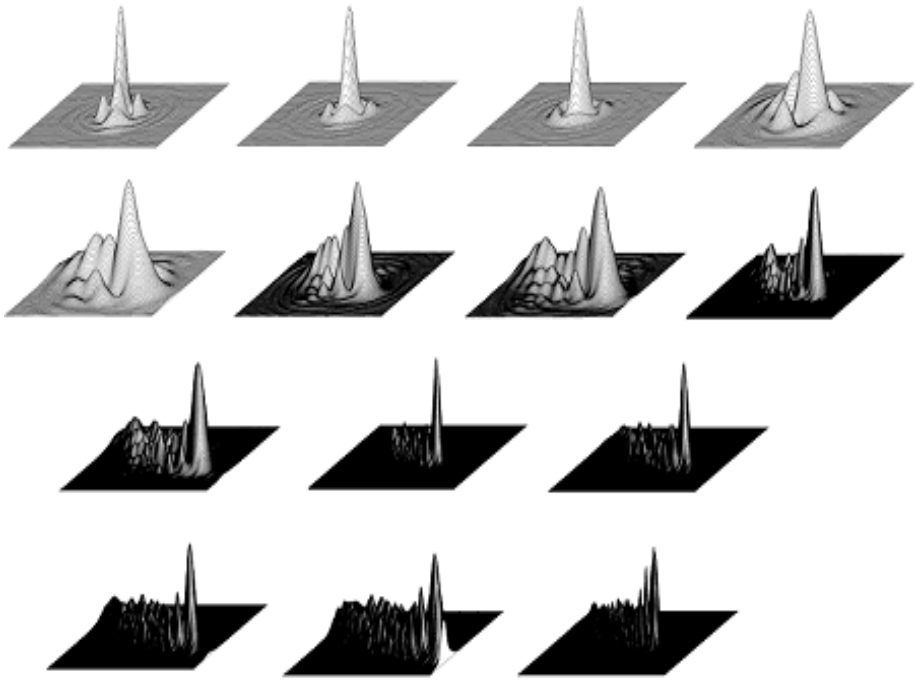

Figure 2.4: Variation of the Swift UVOT UV-grism point spread function as a function of wavelength in Zemax optical model. The scale is given in size of square in X,Y and resolution is 1 $pixel \simeq 3.2$ Å. From the upper left to the lower right, PSF at 2100 Å, 2350 Å, 2600 Å, 3200 Å, 3500Å, 3800 Å, 4200Å, 4600 Å, 5000Å, 5400 Å, 5800 Å, 6200 Å, 6600 Å and 7000 Å. ([Kuin et al.(2015)])

additional limit is encountered when more than a photon arrive in the same portion of the device at the same time, so that overlapping pulse profiles are not counted as two different arrivals, but, on the contrary, only one is detected. Consequently, data acquisition will show a smaller number of sources than the actual ones, and this produces a non-linear response to the brightness of the target. The most limiting factor to Swift's observation is the presence of a bright sky background, which is usually higher than the faintest stellar-type sources.

For a better sensitivity of the instrument, the visible grism optics is blazed at 3600 Å, whereas the UV grism is not blazed and there is a noticeable overlapping from the second-order spectrum, which has to be accounted for in the analysis. Both V and UV grisms allow choice of the operating arrangement, either a *nominal* or *clocked* mode depending on the rotation of the filter wheel and the corresponding alignment and aperture of the field of view. The optics of the UV grism is mounted in the converging beam of the telescope, hence the instrument has a convex surface in order to avoid the appearance of a shift in the focus. The structure of the grism design guarantees an optimisation of the UV first order around 2600 Å and 4200 Å for the visible light. Table 2.3 summarizes some of the properties of the two grisms.

Properties	**Visible grism**	**Ultraviolet grism**
Spectral resolution	100 at 4000 Å	75 at 2600 Å
Effective wavelength range (1st order)	2900-6600	1730-6700 Å
Effective wavelength range (2nd order)	-	1700-2250 Å
Effective wavelength range (3rd order)	-	3600-5500 Å
Wavelength accuracy	12 Å	22 Å
Overlap of the 2nd on the 1st order	5700 Å	> 2750 Å
Effective magnitude range	13-17 V mag	11.5-15.5 V mag
Astrometric accuracy (1st order anchor point)	1.2 arcsec	3.5 arcsec
Scale	0.57 arcsec/pixel	0.57 arcsec/pixel
Dispersion	5.9 Å/pixel at 4200 Å	3.2 Å/pixel at 2600 Å
Coincidence loss above	$\sim 10^{-13}\ erg/cm^2/s/$Å	$\sim 5 \times 10^{-13}\ erg/cm^2/s/$Å
0th order magnitude zero-point	17.7 mag	19.0 mag

Table 2.3: Properties of the Swift UVOT grisms set-up ([Kuin(2014b)])

The optimal configuration for the set-up is to place the target on the lower half of the device and to select the clocked mode during the observation in order to limit the effect of both the background and the brightest sources. In the UV images of luminous objects, a large halo may form around the 0th order, showing the mod-8 pattern; a similar pattern may arise in the 1st order images of the most intense targets, with the result that almost all spectral and flux information gets lost in the acquisition. The result is that there will be dispersion in the spectra of any object in the field of view of the telescope, with the appearance of secondary spectra for every order; the degree of dispersion is different depending on the wavelength sensitivity and the position of the target on the detector: in particular, it is convenient to place the object of interest near the centre or in the lower half, because such a configuration will result in a less dispersed image.

2.1.2 The UV grism

A sample of image taken with the UV grism in clocked mode is shown in Fig.2.5.

As already pointed out, the main structural difference between visual and ultraviolet grisms is that the UV is not blazed, therefore the response and other technical characteristics varies with respect to the other device. The set-up of the UV grism provides an optimised response in the wavelength range $2000 - 3400$ Å, with slightly different attributes according to the order. For instance, the zeroth order shows a dispersion law going with the inverse of the wavelength and an extended tail which is usually hidden in the background noise but noticeable for brightest sources. The main peak of the zeroth order displays a $\sim 300\ pixels$ separation from the first and minus-first orders, whereas the second and third orders always overlap the first. Analogously to the dependence of the sensitivity upon the location onto the device, contamination of spectral orders also depends on the part of the detector on which the photons

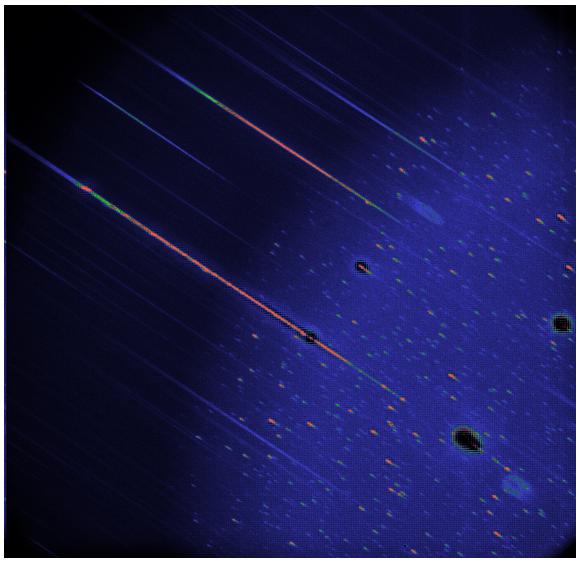

Figure 2.5: Example of a raw image acquired by the Swift UVOT UV grism. The target is RS Ophiuchi ($\alpha = 267.55\ deg$, $\delta = -6.71\ deg$) and the image has been taken on March 13th 2006 (MJD 53807.8), for a total exposure $t_{exp} = 1.5\ ks$.

arrive. If the pointing is such that the target is placed in the lower half of the image, the overlap of the 1st order starts at 2750 Å and, if the source is not particularly blue, at around 2950 Å. In the upper half, instead, the second order shows a curvature displacing it away from the first order with an additional lateral shift; if the source is located in this region, the second order will not overlap on the first even for the bluest objects shortward of 4500 Å . The sensitivity peak varies according to the order, for example it is further in the UV (at about 2700 Å) for the 2nd than the 1st order. Additional contamination occurs at around 4900 Å, where the 3rd order overlays the 1st and a strong emission can provoke a jump in the flux if the source is very blue. However, the 3rd order is usually weak for the vast majority of objects and can be rendered insignificant for the 1st order if the spectrum falls on the upper portion of the detector.

2.1.3 Wavelength calibration

One consequence of the design and, in particular, of its slitless configuration, is that the UVOT spectrum is very likely contaminated by neighboring background sources which make both data reduction and interpretation more complicated. The overlapping spectral orders add further complications to the elaboration. The tailored routine for the extraction and calibration of the spectra is the UVOTPY UVOT/grism data-reduction software ([Kuin(2013a)], [Kuin et al.(2015)]). The procedure for wavelength calibration is based on a Zemax optical model and is the same for both operational modes of the grism. Calibration consists of two steps: (1) mapping of grism image to get the target position on the sky and the position of the *anchor point* - the reference point for the wavelength scale on the image -, at given wavelengths, and (2) the dispersion law determination relative to the anchor position. In addition, spectra taken with the UV grism in clocked mode use lenticular filter observations taken right before and after the exposure to independently determine the drift during the pointing.

When the instrument is pointed at a source, the sensor registers the position as a function of two *sky angles*, measured along the axes of the image and then translated into the couple parameters determined by the focal length and pixel scale. The derived angles are generally used as indices for the wavelength calibration, in particular to calculate the so-called *anchor point*, chosen to be 2600 Å for the UV and 4200 Å for the V grism. The reason for the existence of this point is the difference between the actual position of the target on the field of view and the one registered by the detector, that will change according to the filter and the boresight position in that particular filter. In principle, it is possible to associate the boresight to each wavelength: since the boresight is common for all the filters and any wavelength is always in the same location of the spectrum, for a given filter the boresight remains the same and gives

identical coordinates for any source located in it. Thus, the position of a source on any part of the image can be assessed knowing the boresight's position and the angles between the source and the boresight. The anchor positions are determined through the following procedure: first, spectral lines positions are measured in the calibration images, then the anchor position on each image is derived and corrected in the lenticular filter images with respect to the boresight location at the time of the observation; next, the boresight location of the anchor and the mapping from the lenticular filter are determined on the grism image, the modelled anchor positions are shifted to align the observations to the prediction and finally the model is scaled to align all anchors to within 20 Å and a bispline is used to further correct the data. This algorithm ensures high accuracy (of about 0.5") for the positions in the lenticular filter, while the accuracy of the mapping depends on the calibration and the pointing during observations. In UV grism spectra, the 2nd order anchor point can be determined at the offset from the centre where the separation from the 1st order lies; in this case, measurements are made through the strongest visible spectral features, for example the 1910 CIII] line. Work in this regard is still in progress and some issues remain unsolved, anyway it is possible to evaluate the position of the anchor point as pixels distance between the 2nd and the 1st order and the dispersion from spectral lines between 1750-2600 Å.

The distance between the 0th and 1st orders is usually 200 pixels or so, but this value changes according to the source: blue stars show contamination of a strong 2nd order around 2750-2950 Å, whereas the overlapping begins in successive spectral ranges for objects with red spectra, so that there may be no 2nd order contamination for sources like K0 stars. When calculated with the anchor point in the zeroth order, the dispersion relation provides a wavelength calibration with smaller errors than $\simeq 30$ Å. Instead, when the anchor point lies in the 1st order, the dispersion is calculated by comparing calibration spectra taken at different positions on the detector, which are then used to extract the dispersion law as polynomial coefficients; the main problem with this procedure is that, even if the dispersion angle and the direction of the various orders on the image are consistent between the model and the detector, individual orders may show some curvature and an angle that varies depending on the anchor position.

To perform wavelength calibration, the acquired images by UVOT/UV-grism are processed in the following way. First, data are formatted in a raw image with 2048x2048 size. Then it is corrected with an algorithm that uses the distortion previously extracted from the lenticular filters. Finally a detector image is generated by applying the distortion correction to the raw grism image. Because of possible biases in the lenticular filters, transformation of the various images can be affected by additional distortion components. One of the primary differences between images is the coordinate system. The raw image displays pixel coordinates measured from the bottom left corner, while the detector image considers the center as the reference for the coordinates frame, measured in mm with a scale factor of $0.009075\ mm/pix$ for the conversion. As already underlined in the previous description, dispersion is not the same for spectra with different slopes across the detector, so it is necessary to rotate the detector images by the spectral slope angle evaluated from the calibration file before the extraction of the strip corresponding to the spectrum and the background field. The spectrum is usually curved, so it is also necessary to project the anchor point to the peak of the cross-cut spectrum to calculate the wavelengths with a certain agreement to the model. The exact wavelength determination is limited by the accuracy of the predicted anchor position, which produces a shift in the position of the reference wavelength, and the internal consistency of the dispersion, which is related to the precision of the model. Once the identification of known lines in WR-stars spectra has been made and the new dispersion law obtained, the spectrum of the target is extracted again with improved calibration; at this point of the procedure, several comparisons between wavelengths and anchor point values before and after the correction are made in order to re-iterate the process and further improve the calibration.

A comparison between the two images - before and after the processing - is shown in Fig.2.6 for RS Ophiuchi in outburst. In general, this method provides two parallel results, on the one hand the calibration of UV grism in clocked mode is affected by smaller errors due to the determination of the anchor point but, on the other hand, the global dispersion law, and wavelength calibration of the spectra is better established for the nominal mode. For the nominal grism, evaluation through the dispersion relation is such that wavelengths usually fall within 18 Å of the correct value, with slightly different results in distinct parts of the detector, with the biggest separation in the top left and bottom right corners; for this operational mode, the shift due to the anchor position is less than 35 Å. For spectra acquired in clocked mode by the UV grism, shift is less than 17 Å and the typical error in wavelengths is about 11 Å below 4500 Å and

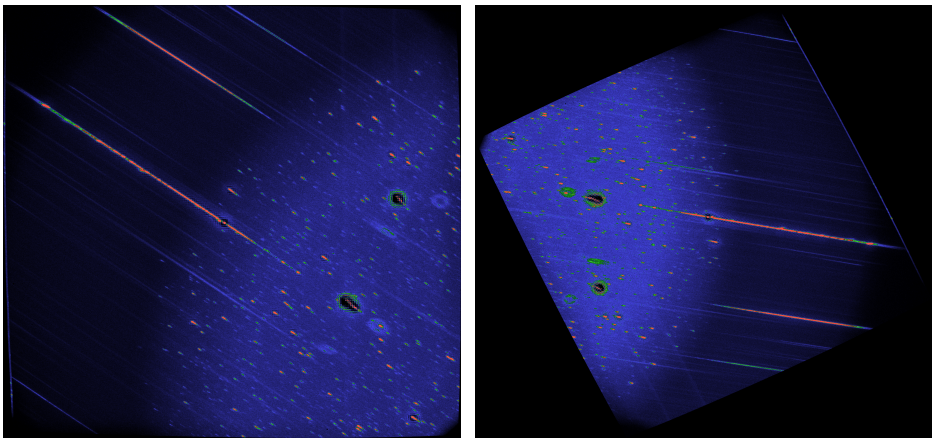

Figure 2.6: Spectrum acquired by the Swift UVOT/UV-grism of the symbiotic recurrent nova RS Ophiuchi ($\alpha = 267.55\ deg$, $\delta = -6.71\ deg$) during its outburst on March 24th 2006 (MJD 53818.02) for a total exposure time $t_{exp} = 29\ ks$. On the left, the detector image; on the right, the re-processed image.

21 Å between $4500 - 6000$ Å , with a somewhat higher value for spectra close to the edge of the detector and smaller if the spectrum is near the centre. The reason for the increased error toward the end of the wavelength range is the discrepancy between model, distortion correction and observation, but the actual cause has yet to be determined. If the UV grism works in data acquisition without a lenticular filter, anchor misalignment provokes a wavelength shift ≤ 35 Å in nominal mode and ≤ 47 Å in clocked mode, while the error in the dispersion law is ≤ 15 Å between $2000 - 4500$ Å in nominal mode, ≤ 11 Å below 4500 Å and within 21 Å between $4500 - 6000$ Å for clocked mode.

An additional complication for the extraction of spectra from Swift images is *coincidence loss*. When multiple photons reach the same area on the detector, their arrival is not counted because of the finite time over which the instrument integrates each exposure (*frame time*). The most evident outcome is that instrumental spikes and valleys will show up in spectra above a certain brightness limit. Photons at high coincidence loss are erroneously counted and will show a modulo-8 pattern on the grism image, producing a variation in the brightness distribution of the extracted spectra.

2.1.4 Flux calibration

UVOTPY software was used for the flux calibration of Swift UV grism data. It uses known stellar fluxes for comparison and provides a calibration within 10% or better over the detector, with the highest uncertainty where flux is subjected to a sudden drop in response ([Kuin(2013b)]). The largest errors are due to contamination by spectra from other sources in the field and from 2nd order. The procedure for the calibration operates in every part of the detector and also corrects for coincidence losses. For the UV grism, the accuracy is $\approx 5\%$ in the centre and $\approx 10\%$ in other parts of the detector, and $\approx 20\%$ in the V grism. The response also changes according to the mode of operation of the grism, $\sim 5\%$ at the centre to $\approx 200\ pixels$ from the edge in nominal mode, and $\leq 20\%$ in clocked mode, with a strong drop when the spectrum lies in the upper left corner of the device. The first step of the procedure is to convert measured count rates in flux values through the definition of an *effective area* A_{eff} which depends on wavelength and is related to the sensitivity of the device, defined as:

$$A_{eff} = \frac{hc}{\lambda} \times \frac{C_r^{in} \times r(t)}{F_{cal} \times \frac{\Delta\lambda}{bin}} \tag{2.1}$$

where h is Planck's constant, c the speed of light, λ the wavelength, $\frac{\Delta\lambda}{bin}$ comes from the dispersion law, F_{cal} is extracted from comparison with standard calibrators spectra (Wolf Rayet stars, in this case), C_r^{in} is the count rate per spectral bin after the correction for coincidence loss and the presence of background and r(t) takes into account the sensitivity loss of the detector over time. After the determination of effective

area for several different calibration sources, the results are summed, error weighted and then fit by a smoothing spline to remove noise. The corresponding accuracy depends on the detector, the location of the source and the total exposure.

Since the UV grism is not blazed, the second order also affects the flux calibration when there is some partial or total overlap between two adjacent orders. When the 1st and 2nd order completely overlap, the effective area for the latter is found by subtraction once A_{eff} is known from independent measurements. To include the coincidence loss effects, the two orders are not separated, hence the flux is given by the sum of the two contributions. When there is an offset between the positions of the orders, count rates can be measured separately for the 1st and the 2nd order.

2.1.5 Swift UVOT/UV-grism dataset

The study of outburst evolution of Symbiotic-like Recurrent Novae includes a set of UVOT spectra acquired during the 2006 outburst of RS Ophiuchi and in 2019 for V3890 Sgr, which are not corrected for reddening effects. The extraction of this previously unused dataset has been made using UVOTPY ([Kuin(2014a)]). The software provides several different tools to quickly extract a spectrum, sum many consecutive images or manually adjust wavelength shifts due to coincidence loss or miscalculations of the anchor position. The program follows the steps of spectra extraction, wavelength calibration to find the anchor position and wavelength dispersion, and then flux calibration along with coincidence loss correction. However, because of the design of the instrument and the extraction procedure, some intrinsic features and instrumental effects are always present in the data even if re-processed and corrected. When light beams enter the detector and pass through the cathode and the micro-processor, they are spread out by the electrons and this results in a first broadening - with a Gaussian shape - of the light distribution, which results in a broadening of the observed spectral line profile. The grism configuration is an additional source of broadening, affecting the profiles with different widths for different orders. A further and final broadening is the influence of coincidence loss, hence the resulting line profiles are the sum of all these effects. Extraction of the spectra uses a Gaussian function to fit the counts rate and the pixel distance from the centre of the track:

$$f(x) = a \exp^{-(\frac{x-x_0}{\sigma})^2} \tag{2.2}$$

where x is the cross-dispersion pixel coordinate, a the peak count rate, x_0 the centre of the spectral track and σ the width of the Gaussian, being equal to $\simeq 2.9\ pixels$ at 1700 Å and $3.3\ pixels$ at 6000 Å in the first order, and $\simeq 4.5\ pixels$ in the second order. For the visible grism, spectral tracks are usually straight, while in the UV each order is curved showing similar intensities for the zeroth and first order. The 0th order is normally extended and equipped with a small tail due to the UV response, while the first order generally overlaps with higher ones. Once processed through the uvotpy routine, the extracted spectral data are written in standard FITS files containing wavelengths, count rate of the target and the background before and after coincidence loss correction, fluxes, coincidence loss correction factors, channel numbers and aperture correction factors.

The analysed archive of spectra includes 70 and 26 sets of grism images for RS Oph and V3890 Sgr respectively, corresponding to virtually every phase of the evolution of the symbiotic Novae: in RS Oph, from about a month after the beginning of the event to quiescence one year later. For V3890 Sgr day 5 to day 21 after the outburst is covered. The first RS Oph spectrum was taken on March 14th 2006 (MJD 53807.8), 30 days after the beginning, while the last one on 13th May 2007 (MJD 54170.1), for a total exposure time of $t_{exp} = 2360\ ks$. For V3890 Sgr, observations lasted from the 2nd until the 21st of September 2019 (MJD 58728.1 - 58747.9), for a total exposure time $t_{exp} = 12.66\ ks$. The wavelength range is $1700 - 5000$ Å for each spectrum, the resolution $\frac{\lambda}{\Delta\lambda} \simeq 75$.

2.2 International Ultraviolet Explorer

The International Ultraviolet Explorer (*IUE*) was a satellite that operated continuously for 18 years and 9 months, from January 26, 1978 to September 30, 1996. It was a joint National Aeronautics and Space Administration (*NASA*), European Space Agency (*ESA*) and the United Kingdom's Science and Engineering

Research Council (*SERC*) mission equipped with two ultraviolet spectrographs and four cameras. Spectrophotometric studies could be performed at both high ($0.1 - 0.3$ Å) and low ($6 - 7$ Å) resolution in the ultraviolet spectral range, from 1150 to 3200 Å.

IUE was equipped with two spectrographs, both of which could be used with either of the two supplied apertures. The large aperture was a slot of about 10 to 20 arcseconds and provided the two possibilities of *small-wavelength large aperture (SWLA)* and *long-wavelength large aperture (LWLA)*, while the small aperture was a $\sim 3\ arcsec$ diameter circle, providing either *small-wavelength small aperture (SWSA)* or *long-wavelength large aperture (LWSA)*. The large aperture was used more frequently because, since the image quality of IUE's telescope yielded a $\sim 3\ arcsecs$ image, some light loss always occurred in the small aperture, whereas the large one could provide better photometric reliability, with virtually no resolution losses. The long wavelength spectrograph used to operate in the range $1850-3300$ Å, the short wavelength one between $1150 - 2000$ Å and each of them was yielded with two dispersion modes: high-resolution using an echelle and a cross-disperser gratings giving roughly 0.2 Å resolution, and low resolution that employed the cross-disperser alone with a resulting resolution around 6 Å. In addition, each spectrograph was assembled with two cameras, one indicated as *prime* and the other as *backup*. In the long wavelength range, both the prime camera (LWP) and the redundant (LWR) were used, whereas the short wavelength range operations worked with only the prime camera (SWP). The redundant camera (SWR) was only used to obtain early images for the mission. Each exposure was obtained by an integration over the requested time interval and, then, a destructive readout of the camera target, which makes the signal digitalised and trasmitted to the ground via the spacecraft telemetry stream. IUE images, each of them is a 768-by-768 pixels array of 8-bit values (0 to 255), are archived together with an header containing recording telescope operator comments, automatic activity log and spacecraft engineering data.

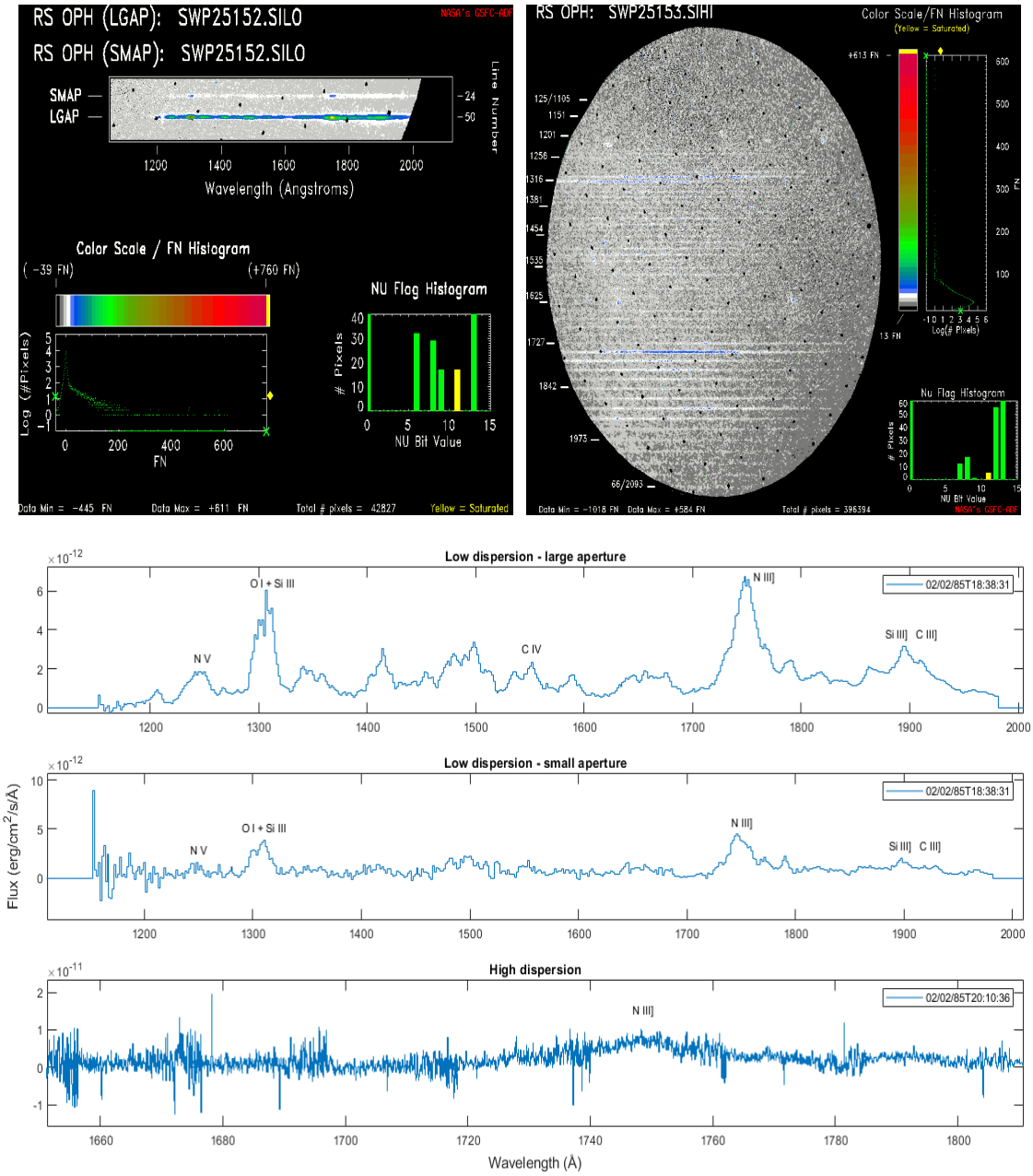

Figure 2.7: IUE images of RS Oph during its 1985 outburst. The upper panel contains the raw images from the spacecraft, the lower panel shows the corresponding extracted spectra for the present work. Merging of only a few orders are displayed for the high dispersion extracted spectrum.

Fig. 2.7 shows the differences in acquired spectra with the two instruments, in particular between images acquired with an echelle spectrograph rather than a non-echelle one. Some examples of RS Oph data acquired on MJD 46098.5 with IUE are displayed: the upper left and upper right images are the low dispersion raw spectrum at large and small aperture and the high dispersion raw spectrum with the several spectral orders pointed out, both associated to the color scale/FN histogram and ν flag histogram; the lower image contains the three corresponding extracted spectra, previously processed by the NEWSIPS software.

2.2.1 IUE dataset

From the IUE archive, both long and short wavelength spectra, taken with either small and large apertures of RS Ophiuchi, V745 Scorpii, V3890 Sagittarii and T Coronae Borealis were downloaded and analysed. The RS Oph and T CrB sets contain both low and high resolution data.

- RS Oph spectra cover the entire evolution of the 1985 outburst, with low resolution data obtained from February 2nd 1985 (MJD 46098.8, 6 days after the beginning of the explosion at MJD 46092, on January 27th) throughout the later stages and quiescent phases too, with the latest images acquired by the SWP on September 15th 1995 (MJD 49975.7) and by the LWP camera on March 2nd 1991 (MJD 48317.5). Total exposure time is $t_{exp} \simeq 197\ ks$. The high resolution dataset includes 21 spectra taken in 59 different spectral regions each and cover the outburst interval from February 14th 1985 (MJD 46110.4, 18 days after time zero) to May 17th 1985 (MJD 46202.1), 3 months after the beginning, for a total exposure time of $t_{exp} \simeq 86\ ks$. The total wavelength ranges covered by these spectra are $1100 - 2000$ Å and $1800 - 3300$ Å.
- V745 Sco spectra trace the 1989 outburst progression from 4 to 14 days after the eruption with both small and large apertures, in both small and long wavelength ranges, but they have been collected in the low resolution mode alone. The images are 11 for a total exposure time $t_{exp} \simeq 56\ ks$, the first one obtained on August 3rd 1989 (MJD 47741.3), the last one on August 19th 1989 (MJD 47757.7).
- V3890 Sgr underwent outburst between April 25-27th 1990 and IUE observations of this binary began on May 15th 1990 (MJD 48026.2), 19 days after the explosion and lasted until September 16th 1990 (MJD 48150.8), only at low resolution, in the wavelength ranges $1800 - 3400$ Å and $1200 - 2000$ Å. Total exposure time is $t_{exp} \simeq 46\ ks$.
- The acquisitions for T CrB have been used only for comparisons between the lines profile during outburst and quiescence, however they cover long evolution periods of this currently "quiet" nova, with spectra at both low and high resolution. For the low dispersion dataset, the exposure time is $t_{exp} \simeq 177\ ks$, while the high resolution one covers an interval $t_{exp} \simeq 146\ ks$.

2.3 European Southern Observatory

One of the spectroscopic tools provided by the *European Southern Observatory (ESO)* is the *Ultraviolet and Visual Echelle Spectrograph (UVES)*, a high-resolution optical spectrograph mounted on VLT at the Nasmyth B focus of UT2. It is a cross-dispersed echelle spectrograph operating with high efficiency from 300 to 1100 nm.

The instrument is equipped with two dichroics so each beam of light coming from the telescope is split in two arms - UV ($\lambda\lambda 3000 - 5000$ Å) to Blue, Visual ($\lambda\lambda 4200 - 11000$ Å) to Red -, which have an identical layout and can be adapted separately or in parallel, via a dichroic beam splitter. The resolving power is about 40000, reaching a maximum two-pixels resolution of 80000 in the Blue Arm and 110000 in the Red one, respectively. Table 2.4 lists the spectral features of UVES data.

Instrument mode	Accessible wavelength range (nm)	Maximum resolution (nm)
blue arm	300-500	80000
red arm	420-1100	110000
dichroic #1	300-400 and 500-1100	80000 and 110000
dichroic #2	300-500 and 600-1100	80000 and 110000
iodine cell	500-600	110000

Table 2.4: Technical details of the ESO UVES spectrograph

The archival data comprise a set of 25 spectra obtained during the 2014 outburst of V745 Sco, at a very high resolution ($R > 40000$), from March 22nd 2014 (MJD 56738.3) throughout the explosive stages to quiescence on May 1st 2015 (MJD 57143.4). The two investigated wavelength ranges are $3600 - 5000$ Å and $5500 - 9500$ Å, total exposure time $t_{exp} \simeq 31\ ks$.

2.4 South African Astronomical Observatory

The *South African Astronomical Observatory (SAAO)* is a research center for optical and infrared astronomy and it is operative since 1972. The site is composed of several telescopes and instruments, including a 1.9-m Radcliffe Telescope on which the *Spectrograph Upgrade: Newly Improved Cassegrain (SpUpNIC)* is mounted. The dispersion and the resolving power vary depending on the grating, but in general this instrument has a dispersion between $30 - 210$ Å mm^{-1} and a resolution of $0.5 - 5$ Å. Instead, the resolving power goes from 700 for the grating G7 to 6500 for G5 ([Crause et al.(2016)]).

The data used for the study of Symbiotic Recurrent Novae consist of V745 Sco spectra taken during its 2014 outburst. Specifically, the coverage goes from February 8th 2014 (MJD 56696.1, 2 days after the beginning of the event) to May 3rd 2014 (MJD 56780.9), a total exposure of $t_{exp} \simeq 3.5\ ks$. The data are all flux calibrated and taken in two wavelength regions, $3500 - 7000$ Å and $6000 - 6800$ Å.

2.5 Cerro Tololo Inter-American Observatory

The *Cerro Tololo Inter-American Observatory (CTIO)* provides a highly stable cross-dispersed echelle spectrometer, *CHIRON*, mounted on the 1.5-meter *Small and Moderate Aperture Research Telescope System (SMARTS)* telescope. This spectrograph is fed by fiber (FEM) and primarily used for precise radial velocity measurements.

Spectra are acquired through 3-pixel samplings in the spectral range $4100 - 8700$ Å, with a fixed total efficiency of $\approx 6\%$. Resolution depends on the particular instrument at use: $R = 80000$ for the image slicer in normal or iodian mode, $R = 25000$ in fiber mode, $R = 140000$ when the narrow slit is used for bright stars ([Schwab et al.(2011)]). In 2014, it recorded the outburst of V745 Sco at high resolution, following its early evolution from February 9th to February 13th (MJD 56697.4 - 56701.4), for a total interval of $t_{exp} \simeq 8\ ks$ from 3 to 12 days after the explosion. CTIO also followed the previous outburst of this particular binary system for $t_{exp} \simeq 9\ ks$ of total exposure, from August 1st 1989 (MJD 47740.0) to quiescence on April 4th 1992 (MJD 48716.2).

2.6 Nordic Optical Telescope

Located at Roque de los Muchachos Observatory in the Canary Islands, the *Nordic Optical Telescope (NOT)* is a 2.56-m diameter telescope actively operating since 1990. It presents a Cassegrain-type focus station, a Ritchey-Chrétien-type primary mirror and an high-resolution *FIbre-fed Echelle Spectrograph (FIES)*. FIES is a cross-dispersed high-resolution spectrograph with maximum spectral resolution $R = 67000$ which covers the entire spectral range up to 9000 Å without gaps. The configuration and structure of the mounted fibres are such that three spectral resolutions can be achieved: a 1.3 arcsecs fibre offers both a mid-resolution of $R = 46000$ and a high-resolution about $R = 67000$, while an additional fibre with a larger aperture of 2.5 arcsecs provides spectra with lower resolution of $R = 25000$.

In 2010 and 2014, FIES registered $t_{exp} \simeq 19\ ks$ and $t_{exp} \simeq 5.46\ ks$ of the activity of the symbiotics V407 Cyg and V745 Sco. For V407 Cyg, spectral acquisition began on April 2nd (MJD 55288.2), 23 days after the start of the event, and ended on July 16th of the same year (MJD 55393.0), while V745 Sco was observed on MJD 56700.3 and MJD 56707.3 The 21 resulting spectra are not absolutely flux calibrated in the wavelength region $3500 - 7500$ Å and can be used for comparison with other datasets, especially for line profiles.

2.7 Ondřejov Observatory

The *Ondřejov Echelle Spectrograph (OES)* ([Koubský et al.(2004)]) is fed by a coudé train connected with 3 flat mirrors and an f/32 collimator B producing a beam of diameter 142 mm and effective grating length of 408 mm. The design of the instrument is illustrated in Fig. 2.8. The first intermediate spectrum is imaged with a parabolic mirror of 1628 mm focal length after the reflection on a small flat mirror; then an f/3.1 parabolic secondary collimator of 1086 mm focal length forms a "white pupil" in parallel light, corresponding to the image of the echelle grating reduced to a diameter of 95 mm. A 54.5° LF5 prism -

placed in front of a CANON EF 200 f/1.8 camera lens of 200 mm focal length - carries out the dispersion of the light beam and, subsequently, the orders are recorded on an EEV 2048x2048 array I with $13.5\ \mu m$ pixels, with a distance between orders equal to 12 pixels in the red and 27 in the blue end of the spectrum. The linear reciprocal dispersion is 2.4 Å mm^{-1} at 5000 Å and, if the slit width is set to $600\ \mu m$, the image has a $40\ \mu m$ width in the camera, resulting in a resolution of 51600 at 5000 Å and a two-pixels resolution of 77000. Moreover, from 4500 Å onward, uncovered gaps in the spectrum between neighbouring orders make their appearance. In summary, OES yields a spectral resolution of 50000 and a wavelength coverage between $3700 - 8500$ Å.

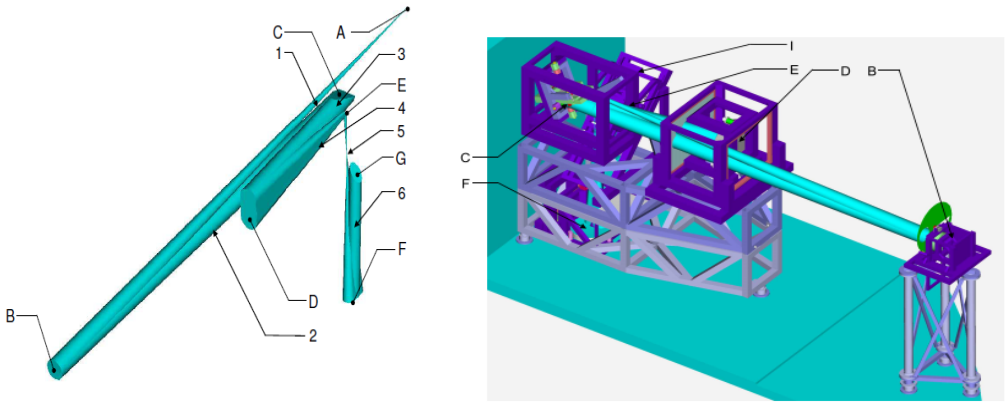

Figure 2.8: Optical layout and perspective view of OES. A: slit, placed in the focus of the collimator B. C: echelle grating. D: parabolic mirror, it images the first intermediate spectrum. E: small flat mirror. F: parabolic secondary collimator, it forms a white pupil in parallel light. G: prism for dispersion crossing. The Canon EF camera lens (H) and EEV 2048x2048 camera array are not shown. The origin for the coordinate system is taken as the point where the polar axis (in the vertical XY plane) crosses the deflection mirror, while 1, 2, 3, 4, 5, 6 indicate the axis of the beam from B to c, C to D, D to E, E to F, F to G, G and H ([Koubský et al.(2004)])

From March 24th 2010 to April 22nd 2011 (MJD 55279.1 - 55674.0), the Ondřejov Observatory's attention was toward the outburst of V407 Cyg, providing high resolution and absolutely flux calibrated spectra of all the evolutionary phases, for an overall exposure of $t_{exp} \simeq 87\ ks$.

2.8 Astronomical Ring for Access to Spectroscopy

The *Astronomical Ring for Access to Spectroscopy (ARAS)* archive is a web open-access database ([Teyssier(2019)], [Jasinsky et al.(2015)]) containing spectra collected by volunteers with the aim of promoting cooperation between professional and amateur astronomers in the field of spectroscopy and creating a global observation network. The archive contains several spectra from both outburst and quiescence of Symbiotic-like Recurrent Novae in the visible wavelength range, for a total exposure time $t_{exp} \simeq 352\ ks$ for RS Oph, $texp \simeq 297\ ks$ for V3890 Sgr and $t_{exp} \simeq 1364\ ks$ for T CrB. In particular, spectra are taken during the 2019 outburst of V3890 Sgr from August 28th to October 3rd (MJD 58723.8 - 58759.1) and during the quiescence of RS Oph in various interval between 2012 and 2020.

Chapter 3

Data Analysis

The study of Symbiotic-like Recurrent Novae evolution during outburst was accomplished through a detailed analysis of spectral lines. Due to the different adopted standards for data storage, various pipelines have been used to extract and examine spectra from distinct archives. However, the whole dataset was elaborated using the MATLAB software, except for the first steps in the extraction of spectra acquired with Swift UVOT/UV-grism: for these ones, the Python software UVOTPY has been used ([Kuin(2014a)]).

3.1 Data reduction

3.1.1 Swift spectra

Among the overall set of spectra, the most careful early elaboration was required by the one from Swift UVOT UV grism. All the available data in the archive consist of several directories, the most relevant of which are the one including auxiliar files (TLE orbit file, corrected attitude file, job parameter file, FITS format tape contents, processing parameter file, makefilter filter file, attitude/orbit-related filter values, spacecraft attitude file, S/C engineering data, UTC corrections file) and the other one containing the actual uvot files (instrument engineering data, detector coordinate images, raw coordinate images, uvot filter sky images, exposure map and sky coordinate images). These all are needed for image processing through the uvotpy routine. It operates calibrating the images both in wavelength and flux as described in Sections 2.1.3 and 2.1.4 and translating all the essential information in standard format FITS files for further analysis and elaboration. For spectra extraction to be performed, the program requires the coordinates (right ascension and declination) of the target in the sky, the identifier code for the observation and the grism detector file extension as input parameters. These all can be found in the header of the image file. Then, it operates autonomously to calculate the anchor position and calibrate the data. To do so, the software uses lenticular filter and grism detector images, in addition to calibration files. Once the anchor position is known, the spectrum can be extracted and rotated, with an attempt of separating the 1st from the 2nd order. After spectrum production and wavelength calibration, the program applies coincidence loss correction and flux calibration through the determination of the effective area, along with a rough estimate of the 2nd order spectrum. In the grism images, the streak corresponding to the spectral track changes with exposure: to obtain better internal coherence and consistency between the data, spectra are fitted with a Gaussian function before extraction. Then, result of the fit is automatically interpolated with a polynomial to smooth out the modulo-8 pattern.

In other words, to extract flux and wavelength values from the image of a stellar spectrum, as a first step the uvotpy procedure determines the anchor position, then rotates the image around the anchor by the dispersion angle and cuts the result 100 pixels above and below the centre in order to measure the curvature of the spectrum and improve the determination of the distance between the anchor and the centre of the spectral track; then, an adjustment to the image is made by the subsequent Gaussian fit and polynomial interpolation, which lead to counts extraction in a curved slit with default halfwidth $2.5\ \sigma$, where σ is the width of the previously applied Gaussian curve. At this point of the procedure, the routine calculates aperture correction and flags, then stores the information about slit parameters and coincidence

loss. Finally, background counts are removed from the image and data can be subjected to further elaboration ([Kuin et al.(2015)]). Every single step of the elaboration and extraction procedure is registered in the header of the files, which contains all the needed information for an accurate analysis of the resulting spectra. An illustrative example of Swift initial and extracted data is shown in Fig. 3.1. In Fig.3.2, various stages of spectral development for RS Oph during its 2006 outburst in Swift data.

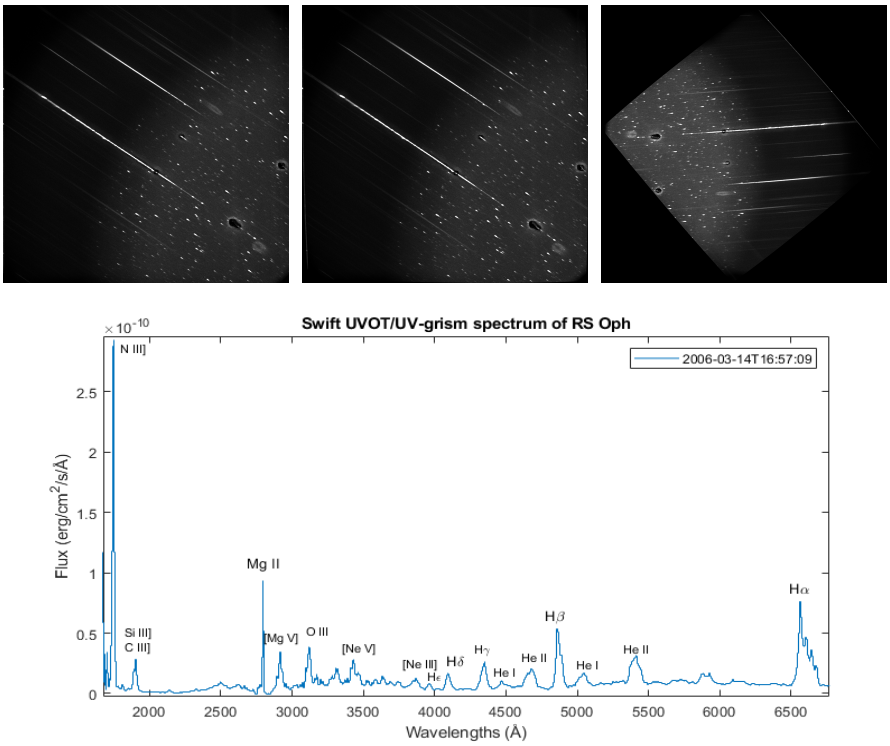

Figure 3.1: Images of the 2006 outburst of RS Ophiuchi acquired by the UV grism of Swift Ultraviolet and Optical Telescope on MJD 53808.7 ($t = 30\ days$) and used for this thesis. In the upper panel, from the left to the right: raw coordinates image, detector coordinates image, reprocessed image in sky coordinates. In the lower panel, the extracted spectrum.

The main problems with Swift data, as mentioned in Section 2.1, are the difficult determination of correct wavelengths and the varying sensitivity with the detector position. Another issue is the modest signal-to-noise ratio (S/N) provided by the UV grism due to the high background contamination. To give an estimate, for a source at high Galactic latitude with monochromatic flux of $10^{-14}\ erg\ cm^{-2}\ s^{-1}$ Å^{-1} observed at 2500 Å in $t_{exp} = 2\ ks$, then the theoretical $S/N \simeq 4.3$ because the expected source rate is $\simeq 0.048\ cps$ and the actual value is even lower due to additional noise created by faint star and first-order spectra. This significantly affect the quality of the data. Because of instrumental problems of misalignment, shifts are around 15 Å in most of the spectra, greater at lower and higher wavelengths ($\lambda < 1900$ Å, $\lambda > 4000$ Å) rather than in the central part of the spectra. As a result, calibration of the line profiles is not so accurate and made even more complicated by the appearance of significant shifts in the wavelengths. Over time, the corresponding values of such shifts tend to slightly decrease because the responsible processes for the imprecise calibration are less determining and the eventual physical mechanisms causing blue-shift diminish their efficiency in later stages of the outburst. Moreover, additional blue-shift due to physical effects (the presence of the wind and the Strömgren sphere, for example) affects lines in various ways: highest ionisation lines are usually more shifted than low ionisation and permitted resonance lines, with respect to their reference rest wavelength. Anyway, every image of the database is affected by this type of contamination. Consequently, every line in the spectra will show some kind of shift, even if the magnitude for this effect will be different depending on the position of the corresponding spectrum on the detector image, the location of the line in the spectrum itself and other determining factor, like for example the

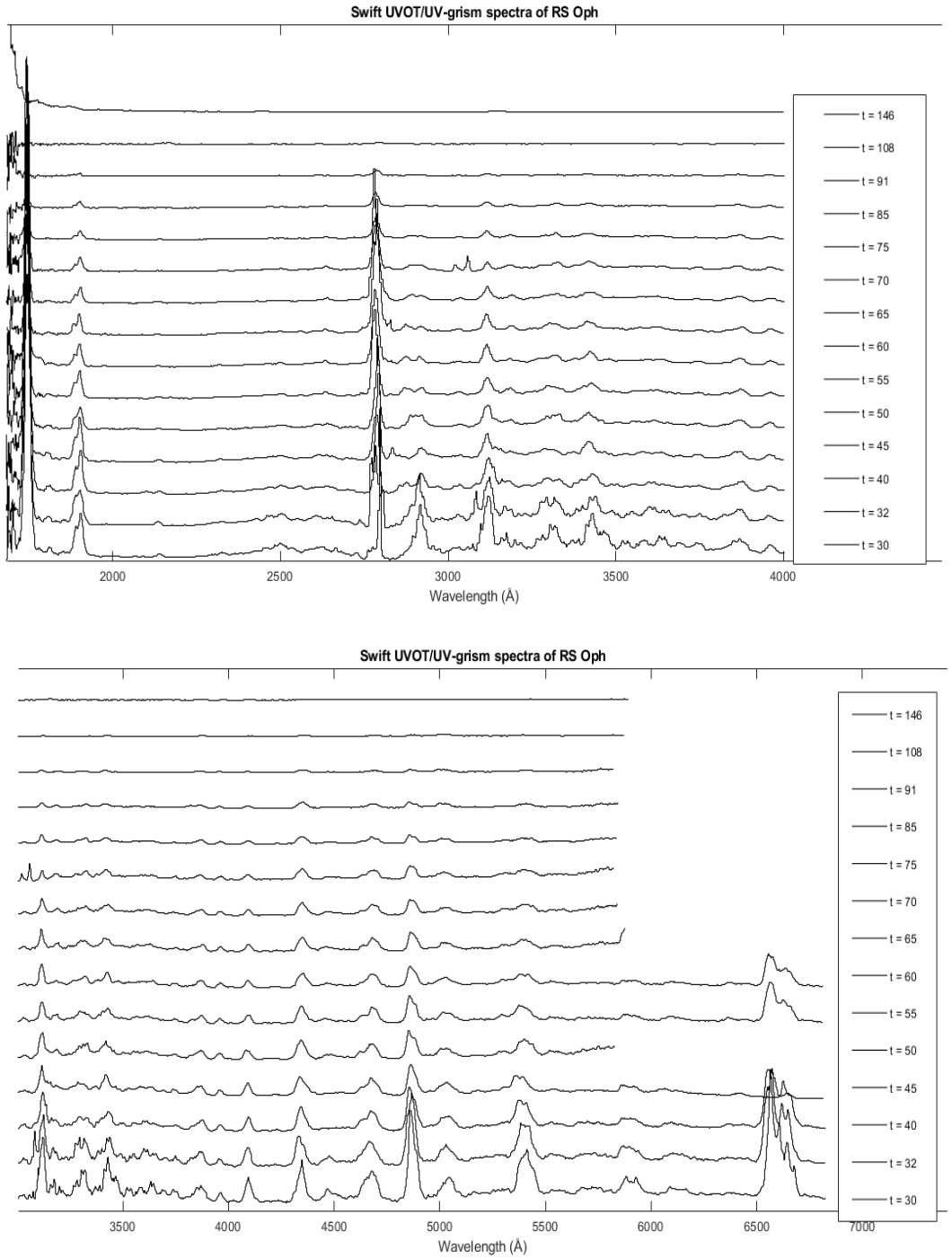

Figure 3.2: Development of RS Ophiuchi spectral sequence at various stages during its 2006 outburst in UVOT data. In the upper and lower panel, the regions $1750 - 4000$ Å and $3000 - 7000$ Å, respectively.

stage of the outburst for physical processes contamination. Uvotpy itself offers a solution to the problem, in fact it contains a sub-routine whose purpose is to manually adjust the values of wavelength and shift the spectra in order to re-calculate and improve the dispersion, for a better lines calibration. Although this correction, the effect is still substantial.

3.1.2 IUE spectra

Like Swift data, the IUE spectra have a relatively low signal-to-noise internal (it was a vidicon system and saturated at 255 counts/pixel), but their resolution is higher than for the UVOT/UV grism set. Although they are all in standard FITS format, data from IUE archive - from both SPW and LPW, the two detectors described in Section 2.2 -, come in two different types: *Low-Dispersion Merge Extracted Image FITS File (MXLO)* and *High-Dispersion Merged Extracted Image FITS File (MXHI)*. The storage for MXLO and MXHI spectra use different conventions but contain all the relevant information about wavelength calibration (starting point and increment), the net flux spectrum, the background flux spectrum, sigma vector, ν flags and the absolutely-calibrated net flux spectrum. In MXHI files, the information contained in the header are more numerous because multiple spectral orders are present in each. All the files from the archive had been already calibrated using the *New Spectral Image Processing System (NEWSIPS)* software ([Garhart et al.(1997)]) and every step of the extraction and calibration procedure is registered in the file header, which contains FITS keywords describing the image, the spectra by aperture, information about the original observation and the processing log. Spectra are also corrected for the motion of the Earth and spacecraft, providing a heliocentric wavelength scale.

For the purposes of this work, IUE data at both dispersion levels have been used and all the preceding considerations taken into account for extraction and analysis of the spectra.

3.1.3 ESO, SAAO, CTIO, SMARTS, NOT, OES and ARAS spectra

With the exception of Swift and IUE data, the other series of spectra show no particular problem regarding their extraction and examination. In most cases, header of the FITS files contains all the necessary information about target, observation conditions (date, time, Julian date, exposure time, resolving power and ambient conditions for the instrument and/or the observatory), dispersion law for wavelength calibration, spectral stored quantities like flux or intensity values, the single steps of the elaboration process (already performed by the instrument routines), whether bias/flat/dark and background subtraction or radial velocity correction have already been applied and similar stuff. Then, the second stage of the procedure after derivation of such data was the extraction and visual representation of single spectra through plots. Almost all the spectra are flux calibrated, but only those from the ARAS archive and NOT and Ondřejov observatories are not, hence some V3890 Sgr, V745 Sco and V407 Cyg figures are in relative intensity or counts rather than flux. A fundamental property needs to be taken into account when dealing with ARAS sequences: since the archive is a collection of data acquired by different observers and instruments, individual resolving power is important to compare spectra and derived quantities. For the remaining datasets under examination, the repository is done in such a manner that every image contains a single complete spectrum, each comprising a different wavelength range.

Fig. 3.3 represents some examples of spectra extracted from these datasets, to show how different they can appear at different resolutions with different instruments. From the upper left to the lower right: ARAS spectra of V3890 Sgr during outburst on MJD 58729.5, RS Oph in quiescence at MJD 57614.5 and T CrB in quiescence at MJD 58629.5, NOT and OES spectra of V407 Cyg during outburst on MJD 55288.5 and MJD 55294.5, CHIRON and SMARTS spectra of V745 Sco in outburst at MJD 56701.5 and MJD 47739.5, ESO and SAAO spectra of V745 Sco on MJD 56784.5 and 56698.5 during outburst.

3.2 Early analysis

After the processing of the images, all the spectra were ready for the next steps of analysis. Plots have been analysed in wavelengths at first, with the main primary purpose of spectral line identification. To do so, the observed wavelengths have been compared to the theoretical values found on the NIST Atomic Spectra Database ([NIST]) and some other line lists, e.g. [Wahlgren and Shore(2012)], [Doschek and Feibelman(1993)],

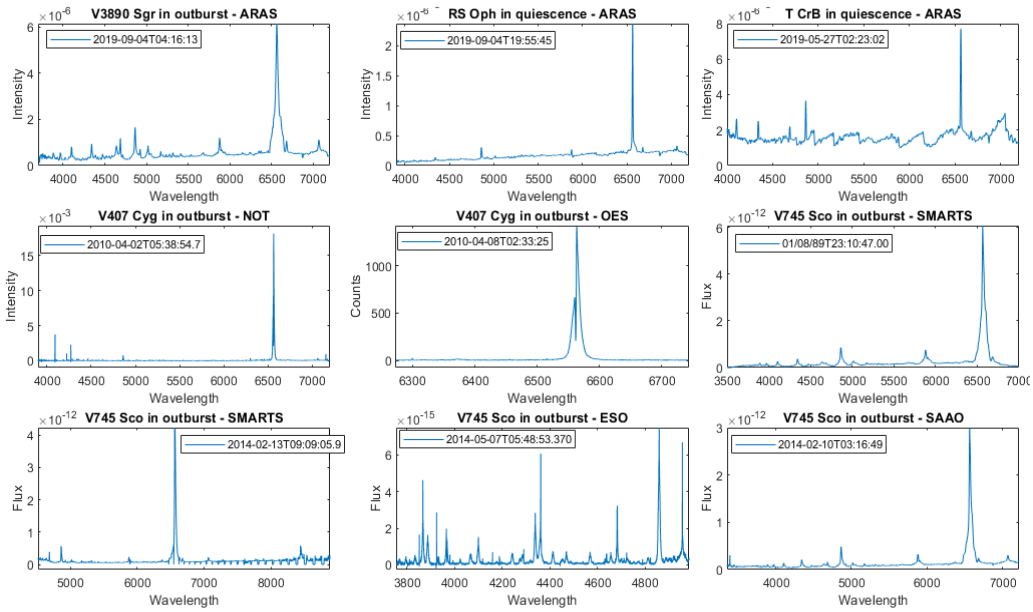

Figure 3.3: Examples of extracted spectra.

[Aufdenberg(1993)], [Dean and Bruhweiler(1985)], [Penston and Lago(1983)], [Young], [Ardila et al.(2002)], [Bell et al.(1966)].

3.2.1 Radial velocity

Since the main goal is to study shock phenomena driven by explosive outbursts, circumstances require a different approach for the inquiry. To this end, wavelengths have been translated into radial velocity values. Since the sources are all spatially unresolved,

$$v_r = \frac{\lambda_{meas} - \lambda_0}{\lambda_0} \cdot c + v_{hel}. \tag{3.1}$$

In Eq.3.1, λ_{meas} is the determined value for the wavelength of the line, λ_0 the corresponding wavelength in a stationary system (here the reference value is the laboratory wavelength of the line), c is the speed of light and the resulting speed value is in $km\ s^{-1}$. The heliocentric correction v_{hel} is applied to each spectrum separately. In some of the data, errors in velocity evaluation are quite large due to the high uncertainty in wavelength determination, which further increase when converted. This is particularly critical in the UV part of the spectrum, since the correspondence is 1 Å$\simeq 250km\ s^{-1}$, while 1 Å$\simeq 60km\ s^{-1}$ in the optical. Unlike grating spectra, the prismatic dispersion and resolution issues in Swift acquisitions have huge effects on the systematics. In the UV, wavelength shift of about 15 Å translate into velocities of the order several thousands of $km\ s^{-1}$. This affects line profiles and related measurements.

3.2.2 Measurement of the spectral lines

Peak line fluxes (they rarely correspond to the center of the line) were measured, either in intensities or fluxes depending on the specific spectrum. An important issue for spectra of this kind is that continuum can often be quite intense, especially in the UV during peak phases of explosive events, thus the directly measured line depth is not actually a reliable measure of the intensity or the flux. This can only become comparable between different values if it is considered in relation to the continuum, in order to have an absolute value. Consequently, to obtain a better coherence between different lines and avoid misinterpretation of the data, the first idea was to calculate lines peaks relative to the local continuum level, depending on whether the spectrum is flux calibrated or not.

More trustworthy quantification for the intensity (or flux) for an emission line is given by the *integrated intensity* and *integrated flux*, which are convenient because they provide an estimate of the strength of a certain spectral line independently from all the unfactual alterations that may concern intensity/flux peaks. To make the calculation, the enclosed region under each emission lines profiles has been integrated without fitting an assumed formal profile. For every peak, shift in velocity from the reference zero point was estimated. Some lines, especially in the IUE spectra, show deformed profiles due to saturation. Similar profiles to those displayed in Fig.3.4 were excluded.

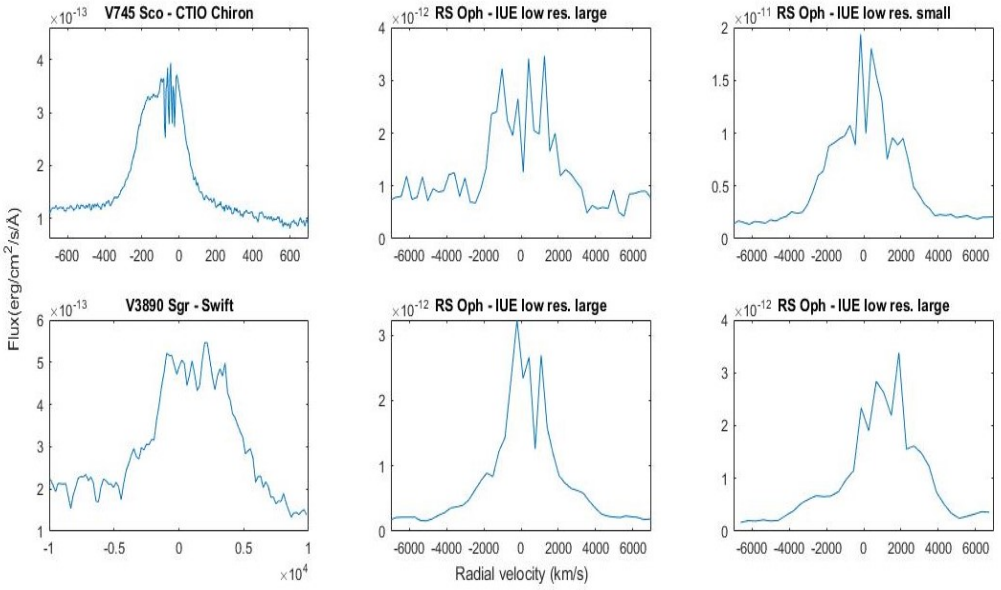

Figure 3.4: Saturated lines in various spectra. From the upper left to the lower right: He II 4686 Å on MJD 56697.4 in SMARTS spectra of V745 Sco, Mg II 2798 Å on MJD 46117.4 in IUE low resolution - large aperture spectra of RS Oph, Mg II 2798 Å on MJD 46098.8 in IUE low resolution - small aperture spectra of RS Oph, Hα 6563 Å in Swift spectra of V3890 Sgr in MJD 58735.5, C IV 1549 Å on MJD 46147.2 and N V 1240 Å on MJD 46117.5 in IUE low resolution - large aperture spectra of RS Oph.

The *Full Width at Zero Intensity (FWZI)* was measured for each line: this quantity is defined as the base width at continuum level and was calculated as the difference, in $km\ s^{-1}$, between the two points where the wings of the line meet the continuum. Another useful quantity to have an idea of how different components affect a spectral line profile is the *Full Width at Half Maximum (FWHM)*, defined as the line width (in $km\ s^{-1}$ in the calculation) at half height between the continuum and the peak. Unlike Gaussian profiles, these quantities are independent and parametrise the profiles.

The set of spectra for the analysis comprises highly heterogeneous and various data, whose features are affected by resolution and instrumental effects other than physical processes. Therefore, the line profiles show a variety of characteristic features, and a global or unified description is hard to make.

3.3 Light curves

To put things in perspective and better understand the setting, an useful tool is looking at the light curves for the evolution of these binaries throughout their explosive events. Photometry was obtained in a range of wavelength bands by the *American Association of Variable Star Observers (AAVSO)*. Most SyRNe exhibit similar behavior, with few variations because of different characteristics of the individual objects and, even more importantly, the evolution is comparable between successive outbursts.

For instance, the optical and X-rays light curves of RS Oph in Figs.3.5, 3.6 and 3.7 were taken during the 1985 and 2006 outbursts.

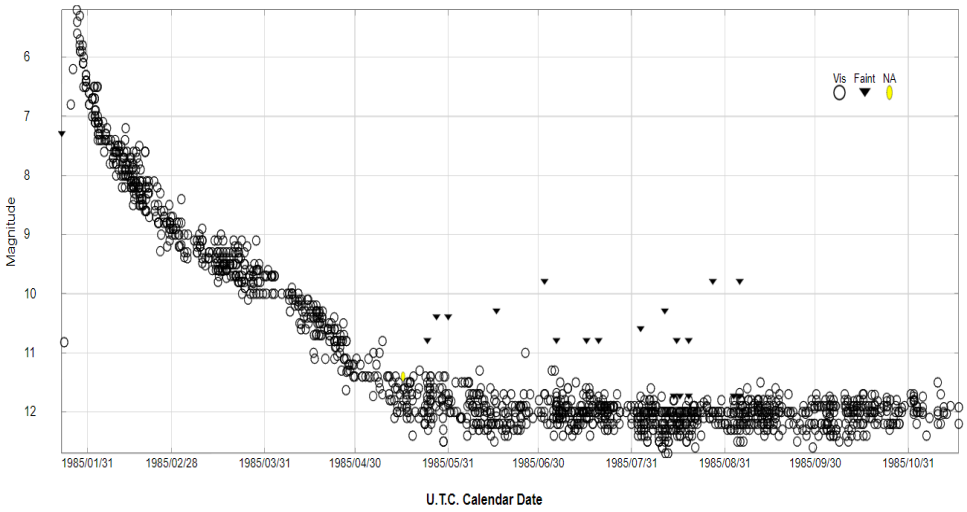

Figure 3.5: RS Oph 1985: AAVSO visual light curve during the outburst.

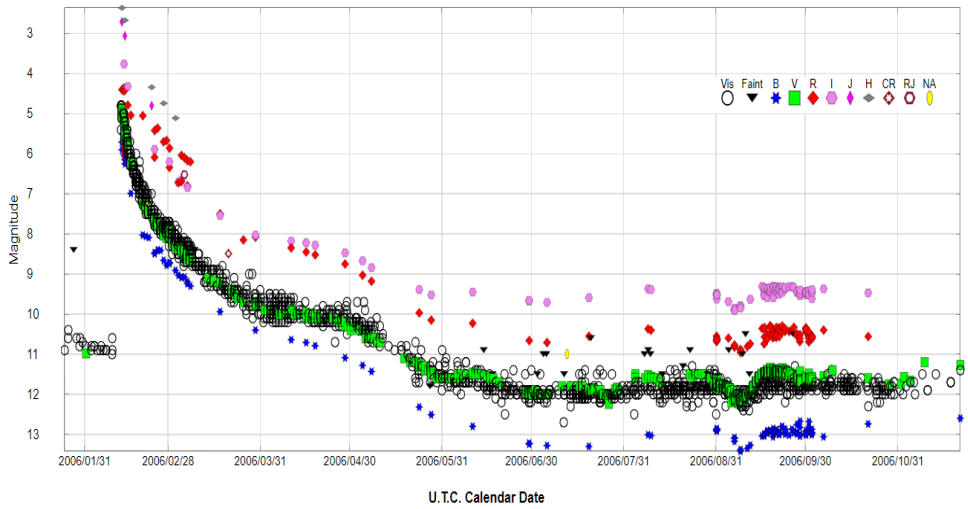

Figure 3.6: RS Oph 2006: AAVSO light curves in different color bands during the outburst.

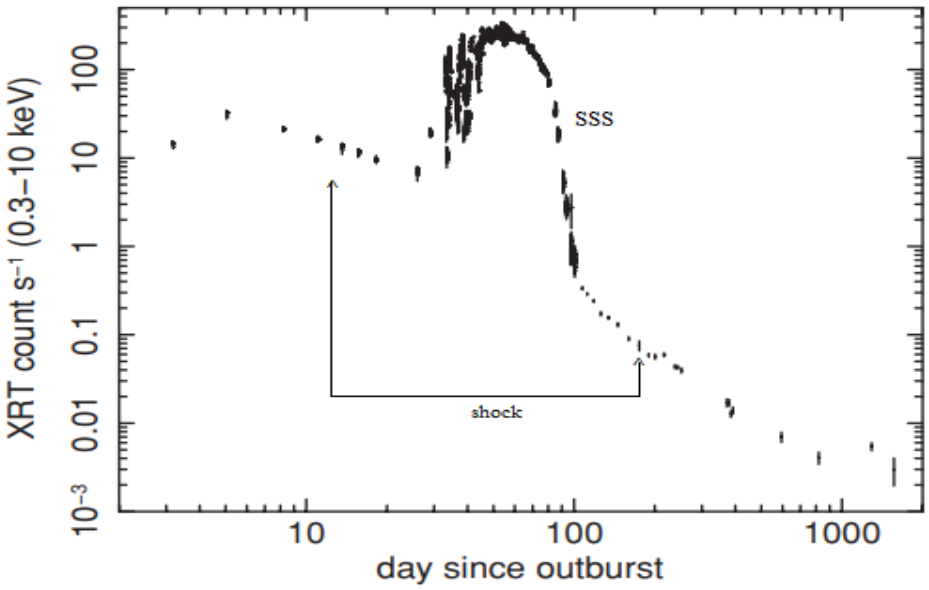

Figure 3.7: RS Oph 2006: Swift XRT light curve during the outburst ([Osborne et al.(2011)].

The two events are striking similar. In 1985, the peak brightness was recorded on January 29 at $m_V = 5.7$. In 2006, optical, UV and X-rays observations began just a few days after the maximum in visible light on February 12. As common in Sy-RNe and differently from the CN case, in both events the free expansion phase lasted only an extremely short time, of the order $4\ days$ at most. Then, both events displayed a rapid decline in the first $\sim 40\ days$ from the outburst associated with the shock wave generation (and subsequent propagation) (e.g., [Mondal et al.(2018)]). After that, a kind of plateau with nearly constant brightness $m_V \simeq 10$ around $40 - 77\ days$, corresponding to the nebular stage in the spectral evolution. In X-rays observations, before around 26 days, the decline in XRs is consistent with the shock propagation. Around 26 days, the so called *Super Soft Source (SSS)* phase begins and increases some orders of magnitudes in just a few days. The XR SSS phase ([Osborne et al.(2011)]) arises when the photosphere of the WD reaches a constant bolumetric luminosity due to continued nuclear burning (CNO processing) occurring in its envelope. This phase lasted approximately for the subsequent $30 - 40\ days$, making the WD temperature increase from ~ 65 to $\sim 90\ eV$ until $t \simeq 60\ days$, followed by a decrease first slowly and then more rapidly, after about 80 days. At this time, the fading of the SSS coincides with the presumed ending of the shell-hydrogen burning phase for the WD. The appearance of the SSS component is common in all novae, including the SyRNe, e.g. V745 Scorpii 2014. Multi-filters data for this outburst are reported in Figs.3.8 and 3.9. The reference is the discovery date, on 2014 February 6.694 UT, when the nova reached $m_V = 9.0$.

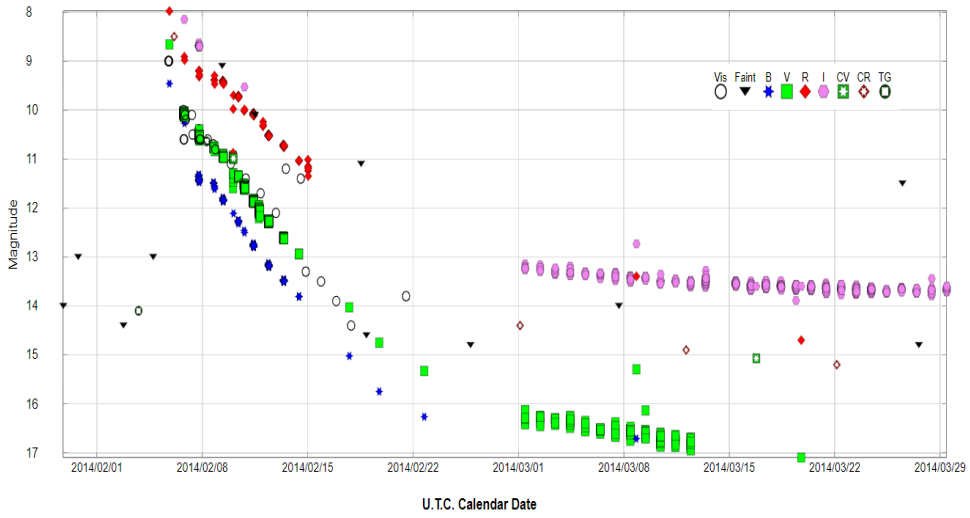

Figure 3.8: V745 Sco 2014: AAVSO light curves during the outburst in multiple wavelength bands.

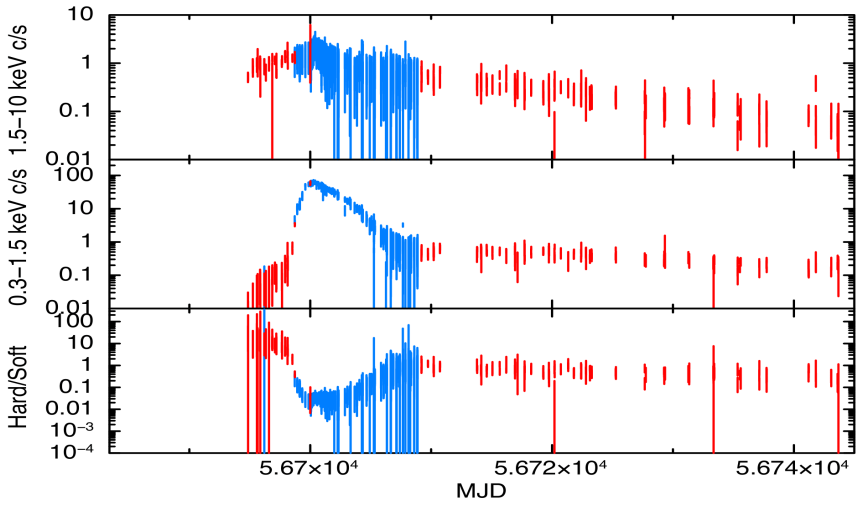

Figure 3.9: V745 Sco 2014: Swift XRT light curves during the outburst.

In V745 Sco, the SS emission was detected from 4 to 6 days after the optical maximum. In addition, the 2014 event was recorded by Swift ([Page et al.(2015)]) using three UV filters - uvw1, uvm1 and uvw2, with central wavelengths 2600 Å, 2246 Å and 1928 Å, respectively -, and a u-band filter centered on 3465 Å for the whole duration of the event from 6 hours to 90 days after the beginning. Optical and infrared data were also collected with SMARTS and AAVSO. While in X-rays the nova showed an early increase, emission in UV and optical wavelengths constantly declined, even if with different rates depending on the stage. At about 19 days, the various curves show a better agreement, and the UV and XR trend changed: the UV slope went from flat to steep, while the XR emission faded. This similarity is an evidence for the existing connection between the responsible regions for the two emissions.

These two systems displayed different timescale, although morphologically similar light curves. V745 Sco had a much faster decline and overall evolution than RS Oph and other similar binaries. More rapid evolution is associated with a more massive WD, close to the upper limit of the Chandrasekhar mass, so the ejection was more rapid and the SSS phase shorter.

Figs.3.10 and 3.11 show the light curves for V3890 Sgr obtained in 1990 and 2019.

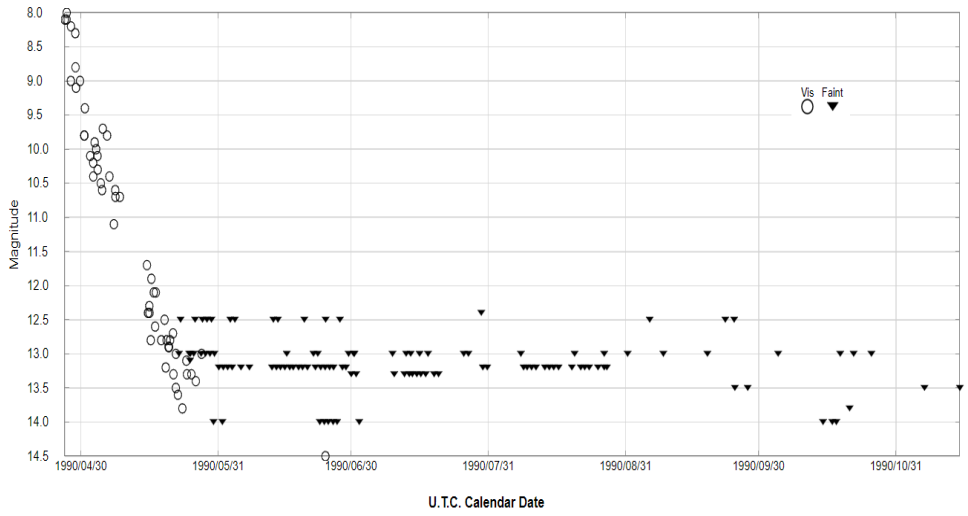

Figure 3.10: V3890 Sgr 1990: AAVSO visual light curve during outburst.

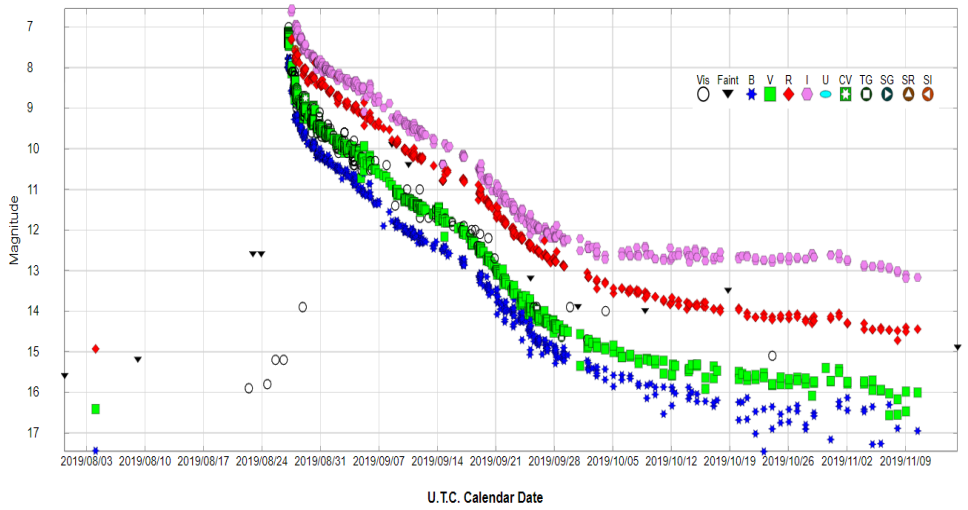

Figure 3.11: V3890 Sgr 2019: AAVSO multi-wavelength light curve during outburst.

In 1990, the nova reached a visual maximum $m_V = 8.5$ on April 27 and then declined with a rate $t_3 \simeq 17\ days$. The 2019 outburst began on September 5.25 UT and showed an early rise of hard X-rays already on the second day, while the SSS turned on around 8.4 days later. It can be seen, from both events, that V3890 Sgr shows a faster development than RS Oph, but its light decreases less rapidly than V745 Sco.

As a final example, the outburst light curve of V407 Cygni is illustrated in Figure 3.12.

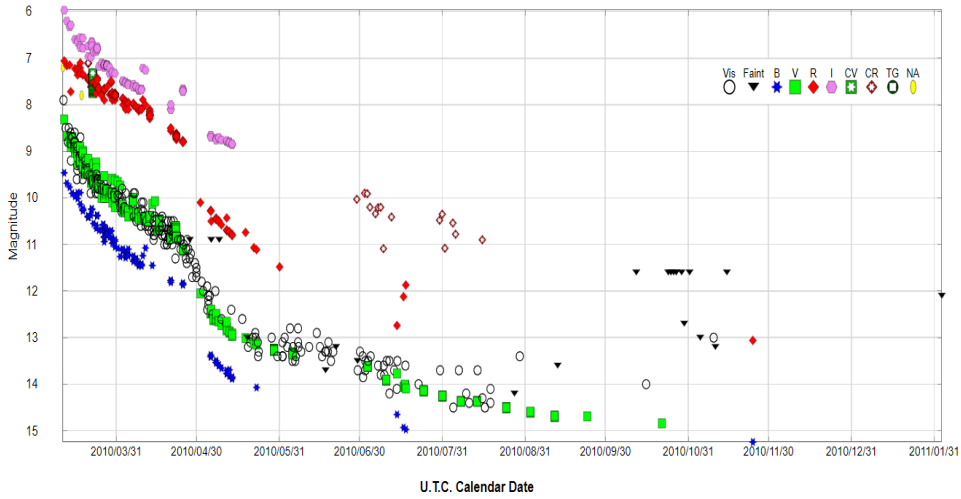

Figure 3.12: V407 Cyg 2010: AAVSO multi-wavelength bands light curves during the outburst.

The optical maximum occured on March 10.81 U.T. at $m_V = 6.8\ mag$, thereafter the Nova declined at rate $t_2 = 6.1\ days$ until 56 days later in X-rays and around 40 days in the UV, when the XR count rate stopped decreasing and the UV entered a phase of slower decrease. As noted in [Shore et al.(2011)], V407 Cyg shows almost identical optical light curves to the 1985 and 2006 outbursts of RS Oph, even if on different timescales; V407 Cyg was faster in every wavelength range.

3.4 Line profiles overview

The next step of data analysis consisted of both a qualitative and quantitative study of single profiles evolution over time for the individual systems. In particular, the existence of multiple structures at different times or in correspondence with different species was investigated. For example, the presence of many inhomogeneities is common in the envelopes and between different regions of Novae, hence the fact that emission is produced at different densities in separate components of the envelope alters line ratios and the morphology of profiles. As mentioned in the previous chapters, in SyRNe line profiles usually show two superimposed components, one narrower than the other. The broad contribution is created by the ejecta and shock, the narrow profile by the ionisation front in the RG wind. Another characteristic feature is the appearance, on top of the most intense emission lines (H, He, Fe, for example), of absorption components with very narrow cores and broad P Cyg wings, especially in the earliest days immediately after the eruption. Within these additional components, the features at higher speed come from the explosion ejecta, while the absorption elements originated in the intervening wind material, seen against the white dwarf and the ejecta. An additional structure is expected to be seen in the profiles of some lines, mainly on the narrow components of later spectra displaying absorption components: a wide pedestal structure, showing up at the base of the profile where the central line meets the continuum and formed by the interaction between the fast wind coming from the hot compact stellar component and the wind from the colder red giant, for instance, in He I, N IV, He II and Hα lines in Fig.3.13.

These different components are usually hard to separate ([Nussbaumer et al.(1995)], [Vaytet et al.(2007)], [Shore et al.(1996)]). As mentioned before, lines from various transitions and regions at distinct outburst phases are differently affected by all these physical and dynamical variation of the environment, therefore it is helpful and instructive to have an overview of how individual profiles of specific lines change over time and system characteristics.

3.4.1 Permitted, semi-forbidden and forbidden transitions

Permitted electronic transitions are electric dipole transitions whose probabilities are usually high, $\sim 10^5 - 10^9\ s^{-1}$. As a result, allowed spectral lines - both in optical and ultraviolet wavelength ranges

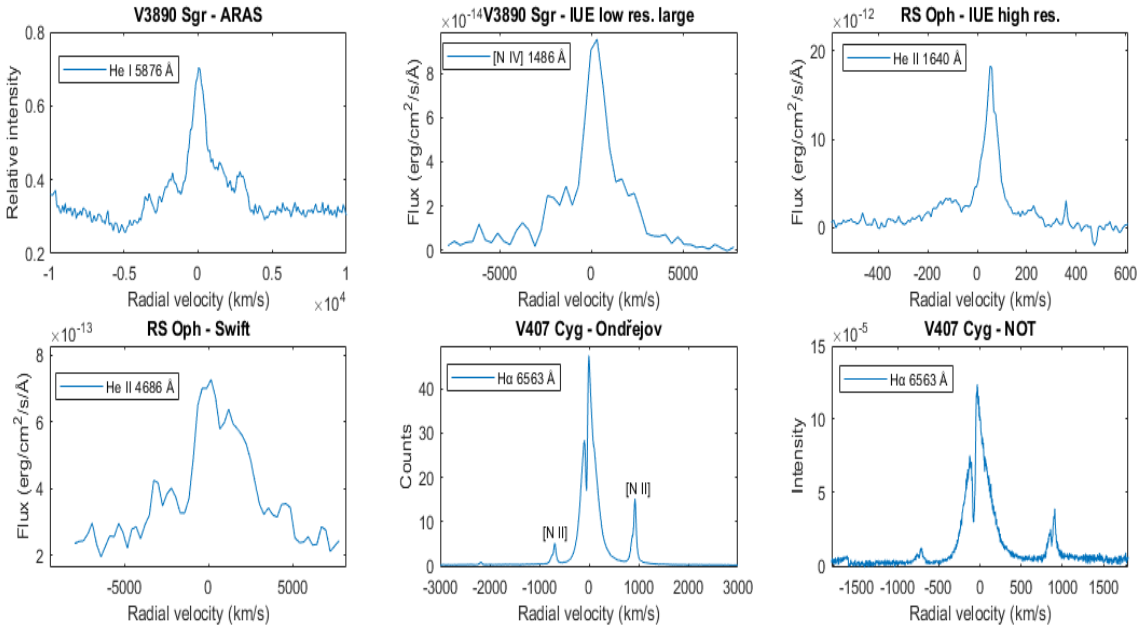

Figure 3.13: From the upper left to the lower right: He I 5876 Å on MJD 58728.8 ($t - t_0 = 5\ days$) in ARAS spectra of V3890 Sgr, N IV 1486 Å on MJD 48034.1 ($t - t_0 = 27\ days$) in IUE spectra of V3890 Sgr, He II 1640 Å on MJD 46164.2 ($t - t_0 = 72\ days$) in IUE spectra of RS Oph, He II 4686 Å on MJD 53913.1 ($t - t_0 = 135\ days$) in Swift spectra of RS Oph, Hα 6563 Å on MJD 55352.0 ($t - t_0 = 86\ days$) and MJD 55334.2 ($t - t_0 = 69\ days$) in Ondřejov and NOT spectra of V407 Cyg. The vast range of resolutions prevent an exact comparison, but the general shape of the profile is evident in all the spectra.

- are detectable in most observed systems, especially during the earliest stages of outburst evolution, right after the maximum light. Permitted emission lines predominantly arise from high-density regions of stellar plasma, from the ejected envelope in Nova objects: at the beginning of Symbiotic-like Recurrent Novae, explosions are characterised by increasing density in very short timescales and values are still large after luminosity peak, then such an environment becomes the ideal setting for the creation of these lines. Permitted transitions are the broadest lines, in general no forbidden lines show similarly wide profiles: the reason is that broad lines forming region is at such high densities that all levels of ions responsible for forbidden transitions are collisionally de-excited. Their transition probabilities, $\sim 10^{-6} - 10^{2}\ s^{-1}$, imply critical electron densities of $\lesssim 10^{8}\ cm^{-3}$. While the evolution proceeds, progressively more ionised species are excited and become responsible for line emission: consequently, as time goes on permitted lines are formed by ionisations of higher order. In the subsequent stages, as the expanding shell evolves and cools, density progressively goes down and permitted transitions progressively fade until they are overcome by other atomic processes.

Differently, semi-forbidden (or intercombination) transitions are characterised by violation of the selection rule of total quantum spin number conservation with the states having different multeplicities.

Forbidden lines are not strictly prohibited as name could suggest, but electrons have much lower probability of being excited to (or de-excited from) these levels with respect to other transitions.

Astrophysical environments in which density is extremely low favor the creation of forbidden lines ([Osterbrock and Ferland(2006)]). Moreover, in the optical spectrum of many objects, even if their transition probability is small, forbidden lines may arise by collisional excitation from ground states of abundant ions. Consequently, spectra showing forbidden lines can be employed to seek out low-density gas. In other words, during outburst of Symbiotic-like Recurrent Novae, forbidden lines are expected to be seen at later stages, when densities have been adequately reduced by the expansion of the system, the interaction between shocks and surrounding material and from photoionisation. Forbidden lines of highly ionised species are usually used to trace the evolution of dynamical features - like shock wave propagation - during outburst.

Fig.3.14 shows a first example of different spectral profiles for permitted, semi-forbidden and forbidden

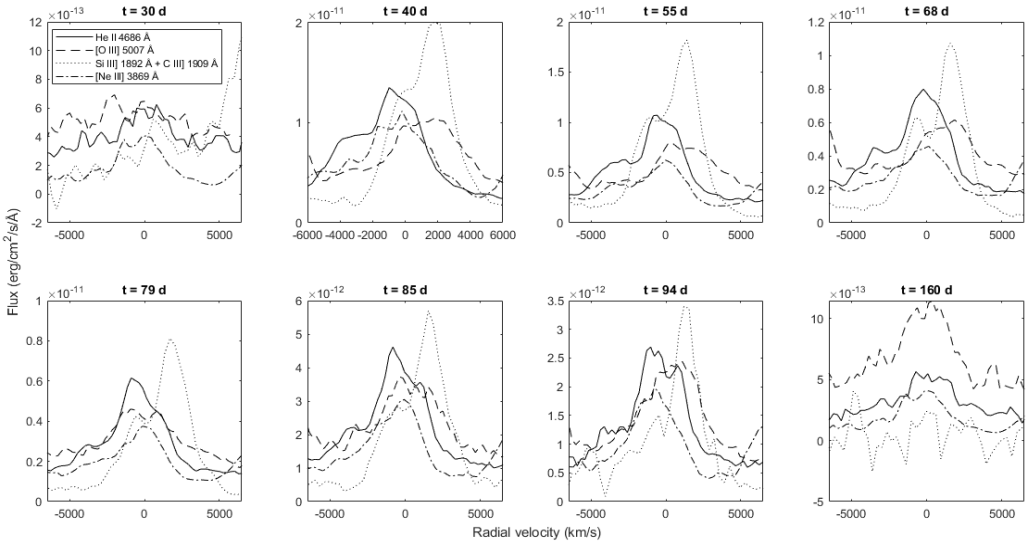

Figure 3.14: Emission line profiles from different permitted, intercombination and forbidden transitions in Swift spectra of the 2006 outburst of RS Oph at different time steps since the beginning on the event. The Si III] + C III] blend is centered on Si III] λ 1892 Å.

lines: permitted He II 4686 Å, semi-forbidden Si III] 1892 Å and C III] 1909 Å, forbidden [O III] 5007 Å and [Ne III] 3869 Å. In the following sections, properties and behavior of specific transitions and related spectral line appearance is explored.

3.4.2 The Balmer series

The Balmer series of the hydrogen atoms, the most abundant species, is ubiquitous and arise from collisional and radiative shock excitation and recombination. The most prominent lines of the sequence are Hα, Hβ, Hγ and Hδ, whereas Hϵ appears only in some spectra and may be contamined by interstellar lines, for example Ca II (H) λ 3968 Å in ESO spectra of V745 Sco, and Hζ is either blended with other profiles or absent in most data. The *Balmer decrement*, i.e. intensity decreasing with decreasing wavelength, depends on the electron density and temperature. Figures 3.16 and 3.15 show the evolution of Balmer lines in Swift spectra: Hα 6563 Å has the strongest and broadest profile but, at the same time, it is affected by the presence of blended multiplets, probably originated by molecular bands - especially TiO absorption bands, which are dominant in the regions $\lambda\lambda 6600 - 6900$ Å, $\lambda\lambda 7600 - 8000$ Å, $\lambda\lambda 8200 - 8500$ Å -, which arise in higher layers of the atmosphere of the RG and can show up in the longer-wavelengths part of the spectrum, covering other emission lines. Other than in Swift data, TiO molecular bands are also visible in other sequences, in particular ARAS and SMARTS, in which the reddest part of the spectra is clearly dominated by the RG component. In addition, the reddest part of Swift grism data is most affected by sensitivity drops of the instrument, too. The Hα profile is not resolved in the Swift sequence. Besides the TiO bands, this is due to overlapping lines from the third order dispersion in the grism.

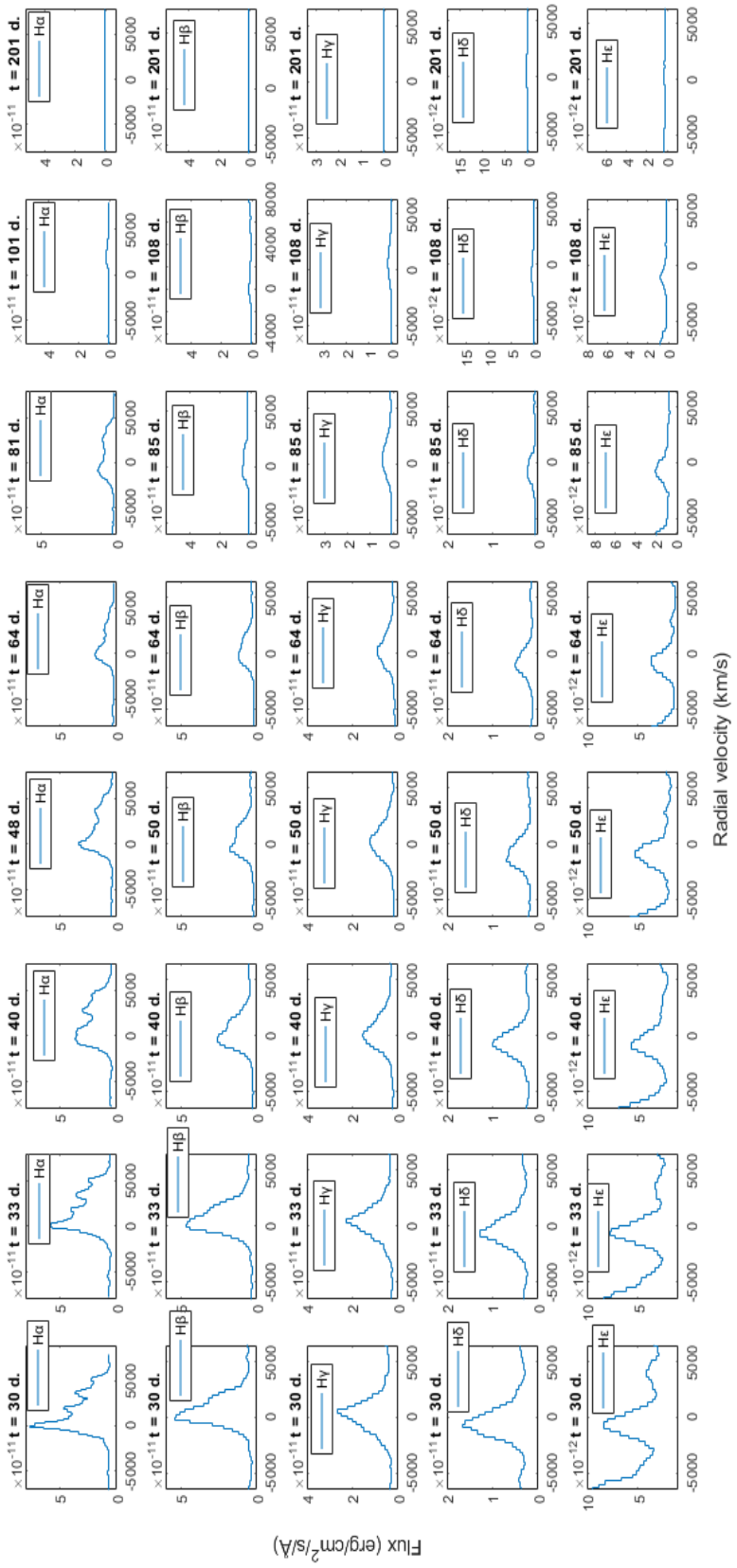

Figure 3.15: RS Oph 2006: spectral sequence of H Balmer emission lines during the outburst in Swift UVOT UV grism spectra. The title of each panel indicates the stage of the outburst since the visible maximum.

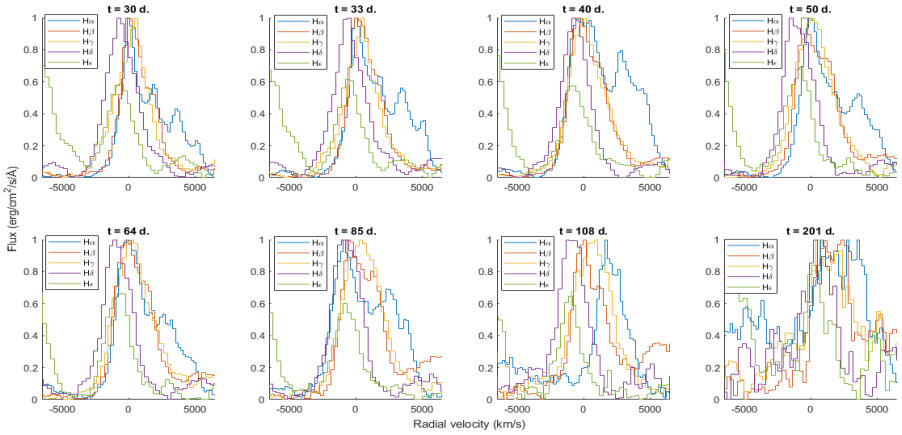

Figure 3.16: RS Oph 2006: sequences of spectral evolution for lines of the Balmer series in Swift UVOT UV grism spectra. Hα 6563 Å, Hβ 4861 Å, Hγ 4341Å, Hδ 4101 Å and Hϵ 3970 Å at various stages. Fluxes are re-scaled for better comparison and graphic optimisation.

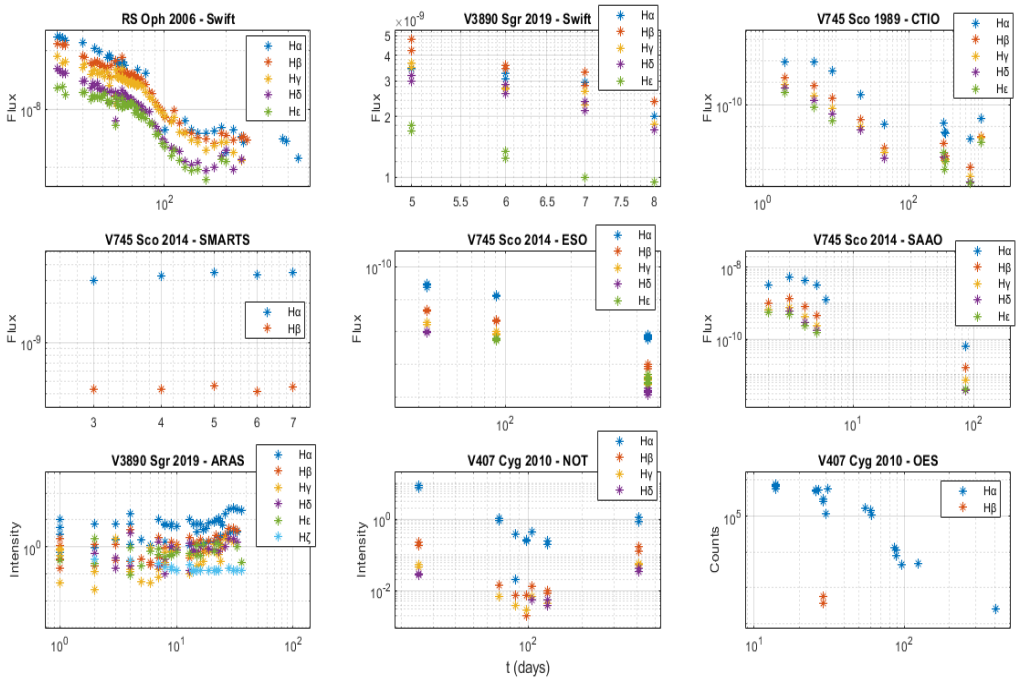

Figure 3.17: Hydrogen Balmer lines evolution during the outburst of Symbiotic Recurrent Novae. All the panels display integrated quantities as functions of time since the beginning of the event, with logarithmic scales on both axes.

Time-dependent evolution of single Balmer lines sequences is shown in Fig.3.17, which tracks integrated fluxes over time for separate systems, while Figs.3.19 - 3.27 show how the profiles of these lines change at various stages. Balmer lines are ideal tracers of the explosive event: early phases show extended emission component (originated by the very fast ejecta) with extremely thin, sharp and intense central peaks, formed by ionisation induced by the high-energy radiation on the surrounding medium. As recombination becomes progressively more important, the narrow peak decreases. In later stages, the two components become gradually less distinguishable and this is because ejecta go on expanding, cooling and decelerating through the wind and the rest of the environment. In Swift data in particular, an interesting feature shows up at later times. As displayed in the first panel of Fig.3.17, after the decline phase consistent with the nova evolution during early stages of the outburst, the integrated flux begins rising again after

about 160 days. The enhanced strength of Hδ and Hϵ lines in the last three points may be emission from a newly formed accretion disc around the WD. A similar trend was observed for other transitions, He II 4686 Å and He I 5048 Å above all, as described later. Another key issue is the change in the slope corresponding to the point at which the shock reaches and overcomes the giant wind: as appreciable in Swift data, the *break-out* stage occurs about 80 days after the beginning of the outburst for RS Oph. By applying power-law $F \propto t^{\alpha}$ fits to the data with 95% confidence bounds, the effect of break-out on α is listed in Table 3.1 and shown in Fig.3.18.

Spectral line	Before breakout	After breakout
Hα	-1.46±0.39	-3.26±1.36
Hβ	-1.46±0.30	-3.19±0.45
Hγ	-1.10±0.28	-3.36±0.33
Hδ	-1.52±0.23	-3.60±0.53
Hϵ	-1.07±0.25	-3.83±0.34

Table 3.1: RS Oph 2006: power law index of the integrated flux of Balmer lines series as a function of days since the beginning of the outburst in Swift data.

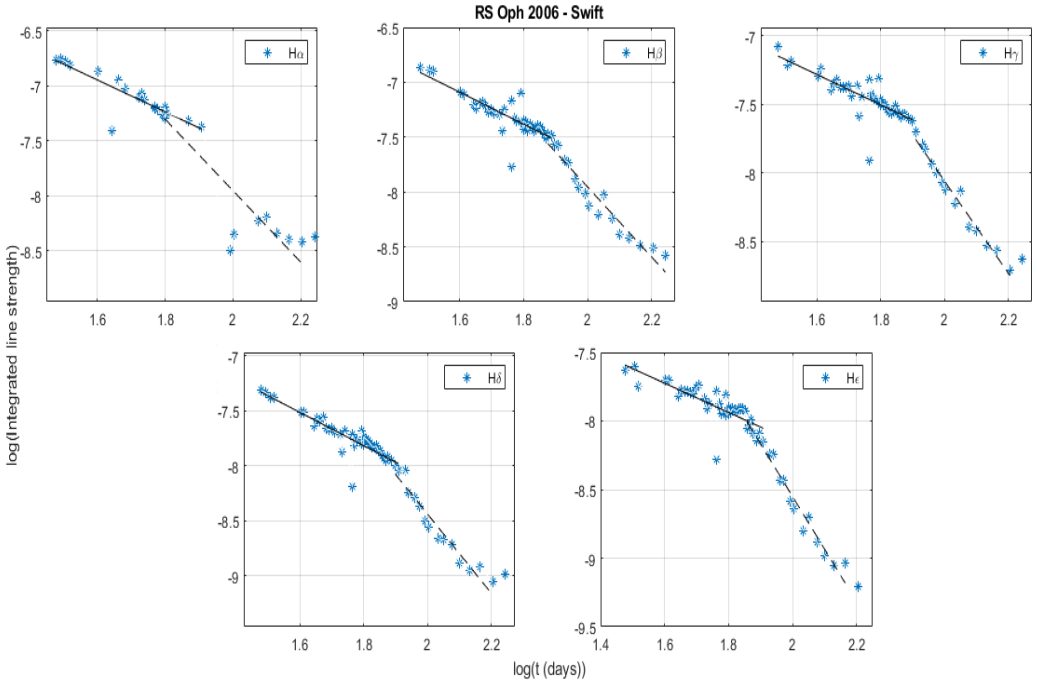

Figure 3.18: RS Oph 2006: power-law fits of hydrogen Balmer lines evolution during the outburst in Swift UVOT/UV-grism spectra.

Note that the Hα profile is unresolved in the later Swift data. Resolved profiles, instead, show a different slope.

This result agrees with evidences for other spectral lines and observations of the previous outbursts. Despite substantial differences of timescales and observations history, the systems all show similar characteristics. Specifically, H line profiles of every recorded outburst show the double components structure, with a narrower core and very broad wings extending up to 2000 $km\ s^{-1}$, even 6000 $km\ s^{-1}$ in Swift spectra. In Swift spectra, the width of the narrow component of Balmer lines is around $\sim 500 - 1000\ km\ s^{-1}$, while the total width of the profiles is given by $FWZI \sim 6000 - 12000\ km\ s^{-1}$ at early times and $FWZI \sim 3000 - 7000\ km\ s^{-1}$ later on. During quiescence instead, ARAS spectra provides H lines with values of FWZI that never exceed $\sim 870 - 900\ km\ s^{-1}$. The highest values are found for Hα, the

other lines of the series are generally narrower and weaker. On the other hand, only V407 Cyg during the main stages of outburst events shows strong P Cygni absorption in correspondence the peaks of H lines, whose strength decreases as the evolution continues, originating in non-shocked ejected material. The disappearance of narrow absorption components on Hβ (and the variations in line profiles of high ionisation species) signals noteworthy acceleration of ambient medium in V407 Cyg. The 2010 eruption of V407 Cyg was remarkably similar to RS Oph 1985 [Shore et al.(2011)]. Even if Balmer lines systematically showed lower velocity and profiles similar to Gaussians more than power laws in V407 Cyg, the spectroscopic development was substantially analogous.

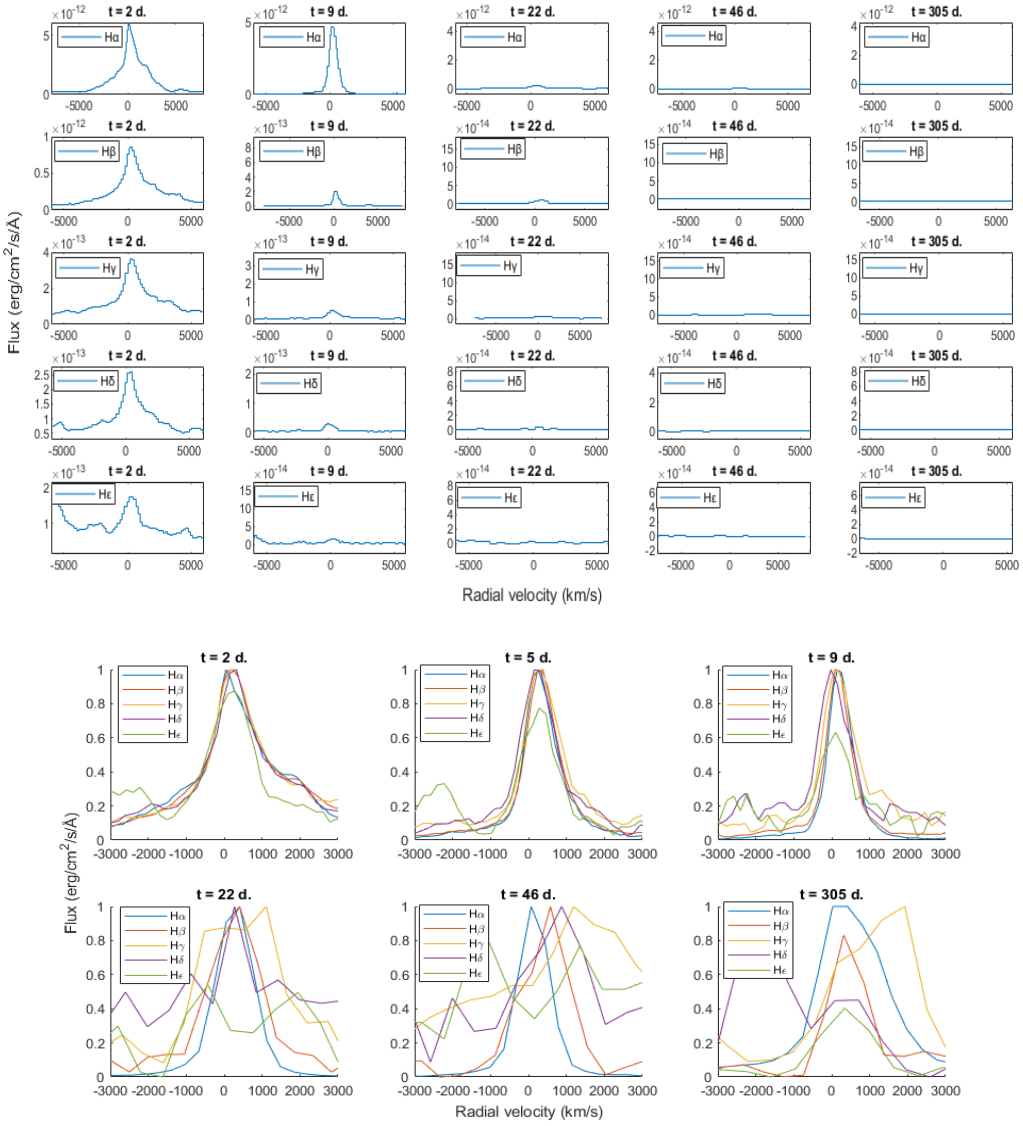

Figure 3.19: V745 Sco 1989: sequences of spectral evolution for lines of the Balmer series. Hα 6563 Å, Hβ 4861 Å, Hγ 4341Å, Hδ 4101 Å and Hϵ 3970 Å in CTIO spectra at various stages of the outburst. In the lower panel, fluxes are re-scaled for optmised graphic representation.

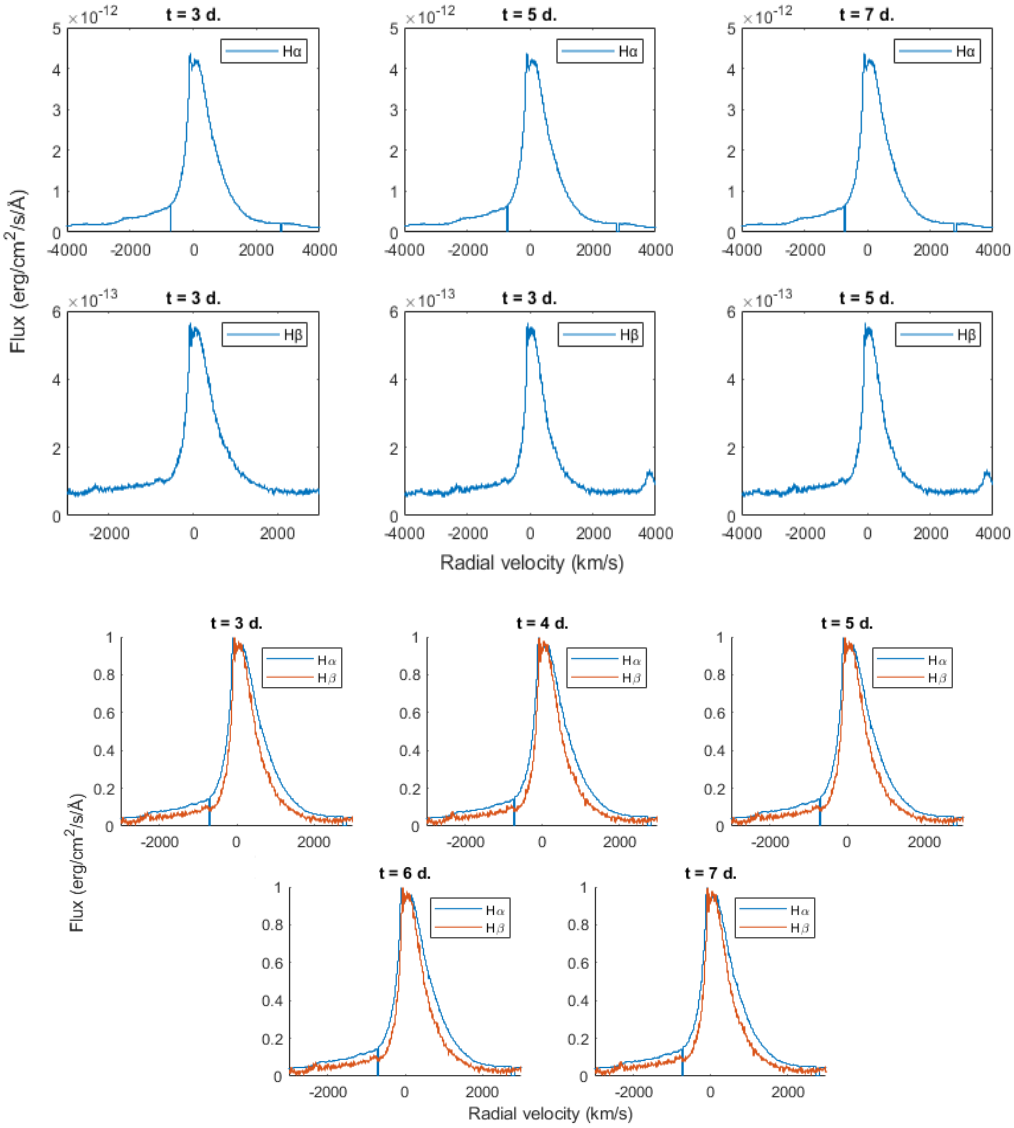

Figure 3.20: V745 Sco 2014: sequences of spectral evolution for the Balmer series: Hα 6563 Å and Hβ 4861 Å in SMARTS spectra at various stages of the outburst.

About 22 days after the 1989 outburst of V745 Sco in CTIO data, lines of the Balmer series almost completely vanished, especially Hγ, Hδ and Hϵ. In the previous spectra, lines clearly show the double component, with a narrow central peak whose width is $FWZI \sim 2500 - 3000\ km\ s^{-1}$ and extended asymmetric wings, for a total width $FWZI \sim 5000 - 8000\ km\ s^{-1}$ in most profiles.

SMARTS data from the 2014 outburst of V745 Sco show similar features on the central peak of the narrow component. It is an actual structure and not an artifact, also observed on $H\alpha$ in ESO spectrum at $t = 44\ days$ (first panel in Fig.3.21) and both Hα and Hβ in the panels of Fig.3.23 for the NOT sequence. A possible explanation for the presence of such glitches may be the fact that the RG undergoes periodic pulsations, which create structures of different densities and velocity in the surrounding wind. As the precursor crosses the circumstellar gas, the encounter with these regions provokes changes in intensity and additional complex features on the emission profiles, which are slightly different from pure absorption by the wind.

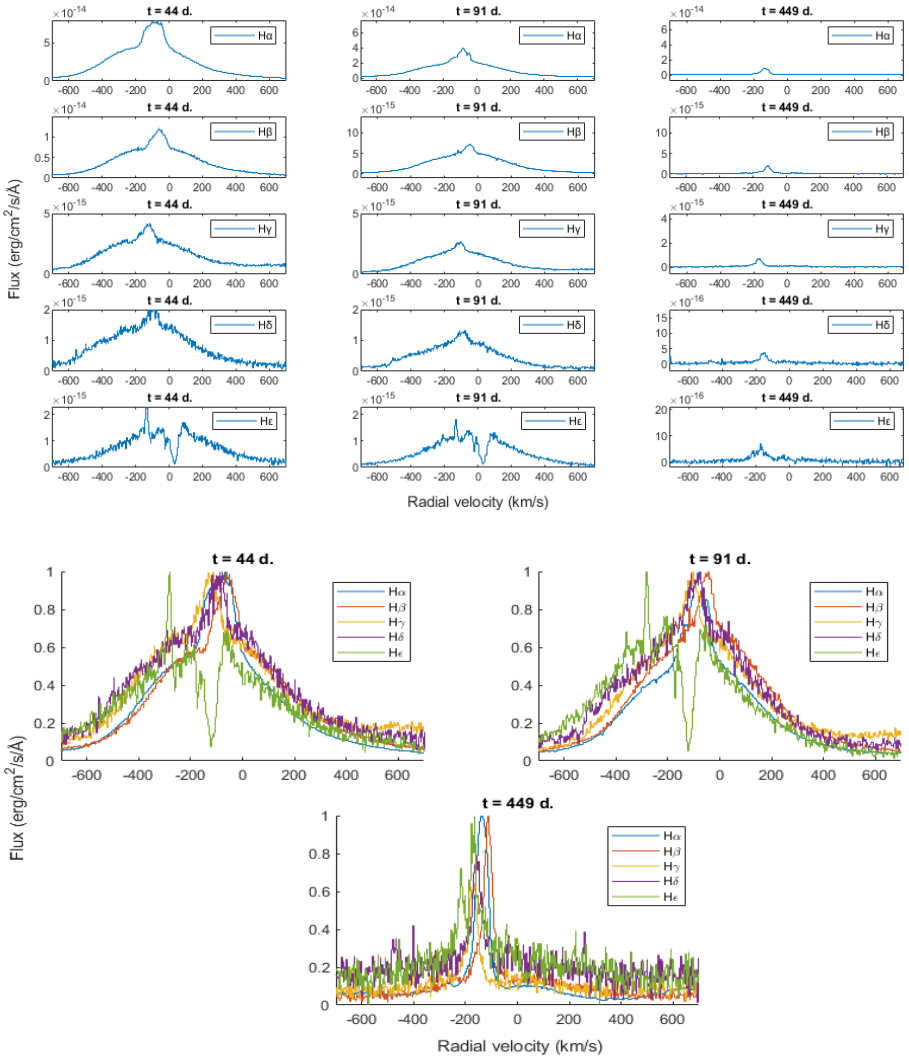

Figure 3.21: V745 Sco 2014: sequences of spectral evolution for lines of the Balmer series in ESO spectra. Hα 6563 Å, Hβ 4861 Å, Hγ 4341Å, Hδ 4101 Å and Hϵ 3968 Å in ESO spectra of V745 Sco at various stages of the 2014 outburst. In the lower panel, fluxes are re-scaled for comparison between the profiles and graphic optimisation.

ESO spectra also show a noticeable absorption component at $\simeq 25\ km\ s^{-1}$ on the Hϵ profiles. Another important feature of Balmer lines in this sequence is the blueshift in the central peak. It increases over time, from $\simeq -65\ km\ s^{-1}$ at $t = 44$ to $\simeq -135\ km\ s^{-1}$ at $t = 449$ for Hα and Hβ, from $\simeq -115\ km\ s^{-1}$ at $t = 44$ to $\simeq -165\ km\ s^{-1}$ at $t = 449$ for Hγ, from $\simeq -76\ km\ s^{-1}$ at $t = 44$ to $\simeq -158\ km\ s^{-1}$ at $t = 449$ for Hδ and $\simeq -170\ km\ s^{-1}$ at $t = 449$ for Hϵ. Again, this is the wind radial velocity.

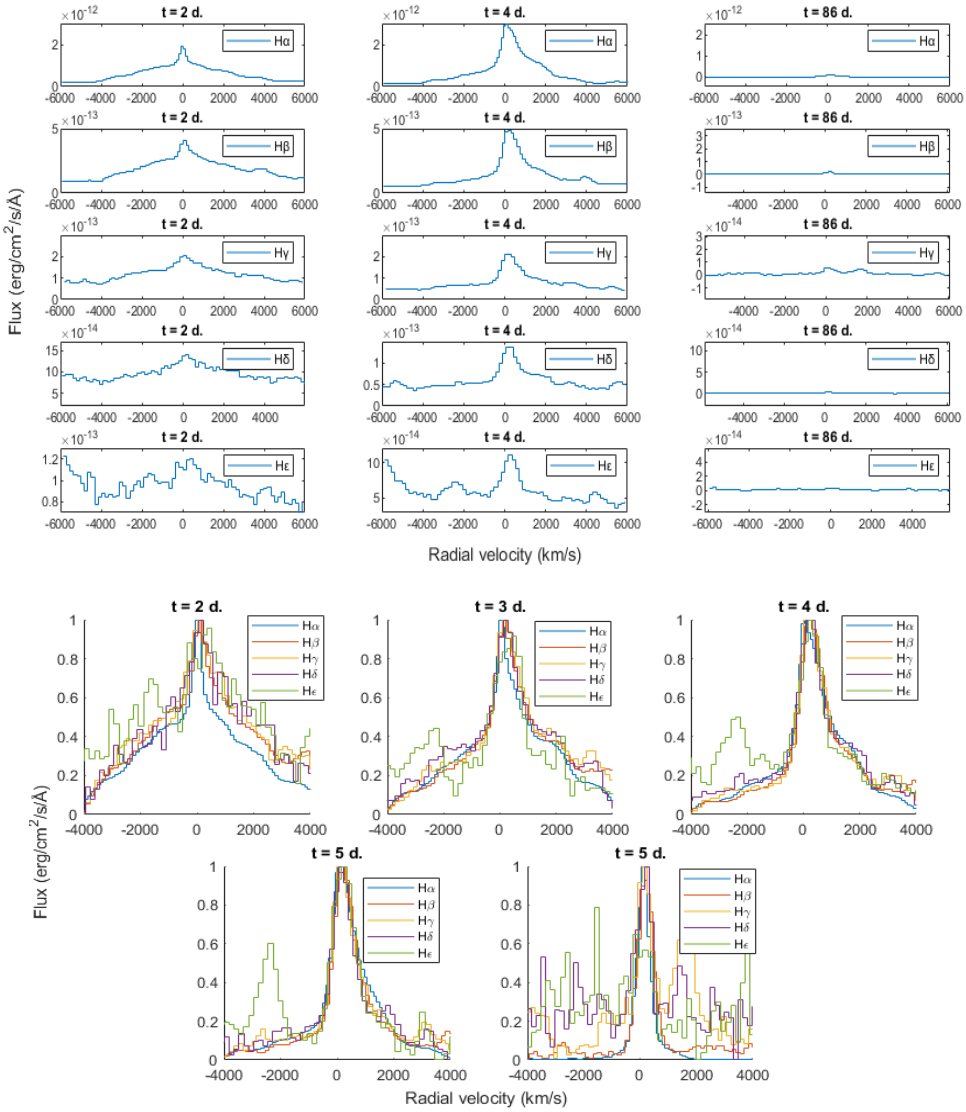

Figure 3.22: Sequences of spectral evolution for lines of the Balmer series: Hα 6563 Å, Hβ 4861 Å, Hγ 4341Å, Hδ 4101 Å and Hϵ 3970 Å in SAAO spectra of V745 Sco at various stages of the 2014 outburst. In the lower panel, fluxes are re-scaled for optmised graphic representation.

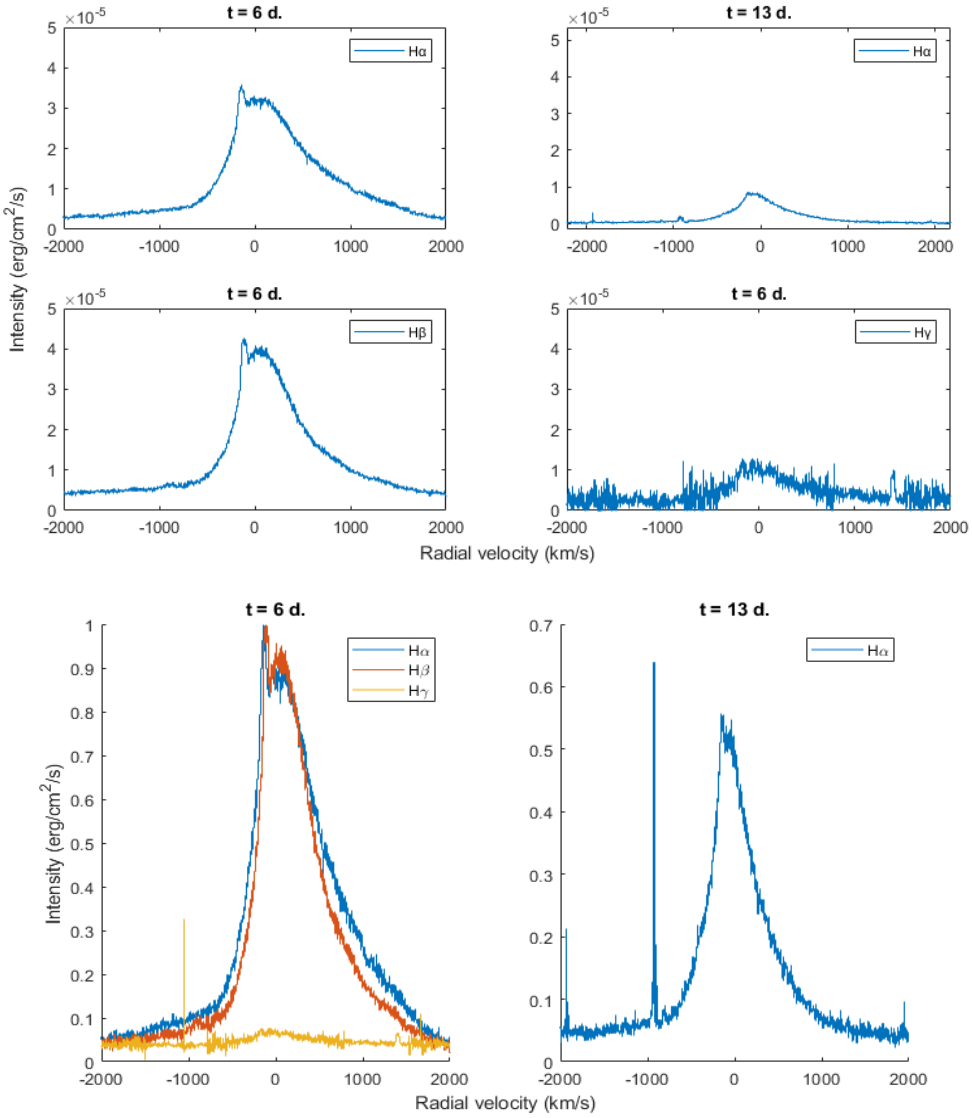

Figure 3.23: V745 Sco 2014: sequences of spectral evolution for lines of the Balmer series. Hα 6563 Å, Hβ 4861 Åand Hγ 4341Åin NOT spectra at various stages of the outburst. In the lower panel, lines strength is re-scaled for profile comparison and graphic optimisation.

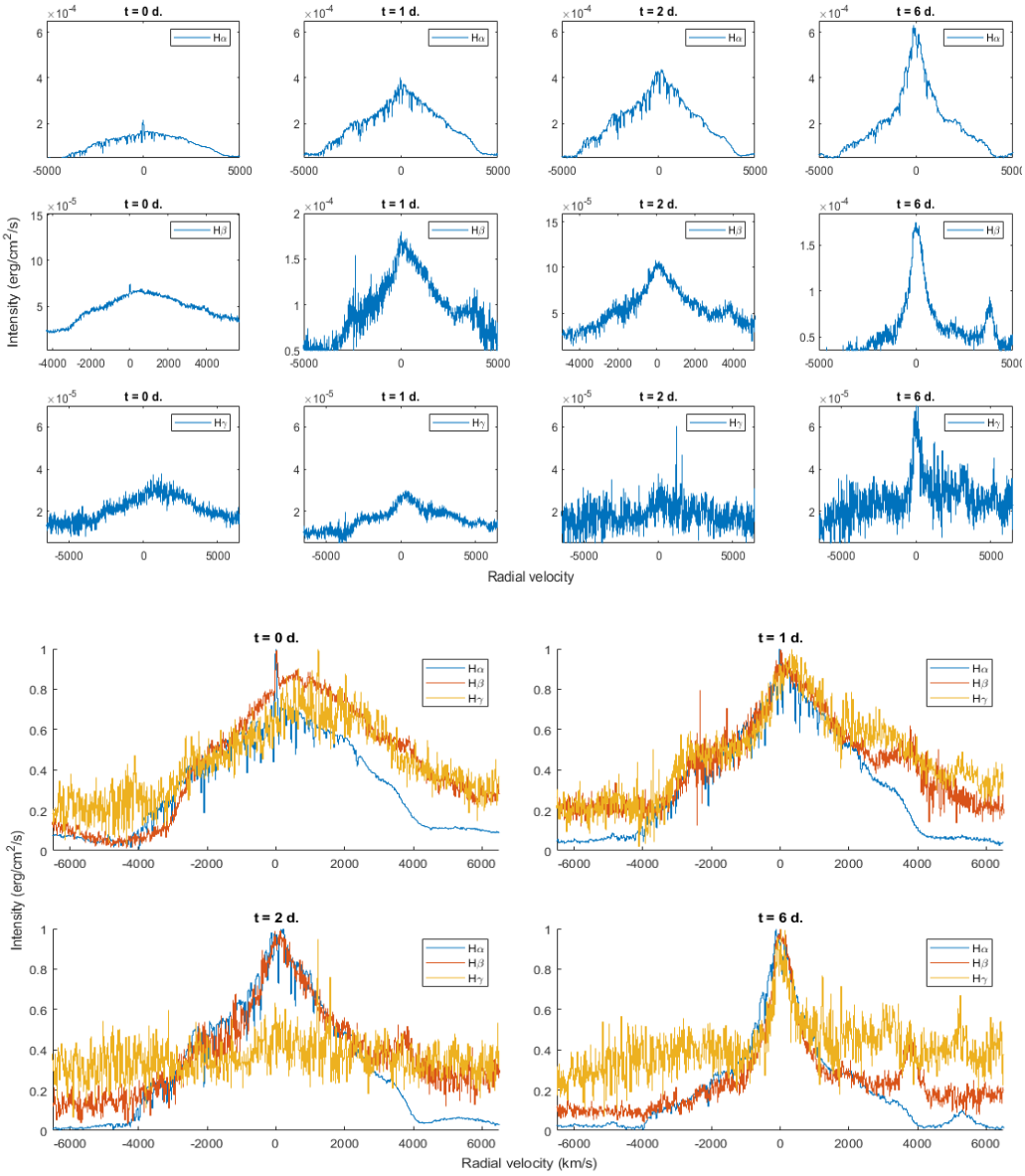

Figure 3.24: V3890 Sgr 2019: sequences of spectral evolution for lines of the Balmer series: Hα 6563 Å, Hβ 4861 Å, Hγ 4341Å in higher ($>$ 8000) resolution ARAS spectra of V3890 Sgr at various stages of the outburst. Intensities in the lower panel are re-scaled for optmised graphic representation.

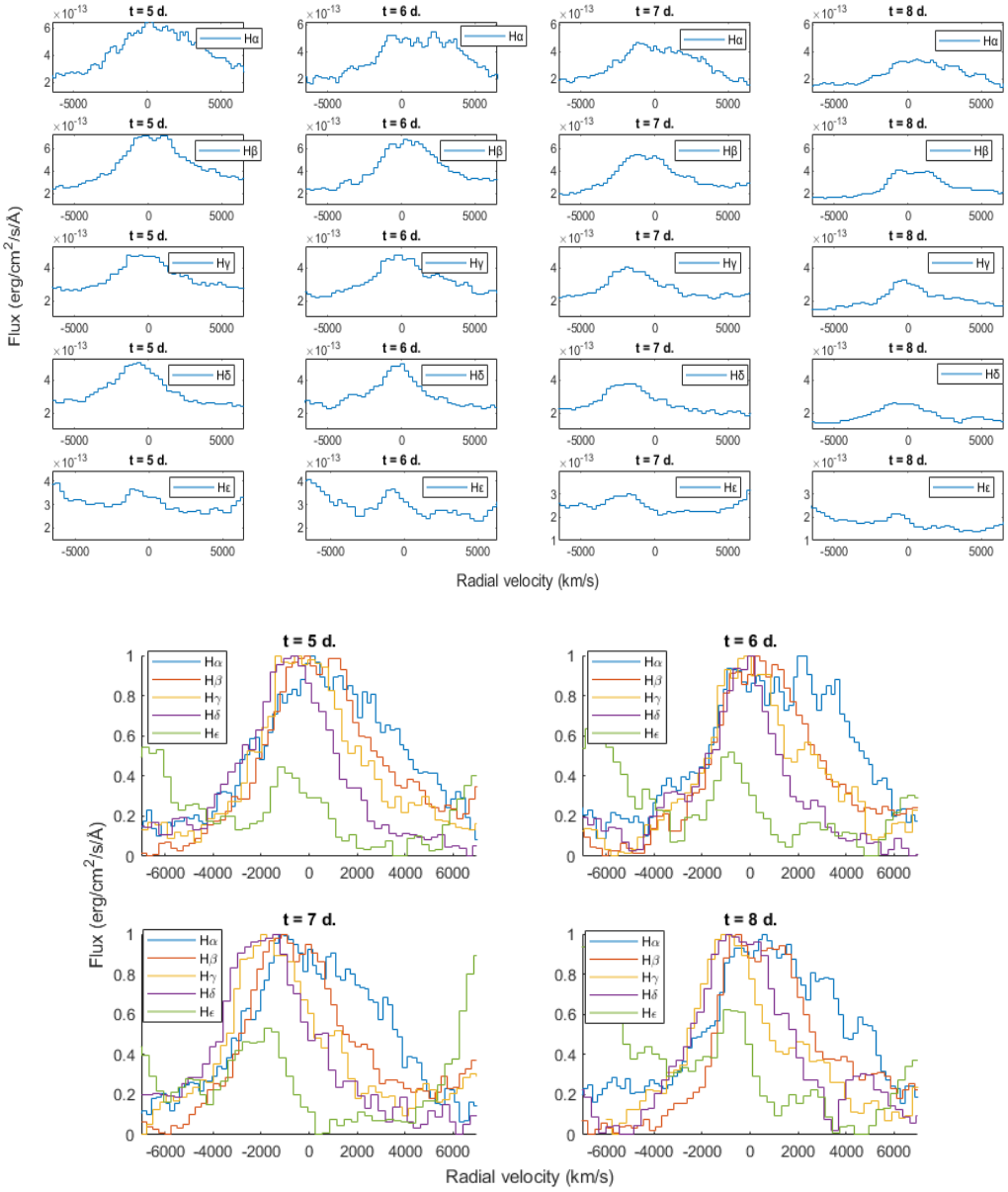

Figure 3.25: V3890 Sgr 2019: sequences of spectral evolution for lines of the Balmer series. Hα 6563 Å, Hβ 4861 Å, Hγ 4341Å, Hδ 4101 Å and Hϵ 3970 Å in Swift spectra at various stages of the outburst. In the lower panel, fluxes are re-scaled for graphical optimisation of profiles comparison.

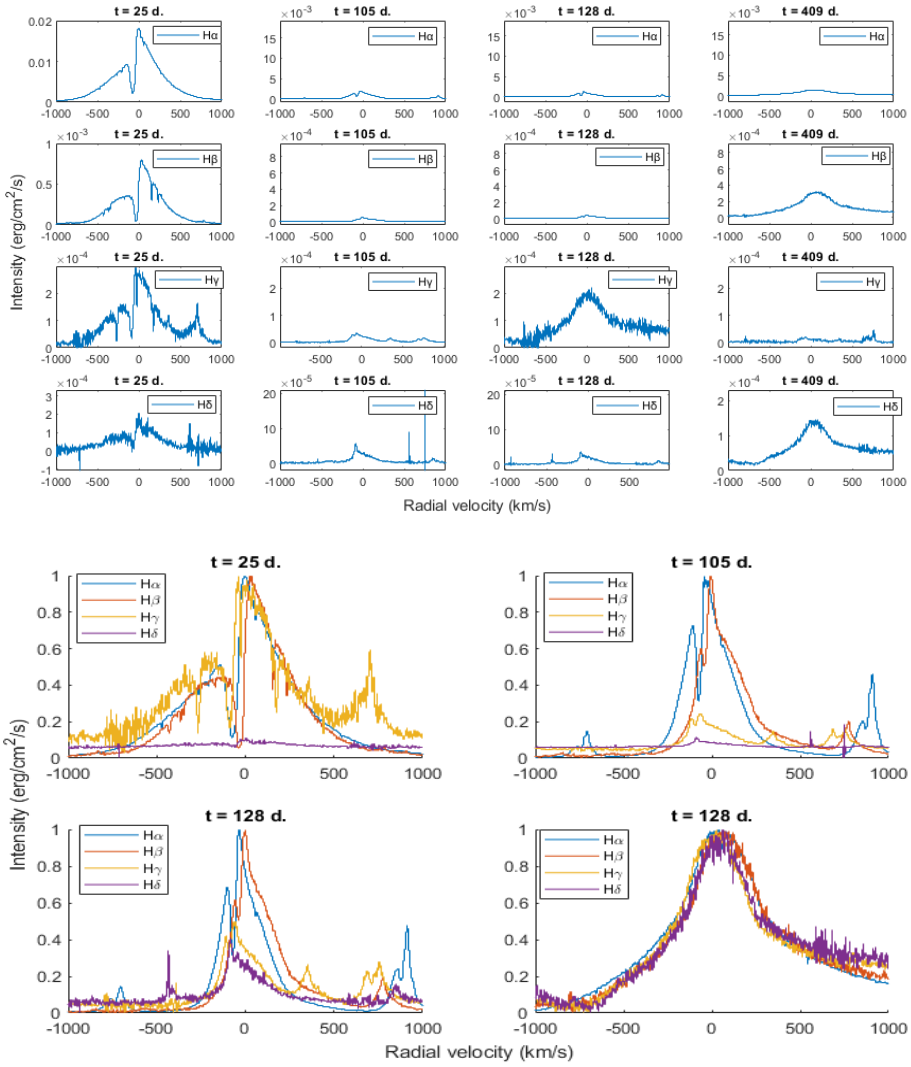

Figure 3.26: V407 Cyg 2010: sequences of spectral evolution for lines of the Balmer series. Hα 6563 Å, Hβ 4861 Å, Hγ 4341Å and Hδ 4101 Å in NOT spectra at various stages of the 2010 outburst. In the lower panel, intensity is re-scaled for optmised graphic representation.

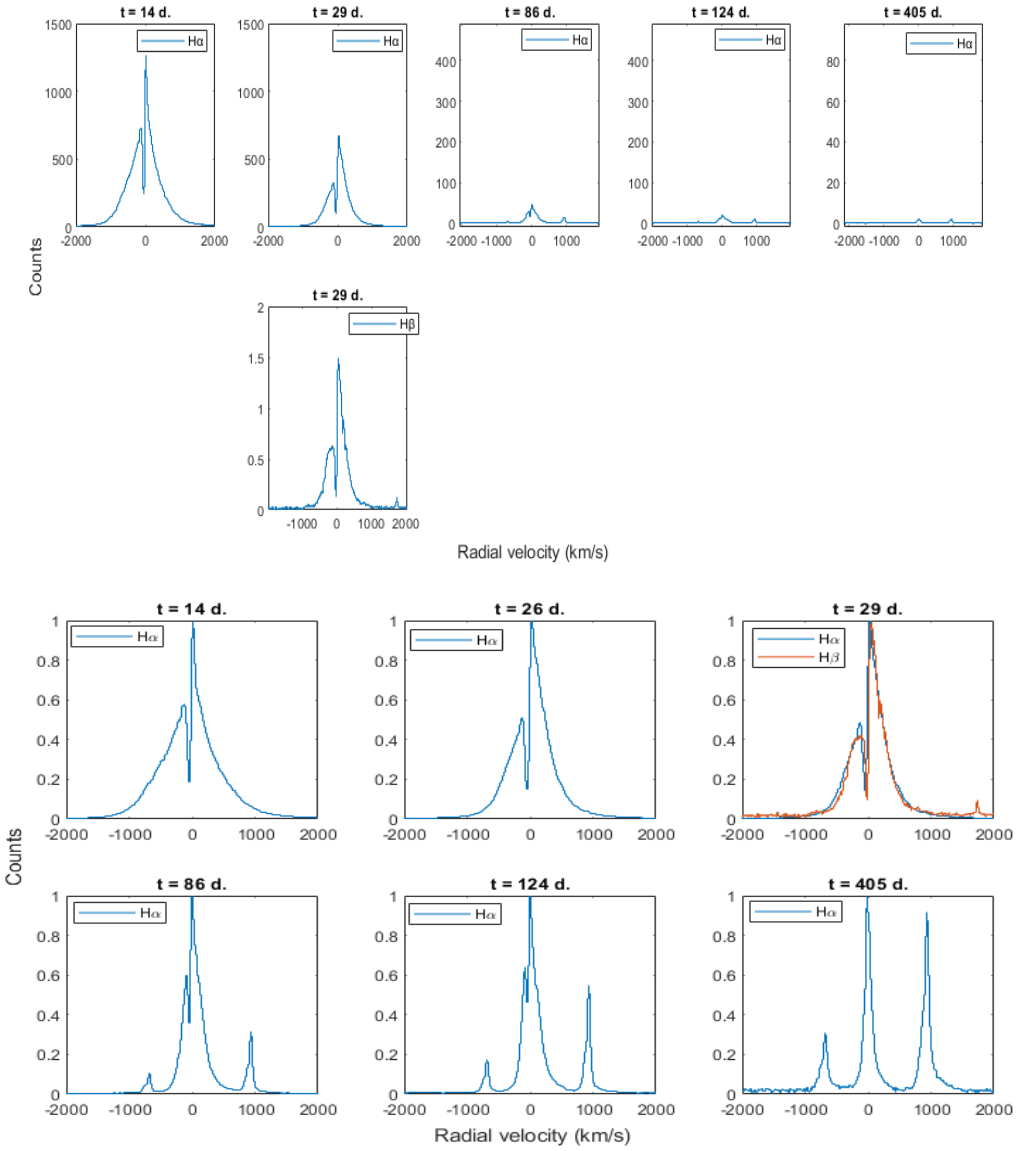

Figure 3.27: V407 Cyg 2010: sequences of spectral evolution for lines of the Balmer series. Hα 6563 Å and Hβ 4861 Å; in OES spectra at various stages of the outburst. In the lower panel, lines are re-scaled for better comparison and graphic representation.

NOT and OES spectra of the 2010 outburst of V407 Cyg are the only ones showing clear evidence of P Cygni profiles overimposed on emission lines. The absorption is deeper in the first plots of the sequence, then it progressively diminishes until it is no longer visible after $t \simeq 400\ days$, at which point the ejecta is no longer strongly interacting with the surrounding wind from the giant. The wind component appears in NOT data between $\simeq -80$ and $-73\ km\ s^{-1}$ on Hα, $\simeq -40$ and $-37\ km\ s^{-1}$ on Hβ, $\simeq -100$ and $-92\ km\ s^{-1}$ on Hγ, $\simeq -70$ and $-52\ km\ s^{-1}$ on Hδ. In Ondřejov spectra, the absorption lies between $\simeq -65$ and $-50\ km\ s^{-1}$ on Hα and $-170\ km\ s^{-1}$ on Hβ. These values are compatible with the typical velocities of RG winds similar to the one in this system.

For profile width, Figs.3.28 and 3.29 show the trend of FWZI in velocity over time. To reduce redundance and excessive confusion in the graphic representation, points are binned and averaged over time intervals of 4 days, with the exception of SMARTS 2014, ESO, SAAO and NOT data, for which ranges are of 3 or 2 days due to lower number of spectra.

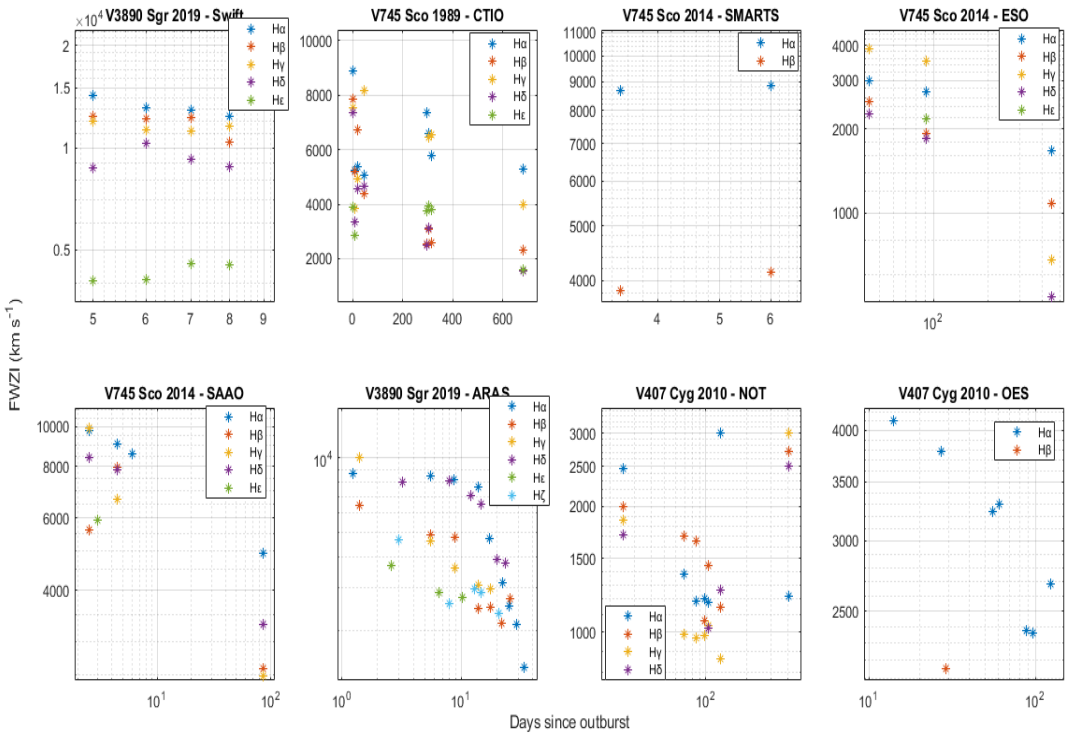

Figure 3.28: Full width at zero intensity for Hydrogen Balmer lines evolution during the outburst of Symbiotic Recurrent Novae. Logarithmic scales are displayed on both axes of every panel.

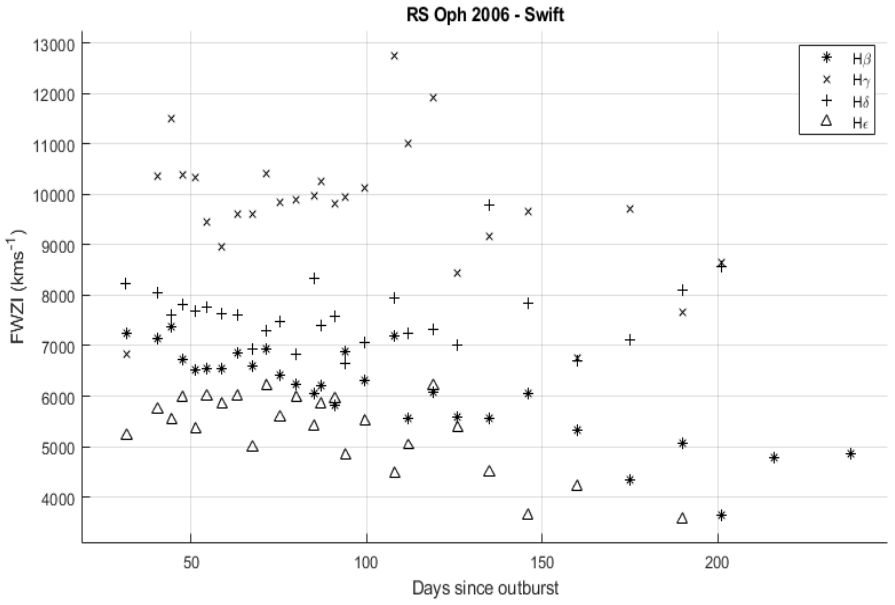

Figure 3.29: Full width at zero intensity for Hydrogen Balmer lines evolution during the 2006 outburst of RS Oph in Swift UVOT UV grism spectra. Both axes are in logarithmic scales and data are binned and averaged over intervals of 4 days each.

3.4.3 The Helium lines

The second most abundant element in stellar plasmas is Helium. In Sy-RNe during outburst, permitted lines from neutral He atoms arise a few days after the luminosity peak together with possible glimmers of singly ionised lines, but these are usually still little evident and/or blended with other profiles. Several days later, He II lines due to recombination appear and reach maximum intensity, He I is still visible even if it shows narrower and weaker profiles. For instance, Fig.3.30 shows how the profile of He II 1640 Å emission line evolves during the outburst of RS Oph in IUE spectra from MJD 46097.5 to MJD 46201.5 (from 6 to 117 days after outburst). Similarily, Fig.3.31 displays how the profile of He II 4686 Å emission line evolves during the outburst of RS Oph in Swift spectra, from MJD 53807.5 to MJD 54029.5 (t = 30 - 252 days after the beginning) and one year later, at MJD 54149.5.

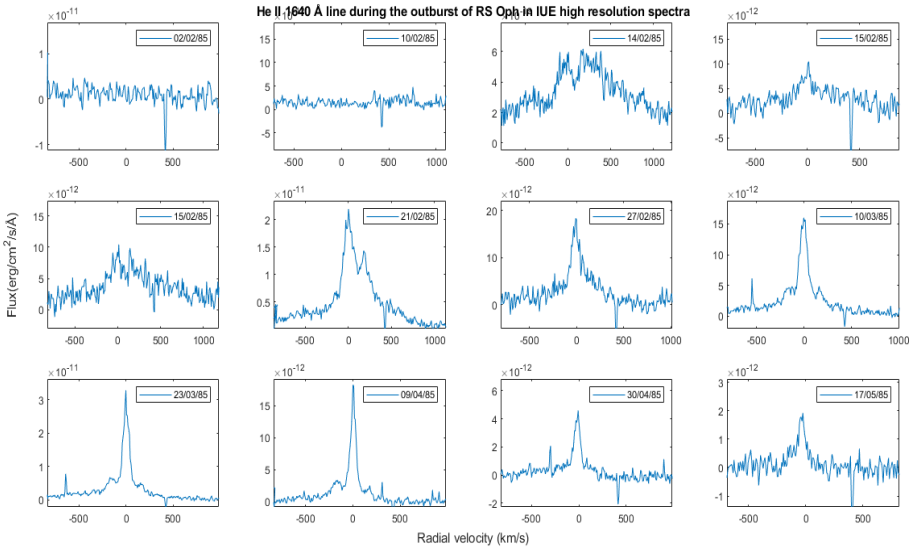

Figure 3.30: Evolution of He II 1640 Å UV emission line profile during 1985 outburst of RS Ophiuchi in high resolution IUE spectra.

He II 1640 Å appears in almost every IUE spectrum of all systems since the very beginning right after the outburst peak, from 6 days onwards, and remains visible until about 250, 14 and 145 days for RS Oph, V745 Sco and V3890 Sgr respectively. He II 4686 Å shows a similar evolution: as with He II 1640, this other line shows up at $t \simeq 5\ days$, as deduced by ARAS sequence of V3890 Sgr, where it is absent in the earliest spectra; the line reaches its maximum strength between 1 and 2 months later and thereafter it is distinguishable longer than 100 days in RS Oph and V407 Cyg, while it starts fading at around 20 days for V745 Sco and V3890 Sgr. The profiles are broad in each spectrum, with wings extending up to $\gtrsim 2100\ km\ s^{-1}$ in the UV and even $\sim 5000\ km\ s^{-1}$ for the optical line in Swift spectra. A comparison between profiles is shown in Fig.3.32. The only exception is V745 Sco in the spectrum from ESO, observed at later times. In more detail, the observed lines are taken from the last detected spectrum before the time of break-out, when the slope of declining spectral strength clearly changes: 72, 27, 7 days after the start for He I lines in RS Oph, V3890 Sgr and V745 Sco, 79, 9, 44 and 5 days for Swift, SMARTS, ESO and SAAO data, respectively. It is important to notice that, since data come from different observations and were detected using different instruments and different resolutions. In particular, with lower resolution instruments significant information is lost.

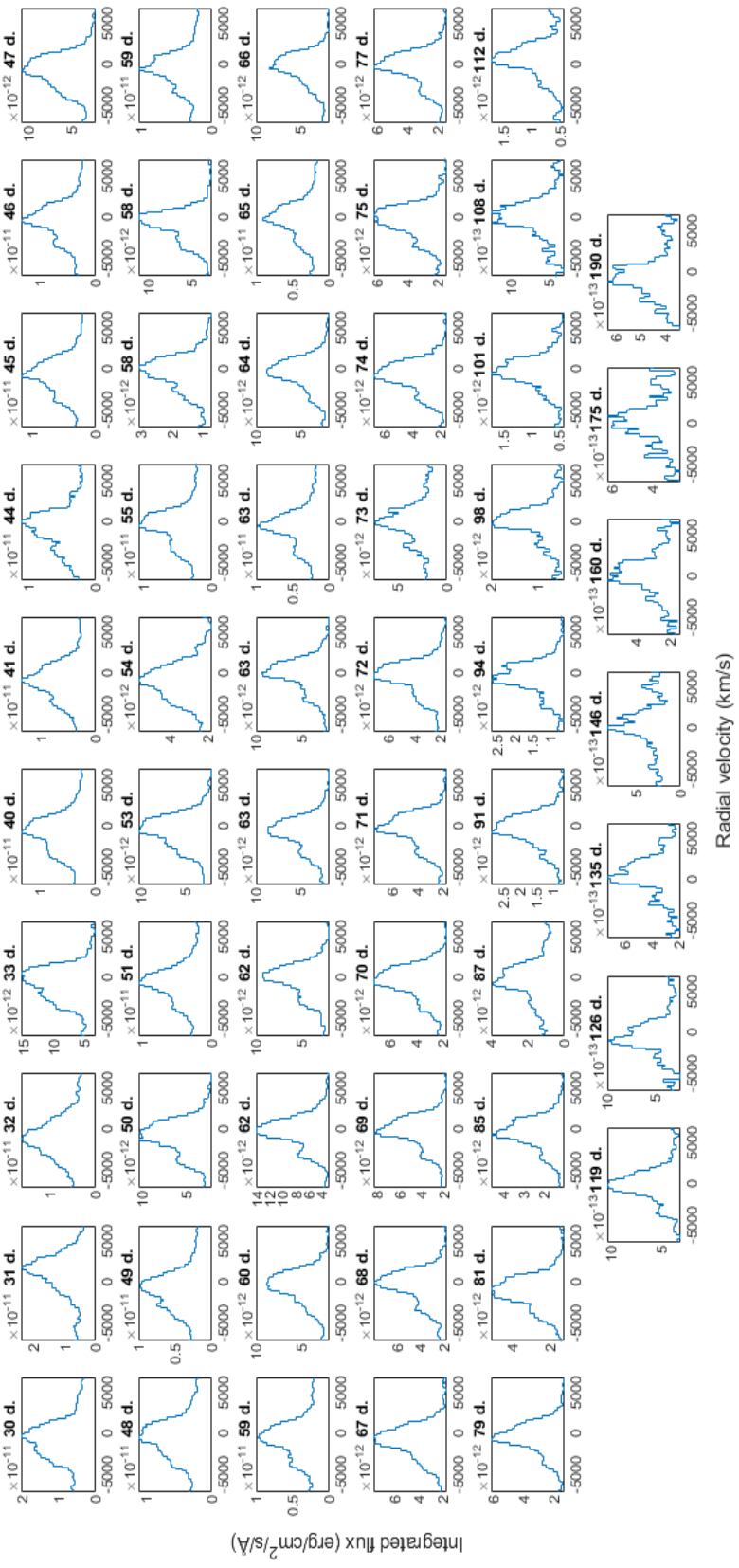

Figure 3.31: Evolution of He II 4686 Å optical emission line profile during 2006 outburst of RS Ophiuchi in Swift spectra. In each panel, the label indicates the stage of the outburst in days since the beginning.

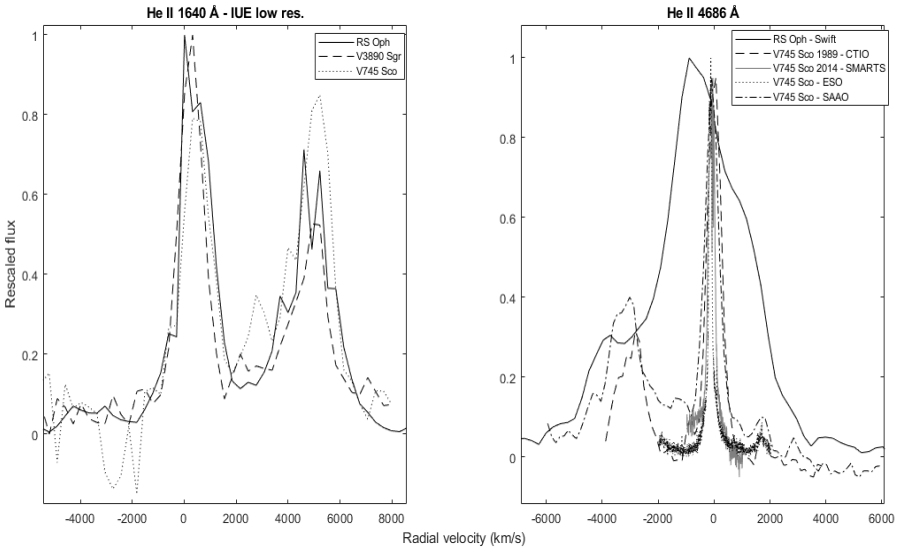

Figure 3.32: Comparison between He II $\lambda 1640$ Å and He II $\lambda 4686$ Å line profiles in Symbiotic-like Recurrent Novae at similar stages during outburst. Fluxes are all re-scaled between [0,1] for graphic optimisation.

Lines from He II transitions are produced by shocked ejected material during its cooling phase in the first months after outburst, whereas unshocked ejecta are responsible for He I emission, whose origin - and subsequent behavior - by recombination and not just collisional excitation is similar to H lines. In IUE spectra at high resolution, as shown by Fig.3.30, another interesting feature appears. On the red wing of He II 1640 Å line, during peak phases of outburst, an additional emission shows up: it is the resonance [O I] multiplet, a $2p^4\ ^3P \rightarrow 3s^3\ S^0$ forbidden transition which is, in turn, originated by the $2p^4\ ^1D \rightarrow 3s\ ^3S^0$ forbidden transition from the upper energy level of the $\lambda 1302$ Å line ([Shore and Aufdenberg(1993)], [Shore et al.(2011)]). The appearance of this line is connected with high column densities in the neutral wind material: O I 1302 Å emission from the ejecta pumps the O I] 1641 Å , [O I] 6300, 6364, 5577 forbidden lines. The 6300 Å doublet is usually observed in all symbiotic systems (but the 1641 line is only observable in high resolution UV spectra, hence the current available dataset is limited in this sense), and is an useful diagnostics for either cold neutral medium and lower layers of the chromosphere in the late-type giant in these binaries. The 6300 blend initially strengthens until about day 40, then its intensity gradually decreases, at a progressively faster rate as the nova approaches breakout stage, at which the expanding shell and corresponding driven shock escape from the giant wind. Regardless of the presence of additional [O I] emission, the analysis of spectral sequences reinforces the evidence of rapid early rise and then fast decline of emission line strength as the outburst progresses and breakout occurs, along with the strict correlation between emissivity of these lines and advance of the ejecta. An evidence for this is provided by the trend of integrated flux as a function of days since outburst in all investigated systems, which is illustrated in Fig.3.33. Another illustrative example is given by He I lines in RS Oph 2006, shown in Fig.3.34.

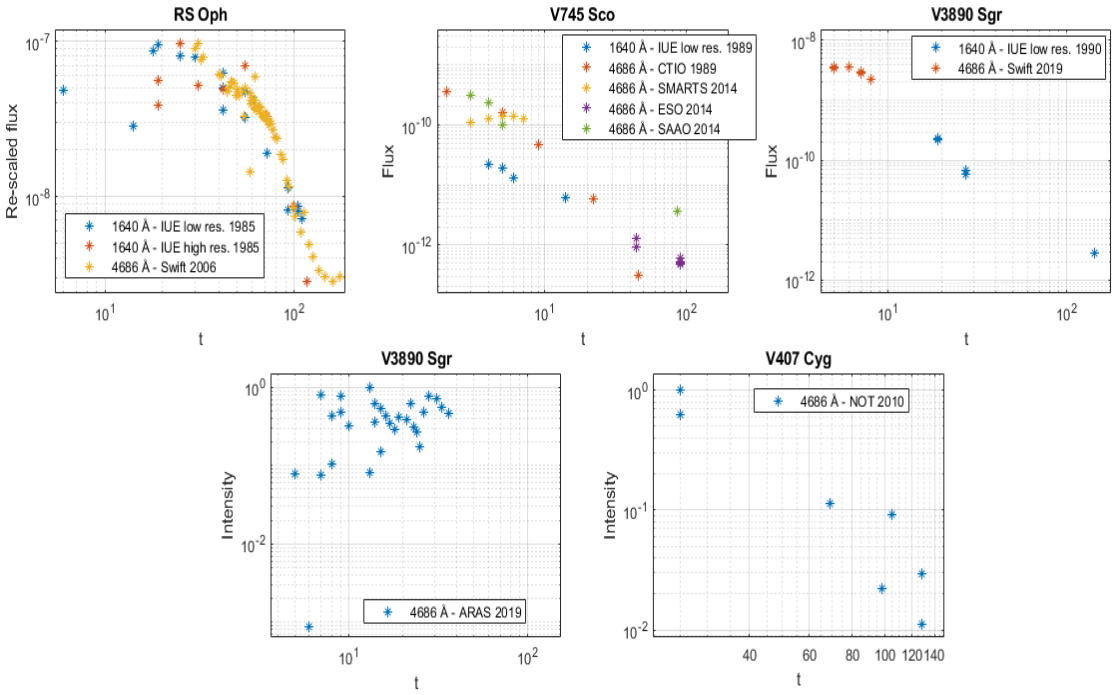

Figure 3.33: Integrated fluxes evolution of He II lines in SyRNe outburst over time, in days after outburst. Axes are in logarithmic scale for each panel.

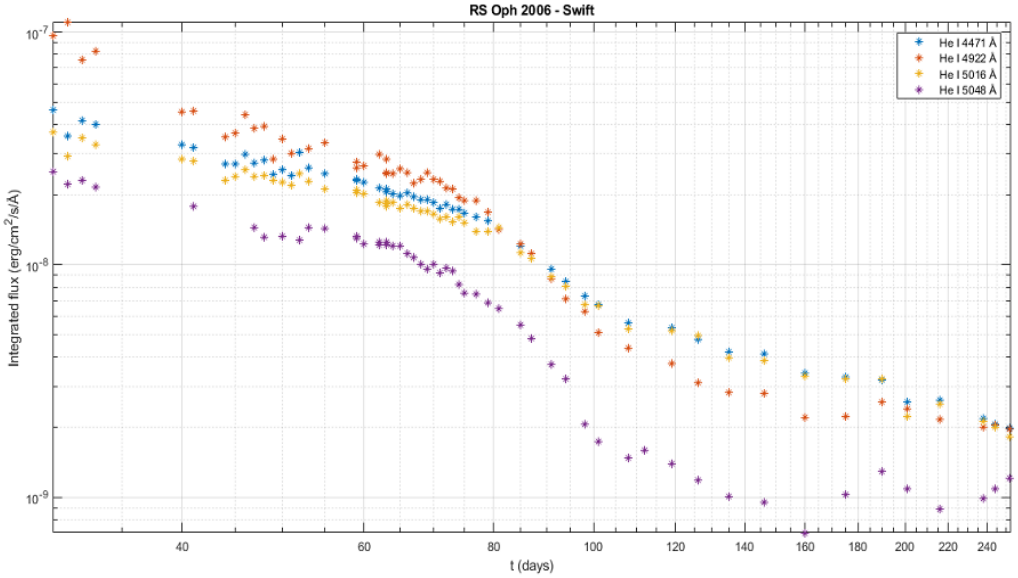

Figure 3.34: RS Oph 2006: integrated fluxes evolution of He I lines in Swift UVOT grism over time. Axes are in logarithmic scale.

As discussed in [Shore and Aufdenberg(1993)], in RS Oph events two effects are hidden behind the He II flux, extinction and wind obscuration. The position of the WD with respect to the observer changes within the wind of the RG on timescales $\simeq$ 1−few years. Hence, the extinction effect on the compact star depends on phase and the luminosity does not suffer any bolumetric redistribution. Any observation of the dwarf outer envelope or its nebula is affected by wind absorption and obscuration. He II 1640 is particularly influenced by such apparent eclipse, and the evidence is that ionisation apparently changes as

the obscuration keeps going.

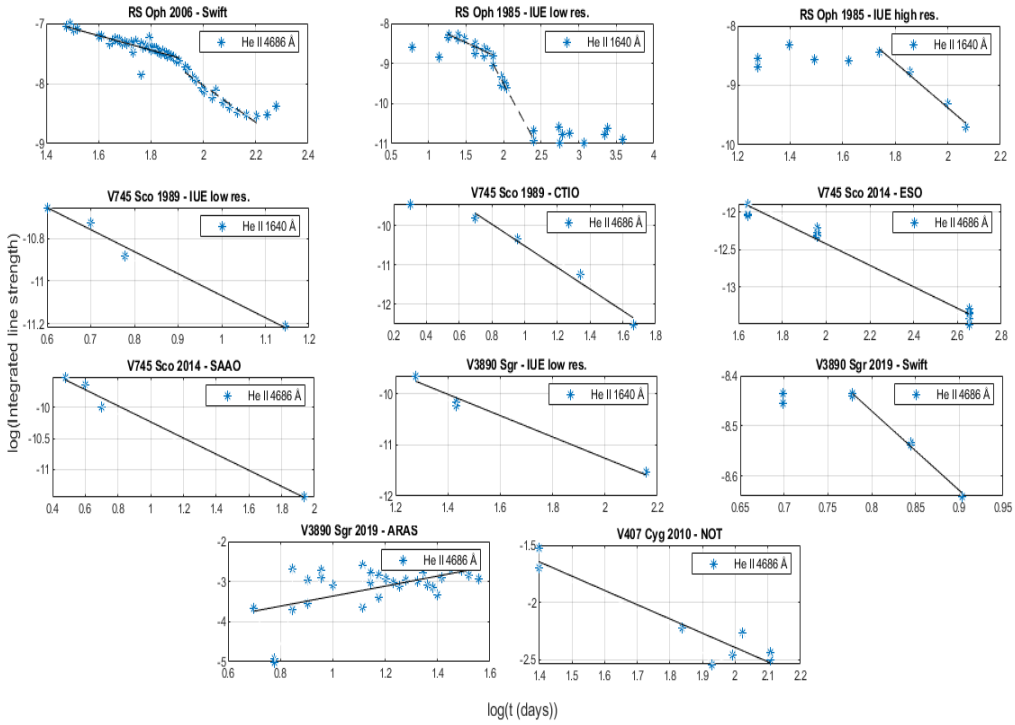

Figure 3.35: Power-law fits of the integrated strength of He II lines in Symbiotic-like Recurrent Novae outburst over time.

If power-law fits $F \propto t^{\alpha}$, where F is the strength of the line - either flux, intensity or counts depending on the dataset -, and t the stage of the outburst in terms of days since the beginning, are applied to the data, helium lines give the results in Fig.3.35 and Table 3.2.

Spectral line (Å)	Event and dataset	Days since outburst	α
4686	RS Oph 2006 - Swift grism	$30 \leq t \leq 81$	-1.20 ± 0.24
4686	RS Oph 2006 - Swift grism	$81 \leq t \leq 146$	-3.06 ± 0.53
1640	RS Oph 1985 - IUE low res.	$18 \leq t \leq 72$	-0.87 ± 0.29
1640	RS Oph 1985 - IUE low res.	$72 \leq t \leq 252$	-3.46 ± 0.53
1640	RS Oph 1985 - IUE high res.	$55 \leq t \leq 117$	-3.79 ± 1.61
1640	V745 Sco 1989 - IUE low res.	$4 \leq t \leq 14$	-1.03 ± 0.42
4686	V745 Sco 1989 - CTIO	$5 \leq t \leq 46$	-2.76 ± 1.26
4686	V745 Sco 2014 - ESO	$44 \leq t \leq 449$	-1.44 ± 0.13
4686	V745 Sco 2014 - SAAO	$3 \leq t \leq 869$	-1.30 ± 0.45
1640	V3890 Sgr 1990 - IUE low res.	$9 \leq t \leq 143$	-2.09 ± 0.62
4686	V3890 Sgr 2019 - Swift grism	$6 \leq t \leq 8$	-1.59 ± 0.22
4686	V3890 Sgr 2019 - ARAS	$5 \leq t \leq 36$	1.25 ± 0.77
4686	V407 Cyg 2010 - NOT	$25 \leq t \leq 128$	-1.24 ± 0.43

Table 3.2: Power law index of the integrated flux of He II lines as a function of days since the beginning of the outburst for various Symbiotic-like Recurrent Novae.

Again, the change in the trend after about 80 days in RS Oph follows the shock break-out stage. Another issue is the increase in the He II strength after 160 days, in agreement with the observed behavior of Hδ and Hϵ line of the Balmer series and presumably associated with the brightening of the accretion disc around the WD. The other systems show similar sequences but on different timescales, for example both V745 Sco and V3890 Sgr evolve much more rapidly, and this is clearly seen in the sharp slope variation already

around 5-6 days since the beginning. This change is not detected in V407 Cyg, for which the strength of He lines steadily declines during the whole sequence, from 25 days onward.

3.4.4 Si III and C III

The evolution of these two spectral lines is particularly important as diagnostics of the environment: Si III] $3s^2\ ^1S_0 \rightarrow 3s\ 3p\ ^3P_1^0$ λ 1892 Å and C III] $2s^2\ ^1S_0 \rightarrow 2s\ 2p\ ^3P_1^0$ λ 1909 Å are intercombination low excitation lines originated by electric-dipole transitions appearing when physical conditions are such that multiple ionisations of ambient ions are possible. These species are characterised by the following values of ionisation potentials and critical densities:

Element	Ionisation potential for creation (eV)	Ionisation potential for destruction (eV)	Critical density (cm^{-3})
Si III	16.3	33.5	1.1×10^{11}
C III	24.4	47.9	5×19^9

Table 3.3: Properties of Si III and C III ([Osterbrock and Ferland(2006)], [Draine(2011)]).

Intercombination lines in RNe spectra are formed in the region behind the photo-ionisation front, which is still unshocked relative to the expanding ejecta and, because of such high critical densities for both transitions, these lines can be used as diagnostics in dense environment. Moreover, because of the close proximity of lines from Si III and C III multiplets, there is no problem of reddening and line ratio is simultaneously highly dependent on electron density of the medium and independent from temperature ([Nussbaumer and Stencel(1987)], [Keenan et al.(1992)], [Keenan et al.(1987)], [Feibelman and Aller(1987)], [Aoki and Yoshida(1998)] and [Kjeldseth Moe and Nicolas(1977)]). In general, ions with one or more accessible levels with similar energy can be adopted to study how the ratio of level populations due to collisional excitation change with density: in more rarefied environments, spontaneous radiative decays always occur after any collisional excitation, whereas at high densities energetic states are occupied without any correlation with their own degeneracy; as a result, densities in line formation regions can be obtained from calculations of relative level populations and corresponding emission line ratios ([Draine(2011)], [Osterbrock and Ferland(2006)]). More specifically, $^{S\ III]}/_{C\ III]}$ can be used as a diagnostic from observed fluxes without requiring extinction corrections, unlike He II, and used as a density indicator: it is higher for greater densities. Figs. 3.36 and 3.37 shows the evolution of line profiles and integrated fluxes.

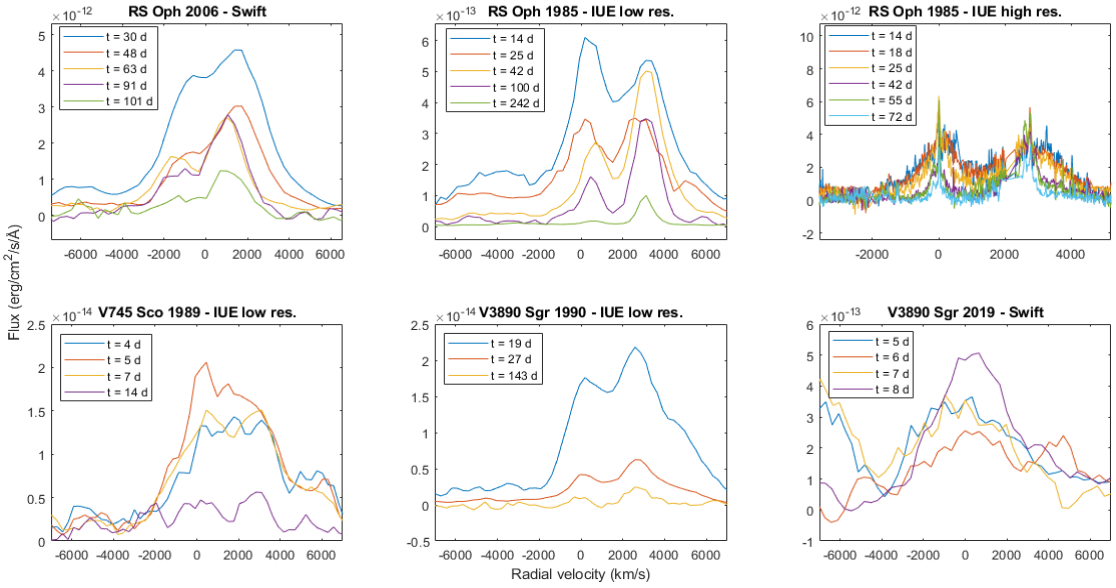

Figure 3.36: Sequences of spectral evolution for Si III] 1892 Å and C III] 1909Å lines at various outburst stages. Velocities are calculated with reference to the rest wavelength of silicon line. Early time fluxes are re-scaled for graphic optimisation in all but RS Oph IUE at high resolution and V389 Sgr Swift spectra.

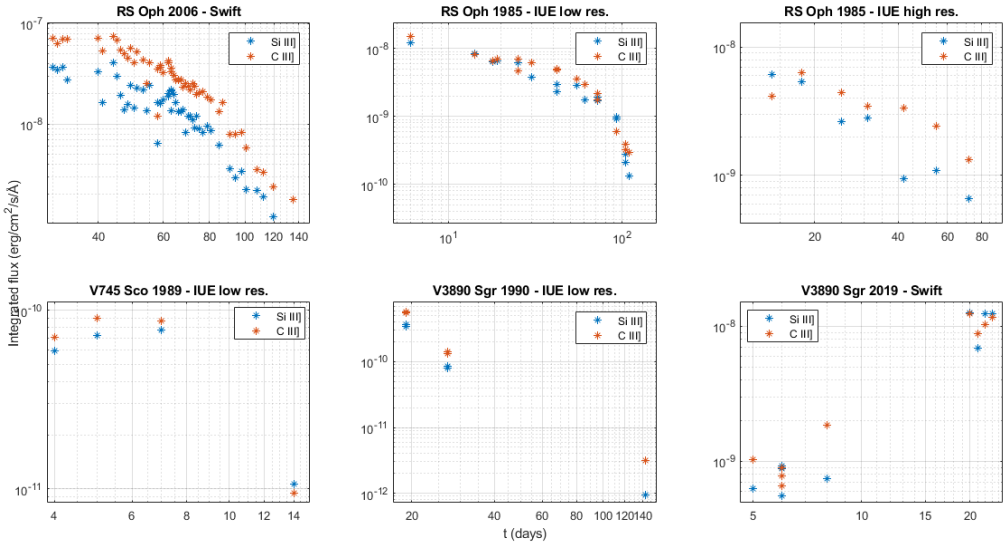

Figure 3.37: Intercombination Si III] 1892 Å and C III] 1909Å lines evolution during the outburst of Symbiotic Recurrent Novae. Axes are all in logarithmic scale.

Power-law fits applied to the integrated flux $F \propto t^{\alpha}$ gives the values for α in Table 3.4 and the results in Fig.3.38 for RS Oph at different epochs.

Spectral line	Event and dataset	Days since outburst	α
Si III]	RS Oph 2006 - Swift grism	$30 \leq t \leq 81$	-1.36 ± 0.35
Si III]	RS Oph 2006 - Swift grism	$77 \leq t \leq 119$	-4.61 ± 0.75
C III]	RS Oph 2006 - Swift grism	$30 \leq t \leq 85$	-1.55 ± 0.29
C III]	RS Oph 2006 - Swift grism	$85 \leq t \leq 135$	-4.83 ± 0.98
Si III]	RS Oph 1985 - IUE low res.	$6 \leq t \leq 72$	-0.86 ± 0.15
Si III]	RS Oph 1985 - IUE low res.	$72 \leq t \leq 110$	-5.53 ± 2.70
Si III]	RS Oph 1985 - IUE low res.	$110 \leq t \leq 2225$	-0.58 ± 0.53
C III]	RS Oph 1985 - IUE low res.	$6 \leq t \leq 72$	-0.75 ± 0.18
C III]	RS Oph 1985 - IUE low res.	$72 \leq t \leq 110$	-4.21 ± 0.60
C III]	RS Oph 1985 - IUE low res.	$110 \leq t \leq 3883$	-0.61 ± 0.50
Si III]	RS Oph 1985 - IUE high res.	$14 \leq t \leq 72$	-1.43 ± 0.42
C III]	RS Oph 1985 - IUE high res.	$14 \leq t \leq 72$	-0.73 ± 0.49

Table 3.4: Power law index of the integrated flux of Si III] and C III] lines as a function of days since the beginning of the outbursts of RS Oph.

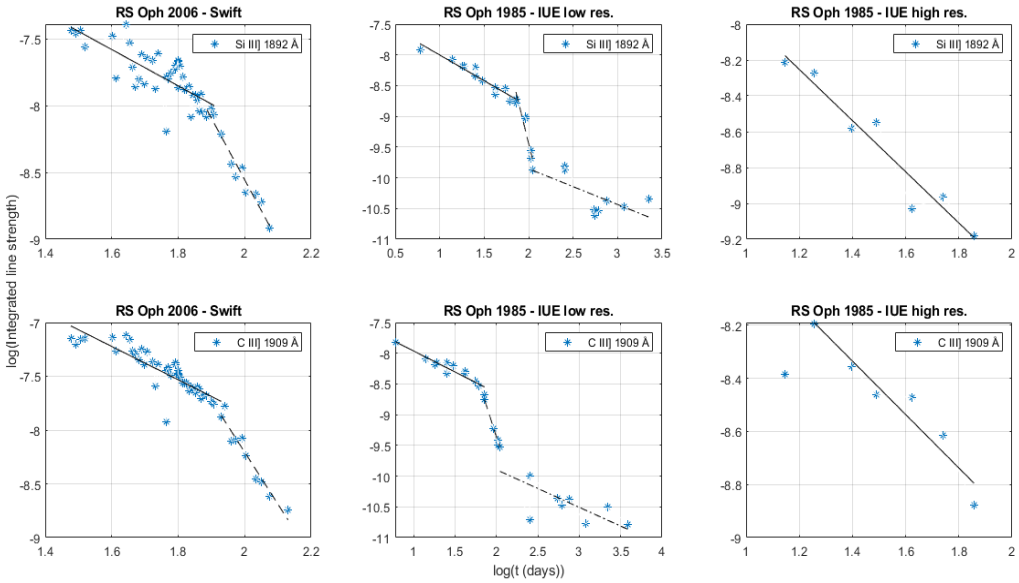

Figure 3.38: Power-law fits of intercombination Si III] 1892 Å and C III] 1909Å lines during the outbursts of RS Oph.

From integrated flux values for both lines, the ratio $r = {}^{S\ III]}/_{C\ III]}$ was derived: in Table 3.5, minimum and maximum values of the ratio are listed together with the corresponding epochs.

Event	Archive	r_{min}	t (min)	r_{max}	t (max)
RS Oph 1985	IUE low res.	0.35	MJD 46196.5	1.12	MJD 46098
RS Oph 1985	IUE high res.	0.44	MJD 46163.5	1.11	MJD 46110.5
RS Oph 2006	Swift	0.19	MJD 53885.5	0.62	MJD 53840.5
V3890 Sgr 1990	IUE low res.	0.42	MJD 48149.5	0.78	MJD 48025.5
V3890 Sgr 2019	Swift	0.40	MJD 58730.5	1.40	MJD 58729.5
V745 Sco 1989	IUE low res.	0.81	MJD 47750.5	1.16	MJD 47741.5

Table 3.5: Ratio of integrated fluxes of Si III] 1892 Å and C III] 1909 Å lines and corresponding times during the outburst of various Symbiotic Recurrent Novae.

Using the line ratio, $R = \frac{F(\lambda 1909\ C\ III)}{F(\lambda 1892\ Si\ III)}$, [Feibelman and Aller(1987)] found an average value $log(R) \simeq 0.74$ in symbiotic stars. For RS Oph $log(R) = 0.68$ in Swift, $log(R) = 0.46$ in IUE, for V745 Sco $log(R) = 0.10$ in IUE, for V3890 Sgr $log(R) = 0.62$ in IUE. With different timescales but similar be-

havior, R increases in the first few days, then decreases in successive phases until between 60-100 days after the beginning and eventually starts increasing again at later stages. Since the two quantities are related, electron density of the medium follows an analogous trend. The evolution for r in the complete sequence is depicted in Fig. 3.39, while Fig. 3.40 shows the single sequences.

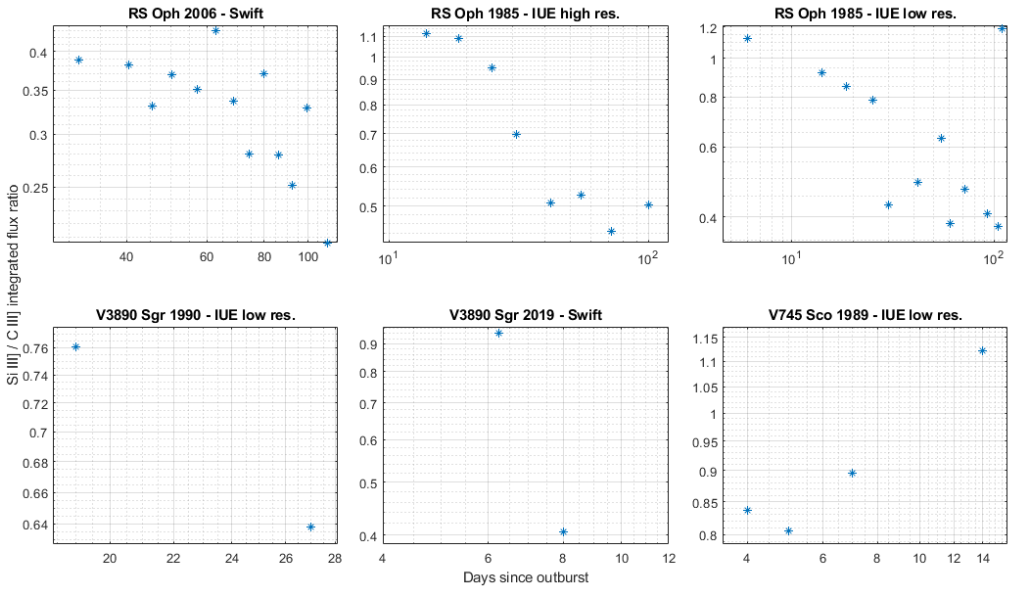

Figure 3.39: Ratio of Si III] and C III] integrated fluxes as a function of days since the beginning of the outburst. Data are averaged over a few days: for RS Oph 6 in Swift, 5 in IUE low resolution and 2 for RS Oph in IUE high resolution spectra, 3 for V3890 Sgr in Swift spectra, 2 days for V3890 Sgr in IUE low resolution spectra.

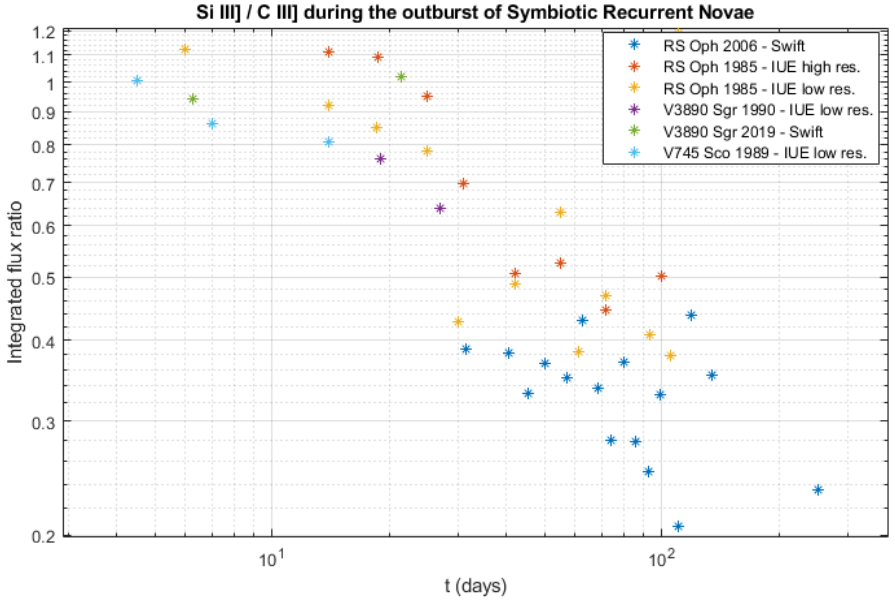

Figure 3.40: Ratio of Si III] and C III] integrated fluxes for single events as a function of days since the beginning of the outburst. To reduce Swift data are averaged over 5 and 3 days for RS Oph and V3890 Sgr, respectively.

3.4.5 Multiple ionised lines

It has been already outlined that physical properties of the environment during different stages of violent events like Sy-RNe outbursts profoundly affect the spectral features of detected species. In particular, right after the eruption densities of the ambient gas are sufficiently high that emission is constrained, for the most part, to permitted transitions radiation; later on, density goes more and more down and expanding shell begins emitting auroral and then nebular lines, with high excitation ones emerging first because they usually have higher critical density than low excitation transitions. While time progresses and density decline keeps going, forbidden lines make their appearance and gain progressively greater importance. Simultaneously, ionisation level always increases, hence - permitted but, even more, forbidden - lines from high ionisation species are essential for late-time inspection. During these phases, high ionisation lines are also a very powerful diagnostic tool for the characterisation for the shock front passing through the wind: these emission lines are formed near the front, hence they probe physical conditions in the region just behind and ahead of the shock. For instance, Mg II UV doublet at $\lambda\lambda 2798 - 2802$ Å is fomed in the gas immediately behind the shock, where excitation, ionisation and outward velocity are maximised, whereas O III, Ne III and Ne V lines (especially forbidden ones) are produced by collisional excitation due to the high velocities and electron temperatures of the precursor and N III arises from the entire structure of the shock region. Ne/H spectra are typical of very fast novae, such that [Ne III] and [Ne V] lines are produced by extremely high-velocity shocks during transition phases, when UV becomes transparent and the main nebular lines appears. Consequently, profile and strength changes of ionised lines from Mg, N, O and Ne are important to follow the corresponding evolution of shock waves. Table 3.6 indicates some properties of the transitions ([Draine(2011)]).

Species	Ionisation potential (eV)	Transition	Spectral line (Å)	Type of transition
Mg II	15.0	$^2S_{1/2} \rightarrow ^2P^0_{1/2}$	2803	resonance - permitted
Mg II	15.0	$^2S_{1/2} \rightarrow ^2P^0_{3/2}$	2796	resonance - permitted
N III	47.4	$^2P^0_{3/2} \rightarrow ^4P_{5/2}$	1750	resonance - intercombination
N III	47.4	$^2P^0_{3/2} \rightarrow ^2D_{5/2}$	4638	fluorescence - permitted
O III	54.9	$^3P_1 \rightarrow ^5S^0_2$	1663	resonance - intercombination
O III	54.9	$^3P^0_2 \rightarrow ^3S_1$	3133	fluorescence and shock - permitted
O III	54.9	$^3P_2 \rightarrow ^1D_2$	5007, 4959	forbidden
O III	54.9	$^1D_2 \rightarrow ^1S_0$	4363	forbidden
Ne III	63.4	$^3P_2 \rightarrow ^1D_2$	3869	forbidden
Ne V	126.2	$^3P_2 \rightarrow ^1D_2$	3426	forbidden
N V	97.9	$^2S_{1/2} \rightarrow ^2P^0_{1/2}$	1242	resonance - permitted
N V	97.9	$^2S_{1/2} \rightarrow ^2P^0_{3/2}$	1238	resonance - permitted

Table 3.6: Properties of transitions for ionised species.

Swift UV grism does not cover the range below 1700 Å , therefore O III λ1663 Å and N V λ1240 Å are not detected in the spectra. Profiles from all the other transitions are observed throughout the 2006 outburst, with broad profiles coherent with both instrumental resolution and dynamical processes that generate them. Some examples are shown in Fig.3.41 at various stages.

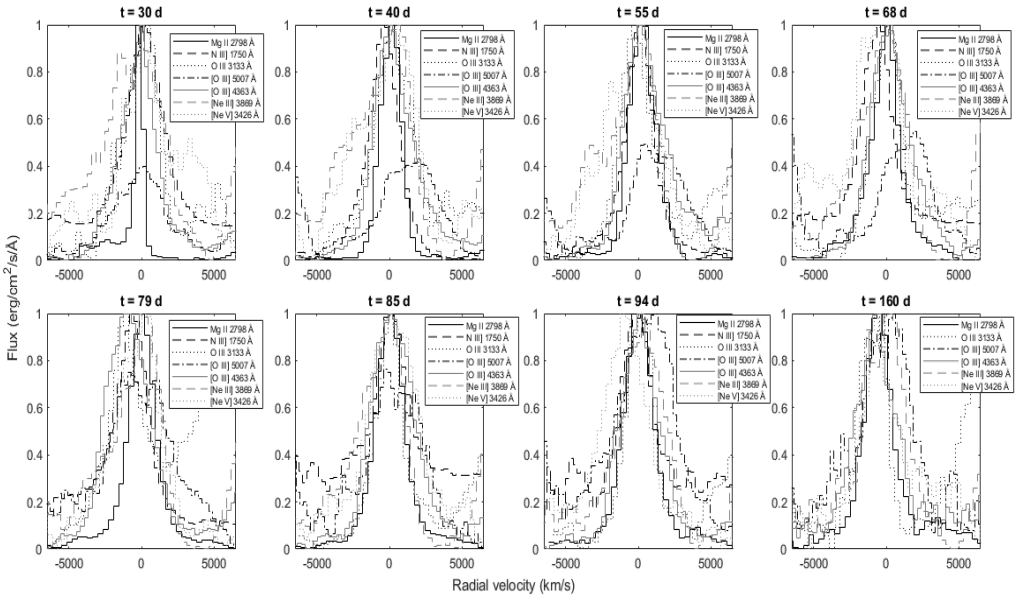

Figure 3.41: Evolution of spectral line profiles from ionised species in RS Oph spectra acquired with Swift UVOT/UV-grism at different stages of the 2006 outburst. Fluxes are re-scaled for a better graphical representation.

The thing that immediately catches the eye is that Mg II $\lambda 2798$ Å profile broadens with time: FWZI increases from $\sim$ 6000 $km\ s^{-1}$ on MJD 53808.7 to more than $\sim$ 10^4 $km\ s^{-1}$ on 53851.8 and then diminishes, reaching $\lesssim 5500\ km\ s^{-1}$ at MJD 53938.6. Fig.3.42 shows the integrated flux of [O III] $\lambda 5007$ Å in days since outburst.

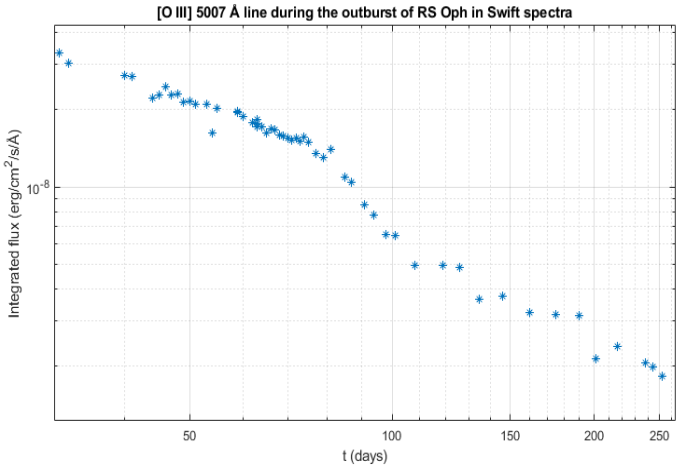

Figure 3.42: RS Oph 2006: integrated flux as a function of time for [O III] $\lambda 5007$ line in Swift UVOT/UV-grism spectra. Axes are in logarithmic scale.

What comparison indicates is that, during outburst, the strength of this line tracks the underlying continuum, which is seen to rise above the zero level between consecutive stages. As a consequence, the actual flux for the profile is different from the peak value. Apart from this difference with other lines, the behavior over time is coherent, as shown in Fig.3.43 for O III $\lambda 3133$.

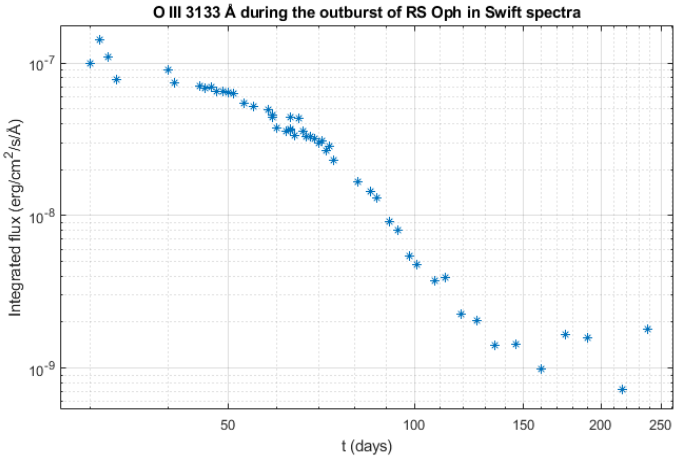

Figure 3.43: RS Oph 2006: integrated flux as a function of time for O III $\lambda 3133$ line in Swift UVOT/UV-grism spectra. Axes are in logarithmic scale.

Oxygen lines, forbidden ones above all but permitted ones as well, are particularly important because they trace the shock throughout their evolution during the event. In fact, the forbidden [O III] lines reflect shock excitation because they usually originate close to the shock front and the environmental conditions for ionisation are greatly dependent on shock conditions. If power law fits are applied to these two lines, for $F \propto t^{\alpha}$ [O III] $\lambda 5007$ Å provides $\alpha = -0.95 \pm 0.23$ for $30 \leq t \leq 79$ and $\alpha = -2.19 \pm 0.40$ for $79 \leq t \leq 146$ respectively, while for O III $\lambda 3133$ Å $\alpha = -1.62 \pm 0.39$ for $30 \leq t \leq 74$ and $\alpha = -4.72 \pm 0.57$ for $74 \leq t \leq 146$. Graphic results for the fits are shown in Fig.3.44. As previously noticed for other spectral lines, the sharp change in the slope of integrated flux around 80 days corresponds to the break-out stage of the shock from the wind of the RG. Similarly to H and He lines, even O III flux rises again after 160 days since the beginning of the outburst.

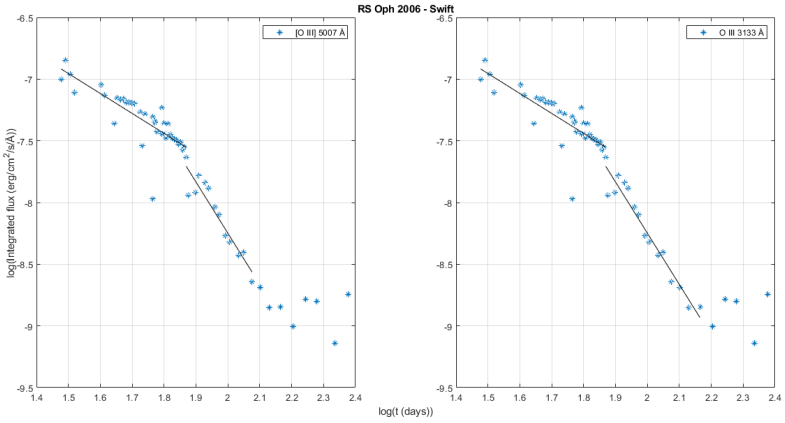

Figure 3.44: RS Oph 2006: power-law fits of the integrated flux as a function of time for $[O\ III]$ $\lambda 5007$ and O III $\lambda 3133$ lines in Swift UVOT/UV-grism spectra.

Fig.3.45 shows how lines from different neutral and ionised species evolve during various outburst events of the Galactic Sy-RNe. Instead, Fig.3.46 displays how power-law fits $F \propto t^{\alpha}$ apply to the most numerous data (the datasets with only a few points have been neglected from the evaluation), where F is the integrated line strength and t expressed in days since the beginning of the outburst. Correspondent values of the slope are given in Table 3.7 and coefficients are calculated with 95% confidence bounds.

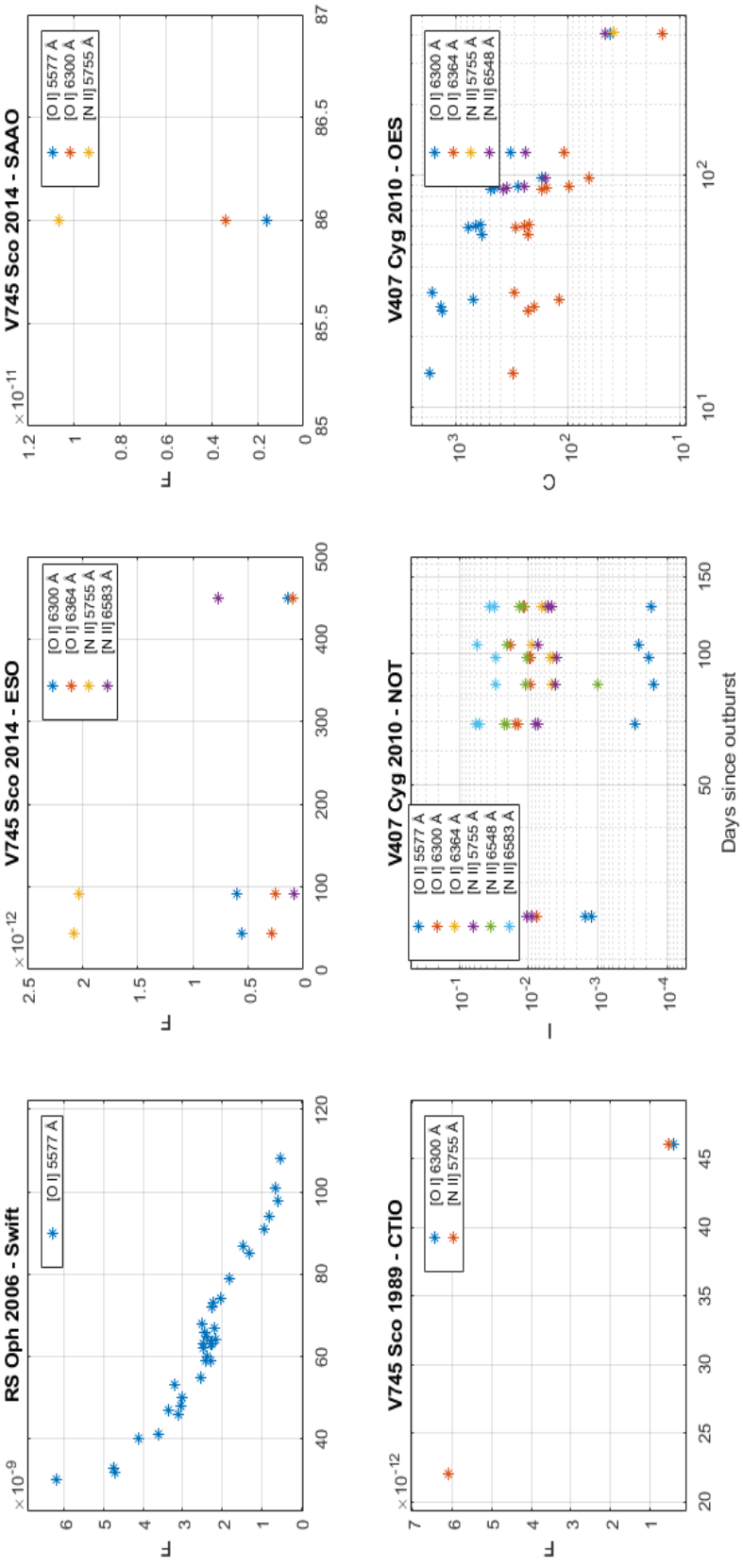

Figure 3.45: Neutral and multiple ionised lines during the outburst of Symbiotic-like Reccurent Novae: integrated line strength as a function of days since the beginning of the event. Axes are in logarithmic scale.

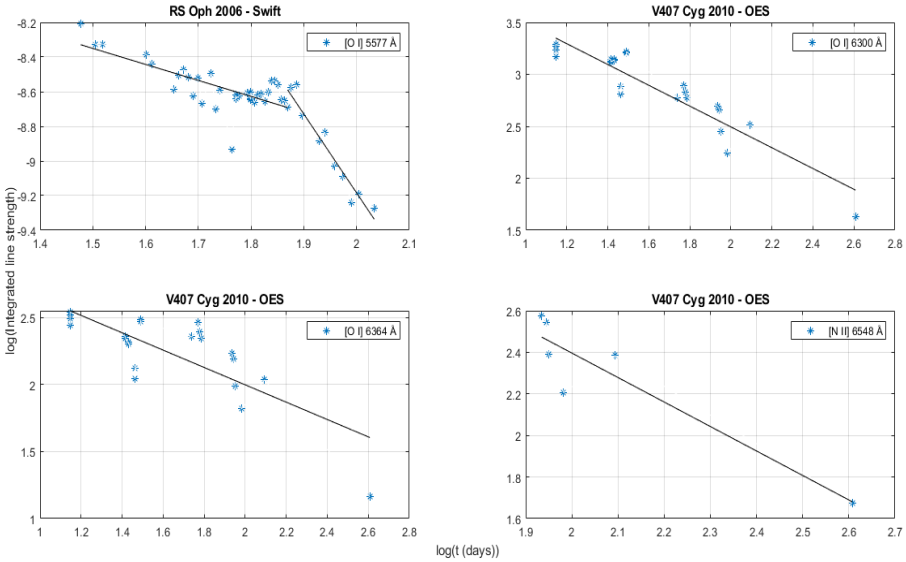

Figure 3.46: Power-law fits of various ionised lines during the outburst of Symbiotic-like Reccurent Novae: integrated line strength as a function of days since the beginning of the event.

Line (Å)	Event and dataset	Days since outburst	α
$[OI]$ 5577	RS Oph 2006 - Swift	$30 \leq t \leq 74$	-0.92 ± 0.30
$[OI]$ 5577	RS Oph 2006 - Swift	$74 \leq t \leq 108$	-4.55 ± 0.91
$[OI]$ 6300	V407 Cyg 2010 - OES	$14 \leq t \leq 405$	-1.00 ± 0.17
$[OI]$ 6364	V407 Cyg 2010 - OES	$14 \leq t \leq 405$	-0.78 ± 0.35
$[NII]$ 6548	V407 Cyg 2010 - OES	$86 \leq t \leq 405$	-1.18 ± 0.65

Table 3.7: Power-law index for the ratio of integrated fluxes of several ionised lines as a function of time during the outburst of various Symbiotic Recurrent Novae.

The next Figures 3.47 - 3.54 show how profiles from various transitions of ionised species evolve over time in several samples of the spectral dataset.

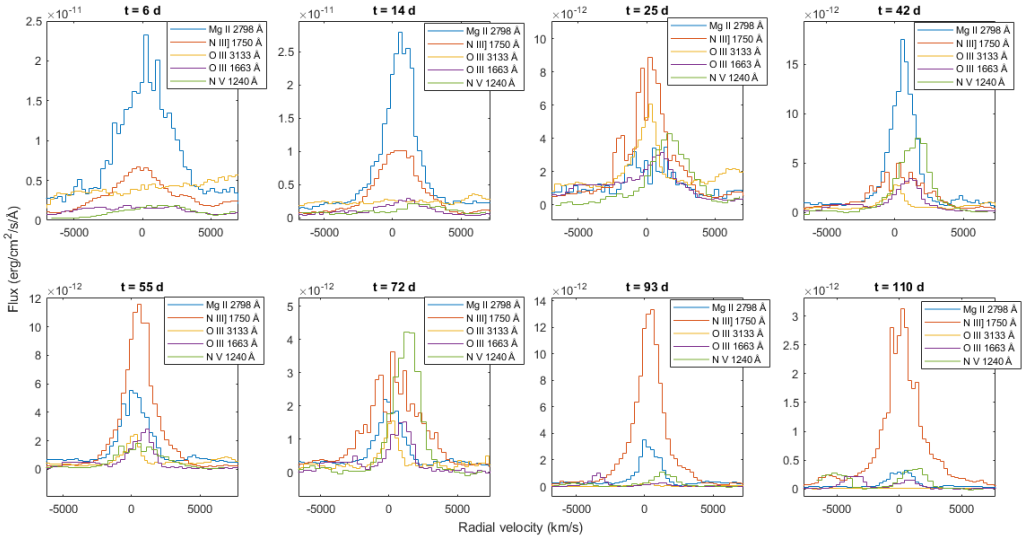

Figure 3.47: Line profiles from ionised species in IUE low resolution spectra of RS Oph at various stages of the 1989 outburst.

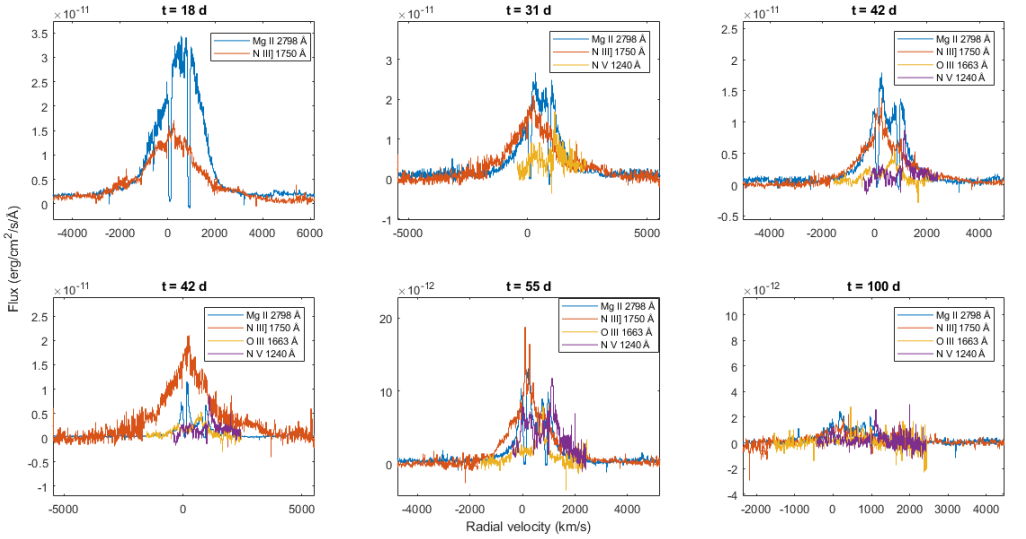

Figure 3.48: RS Oph 1985: line profiles from ionised species in IUE high resolution spectra at various stages of the outburst.

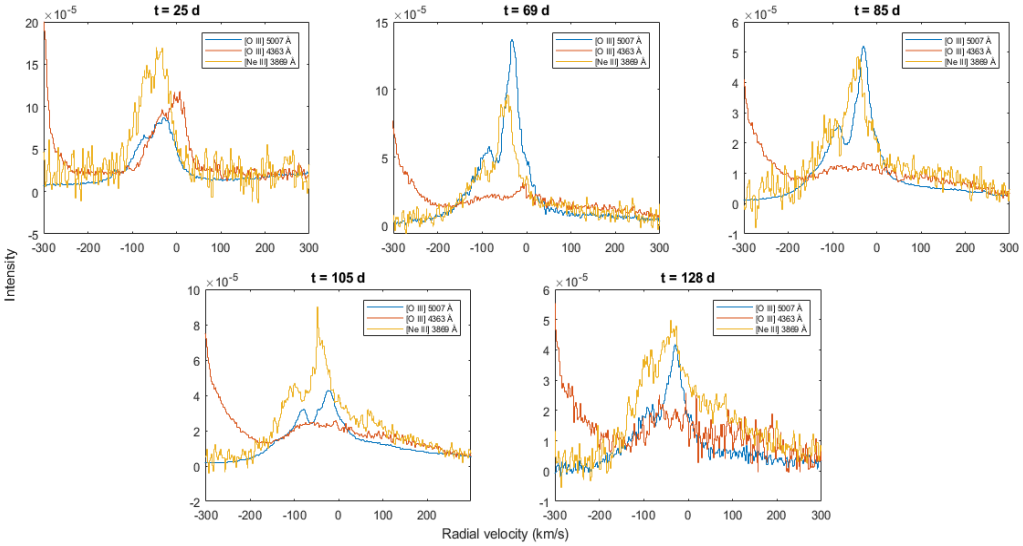

Figure 3.49: V407 Cyg 2010: line profiles from ionised species in NOT spectra at various stages of the outburst.

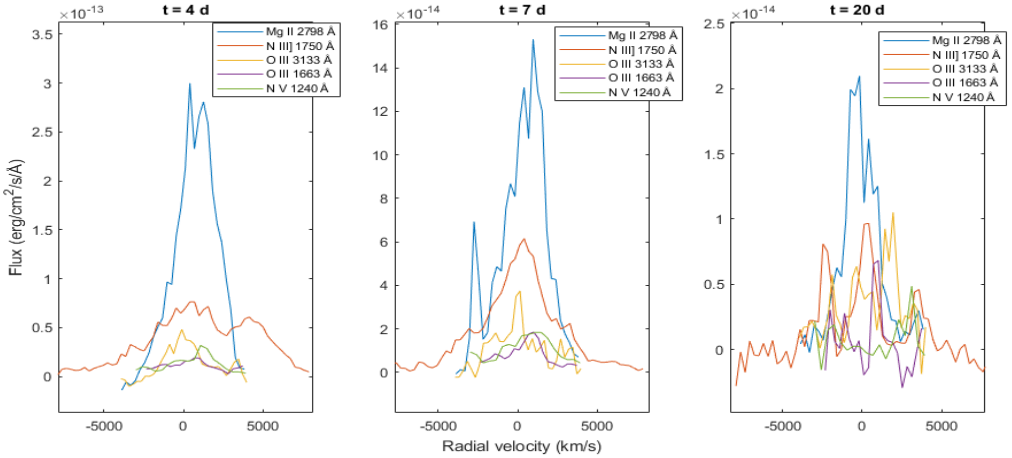

Figure 3.50: V745 Sco 1989: line profiles from ionised species in IUE low resolution spectra at various stages of the outburst.

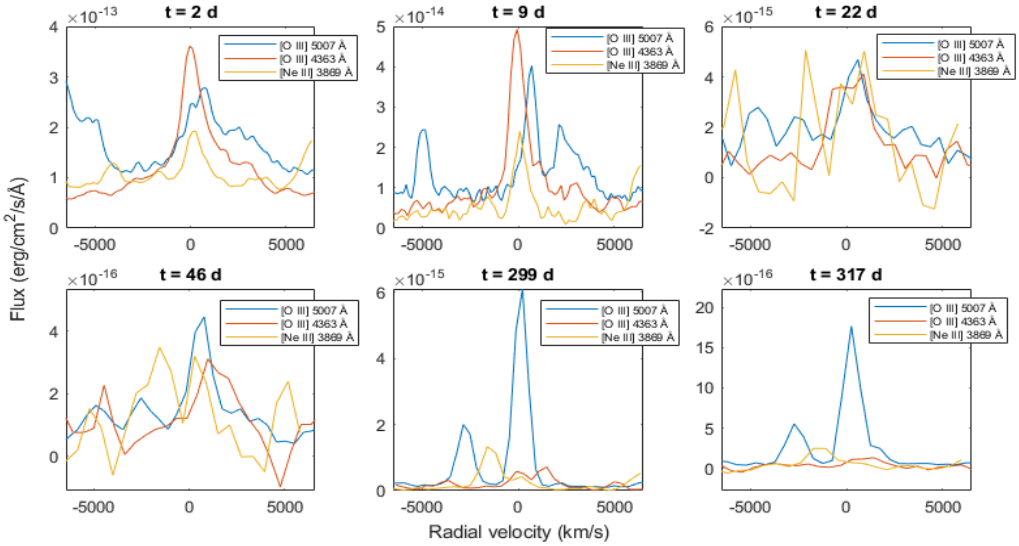

Figure 3.51: V745 Sco 1989: line profiles from ionised species in CTIO spectra at various stages of the outburst.

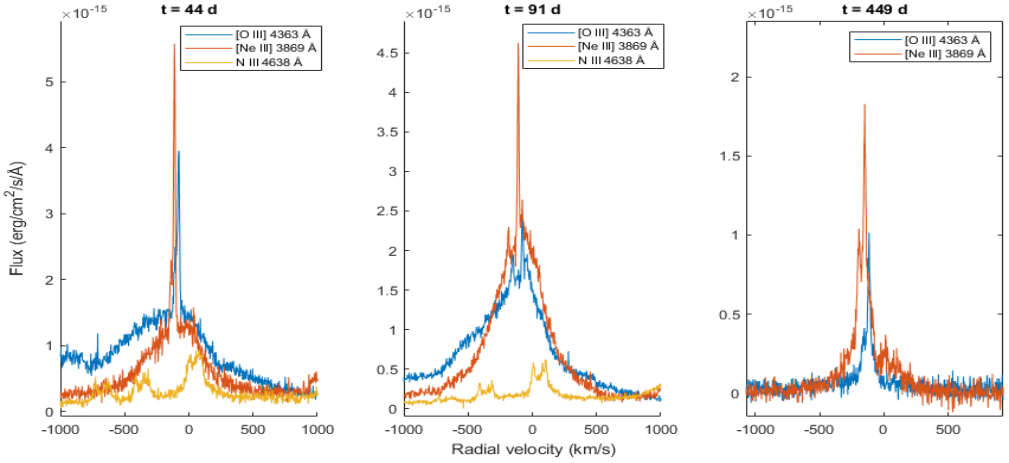

Figure 3.52: V745 Sco 2014: line profiles from ionised species in ESO spectra at various stages of the outburst.

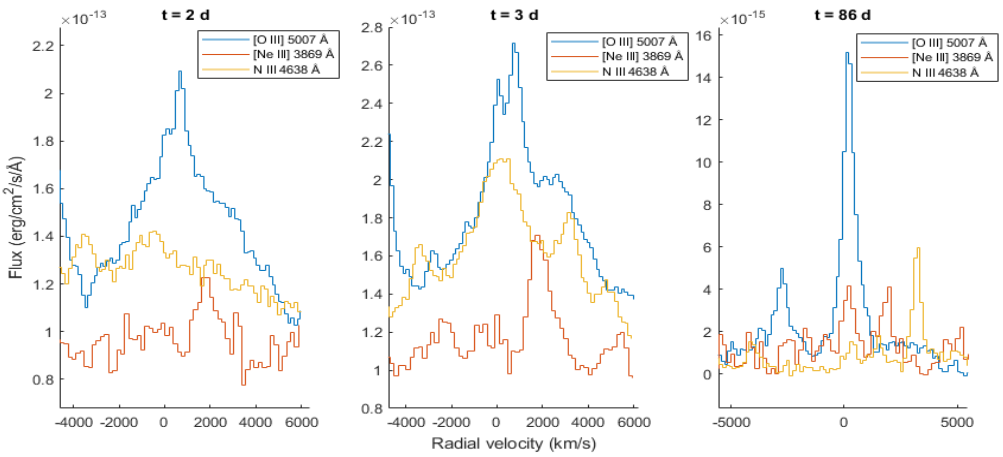

Figure 3.53: V745 Sco 2014: line profiles from ionised species in SAAO spectra at various stages of the outburst.

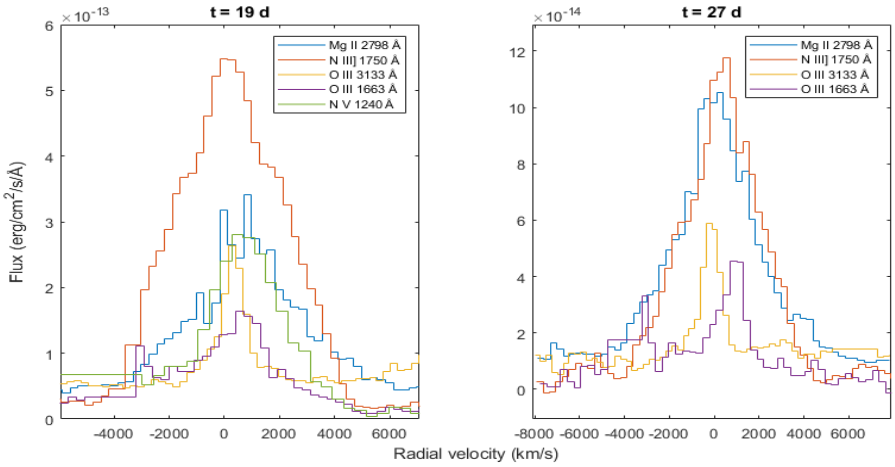

Figure 3.54: V3890 Sgr 1990: line profiles from ionised species in IUE low resolution spectra at various stages of the outburst.

All the sequences clearly show the appearance of a double component, in some cases even more clearly than in profiles from other transitions of different type due to the nature of such highly ionised species. The coexistence of broad components due to the expanding ejecta and the shock and narrow ones originated by the wind are particularly evident during the outbursts of V745 Sco: in ESO spectra, for example, the narrow component of [O III] 4363 Å has $FWZI = 78, 126, 64\ km\ s^{-1}$ on $t = 44, 91, 449\ days$ while for the wider one $FWZI = 1018, 1290, 188\ km\ s^{-1}$ on $t = 44, 91, 449\ days$ respectively. In the same sequence, for [Ne III] 3869 Å the two components have $FWZI = 104, 141, 89\ km\ s^{-1}$ and $FWZI = 708, 1057, 316\ km\ s^{-1}$ on $t = 44, 91, 449\ days$ respectively and, at $t = 449\ days$, also an absorption features appears at $\sim -175\ km\ s^{-1}$. N III profiles, instead, display a composite structure similar to the one detected on top of H lines in NOT and SMARTS spectra and interpreted as the expansion of the precursor in the circumstellar medium. From SAAO data, in [O III] 5007 Å profiles $FWZI(narrow) \simeq 1390, 610\ km\ s^{-1}$ and $FWZI(broad) \simeq 8100, 2600\ km\ s^{-1}$ at $t = 3, 86\ days$ and a $250\ km\ s^{-1}$ absorption component shows up at $t = 3\ days$. Additional structures are also detected in a few spectra. For example, as already noticed for Balmer lines, only the binary V407 Cygni exhibits evident P Cygni profiles superposed on emission lines, and they are signatures of the strong wind emitted by the Mira variable, which almost completely suppresses [O III] $\lambda 5007$ Å emission after about two months, while emissivity from other ions continues decreasing. On [O III] 5007 Å, the absorption component is present on all spectra from $t = 25\ days$ to $t = 128\ days$ between $\sim -71\ km\ s^{-1}$ and $\sim -61\ km\ s^{-1}$, while for

[N III] 3869 Å it lies at $-51\ km\ s^{-1}$ at $t = 25\ days$ and between $\sim -84\ km\ s^{-1}$ and $\sim -78\ km\ s^{-1}$ for $69 \leq t \leq 128\ days$. These values are compatible with the ones found for the lines of the Balmer series.

3.4.6 Coronal lines

So called *coronal lines* are collisionally excited atomic transitions predominantly from highly ionised states elements of the iron group of elements. These lines were first observed in the Solar corona - hence the name - and, because of their nature, are produced when physical conditions in the environment are such that temperatures are sufficiently high and electron density fairly small to excite electrons into high ionisation transitions.

In SyRNe, the conditions producing the species are very different than in stellar coronae but the line excitation is actually the same. In coronal gas, which is magnetically confined to a fraction of the overall structure at the base of the wind, the densities are high enough for collisional excitation to occur, low enough for the line to be emitted, and hot enough that the ionisation state is achieved by collisions. This is also called *collisional ionisation equilibrium* (CIE) and also applies to winds from evolved stars, e.g., the giant companion in a SyRN system. But in these systems, strong photoionisation also produces these high ions, especially when the continuum is harder than 1 keV. Since this is directly observed, not just inferred, from Swift and Exosat observations of RS Oph during outburst (and other systems in this thesis), production of states from, say, Fe^{+6} through Fe^{13+} is possible. The line emission does not, however, require such high electron temperatures (T_e) as would be required to produce the ions. The optical and near UV transitions are ground state and all around a few eV, hence T_e of order a few 10^4 K, which is easily achieved in the post-precursor processed gas and, later, in the collisionally induced ionisation of post-shocked material. Forbidden lines, such as [Fe XI], [Fe XII], [Fe XIV], [Mg V], [Ar X], appear in post-maximum light spectra of SyRN outbursts. They are strongest in the earliest stages and arise from two separate regions, the precursor and ionised wind (where $T_e \sim 10^4$ K) and the post-shocked ejecta and wind ($T_e > 10^6$ K); the contributions are distinguished by line widths since the permitted lines show shock speeds of a few thousand km s^{-1}. The particular conditions are required for such the coronal species formation and excitation occur in the earliest post-maximum stages, typically after the start of the narrow-line phase - when temperature has dropped the initial value $T \simeq 10^7\ K$ to $\sim 1.2 \times 10^6\ K$. For example, these lines made their appearance in RS Oph spectra around 20-30 days, then they began a rapid decline until about day 120 and completely disappeared at $t \simeq 200\ days$, when $T_e \leq 6 \times 10^5$. This signals the weakening of the shock and is separate from the breakout phenomenon that drives the light curve and permitted lines ([Gorbatskii(1972)], [Gorbatskii(1973)]). Throughout spectral evolution, both intensity and width of coronal lines decrease over time due to deceleration of the ejecta.

Only a few coronal lines are clearly visible and fairly intense in the available dataset, in most sequences they are either blended and/or too weak and confused to be distinguished. When they are detected, coronal lines are only in emission. The most prominent are [Fe XI] $\lambda 2648$ Å and [Ar X] $\lambda 5535$ Å, which show up in almost all optical spectra with occasional occurrence of [Fe XIV] $\lambda 5303$ Å and [Fe X] $\lambda 6374$ Å, while in UV the most frequently observed are [Mg V] $\lambda 1815$ Å and [Fe XII] $\lambda 2405$ Å; the identification of other lines is uncertain. A blend of [Fe VII] and [Ca V] 6087 Å is probably present in some Swift spectra of RS Oph, but the profiles are unresolved and the ascription unclear. Fig.3.55 displays the evolution of emission line intensity over time for several systems.

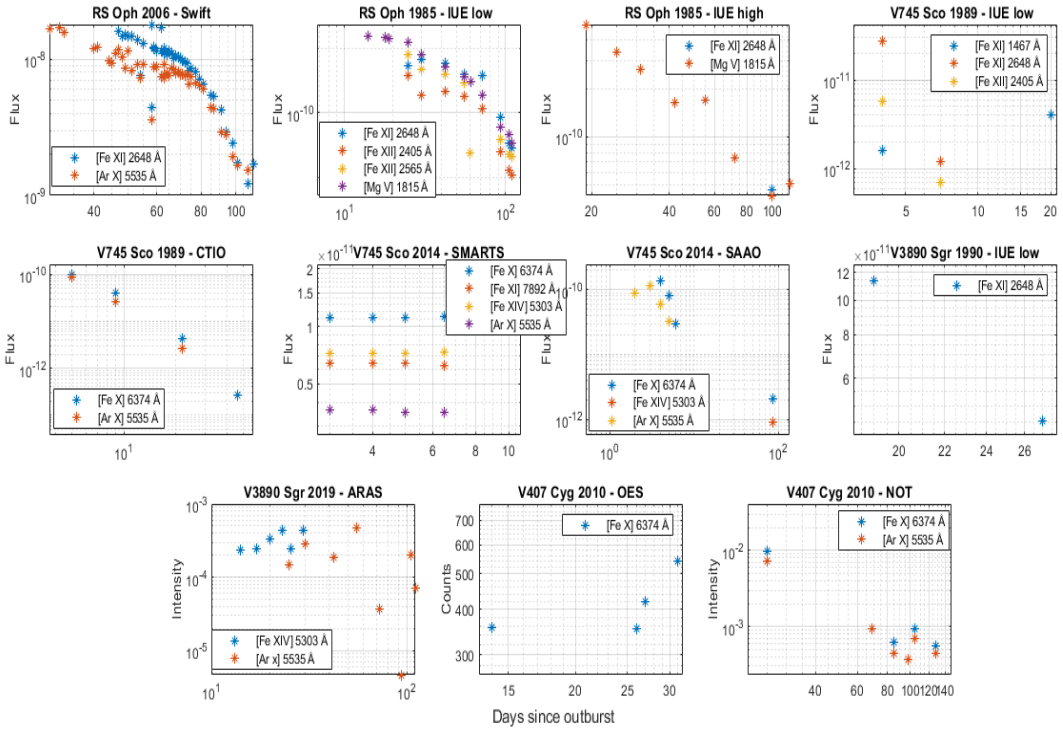

Figure 3.55: Integrated line strength of coronal species as a function of days since the optical maximum in several datasets of Symbiotic-like Recurrent Novae outbursts. The ARAS spectra have been binned to 4 day intervals)

As in [Shore et al.(1996)], coronal lines follow the evolution of XR light curves, they appear and peak between 51-130 days in both events of RS Oph, with line profiles softening over time. Similar development is displayed by coronal species in V407 Cyg [Shore et al.(2011)], [Shore et al.(2012)]: at first lines strength increases, then declines after the maximum XR luminosity. [Fe X] lines are important diagnostic tools for the shock evolution because of this strong correspondence with XRs. After the peak in XRs, coronal lines continue weakening, while their profiles become progressively more asymmetric. In this, the evolution is also analogous to that of He lines. The variation of [Fe XI] and [Ar X] in Swift data for RS Oph is comparable to permitted lines – the Balmer series in the first panel of Fig.3.17, Oxygen transitions, as in Figs.3.42 and 3.43 and intercombination lines as in Fig.3.37, but the slope clearly changes. Power-law fits $F \propto t^{\alpha}$ give $\alpha = -1.04 \pm 0.65$ at $47 \leq t \leq 77$ and $\alpha = -5.64 \pm 0.81$ at $77 \leq t \leq 108$ for [Fe XI], while for [Ar X] $\alpha = -0.90 \pm 0.24$ at $30 \leq t \leq 77$ and $\alpha = -5.34 \pm 0.67$ at $77 \leq t \leq 101$. The results are displayed in Fig.3.56. The change in emissivity shows how sensitive the coronal lines are to the ionisation state of the gas: a drop in the shock powering leads to rapid recombination for such high charge states, on timescales of days.

The rapid decline following breakout is expected from the short recombination times for these high ionisation states rather than cooling. In later stages of CNe, these lines would reach a freese-out, when the density decrease from expansion slows the recombination rate ([Vanlandingham et al.(1998)]). In the SyRN, there are two competing effects, both of which rapidly neutralise the wind. Recalling that the ejecta are not in free expansion, the decreased shock photoionisation input is competing with the advective transport of ionised gas from the wind. Turning the source off, neutral gas issuing from the red giant refills the ionised cavity and further decreases the coronal line emission. The lower ionisation states, e.g., Ne^{2+} and Ne^{4+} have ionisation potentials of 63 and 126 eV, respectively, the latter being almost the same as Fe^{6+}. In contrast, O^{2+} requires only 36 eV and its ionisation can be maintained for far longer in equilibrium (similar to what is seen in ordinary symbiotic binaries).

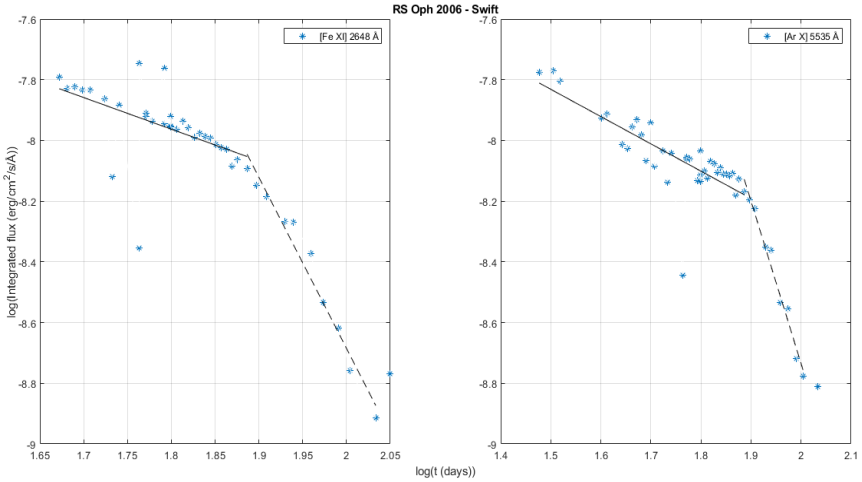

Figure 3.56: RS Oph 2006: power-law fits of coronal [Fe XI] 2648 Å and [Ar X] 5535 Å lines during the outburst in Swift grism spectra.

Analogously to other lines, coronal ones demonstrate the different timescales for the evolution of various systems during outburst: emission from these species arise and then decline from about 20 days in RS Ophiuchi, V3890 Sagittarii and V407 Cygni, whereas V745 Sco shows a faster evolution, with coronal lines appearing and weakening even around 5 days since the beginning of the outburst.

Figs.3.57-3.60 provides some examples of how profiles of coronal transitions appear in the various data.

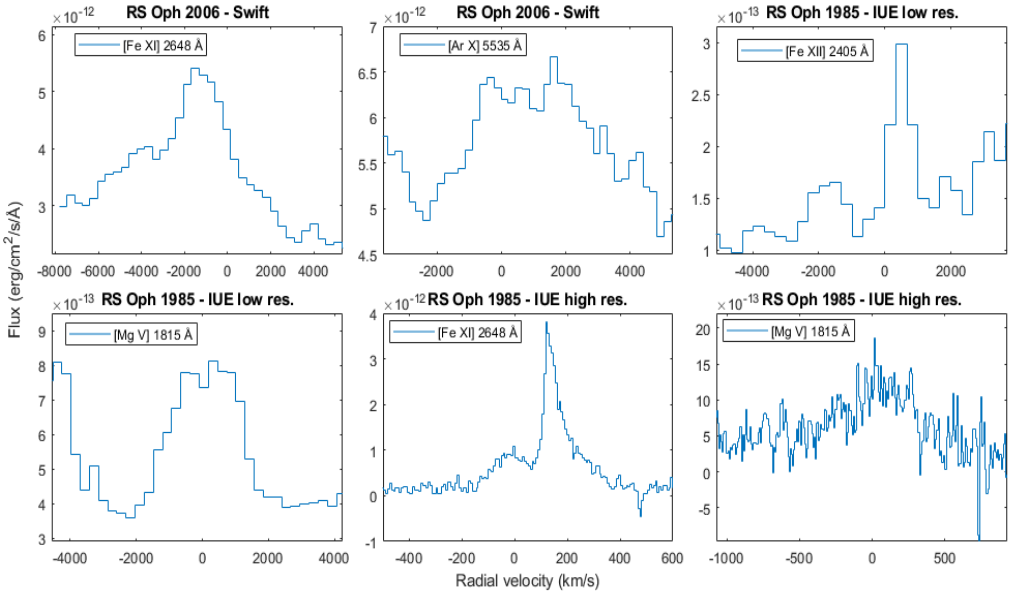

Figure 3.57: Emission profiles from detected coronal lines in RS Ophiuchi spectra during outburst, on MJD 53825.4 ($t = 47\ days$), MJD 46147.2 ($t = 55\ days$), MJD 46098.0 ($t = 19\ days$), MJD 46164.3 ($t = 72\ days$), MJD 46117.5 ($t = 25\ days$) respectively.

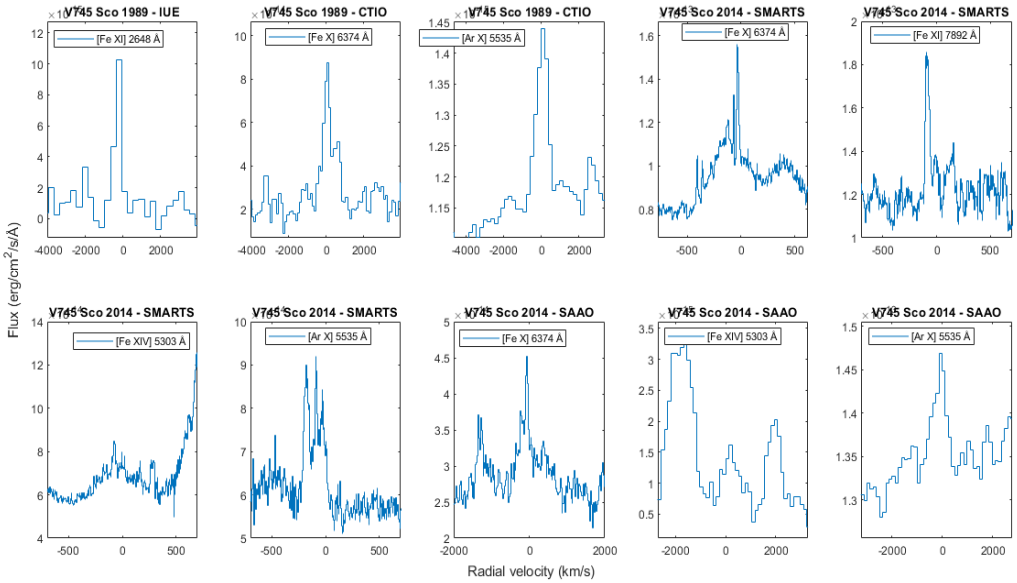

Figure 3.58: Emission profiles from detected coronal lines in V745 Scorpii spectra during outburst, on MJD 47742.6 (t = 4 days), MJD 47757.6 (t = 9 days), MJD 47746.9 (t = 9 days), MJD 47745.9 (t = 6 days), MJD 56700.4 (t = 5 days), MJD 56699.4 (t = 6 days), MJD 56701.4 (t = 7 days), MJD 56700.1 (t = 6 days), MJD 56780.9 (t = 86 days), MJD 56696.1 (t = 2 days).

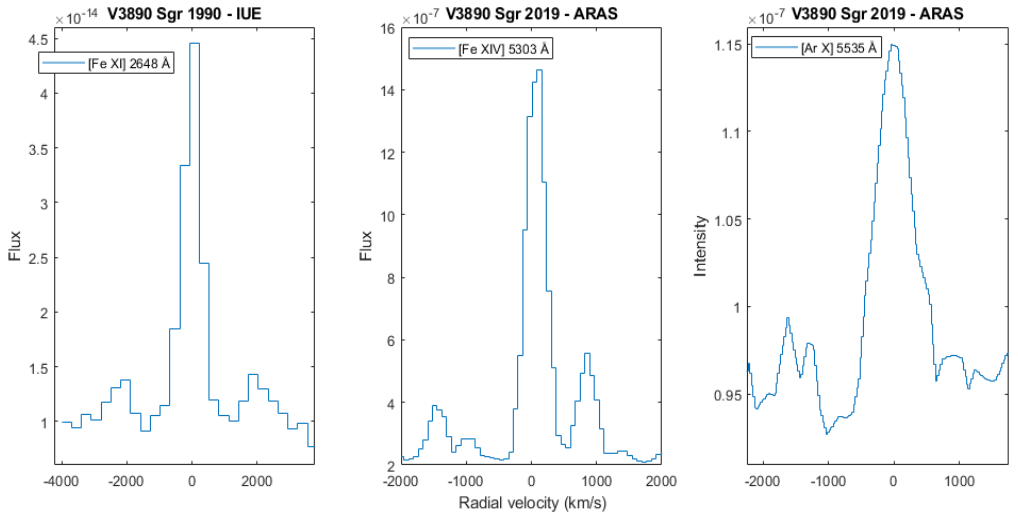

Figure 3.59: Emission profiles from detected coronal lines in V3890 Sagittarii spectra during outburst, on MJD 48034.1 (t = 27 days), MJD 58744.1 (t = 21 days), MJD 58731.8 (t = 7 days).

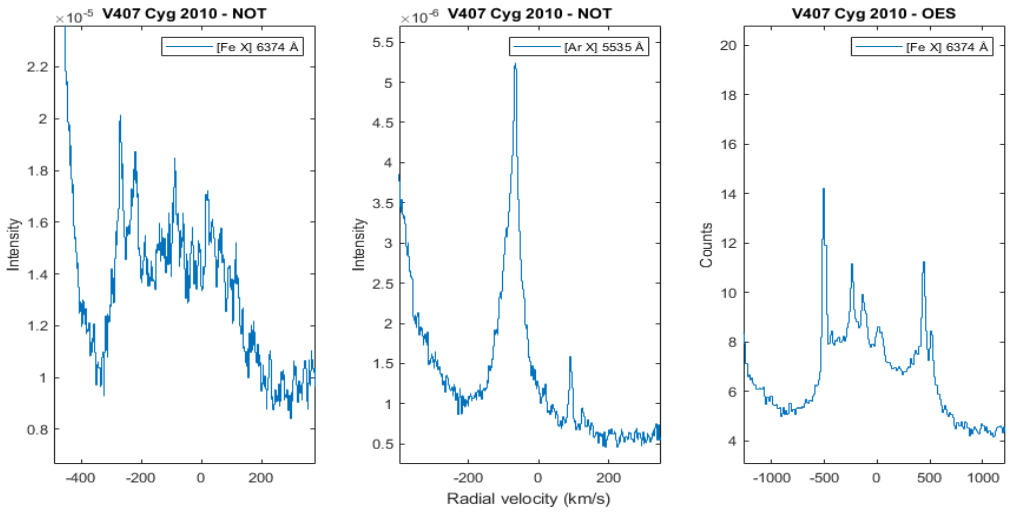

Figure 3.60: Emission profiles from detected coronal lines in V407 Cygni spectra during outburst, on MJD 55320.2 (t = 14 days), MJD 55353.2 (t = 85 days), MJD 55279.1 (t = 14 days).

As expected for forbidden transitions, these profiles are systematically narrower than permitted or semi-forbidden ones but, at the same time, they are almost always blended with other lines, hence it is difficult to accurately determine their actual width. Another reason for the narrow appearance of coronal lines could be the combined effects of enhanced ionisation produced by the expanding Strömgren sphere in the outer part of red giant wind and continuous ionisation by radiation emitted by the wind-shocked ejecta, as already argued in [Shore et al.(1996)] for 1985 IUE spectra of RS Oph.

Chapter 4

Results and Conclusions

Analysis of spectroscopic observations of shock driven processes during outburst events in Symbiotic-like Recurrent Novae has been performed for most of the known Galactic members of the class since their discovery. The majority of past eruptions was recorded and examined at both optical and ultraviolet wavelengths. The principal aim of this work was to add a piece to the general picture outlined since now thanks to the accessible resourches and data. For example, a UV study of the 2006 outburst of RS Oph had never been performed and can provide useful information for a deeper understanding of the phenomenon, even if the only available spectra are those aquired by Swift at lower resolution than the 1985 IUE data and this prevented a panchromatic comparison of the two events.

In the spectroscopic analysis of nova outflows, the time dependent evolution of dynamical structures - more precisely, shocks - can be investigated searching for certain morphological and physical elements. Cues for the presence of shock fronts are, for example, optical spectra showing multiple velocity components, optical and UV emission significantly enhanced by the absorption of the shock in the dense surrounding, light curves evolving with an early rapid rise toward the peak and subsequent spikes at progressively lower wavelengths. In different spectral regions, x-rays emission rising after several weeks or months after the visual maximum, gamma-rays emission in the GeV range, radio thermal emission powered by the interaction of the forward front with the nova ejecta and the dense external shell. The main effect on line profiles is the simultaneous appearance of large absorption lines with P Cyg traits and narrow absorption lines originating in the collision of the dense gas ahead of the principal outflow and the fast outflow coming from behind. The blue side of an individual line is altered by the shock penetrating in the wind, while the red wing comes from the more rarefied periphery ([Shore et al.(2011)]). In RS Oph, for instance, the post-shock gas temperature reached $T \simeq 2.2 \times 10^8 K$ and a velocity $v_s \simeq 4000\ km\ s^{-1}$ that transpose in the appearance of narrow coronal emission lines. In this general picture, thin overlapping profiles are due to emission and absorption in the wind of the red giant ahead of the forward shock. Furthermore, shocks will also affect chemical species responsible for the lines, in fact instabilities of this kind are usually paired with the propagation of ionisation fronts; consequently, when interaction of the shock with the environment dominates the scenario, it will be likely to see more highly ionised species; as the strength of the front diminishes, larger amounts of lines from neutral elements appear in the spectrum. Because of the extreme energies that come into play, lines will be also affected by mechanisms like *fluorescence*, hence it will be possible to observe lines otherwise impossible to detect because pumping is halted by non-sufficient powering. Some examples of this are detectable in IUE spectra of the 1985 outburst of RS Ophiuchi at high resolution. In light of the development of shock waves in the system, the evolution of spectral line profiles can be understood as a change in the nature of the front itself: the thermonuclear runaway produces an early radiative wave that is largely absorbed by the ejecta, then outer layers of the WD envelope are accelerated at high velocities creating a dense slab; as this layer progressively cools, the shock gradually turns into an adiabatic front at later stages. Over time, lines suffer the transformation from greatly asymmetric profiles with extended wings towards the blue part of the spectrum to more symmetric shapes in later phases; the main repercussion of the shock on the profiles shape is seen in the vast and extended wings, much as the wind and the atmosphere of the red giant affect the large component of the peak and the P Cyg absorption.

4.1 Density determination

Section 3.4.4 explained how the ratio of Si III] and C III] emission line fluxes was used to estimate the electron density of the medium and its variation over time. The theoretical approach that was adopted for the evaluation is the same of previous works ([Shore et al.(1996)], [Nussbaumer(1986)], [Cook and Nicolas(1979)], [Nussbaumer and Stencel(1987)], [Nussbaumer and Schild(1979)], [Keenan et al.(1987)], [Shore(2002)], [Osterbrock and Ferland(2006)]). Under the assumption of homogeneous gas, the ratio can be written as:

$$r = \frac{F(Si\ III]\ \lambda 1892)}{F(C\ III]\ \lambda 1909)} = \frac{\epsilon(\lambda 1892)}{\epsilon(\lambda 1909)}, \tag{4.1}$$

where

$$\epsilon(\lambda) = N(X_3^{2+}) h \frac{c}{\lambda} A_{ul} \tag{4.2}$$

is the emissitivity of the line, $N\left(X_3^{2+}\right)$ the number density of the ion under examination - C or Si in our case. Eq.4.1 can be re-written:

$$r = \frac{N(Si)}{N(C)} \frac{N(Si^{2+})/N(Si)}{N(C^{2+})/N(C)} \rho(\lambda 1892/\lambda 1909) \tag{4.3}$$

if

$$N(X_3^{2+}) = N(X) \frac{N(X^{2+})}{N(X)} \frac{N(X_3^{2+})}{N(X^{2+})} \tag{4.4}$$

and

$$\rho(\lambda 1892/\lambda 1909) = \frac{\epsilon(\lambda 1892)/N(Si^{2+})}{\epsilon(\lambda 1909)/N(C^{2+})} \tag{4.5}$$

The electron density dependence explicitly enters as $rate = N_e q_{lu}$ because the ratios of number densities depend on the rates of collisional excitation, that can be expressed as:

$$q_{lu} = \frac{8.63 \times 10^{-6}}{g_l \sqrt{T_e}} \Omega_{lu}\ exp\left(\frac{-\Delta E_{lu}}{k T_e}\right)\ [cm^3 s^{-1}], \tag{4.6}$$

with $g_l = 1$ statistical weight of the ground state, Ω collision strength averaged over a Maxwellian electron distribution of temperature T_e and density N_e, ΔE_{lu} the energy difference between the levels. Using these relations, electron density can be quantitatively determined ([Osterbrock and Ferland(2006)]).

Transition probabilities and related quantities were taken from [Nussbaumer and Storey(1978)] for C III] and [Ojha et al.(1988)], [Keenan et al.(1992)] for Si III] . Table 4.1 reports the electron densities evaluated from Swift spectra of RS Oph, while Tables 4.2 - 4.6 contain the correspondent measurements for the other datasets. The electron density time variation is displayed in Fig.4.1 for the three objects. To make data more reliable due to the uncertainties in flux calibration, values from both eruptions of RS Oph and the 2019 ones of V3890 Sgr are averaged on bins of 3 days each.

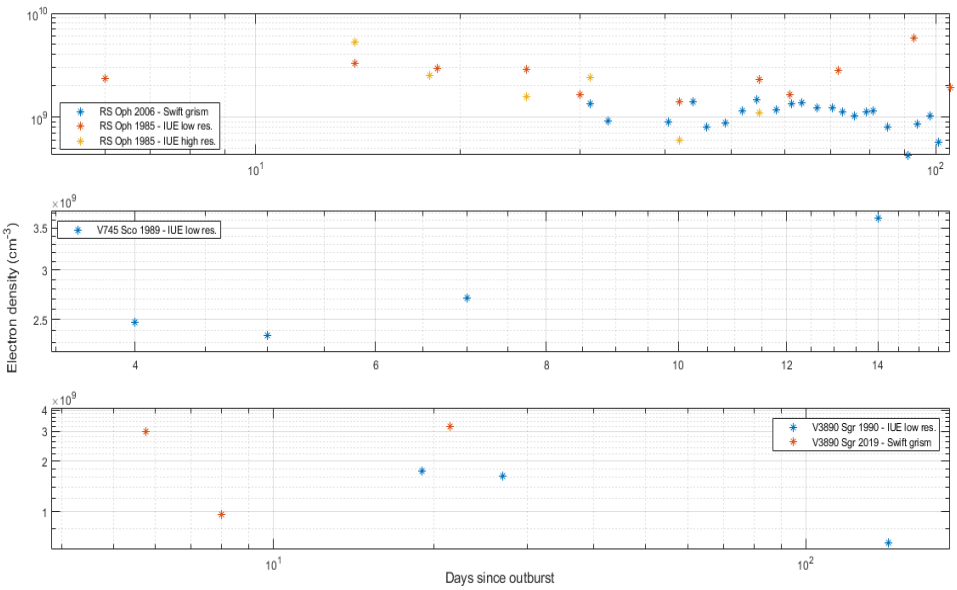

Figure 4.1: Temporal evolution of electron density determined from the ratio of Si III] and C III] emission line fluxes during the outburst events of RS Oph, V745 Sco and V3890 Sgr.

MJD	Days since outburst	Flux ratio	Electron density (cm^{-3})
53809.80	31.0	0.53	1.3×10^9
53811.73	33.0	0.39	9.1×10^8
53818.51	40.5	0.38	8.9×10^8
53822.53	44.0	0.54	1.2×10^9
53825.24	46.0	0.35	7.2×10^8
53828.34	49.0	0.38	9.6×10^8
53831.51	52.0	0.47	1.3×10^9
53833.02	54.5	0.57	1.6×10^9
53837.04	58.3	0.47	1.1×10^9
53840.87	61.3	0.52	1.4×10^9
53843.07	63.6	0.53	1.2×10^9
53846.25	67.0	0.49	1.2×10^9
53848.61	70.5	0.42	1.2×10^9
53852.24	73.0	0.45	1.1×10^9
53855.71	76.0	0.48	1.1×10^9
53858.32	79.0	0.40	9.8×10^8
53863.62	81.0	0.46	4.3×10^8
53869.51	85.0	0.47	8.5×10^8
53872.06	91.0	0.35	1.0×10^9
53876.34	94.0	0.22	5.7×10^8
53879.34	98.0	0.37	8.7×10^8
53886.06	101.0	0.42	1.3×10^9
53890.59	108.0	0.27	8.4×10^8

Table 4.1: RS Oph 2006 - Swift grism: values are binned and averaged over intervals of 3 days.

MJD	Days since outburst	Flux ratio	Electron density (cm^{-3})
46098.83	6	0.80	2.3×10^9
46104.54	14	1.04	3.3×10^9
46106.10	18	0.97	3.0×10^9
46106.15	19	0.94	2.9×10^9
46111.02	25	0.88	2.7×10^9
46117.42	25	0.97	3.0×10^9
46117.47	30	0.61	1.6×10^9
46122.98	42	0.61	1.7×10^9
46134.19	42	0.45	1.1×10^9
46134.32	55	0.78	2.3×10^9
46147.23	61	0.60	1.6×10^9
46147.29	72	0.88	2.7×10^9
46152.98	72	0.95	2.9×10^9
46164.09	93	1.53	5.5×10^9
46164.29	93	1.64	6.0×10^9
46185.11	105	0.66	1.8×10^9
46197.53	105	0.70	1.9×10^9
46197.59	110	0.44	1.1×10^9
46202.05	252	6.78	3.8×10^{10}
46344.72	252	1.56	5.6×10^9
46631.00	540	0.71	2.0×10^9
46632.97	553	0.71	2.0×10^9
46645.99	613	0.68	1.9×10^9
46705.65	764	2.50	1.0×10^{10}
46905.23	1194	1.07	3.4×10^9
48317.71	2225	2.73	1.2×10^{10}

Table 4.2: RS Oph 1985 - IUE low resolution

MJD	Days since outburst	Flux ratio	Electron density (cm^{-3})
46106.17	14	1.51	5.3×10^9
46110.46	18	0.84	2.5×10^9
46117.49	25	0.59	1.6×10^9
46123.02	31	0.82	2.4×10^9
46134.25	42	0.28	6.0×10^8
46147.34	55	0.45	1.1×10^9
46164.17	72	0.50	1.3×10^9

Table 4.3: RS Oph 1985 - IUE high resolution

MJD	Days since outburst	Flux ratio	Electron density (cm^{-3})
47741.29	4	0.84	2.5×10^9
47742.64	5	0.81	2.4×10^9
47744.39	7	0.90	2.7×10^9
47751.95	14	1.12	3.6×10^9

Table 4.4: V745 Sco 1989 - IUE low resolution

MJD	Days since outburst	Flux ratio	Electron density (cm^{-3})
48026.17	19	0.63	1.7×10^9
48026.23	19	0.65	1.8×10^9
48034.04	27	0.60	1.6×10^9
48034.16	27	0.62	1.6×10^9
48150.77	143	0.30	6.5×10^8

Table 4.5: V3890 Sgr 1990 - IUE low resolution

MJD	Days since outburst	Flux ratio	Electron density (cm^{-3})
58743.93	5	0.61	1.7×10^9
58744.39	6	0.62	1.7×10^9
58745.73	6	1.12	3.6×10^9
58746.26	6	1.40	4.9×10^9
58728.74	20	1.01	3.2×10^9
58729.46	21	0.79	2.3×10^9
58729.59	22	1.20	4.0×10^9
58731.25	23	1.07	3.4×10^9

Table 4.6: V3890 Sgr 2019 - Swift grism

In Swift grism spectra, N_e first declines until 40 days for RS Oph and about 10 days in V3890 Sgr, then rises for the next 10 days and decreases again at later stages. The evaluation is consistent with the results of previous analysis, of the 1985 outburst of RS Oph in particular. The trend of electron density is the same noticed by [Cassatella et al.(1985)] and results agree with those found by [Shore and Aufdenberg(1993)], [Shore et al.(1996)], [Sekiguchi et al.(1990)], [Gonzalez-Riestra(1992)] for the different Novae.

Measured values are also in fairly good agreement with the calculations of [Anupama and Prabhu(1989)] and [Anupama and Sethi(1994)], made using H and He I lines instead. In this calculation, IUE and Swift data of RS Oph show consistent values at similar stages of the two events. During the 2006 event, in the first detections the electron density is $\sim 1.3 \times 10^9\ cm^{-3}$, then N_e has a maximum value of $1.69 \times 10^9\ cm^{-3}$ at $t = 62\ days$ and a minimum $N_e = 4.34 \times 10^8\ cm^{-3}$ at $t = 91\ days$. The high resolution spectra of the 1985 explosion peak at $t = 14\ days$ with $N_e = 5.30 \times 10^9\ cm^{-3}$, then the value decreases and reaches a minimum of $N_e = 6.00 \times 10^8\ cm^{-3}$ 42 days after the beginning, in excellent agreement with the computation $N_e = 6.59 \times 10^8\ cm^{-3}$ at $t = 41\ days$ in 2006. This demonstrates that successive outbursts of this SyRN are amazingly similar. Similar densities and analogous behavior are also detected in the other binaries, reinforcing the presumed resemblance between different occurrences.

4.2 Ionisation of the ambient medium

To see how ionisation and recombination proceed, the ratio between integrated fluxes of some spectral lines can be used. Section 3.4.5 already contained information about the proximity of ionisation potential values between neon and oxygen transitions, here it is even more important to notice that the two sets of transitions occur co-spatially ([Bohigas et al.(1989)], [Seaton(1975)]). The shock resulting from the explosion is the main source of ionisation for the ambient medium, and strong emission lines at high ionisation level are produced by the combined effect of the precursor and the shock ([Dopita(1977)]). As underlined by [Contini et al.(1995)] for the 1985 outburst of RS Oph, this ratio depends on the ions stratification downstream and the velocity of the shock front. In particular, forbidden [Ne V] and [Ne III] emission lines are useful diagnostic tools because the ratio between them depends on the *ionisation parameter*, U, the number density of ionising photons divided by that of H atoms. This parameter depends on the luminosity of the ionising source, the distance from the source and the number density of hydrogen. The ionisation parameter can be also employed as a measurement of the variation in the ionisation structure, and $r \equiv \frac{F([Ne\ V]\ \lambda 3426)}{F([Ne\ III]\ \lambda 3869)}$ changes as U^2 ([Gorjian et al.(2007)], [Abel and Satyapal(2008)]). Unfortunately, U is obtainable in only a limited set of data, since forbidden [Ne III] and [Ne V] emission lines are simultaneously observable only in Swift spectra (which extends coverage beyond 3200 Å). Fig4.2 shows the evolution

of the ratio, while the single emission lines are displayed in Fig.4.3. The trend of forbidden Ne lines resembles that of ionised O lines, which confirms that emission from these species arises from close regions and has analogous origin. In particular, as already underlined by [Bohigas et al.(1989)], in Sy-RNe during outburst forbidden lines of this type are excited by fast shocks and are often stronger than permitted transitions, such as those producing Balmer lines.

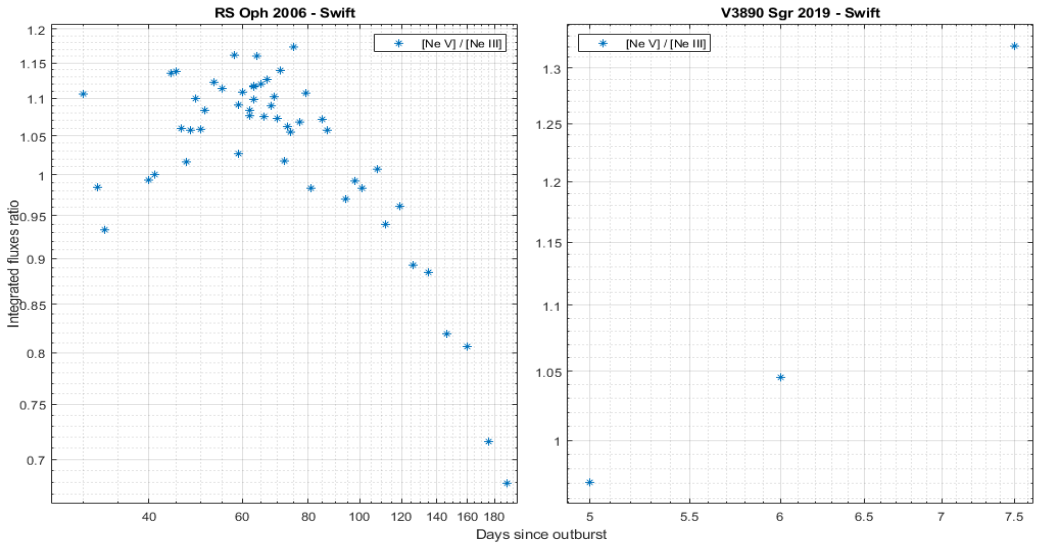

Figure 4.2: Temporal evolution of the ratio between integrated fluxes of [Ne V] λ3426 Å and [Ne III] λ3869 Å emission lines.

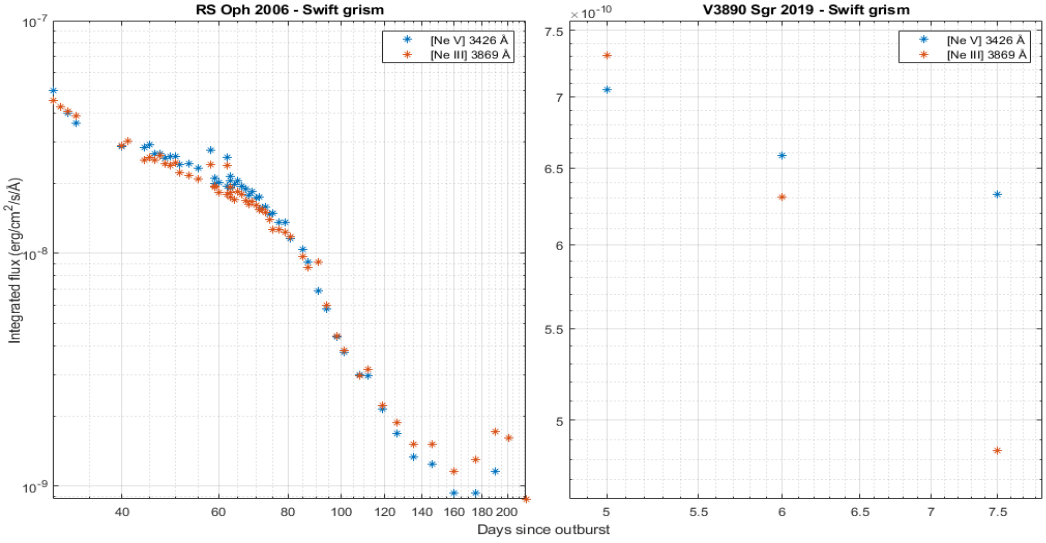

Figure 4.3: Integrated fluxes of [Ne V] λ3426 Å and [Ne III] λ3869 Å emission lines over time during the outbursts of RS Oph and V3890 Sgr in Swift data.

The numerical values corresponding to these trends are listed in Tables 4.7 and 4.8.

Days since outburst	Fluxes ratio	Days since outburst	Fluxes ratio	Days since outburst	Fluxes ratio
30	1.11	59	1.09	77	1.07
32	0.98	60	1.11	79	1.11
33	0.93	62	1.08	81	0.98
40	0.99	62	1.08	85	1.07
41	1.00	63	1.12	87	1.06
44	1.13	63	1.10	91	0.75
45	1.14	63	1.12	94	0.97
46	1.06	64	1.16	98	0.99
47	1.02	65	1.12	101	0.98
48	1.06	66	1.08	108	1.01
49	1.10	67	1.13	112	0.94
50	1.06	68	1.09	119	0.96
51	1.08	69	1.10	126	0.89
53	1.12	70	1.07	135	0.88
54	0.79	71	1.14	146	0.82
55	1.11	72	1.02	160	0.81
58	0.91	73	1.06	175	0.72
58	1.16	74	1.05	190	0.68
59	1.03	75	1.17		

Table 4.7: RS Oph 2006 - Swift grism

Days since outburst	Fluxes ratio	Days since outburst	Fluxes ratio
5	0.91	7	1.25
6	1.00	8	1.44

Table 4.8: V3890 Sgr 2019 - Swift grism

Power-law fits $r \propto t^{\alpha}$ to the measurements give $\alpha = 0.13 \pm 0.07$ for $32 \leq t \leq 75$ and $\alpha = -0.40 \pm 0.06$ for $66 \leq t \leq 190$ for RS Oph, while in V3890 Sgr $\alpha = 0.77 \pm 2.33$ between 5 and 8 days since the beginning of the event. Fig.4.4 shows the fits.

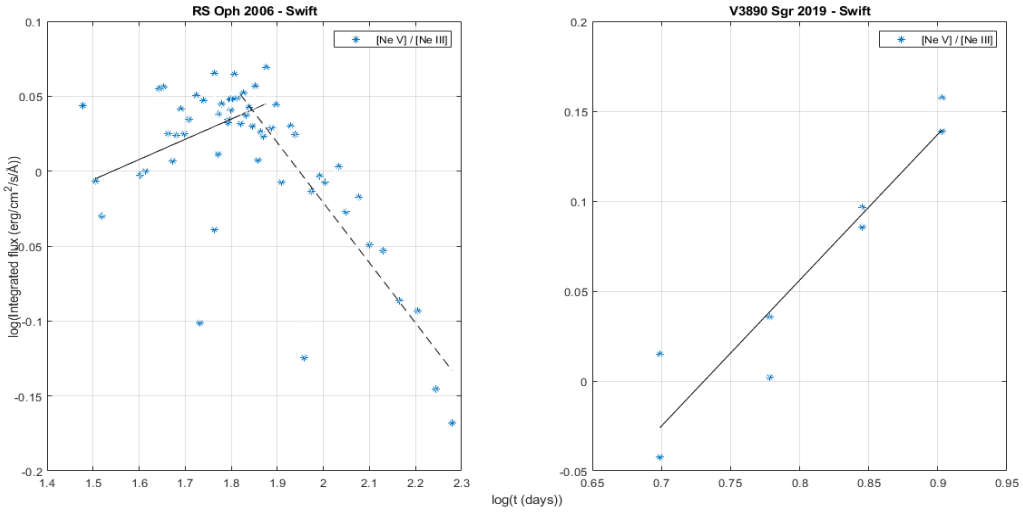

Figure 4.4: Power-law fits of Ne lines over time during the outbursts of RS Oph and V3890 Sgr in Swift data.

The variation of the $^{[Ne\ V]}/_{[Ne\ III]}$ ratio reflects how ionisation proceeds at the various stages of the eruptive event ([Contini et al.(1995)]). Another important diagnostic tool for this evolution would be the ratio of [O III] emission lines. Unfortunately, the plasma diagnostic for [O III] 4959 Å and 4363 Å is not available since the 4363 line is always blended with Hγ in the Swift spectra. The only possible comparison

between these species is the trend of the flux as shown in Fig.4.5 for RS Oph. As expected for emission arising from the same portion of gas, Ne and O lines show similar variations. In the early phase until breakout around 80 days, the different evolution is caused by the fact that the transition at 3133 Å is permitted, whereas the others are forbidden and the O III is additionally fluorescently excited by the Lyman series. However, the evident difference is the behavior of [O III] λ5007 Å relative to the other lines after about 100 days. As discussed in the previous chapter, these low ionisation forbidden lines persist for far longer, driven in part by the continuing UV illumination of the remnant WD. The other lines, instead, decline more rapidly and the corresponding curve shows a clear dip.

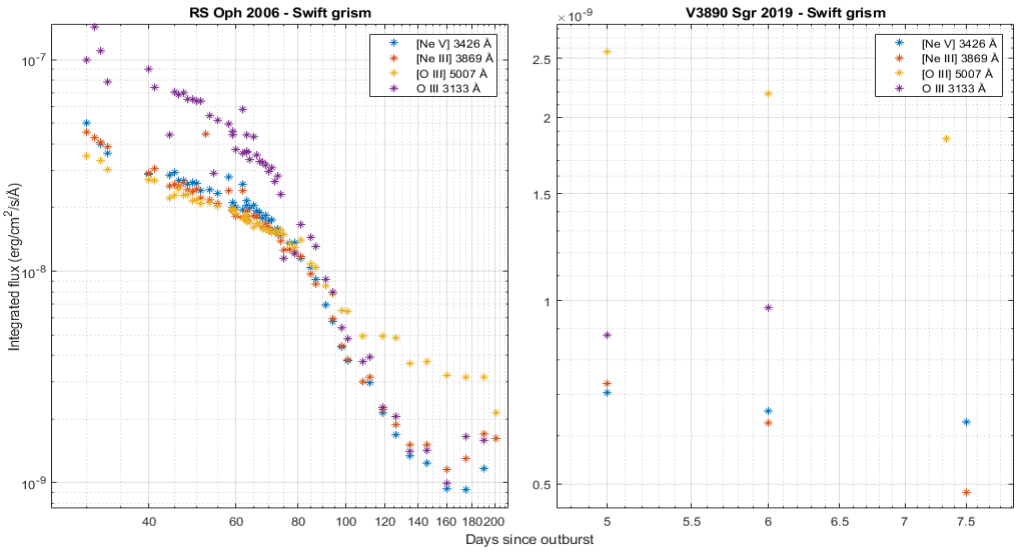

Figure 4.5: RS Oph 2006 and V3890 Sgr 2019: evolution over time of neon and oxygen spectral lines in Swift UVOT UV grism data. The integrated fluxes are useful tools to follow the shock-driven ionisation of the circumstellar gas during outburst.

Looking at these lines is like following the shock development over time. As the front propagates through the circumstellar medium, the gas gets heated at high temperatures and emits high ionisation lines, therefore ionisation increases in the earlier phases, but then the front progressively decelerates as the ejecta go on expanding. The gas cools and starts recombining, the velocity of the shock decreases and ionisation becomes less efficient. This stage is represented by the declining phase in the evolution of r. The ionisation turns off in the later phases, but the presence of the RG wind still provides advection for the gas that has been previously ionised. At the same time, density is decreasing but, since the timescale for this decline is about the same as for recombination, ionisation freeses out at this point and the weakening of lines intensity proceeds at a slower rate. As seen in the previous chapter in regards to coronal lines and [Shore(2008)] for RS Oph 1985, the rate of decline after breakout becomes the same for all the species.

In RS Oph, after about 160 days, [Ne III], [Ne V], and O III fluxes rise again, as shown by some Balmer and He lines. This tendency signals the outset of a new source for ionising photons, arguably renewed accretion from the giant wind. For at least some of the UV lines, a change in the observer's line of sight through the wind could have obscured part of the emitted radiation, which is absorbed by the RG wind. In this case, comparing such spectroscopic results with X-rays photometry is useful because it can help to understand which process is more likely responsible for the observed features. Figure 3.7 reveals that the trend of XRs light curve is marked by a similar slight climb in the latest points. The affinity between the two types of data signals that a restructured accretion disc is probably responsible for the increase in emission.

4.3 Shock breakout

A fundamental epoch of the outburst in the dynamical evolution of these systems is when the propagating shock reaches free expansion stage due to the density gradient of the wind. Unlike atmospheric blasts, there is not a definite border: following the adopted convention in [Shore et al.(1996)], *breakout* is the stage at which the emissivity from the shock front in X-rays - which is due to the interaction between expanding ejecta and stellar wind -, no longer drives wind ionisation. A powerful diagnostic of this stage is to compare optical and ultraviolet spectral profiles, paying particular attention to integrated flux variations over time. In the analysis, shock breakout occurs when the power law that defines the line strength trend abruptly changes and, simultaneously, the narrow emission component begins dominating the profiles. As the analysed spectra show, it is especially noticeable in UV emission line profiles from resonance and high ionisation transitions. The RS Oph Swift sequence shows that the 1985 and 2006 events were extremely similar. Despite different orbital phases (hence lines of sight through the wind), breakout occurred around $\sim\ 80\ days$. This result agrees, for example, with the analysis in [Anupama(2008)]. The outcome is also in line with the observative conclusions that can be drawn from light curves contained in Section 3.3, in Figs.3.5 and 3.6 for the RS Oph events, respectively. The counterpart is the XR light curve in Fig.3.7, in which the SSS is evident. The turnon of this stage is an important regulator for ionisation, but only after the precursor luminosity sufficiently weakened. As a result, the slope changes before the shock is fully weakened: this additional emission maintains the ionisation, but then turns off and the whole system collapses into a lower ionisation state. During eruptions of the other Galactic SyRNe, the breakout stage occurs at different times but with similar characteristics. The various analysed datasets show that the slope for the decline of integrated fluxes of emission spectral lines changes around $\sim 5-7\ days$ in either 1989 and 2014 events of V745 Sco, $\sim 8\ days$ for V3890 Sgr in 1990 and 2019, while the ejecta and the shock exited from the wind of the Mira in V407 Cyg after $\sim 90\ days$ in 2010. Afterwards, the decreasing line strength is entirely due to recombination. The explanation is similar reasons to that of the previous Section regarding ionisation of the medium. When the shock overcomes the giant wind and exits, a net drop in its intensity occurs because the dense compressed shell decreases in density at the rate of free ejecta expansion. This turnaround proves that, once again, shock-driven emission is responsible for high-temperature ionising radiation and alterations in the spectrum. The similarities of the events suggests that the breakout time should scale with a critical ambient density and the energy of the explosion (which depends on the WD mass). For the adiabatic blast solution with an r^{-2} density law and initial energy E_0, then:

$$R(t) \sim \frac{E_0}{\rho_0}^{1/3} t^{2/3} \sim \left(\frac{E_0}{\dot{M}P^{2/3}}\right)^{1/3} t^{2/3}. \tag{4.7}$$

Then if $\rho_{crit} \sim \dot{M}/R^2$ the breakout time varies as $\dot{M}^{3/4}$. The point is that the breakout time increases almost linearly as the mass loss increases. Considered this, we could also expect some dependence on the luminosity class of the giant.

In some SyRNe, the Mira nature of the giant makes mass loss variable. For example, this happens in V745 Sco and, as mentioned in the preceding sections, is signaled by the observed structure of the early profiles. The same would occur in the V407 Cyg events, but unfortunately data have not high enough resolution in the early phases. Despite this, the pre-breakout light curve may display fluctuations because of collisions of the shock with these regions.

4.4 Concluding remarks

Thanks to the huge availability of instruments and resources, in the last decades interest has grown toward the study of binary systems and related physical and dynamical processes. The attempt to better understand the nature of Symbiotic-like Recurrent Novae and the phenomena responsible for the onset of their periodic explosive behavior inserts itself in this comprehensive picture and is made through panchromatic and multiwavelengths studies of known objects.

This work concentrated on the five Galactic binaries of this kind, exploring their behavior during outburst and quiescent stages and collecting information about shock-driven phenomena from spectroscopic

observations in the optical and ultraviolet. The dynamics of the environment was analysed by looking at emission line profiles, temporal evolution and other useful diagnostic tools.

In particular, the Swift grism detection of the 2006 explosion of RS Ophiuchi provided the unique opportunity to contextually investigate diagnostic spectral features that were unattainable in previous surveys or compare earlier results with *new* ones. This added interesting material to the pre-existing knowledge of both the individual object and general description.

Although great progress has been made in this regard, some questions still need to be answered, especially for what concerns the processes that lead to the beginning of explosive events in these binaries and detailed clues about the single steps of successive evolution. Future outbursts of Symbiotic-like Recurrent Novae and concomitant observations in multiple wavelength regions will be fundamental to deepen our insight of the phenomenon.

Appendix A

Journal of observations

A.1 Swift

Spectrograph	λ range (Å)	Dispersion (Å $pixel^{-1}$)	Resolution ($\frac{\lambda}{\Delta\lambda}$)
UV grism	1730 - 5200	3.2	75

Table A.1: Swift UV grism characteristics.

A.1.1 RS Oph

Date (MJD)	Exposure time (ks)	Position angle (deg)	Date (MJD)	Exposure time (ks)	Position angle (deg)
53807	1.49	100.95	53848	6.50	90.13
53808	1.49	98.20	53849	6.50	89.27
53809	1.63	97.60	53850	12.05	88.84
53810	1.63	100.09	53851	12.08	89.44
53811	12.41	86.95	53852	22.97	76.90
53818	28.75	87.73	53853	5.32	75.46
53819	248.86	80.47	53855	12.32	75.16
53822	81.04	80.49	53857	1.01	73.92
53823	81.63	79.79	53859	10.96	72.20
53824	81.62	79.59	53863	6.24	70.63
53825	53.06	78.63	53865	17.59	67.44
53826	65.24	78.15	53869	6.33	65.01
53827	53.54	80.55	53872	34.30	44.31
53828	58.70	80.26	53876	6.13	40.00
53829	52.99	76.80	53879	6.13	31.26
53830	81.38	78.88	53886	17.55	40.27
53831	81.94	76.09	53890	29.52	22.73
53832	69.94	92.10	53897	24.20	329.83
53833	121.08	91.56	53904	12.08	304.97
53836	0.72	77.25	53913	34.71	307.64
53836	0.74	90.73	53924	64.78	293.71
53837	0.74	90.71	53938	23.30	274.09
53837	0.74	81.20	53953	17.59	270.35
53838	0.68	90.24	53968	29.81	276.36
53840	6.13	90.23	53979	47.02	262.77
53840	6.11	89.36	53994	243.01	256.64
53841	6.15	88.59	54016	35.39	262.31
53841	6.11	89.13	54022	52.48	260.47
53841	6.08	89.31	54030	63.64	109.16
53842	6.11	88.90	54150	41.39	106.85
53843	11.02	80.67	54157	52.68	103.60
53844	12.02	80.28	54163	52.77	91.96
53845	17.78	90.94	54170	52.86	84.21

53846	0.42	90.12	54231	24.52	82.20
53847	6.56	90.12	54233	7.30	280.94

Table A.2: RS Oph observations with Swift UV grism.

A.1.2 V3890 Sgr

Date (MJD)	Exposure time (ks)	Position angle (deg)	Date (MJD)	Exposure time (ks)	Position angle (deg)
58739	479.77	257.98	58745	454.77	265.99
58739	479.78	261.98	58746	424.77	258.00
58740	479.77	258.01	58746	479.77	265.99
58740	424.78	261.98	58747	479.77	257.99
58741	361.77	258.01	58747	479.78	265.99
58741	415.78	261.98	58728	479.77	268.01
58742	470.77	257.99	58728	424.86	263.97
58742	415.79	261.99	58729	424.77	268.02
58743	400.76	257.99	58729	424.77	263.99
58743	454.79	266.00	58730	479.78	263.98
58744	370.77	257.99	58730	400.76	268.00
58744	370.77	265.99	58731	400.78	266.59
58745	454.78	258.01	58731	861.77	266.62

Table A.3: V3890 Sgr observations with Swift UV grism.

A.2 IUE

Spectrograph	λ range (Å)	Dispersion (Å $pixel^{-1}$)	Resolution ($\frac{\lambda}{\Delta\lambda}$)
LWP low	1850 - 3300	6	250
SWP low	1150 - 2000	6	250
LWP high	1192 - 1924	0.2	10^4
SWP high	1893 - 3031	0.2	1.5×10^4

Table A.4: IUE spectrograph characteristics ([Macchetto(1976)]).

A.2.1 RS Oph - low resolution

Date (MJD)	Exposure time (ks)	Position angle (deg)	Date (MJD)	Exposure time (ks)	Position angle (deg)
6099.33	299.70	179.47	6099.27	299.70	179.50
6105.03	119.48	176.75	6106.58	179.68	176.09
6106.60	59.68	176.09	6110.91	119.47	174.32
6106.65	209.59	176.06	6111.50	299.70	174.11
6111.52	359.51	174.11	6117.91	179.68	171.77
6117.92	419.72	171.77	6117.94	1259.80	171.76
6117.96	119.48	171.75	6123.49	59.67	169.93
6123.48	10.53	169.93	6134.66	239.49	166.53
6134.68	899.77	166.52	6134.69	2399.72	166.52
6134.82	179.69	166.48	6134.85	119.47	166.47
6147.73	1199.59	162.77	6147.72	119.47	162.77
6147.79	179.69	162.75	6147.75	2999.78	162.76
6153.48	19.54	161.11	6153.57	599.52	161.09
6164.59	1199.59	157.69	6164.56	149.78	157.70
6164.78	59.68	157.63	6164.61	2999.78	157.69
6185.60	1499.83	149.56	6185.59	299.70	149.56
6198.03	599.53	142.39	6185.62	5399.63	149.55
6198.09	1799.66	142.39	6197.99	899.76	142.39
6202.54	2699.55	138.86	6198.05	2699.54	142.39
6345.21	3599.85	339.54	6202.53	899.76	138.88
6631.50	9899.50	11.020	6345.16	3599.84	339.56
6633.47	3599.85	9.3400	6345.26	4199.50	339.53

6646.48	3719.86	0.8500	6633.34	10799.79	9.4400
6706.15	4799.57	340.84	6646.40	6959.79	0.8900
6907.73	11339.65	153.20	6706.06	7019.59	340.86
8318.21	5879.68	169.01	6856.83	9419.85	169.03
4139.42	599.53	343.68	7286.65	10799.79	146.83
5267.86	1799.66	333.17	8317.97	20399.59	169.01
4078.54	1319.60	7.8400	8488.71	16499.78	353.96
4139.43	1919.66	343.68	9976.17	14399.77	345.76
5267.88	3599.84	333.17			

Table A.5: RS Oph observations at low resolution with IUE.

A.2.2 RS Oph - high resolution

Date (MJD)	Exposure time (ks)	Position angle (deg)	Date (MJD)	Exposure time (ks)	Position angle (deg)
110.92	3.00	174.32	110.96	5.16	174.31
111.02	0.72	174.28	111.63	2.70	174.05
111.66	0.42	174.05	111.68	1.20	174.05
123.56	0.66	169.93	117.99	3.60	171.74
134.67	1.38	166.53	123.52	3.30	169.93
147.81	1.80	162.75	134.75	6.01	166.50
164.65	1.80	157.67	147.84	7.44	162.74
164.81	4.32	157.62	164.67	9.01	157.66
185.69	1.80	149.51	185.71	10.32	149.50
099.34	1.80	179.47	202.58	17.40	138.83
106.67	2.10	176.06			

Table A.6: RS Oph observations at high resolution with IUE.

A.2.3 V745 Sco

Date (MJD)	Exposure time (ks)	Position angle (deg)	Date (MJD)	Exposure time (ks)	Position angle (deg)
41.78	0.24	333.09	41.79	3.60	333.09
41.84	1.20	333.09	43.13	5.40	333.56
44.87	0.60	334.13	44.89	12.60	334.13
58.13	3.60	337.66	52.45	13.20	336.29
58.21	14.40	337.68			

Table A.7: V745 Sco observations with IUE.

A.2.4 V3890 Sgr

Date (MJD)	Exposure time (ks)	Position angle (deg)	Date (MJD)	Exposure time (ks)	Position angle (deg)
26.70	1.80	161.08	34.53	3.60	161.33
34.59	5.40	161.33	34.65	10.80	161.34
26.67	1.80	161.08	151.27	15.36	340.07
26.73	4.44	161.08			

Table A.8: V3890 Sgr observations with IUE.

A.2.5 T CrB - low resolution

Date (MJD)	Exposure time (ks)	Position angle (deg)	Date (MJD)	Exposure time (ks)	Position angle (deg)
5818.56	1.50	106.30	4064.68	1.62	24.07
5976.22	1.50	319.68	4069.74	2.40	20.18
6133.81	1.20	158.42	4069.80	4.80	20.18
6174.67	1.20	117.92	4089.29	3.01	6.14
6187.66	1.20	101.19	4137.45	3.30	331.09
6209.65	0.90	71.70	4220.01	3.01	230.59

6453.01	1.19	192.53	4399.48	3.72	52.39
6596.44	0.60	46.60	4652.99	4.20	173.39
6631.34	1.20	16.57	4954.06	3.60	226.61
6949.69	0.84	59.90	5123.62	3.30	59.65
7215.77	0.90	169.01	5455.79	2.70	103.01
7587.85	1.20	163.89	5568.53	2.10	353.68
7587.92	1.68	163.83	5818.63	2.40	106.20
7624.59	1.50	130.76	5976.25	2.40	319.65
7667.68	1.50	75.60	6133.78	2.40	158.44
7667.76	1.20	75.49	6174.70	2.40	117.88
7712.39	1.20	27.99	6187.68	2.70	101.17
7739.57	1.26	7.72	6209.68	2.40	71.65
7931.73	1.20	179.57	6452.97	3.01	192.57
8039.50	1.80	67.16	6453.04	6.06	192.51
8106.52	1.80	6.640	6545.76	2.82	110.61
3879.24	1.80	206.20	6631.37	2.10	16.55
3953.72	2.70	148.77	6631.42	3.60	16.51
4064.66	0.90	24.08	6949.65	2.70	59.95
4069.77	2.10	20.18	7215.72	3.60	169.05
4089.33	3.01	6.12	7587.88	2.70	163.87
4399.44	3.01	52.43	7624.63	3.60	130.72
4399.64	1.20	52.22	7667.62	3.60	75.68
4652.95	2.40	173.42	7667.71	3.60	75.56
4954.00	3.30	226.67	7712.34	3.60	28.04
5123.66	2.40	59.60	7739.50	6.01	7.77
5498.50	1.20	48.88	7931.75	5.40	179.55
5568.55	1.50	353.66	8039.54	5.40	67.11
3879.29	1.50	206.20	8106.44	3.60	6.64
3957.93	4.26	144.94			

Table A.9: T CrB observations at low resolution with IUE.

A.2.6 T CrB - high resolution

Date (MJD)	Exposure time (ks)	Position angle (deg)	Date (MJD)	Exposure time (ks)	Position angle (deg)
5089.63	18.42	104.20	4621.84	26.76	196.28
4407.46	14.40	44.01	5493.48	18.60	54.36
4692.12	10.80	141.50	6596.48	37.20	46.67
4399.66	7.02	52.20	7215.80	13.08	168.99

Table A.10: T CrB observations at high resolution with IUE.

A.3 ESO

A.3.1 V745 Sco

Date (MJD)	Exposure time (ks)	Date (MJD)	Exposure time (ks)
56737.82	0.96	56783.70	1.60
56737.80	0.96	57142.81	0.96
56737.82	0.96	57142.86	0.96
56737.83	0.96	57142.84	0.96
56737.83	0.96	57142.82	0.96
56737.80	0.96	57142.80	0.96
56783.74	1.60	57142.81	9.96
56783.72	1.60	57142.84	9.96
56783.74	1.60	57142.86	0.96
56783.70	1.60	57142.87	9.96
56783.72	1.60	57142.82	0.96
56783.68	1.60	57142.87	0.96
56783.68	1.60	57142.80	0.96

Table A.11: V745 Sco observations with ESO UVES.

A.4 SAAO

A.4.1 V745 Sco

Date (MJD)	Exposure time (s)	Date (MJD)	Exposure time (s)
56696.14	430.00	56699.13	600.00
56697.13	600.99	56700.14	720.19
56698.13	560.52	56780.95	600.03

Table A.12: V745 Sco observations with SAAO.

A.5 SMARTS CHIRON

Spectrograph	λ range (Å)	Dispersion ($\mathring{A}\ pixel^{-1}$)	Resolution ($\frac{\lambda}{\Delta\lambda}$)
CHIRON	4100 - 8700	3	80000

Table A.13: SMARTS CHIRON spectrograph characteristics.

A.5.1 V745 Sco

Date (MJD)	Exposure time (ks)	Date (MJD)	Exposure time (ks)
47739	0.90	48036	0.48
47742	0.45	48042	0.30
47746	1.20	48054	1.80
47759	0.90	48419	0.90
47783	1.80	48716	0.60

Table A.14: V745 Sco 1989 observations with SMARTS.

Date (MJD)	Exposure time (ks)	Date (MJD)	Exposure time (ks)
56697	1.2	56700	1.8
56698	1.2	56701	1.8
56699	1.8		

Table A.15: V745 Sco 2014 observations with SMARTS.

A.6 NOT

Spectrograph	λ range (Å)	Dispersion ($\mathring{A}\ pixel^{-1}$)	Resolution ($\frac{\lambda}{\Delta\lambda}$)
FIES	3700 - 8300	0.023	67000

Table A.16: NOT spectrograph characteristics.

A.6.1 V407 Cyg

Date (MJD)	Exposure time (s)	Date (MJD)	Exposure time (s)	Date (MJD)	Exposure time (s)
55288	125	55350	2564	55674	600
55288	400	55350	500	55674	60
55334	4	55370	500	55959	3600
55334	100	55370	2700	55959	300
55334	1000	55393	270	55363	200

55350	200	55393	2700	55363	3000

Table A.17: V407 Cyg observations with NOT.

A.6.2 V745 Sco

Date (MJD)	Exposure time (ks)
56700.26	1.50
56700.28	0.96
56707.26	3.00

Table A.18: V745 Sco observations with NOT.

A.7 Ondřejov

Spectrograph	λ range (Å)	Dispersion ($\mathring{A}\ pixel^{-1}$)	Resolution ($\frac{\lambda}{\Delta\lambda}$)
OES	6300 - 6770	2.4	51600

Table A.19: Ondřejov Échelle Spectrograph spectrograph characteristics ([Kabáth et al.(2020)]).

A.7.1 V407 Cyg

Date (MJD)	Exposure time (s)	Date (MJD)	Exposure time (s)	Date (MJD)	Exposure time (s)	Date (MJD)	Exposure time (s)
55279.08	1641.73	55290.06	586.42	55308.10	500.00	55354.87	3000.00
55279.08	373.07	55290.08	626.40	55308.10	500.00	55354.91	3600.00
55279.10	447.51	55292.02	936.32	55312.98	4135.92	55354.99	2100.00
55279.10	389.75	55292.04	3759.89	55313.02	1106.99	55361.91	3600.00
55279.10	360.25	55292.97	1255.48	55314.98	800.00	55361.93	1800.00
55279.12	328.05	55293.02	6718.91	55315.08	1999.88	55389.89	3600.00
55279.14	1985.45	55293.08	1996.64	55351.98	3000.00	55670.08	3600.00
55289.08	577.34	55294.10	60.00	55352.00	300.00	55673.02	4500.00
55289.08	586.31	55294.10	300.00	55352.02	2400.00	55674.00	4999.49
55289.08	599.79	55294.10	60.00	55352.06	2000.00	55674.00	4999.49
55290.06	541.99	55294.12	2000.00	55353.89	4499.59	55674.06	3601.79

Table A.20: V407 Cyg observations with OES.

A.8 ARAS

A.8.1 V3890 Sgr

Date (MJD)	Resolution ($\frac{\lambda}{\Delta\lambda}$)	Exposure time (ks)	Date (MJD)	Resolution ($\frac{\lambda}{\Delta\lambda}$)	Exposure time (ks)
58723.77	706	1.54	58736.77	2083	10.38
58723.79	9000	9.63	58737.12	1027	2.72
58723.89	4520	3.09	58737.48	535	3.01
58724.41	4900	1.80	58737.77	1857	9.17
58724.79	723	2.16	58738.12	1041	2.72
58724.79	11000	7.22	58738.75	595	3.62
58724.79	9000	13.0	58738.77	1828	8.43
58724.83	729	1.23	58739.14	1055	2.72
58724.83	4716	6.16	58739.77	1879	7.02
58725.83	525	1.10	58740.75	511	3.62
58725.85	9000	9.63	58740.77	1863	9.14
58726.77	773	4.25	58741.75	540	3.62
58726.87	549	1.10	58742.14	1036	2.72

58727.46	4359	3.03	58742.75	1815	9.45
58727.47	533	1.21	58744.12	1040	2.72
58727.79	698	6.08	58745.12	1031	2.72
58728.77	702	4.25	58746.10	1054	2.72
58729.85	9000	8.42	58746.74	1771	9.26
58729.85	9000	7.22	58747.74	936	3.62
58730.16	1017	1.64	58747.75	1915	7.92
58730.79	605	3.64	58748.74	926	4.83
58730.83	2111	5.77	58749.12	1056	2.72
58731.43	4516	2.41	58750.74	2021	9.06
58731.77	605	5.47	58751.10	1074	2.42
58731.87	534	2.11	58752.75	2048	8.20
58732.14	1008	2.18	58754.10	1064	2.72
58732.56	529	2.43	58755.74	2062	8.23
58732.77	1979	9.69	58756.10	1047	2.72
58733.12	1015	2.72	58756.73	2062	8.25
58736.12	1029	1.81	58759.10	1070	2.72
58736.75	582	6.04			

Table A.21: V3890 Sgr observations from ARAS archive.

A.8.2 RS Oph - quiescence

Date (MJD)	Resolution ($\lambda/\Delta\lambda$)	Orbital phase	Exposure time (ks)	Date (MJD)	Resolution ($\lambda/\Delta\lambda$)	Orbital phase	Exposure time (ks)
57281.01	9000	0.63	6.06	58945.29	14000	0.29	7.39
57581.13	9000	0.29	6.05	58959.28	14000	0.32	7.39
58319.08	12000	0.91	8.59	58962.28	14000	0.32	7.39
58641.14	14000	0.62	11.05	58989.88	8500	0.38	8.02
58663.87	9000	0.67	9.02	58990.22	14000	0.39	8.61
58667.12	14000	0.68	11.04	58993.18	14000	0.39	9.86
58707.05	12000	0.76	10.30	58994.86	8500	0.40	9.91
58709.85	11000	0.77	8.42	58994.93	12118	0.40	7.11
58754.77	9000	0.87	8.42				

Table A.22: RS Oph observations from ARAS archive.

A.8.3 T CrB - quiescence

Date (MJD)	Resolution ($\lambda/\Delta\lambda$)	Orbital phase	Exposure time (ks)	Date (MJD)	Resolution ($\lambda/\Delta\lambda$)	Orbital phase	Exposure time (ks)
57082.26	8723	0.54	6.07	58187.12	11000	0.40	3.73
57132.91	12432	0.78	3.60	58212.89	9000	0.51	3.61
57153.89	16924	0.87	3.60	58228.97	11000	0.58	6.73
57435.15	11000	0.11	1.84	58229.87	11000	0.60	9.57
57447.15	11000	0.16	3.69	58230.12	12000	0.59	9.72
57459.25	9000	0.20	6.59	58257.92	11000	0.71	5.13
57479.09	11000	0.30	3.64	58335.86	11000	0.05	3.68
57494.96	11000	0.37	3.64	58357.18	8972	0.16	4.99
57501.92	11000	0.40	5.61	58529.13	11000	0.90	2.76
57505.86	13454	0.42	3.61	58565.94	13429	0.08	5.40
57506.89	11000	0.41	3.64	58577.92	9000	0.13	4.81
57507.94	30000	0.43	9.94	58601.93	11000	0.22	5.17
57508.93	11000	0.42	2.42	58609.08	14000	0.27	8.59
57522.89	11000	0.48	2.76	58614.92	11000	0.28	4.45
57547.87	11000	0.59	2.77	58615.91	9000	0.30	4.82
57564.88	11000	0.68	2.77	58624.84	9000	0.32	7.22
57575.89	11000	0.71	2.77	58633.90	9000	0.36	6.05
57585.88	11000	0.77	3.65	58635.88	11000	0.37	6.51
57605.87	11000	0.86	3.62	58640.86	9000	0.41	6.28
57622.84	11000	0.92	3.64	58651.87	9000	0.44	6.01
57641.76	11378	0.00	4.80	58655.94	11000	0.46	6.04
57641.76	11378	0.00	4.80	58658.08	14000	0.47	9.82
57774.17	11000	0.60	4.90	58661.86	9000	0.50	7.56

57817.11	11000	0.77	3.72	58676.87	11000	0.55	4.68
57837.07	11000	0.86	4.05	58702.86	11000	0.68	2.83
57838.22	9000	0.88	6.08	58715.17	13238	0.72	7.28
57838.98	14106	0.87	3.60	58728.81	11000	0.78	2.42
57845.97	20068	0.90	3.60	58932.15	11000	0.69	5.17
57852.95	19809	0.93	3.60	58940.18	14000	0.71	9.87
57854.95	11000	0.94	2.97	58944.06	11000	0.74	4.99
57856.95	46891	0.96	4.82	58945.17	14000	0.73	8.63
57865.01	11000	0.98	3.20	58946.04	11000	0.75	5.03
57872.99	16819	0.02	3.60	58959.16	14000	0.79	8.63
57873.96	10536	0.02	6.00	58960.05	11000	0.81	4.90
57884.91	9000	0.07	5.43	58969.92	9500	0.84	6.02
57886.90	11000	0.08	5.26	58983.07	14000	0.91	8.63
57898.92	11000	0.13	4.26	58986.06	11000	0.91	3.74
57904.89	9000	0.16	9.03	58993.08	14000	0.94	7.39
57940.11	13000	0.31	7.29	58993.88	11000	0.96	4.14
58115.21	11000	0.08	4.85	58997.84	11000	0.96	12.64
58159.13	11000	0.29	3.67	59005.90	9500	0.00	8.44
58173.13	11000	0.35	3.63				

Table A.23: T CrB observations from ARAS archive.

Bibliography

[Abel and Satyapal(2008)] Abel, N. P., Satyapal, S. 2008. [Ne V] Emission in Optically Classified Starbursts. The Astrophysical Journal 678, 686–692. doi:10.1086/529013

[Anupama(2002)] Anupama, G. C. 2002. The Recurrent Novae and Their Relation with Classical Novae. Classical Nova Explosions 637, 32–41. doi:10.1063/1.1518174

[Anupama and Prabhu(1989)] Anupama, G. C., Prabhu, T. P. 1989. The 1985 outburst of RS Ophiuchi : spectroscopic results.. Journal of Astrophysics and Astronomy 10, 237–255. doi:10.1007/BF02714998

[Anupama and Sethi(1994)] Anupama, G. C., Sethi, S. 1994. Spectroscopy of the Recurrent Nova V3890-SAGITTARII 18-DAYS after the 1990 Outburst. Monthly Notices of the Royal Astronomical Society 269, 105. doi:10.1093/mnras/269.1.105

[Anupama and Mikołajewska(1999)] Anupama, G. C., Mikołajewska, J. 1999. Recurrent novae at quiescence: systems with giant secondaries. Astronomy and Astrophysics 344, 177–187.

[Anupama(2008)] Anupama, G. C. 2008. The Recurrent Nova Class of Objects. RS Ophiuchi (2006) and the Recurrent Nova Phenomenon 401, 31.

[Anupama(2008)] Anupama, G. C. 2008. One Year of Monitoring of the 2006 Outburst in Optical and Low Radio Frequencies. RS Ophiuchi (2006) and the Recurrent Nova Phenomenon 401, 251.

[Anupama(2013)] Anupama, G. C. 2013. Recurrent Novae: What Do We Know about Them?. Binary Paths to Type Ia Supernovae Explosions 281, 154–161. doi:10.1017/S1743921312014913

[Aoki and Yoshida(1998)] Aoki, K., Yoshida, M. 1998. The Correlation between Si III] 1892/ C III] 1909 and Fe II 4500/ H beta in low redshift QSOs. arXiv e-prints.

[Ardila et al.(2002)] Ardila, D. R., Basri, G., Walter, F. M., Valenti, J. A., Johns-Krull, C. M. 2002. Observations of T Tauri Stars Using the Hubble Space Telescope GHRS. II. Optical and Near-Ultraviolet Lines. The Astrophysical Journal 567, 1013–1027. doi:10.1086/338586

[Aydi et al.(2020)] Aydi, E. and 41 colleagues 2020. Direct evidence for shock-powered optical emission in a nova. Nature Astronomy 4, 776–780. doi:10.1038/s41550-020-1070-y

[Aufdenberg(1993)] Aufdenberg, J. P. 1993. IUE Short-Wavelength High-Dispersion Line List for the Symbiotic Nova RR Telescopii. The Astrophysical Journal Supplement Series 87, 337. doi:10.1086/191807

[Badenes et al.(2007)] Badenes, C., Hughes, J. P., Bravo, E., Langer, N. 2007. Are the Models for Type Ia Supernova Progenitors Consistent with the Properties of Supernova Remnants?. The Astrophysical Journal 662, 472–486. doi:10.1086/518022

[Banerjee et al.(2014)] Banerjee, D. P. K. and 6 colleagues 2014. Near-IR Studies of Recurrent Nova V745 Scorpii during its 2014 Outburst. The Astrophysical Journal 785. doi:10.1088/2041-8205/785/1/L11

[Bell et al.(1966)] Bell, G. D., Paquette, D. R., Wiese, W. L. 1966. Relative Transition Probabilities for Prominent NI i and NI II Lines in the Near-Ultraviolet. The Astrophysical Journal 143, 559. doi:10.1086/148534

[Blair et al.(1983)] Blair, W. P., Stencel, R. E., Feibelman, W. A., Michalitisianos, A. G. 1983. Spectrophotometric observations of symbiotic stars and related objects.. The Astrophysical Journal Supplement Series 53, 573–590. doi:10.1086/190902

[Bloom(1969)] Bloom, G. S. 1969. The Balmer decrement in the emission spectra of astronomical objects. The University of Arizona.

[Bode et al.(2007)] Bode, M. F. and 7 colleagues 2007. Hubble Space Telescope Imaging of the Expanding Nebular Remnant of the 2006 Outburst of the Recurrent Nova RS Ophiuchi. The Astrophysical Journal 665, L63–L66. doi:10.1086/520929

[Bohigas et al.(1989)] Bohigas, J., Echevarria, J., Diego, F., Sarmiento, J. A. 1989. Spectrophotometry of RS OPH during the nebular phase.. Monthly Notices of the Royal Astronomical Society 238, 1395–1405. doi:10.1093/mnras/238.4.1395

[Bode et al.(2006)] Bode, M. F. and 18 colleagues 2006. Swift Observations of the 2006 Outburst of the Recurrent Nova RS Ophiuchi. I. Early X-Ray Emission from the Shocked Ejecta and Red Giant Wind. The Astrophysical Journal 652, 629–635. doi:10.1086/507980

[Bode and Evans(2008)] Bode, M. F., Evans, A. 2008. Classical Novae. Classical Novae, 2nd Edition. Edited by M.F. Bode and A. Evans. Cambridge Astrophysics Series, No. 43, Cambridge: Cambridge University Press, 2008..

[Bode et al.(2008)] Bode, M. F. and 13 colleagues 2008. Swift Observations of Shock Evolution in RS Ophiuchi. RS Ophiuchi (2006) and the Recurrent Nova Phenomenon 401, 269.

[Bode(2010)] Bode, M. F. 2010. The outbursts of classical and recurrent novae. Astronomische Nachrichten 331, 160. doi:10.1002/asna.200911319

[Bondi and Hoyle(1944)] Bondi, H., Hoyle, F. 1944. On the mechanism of accretion by stars. Monthly Notices of the Royal Astronomical Society 104, 273. doi:10.1093/mnras/104.5.273

[Booth et al.(2016)] Booth, R. A., Mohamed, S., Podsiadlowski, P. 2016. Modelling the circumstellar medium in RS Ophiuchi and its link to Type Ia supernovae. Monthly Notices of the Royal Astronomical Society 457, 822–835. doi:10.1093/mnras/stw001

[Brandi et al.(2009)] Brandi, E., Quiroga, C., Mikołajewska, J., Ferrer, O. E., García, L. G. 2009. Spectroscopic orbits and variations of RS Ophiuchi. Astronomy and Astrophysics 497, 815–825. doi:10.1051/0004-6361/200811417

[Cassatella et al.(1985)] Cassatella, A., Hassall, B. J. M., Harris, A., Snijders, M. A. J. 1985. Ultraviolet Observations of the Recurrent Nova Rs-Ophiuchi in Outburst. Recent Results on Cataclysmic Variables. The Importance of IUE and Exosat Results on Cataclysmic Variables and Low-Mass X-Ray Binaries. Proce ESA workshop, Bamberg, Germany, April 17-19, 1985. (ESA Scientific and Technical Pulbs)

[Chandrasekhar(1960)] Chandrasekhar, S. 1960. Radiative transfer. New York: Dover, 1960.

[Chevalier(1976)] Chevalier, R. A. 1976. The hydrodynamics of type II supernovae.. The Astrophysical Journal 207, 872–887. doi:10.1086/154557

[Chevalier et al.(1980)] Chevalier, R. A., Kirshner, R. P., Raymond, J. C. 1980. The optical emission from a fast shock wave with application to supernova remnants.. The Astrophysical Journal 235, 186–195. doi:10.1086/157623

[Chevalier et al.(1980)] Chevalier, R. A., Kirshner, R. P., Raymond, J. C. 1980. The optical emission from a fast shock wave with application to supernova remnants.. The Astrophysical Journal 235, 186–195. doi:10.1086/157623

[Chevalier(1982)] Chevalier, R. A. 1982. Self-similar solutions for the interaction of stellar ejecta with an external medium.. The Astrophysical Journal 258, 790–797. doi:10.1086/160126

[Chevalier(2008)] Chevalier, R. A. 2008. Supernovae in Dense Winds. RS Ophiuchi (2006) and the Recurrent Nova Phenomenon 401, 185.

[Contini and Aldrovandi(1983)] Contini, M., Aldrovandi, S. M. V. 1983. Composite models for the narrow emission line region of active galactic nuclei. I. The infalling filament.. Astronomy and Astrophysics 127, 15–24.

[Contini et al.(1995)] Contini, M., Orio, M., Prialnik, D. 1995. RS OPH at day 201: a test case for shocks in nova shells. Monthly Notices of the Royal Astronomical Society 275, 195–208. doi:10.1093/mnras/275.1.195

[Contini and Prialnik(1997)] Contini, M., Prialnik, D. 1997. The Shell of the Recurrent Nova T Pyxidis: A Model Based on Shocks. The Astrophysical Journal 475, 803–811. doi:10.1086/303555

[Cook and Nicolas(1979)] Cook, J. W., Nicolas, K. R. 1979. Solar C III line intensity ratios observed from Skylab.. The Astrophysical Journal 229, 1163–1178. doi:10.1086/157051

[Crause et al.(2016)] Crause, L. A. and 21 colleagues 2016. SpUpNIC (Spectrograph Upgrade: Newly Improved Cassegrain) on the South African Astronomical Observatory's 74-inch telescope. Ground-based and Airborne Instrumentation for Astronomy VI 9908. doi:10.1117/12.2230818

[Darnley and Henze(2020)] Darnley, M. J., Henze, M. 2020. On a century of extragalactic novae and the rise of the rapid recurrent novae. Advances in Space Research 66, 1147–1168. doi:10.1016/j.asr.2019.09.044

[Darnley(2021)] Darnley, M. J. 2021. Accrete, Accrete, Accrete… Bang! (and repeat): The remarkable Recurrent Novae. The Golden Age of Cataclysmic Variables and Related Objects V 2-7.

[Das et al.(2006)] Das, R., Banerjee, D. P. K., Ashok, N. M. 2006. A Near-Infrared Shock Wave in the 2006 Outburst of Recurrent Nova RS Ophiuchi. The Astrophysical Journal 653, L141–L144. doi:10.1086/510674

[Dean and Bruhweiler(1985)] Dean, C. A., Bruhweiler, F. C. 1985. An ultraviolet line list for O star spectra.. The Astrophysical Journal Supplement Series 57, 133–143. doi:10.1086/190998

[Delgado and Hernanz(2019)] Delgado, L., Hernanz, M. 2019. Early multiwavelength analysis of the recurrent nova V745 Sco. Monthly Notices of the Royal Astronomical Society 490, 3691–3704. doi:10.1093/mnras/stz2765

[Dobrzycka and Kenyon(1994)] Dobrzycka, D., Kenyon, S. J. 1994. A New Spectroscopic Orbit for RS Ophiuchi. The Astronomical Journal 108, 2259. doi:10.1086/117238

[Dopita(1977)] Dopita, M. A. 1977. Optical Emission from Shock Waves. II. Diagnostic Diagrams. The Astrophysical Journal Supplement Series 33, 437. doi:10.1086/190435

[Dopita and Sutherland(1995)] Dopita, M. A., Sutherland, R. S. 1995. Spectral Signatures of Fast Shocks. II. Optical Diagnostic Diagrams. The Astrophysical Journal 455, 468. doi:10.1086/176596

[Dopita and Sutherland(1996)] Dopita, M. A., Sutherland, R. S. 1996. Spectral Signatures of Fast Shocks. I. Low-Density Model Grid. The Astrophysical Journal Supplement Series 102, 161. doi:10.1086/192255

[Doschek et al.(1978)] Doschek, G. A., Feldman, U., Mariska, J. T., Linsky, J. L. 1978. Electron densities in stellar atmospheres determined from IUE spectra.. The Astrophysical Journal 226, L35–L38. doi:10.1086/182825

[Doschek and Feibelman(1993)] Doschek, G. A., Feibelman, W. A. 1993. An Improved Ultraviolet Spectral Line List for the Symbiotic Star RR Telescopii. The Astrophysical Journal Supplement Series 87, 331. doi:10.1086/191806

[Draine(2011)] Draine, B. T. 2011. Physics of the Interstellar and Intergalactic Medium. Physics of the Interstellar and Intergalactic Medium by Bruce T. Draine. Princeton University Press, 2011. ISBN: 978-0-691-12214-4.

[Drake et al.(2016)] Drake, J. J. and 11 colleagues 2016. Collimation and Asymmetry of the Hot Blast Wave from the Recurrent Nova V745 Sco. The Astrophysical Journal 825. doi:10.3847/0004-637X/825/2/95

[Duerbeck(2009)] Duerbeck, H. W. 2009. New Stars and telescopes: Nova research in the last four centuries. Astronomische Nachrichten 330, 568. doi:10.1002/asna.200911218

[Espey and Crowley(2008)] Espey, B. R., Crowley, C. 2008. Mass-loss from Red Giants. RS Ophiuchi (2006) and the Recurrent Nova Phenomenon 401, 166.

[Feibelman and Aller(1987)] Feibelman, W. A., Aller, L. H. 1987. The (C III lambda 1909/Si III lambda 1892) Ratio as a Diagnostic for Planetary Nebulae and Symbiotic Stars. The Astrophysical Journal 319, 407. doi:10.1086/165465

[Feibelman et al.(1991)] Feibelman, W. A., Bruhweiler, F. C., Johansson, S. 1991. Ultraviolet High-Excitation Fe II Fluorescence Lines Excited by O vi, C iv, and H i Resonance Emission As Seen in IUE Spectra. The Astrophysical Journal 373, 649. doi:10.1086/170084

[Fekel et al.(2000)] Fekel, F. C., Joyce, R. R., Hinkle, K. H., Skrutskie, M. F. 2000. Infrared Spectroscopy of Symbiotic Stars. I. Orbits for Well-Known S-Type Systems. The Astronomical Journal 119, 1375–1388. doi:10.1086/301260

[Ferland and Shields(1978)] Ferland, G. J., Shields, G. A. 1978. Heavy element abundances of Nova Cygni 1975.. The Astrophysical Journal 226, 172–185. doi:10.1086/156597

[Fryxell et al.(2010)] Fryxell, B. and 9 colleagues 2010. FLASH: Adaptive Mesh Hydrodynamics Code for Modeling Astrophysical Thermonuclear Flashes. Astrophysics Source Code Library. ascl:1010.082

[Gaposchkin(1957)] Gaposchkin, C. H. P. 1957. The Galactic Novae. Amsterdam, North-Holland Pub. Co.; New York, Interscience Publishers, 1957..

[García et al.(2013)] García, J., Elhoussieny, E. E., Bautista, M. A., Kallman, T. R. 2013. Time-dependent Photoionization of Gaseous Nebulae: The Pure Hydrogen Case. The Astrophysical Journal 775. doi:10.1088/0004-637X/775/1/8

[Garhart et al.(1997)] Garhart, M. P., Smith, M. A., Turnrose, B. E., Levay, K. L., Thompson, R. W. 1997. International Ultraviolet Explorer New Spectral Image Processing System Information Manual: Version 2.0. NASA IUE Newsletter, No. 57, p. 1-267, October 1997. Edited by Walter Feibelman. Greenbelt: IUE Observatory, NASA Goddard Space Flight Center 57.

[Gehrels and Cannizzo(2015)] Gehrels, N., Cannizzo, J. K. 2015. How Swift is redefining time domain astronomy. Journal of High Energy Astrophysics 7, 2–11. doi:10.1016/j.jheap.2015.03.003

[Glass(1974)] Glass, I. I. 1974. Shock waves and man. Toronto (Canada): University of Toronto Press, 12 + 169 p.

[Gonzalez-Riestra(1992)] Gonzalez-Riestra, R. 1992. The 1990 outburst of the recurrent nova V3890 Sgr observed with IUE.. Astronomy and Astrophysics 265, 71–76.

[Gorbatskii(1972)] Gorbatskii, V. G. 1972. Formation of Coronal Lines in the Spectra of Novae. I.. Soviet Astronomy 16, 32.

[Gorbatskii(1973)] Gorbatskii, V. G. 1973. Formation of Coronal Lines in the Spectra of Novae. II. Soviet Astronomy 17, 11.

[Gorjian et al.(2007)] Gorjian, V., Cleary, K., Werner, M. W., Lawrence, C. R. 2007. A Relation between the Mid-Infrared [Ne V] 14.3 μm and [Ne III] 15.6 μm Lines in Active Galactic Nuclei. The Astrophysical Journal 655, L73–L76. doi:10.1086/511975

[Gromadzki et al.(2008)] Gromadzki, M., Mikolajewska, J., Lachowicz, P. 2008. Post-outburst Variations in the Optical Light Curve of RS Ophiuchi. RS Ophiuchi (2006) and the Recurrent Nova Phenomenon 401, 219.

[Hachisu et al.(1999)] Hachisu, I., Kato, M., Nomoto, K. 1999. A Wide Symbiotic Channel to Type IA Supernovae. The Astrophysical Journal 522, 487–503. doi:10.1086/307608

[Hachisu and Kato(2001)] Hachisu, I., Kato, M. 2001. Recurrent Novae as a Progenitor System of Type Ia Supernovae. I. RS Ophiuchi Subclass: Systems with a Red Giant Companion. The Astrophysical Journal 558, 323–350. doi:10.1086/321601

[Hachisu and Kato(2018)] Hachisu, I., Kato, M. 2018. A Light Curve Analysis of Recurrent and Very Fast Novae in Our Galaxy, Magellanic Clouds, and M31. The Astrophysical Journal Supplement Series 237. doi:10.3847/1538-4365/aac833

[Hartquist et al.(2008)] Hartquist, T. W., Dyson, J. E., Falle, S. A. E. G., Pittard, J. M., Wagner, A. Y. 2008. Shocks in Multicomponent Astrophysical Media. RS Ophiuchi (2006) and the Recurrent Nova Phenomenon 401, 177.

[Hernanz and José(2008)] Hernanz, M., José, J. 2008. The recurrent nova RS Oph: A possible scenario for type Ia supernovae. New Astronomy Reviews 52, 386–389. doi:10.1016/j.newar.2008.06.017

[Hernanz and Tatischeff(2012)] Hernanz, M., Tatischeff, V. 2012. High Energy Emission of Symbiotic Recurrent Novae: RS Oph and V407 Cyg. Baltic Astronomy 21, 62–67. doi:10.1515/astro-2017-0359

[Hollenbach and Thronson(1987)] Hollenbach, D. J., Thronson, H. A. 1987. Interstellar processes. Interstellar Processes, Proceedings of a symposium, held at Grand Teton National Park, Wyo., July, 1986, Dordrecht: Reidel, 1987, edited by David J. Hollenbach, and Harley A. Thronson. Astrophysics and Space Science Library, Vol. 134. doi:10.1007/978-94-009-3861-8

[Howell(2011)] Howell, D. A. 2011. Type Ia supernovae as stellar endpoints and cosmological tools. Nature Communications 2. doi:10.1038/ncomms1344

[Iijima(2008)] Iijima, T. 2008. Circumstellar Envelope of RS Ophiuchi. RS Ophiuchi (2006) and the Recurrent Nova Phenomenon 401, 115.

[Iijima(2012)] Iijima, T. 2012. Spectroscopic observations of the symbiotic recurrent nova V407 Cygni .. Memorie della Societa Astronomica Italiana 83, 835.

[Iijima(2014)] Iijima, T. 2014. The Nature of the Symbiotic Recurrent Nova V407 Cygni. Stellar Novae: Past and Future Decades 490, 361.

[Iijima(2015)] Iijima, T. 2015. New Features of the Symbiotic Recurrent Nova V407 Cygni Found in the Outburst in 2010. The Astronomical Journal 150. doi:10.1088/0004-6256/150/1/20

[Jasinsky et al.(2015)] Jasinsky, C. and 4 colleagues 2015. About ARAS initiative. http://astrosurf.com/aras/intro/intro.htm

[Jencson et al.(2021)] Jencson, J. E. and 40 colleagues 2021. AT 2019qyl in NGC 300: Early Outflow Collisions for a Very Fast Nova in a Symbiotic Binary. arXiv e-prints.

[Jose(2016)] Jose, J. 2016. Stellar Explosions: Hydrodynamics and Nucleosynthesis. Stellar Explosions: Hydrodynamics and Nucleosynthesis by Jordi Jose. ISBN: ¡ISBN¿978-1-4398-5306-1¡/ISBN¿. CRC Press/Taylor and Francis, 2016. doi:10.1201/b19165

[Kabáth et al.(2020)] Kabáth, P. and 20 colleagues 2020. Ondřejov Echelle Spectrograph, Ground Based Support Facility for Exoplanet Missions. Publications of the Astronomical Society of the Pacific 132. doi:10.1088/1538-3873/ab6752

[Kahn(1954)] Kahn, F. D. 1954. The acceleration of interstellar clouds. Bulletin of the Astronomical Institutes of the Netherlands 12, 187.

[Kato(2002)] Kato, M. 2002. Recurrent novae, classical novae, symbiotic novae, and population II novae. The Physics of Cataclysmic Variables and Related Objects 261, 595.

[Kaufer et al.] Kaufer, A. and 8 colleagues. Very Large Telescope Paranal Science Operations UV-Visual Echelle Spectrograph User manual. Citeseer

[Keenan et al.(1987)] Keenan, F. P., Kingston, A. E., Dufton, P. L. 1987. The SI III 1892 A/C III 1908 A emission-line ratio in late-type stars. Monthly Notices of the Royal Astronomical Society 225, 859–861. doi:10.1093/mnras/225.4.859

[Keenan et al.(1992)] Keenan, F. P., Feibelman, W. A., Berrington, K. A. 1992. Improved Calculations for the C III lambda lambda 1907,1909 and SI III lambda lambda 1883,1892 Electron Density Sensitive Emission-Line Ratios, and a Comparison with IUE Observations. The Astrophysical Journal 389, 443. doi:10.1086/171220

[Kewley et al.(2019)] Kewley, L. J., Nicholls, D. C., Sutherland, R. S. 2019. Understanding Galaxy Evolution Through Emission Lines. Annual Review of Astronomy and Astrophysics 57, 511–570. doi:10.1146/annurev-astro-081817-051832

[Kjeldseth Moe and Nicolas(1977)] Kjeldseth Moe, O., Nicolas, K. R. 1977. Emission measures, electron densities, and nonthermal velocities from optically thin UV lines near a quiet solar limb.. The Astrophysical Journal 211, 579–586. doi:10.1086/154966

[Kolotilov et al.(2003)] Kolotilov, E. A., Shenavrin, V. I., Shugarov, S. Y., Yudin, B. F. 2003. UBVJHKLM photometry of the symbiotic Mira V407 Cyg in 1998 2002. Astronomy Reports 47, 777–788. doi:10.1134/1.1611218

[Korista et al.(1997)] Korista, K., Baldwin, J., Ferland, G., Verner, D. 1997. An Atlas of Computed Equivalent Widths of Quasar Broad Emission Lines. The Astrophysical Journal Supplement Series 108, 401–415. doi:10.1086/312966

[Koubský et al.(2004)] Koubský, P. and 6 colleagues 2004. Ondřejov Echelle Spectrograph - OES. Publications of the Astronomical Institute of the Czechoslovak Academy of Sciences 92, 37–43.

[Krautter(2008)] Krautter, J. 2008. The Super-soft Phase in Novae. RS Ophiuchi (2006) and the Recurrent Nova Phenomenon 401, 139.

[Kuin(2013a)] Kuin, P. 2013. The Swift UVOT Grism wavelength calibration. SWIFT-UVOT-CALDB-21-R00

[Kuin(2013b)] Kuin, P. 2013. The Swift UVOT Grism: Verification of the Flux Calibration of the uv-grism. Release 0.9.7

[Kuin(2014a)] Kuin, P. 2014. UVOTPY: Swift UVOT grism data reduction. Astrophysics Source Code Library. ascl:1410.004

[Kuin(2014b)] Kuin, P. 2014. The Swift UVOT Grism Documentation

[Kuin et al.(2015)] Kuin, N. P. M. and 18 colleagues 2015. Calibration of the Swift-UVOT ultraviolet and visible grisms. Monthly Notices of the Royal Astronomical Society 449, 2514–2538. doi:10.1093/mnras/stv408

[Kuin et al.(2020)] Kuin, N. P. M. and 25 colleagues 2020. The 2016 January eruption of recurrent Nova LMC 1968. Monthly Notices of the Royal Astronomical Society 491, 655–679. doi:10.1093/mnras/stz2960

[Lamers and Cassinelli(1999)] Lamers, H. J. G. L. M., Cassinelli, J. P. 1999. Introduction to Stellar Winds. Introduction to Stellar Winds, by Henny J. G. L. M. Lamers and Joseph P. Cassinelli, pp. 452. ISBN 0521593980. Cambridge, UK: Cambridge University Press, June 1999. 452.

[Landolt and Blondeau(1972)] Landolt, A. U., Blondeau, K. L. 1972. The Calculation of Heliocentric Corrections. Publications of the Astronomical Society of the Pacific 84, 784. doi:10.1086/129382

[Larsson et al.(2013)] Larsson, J. and 11 colleagues 2013. The Morphology of the Ejecta in Supernova 1987A: A Study over Time and Wavelength. The Astrophysical Journal 768. doi:10.1088/0004-637X/768/1/89

[Ley(2014)] Ley, Hood-Hong. 2014. Analytical methods in plasma diagnostic by optical emission spectroscopy: A tutorial review. Journal of Science and Technology 6, 1

[Lloyd et al.(1993)] Lloyd, H. M., Bode, M. F., O'Brien, T. J., Kahn, F. D. 1993. Bipolar recurrent nova outbursts - I. Hydrodynamic models.. Monthly Notices of the Royal Astronomical Society 265, 457–470. doi:10.1093/mnras/265.2.457

[Luna et al.(2008)] Luna, G. J. M., Sokoloski, J. L., Mukai, K. 2008. High Energy X-ray Emission from Recurrent Novae in Quiescence: T CrB. RS Ophiuchi (2006) and the Recurrent Nova Phenomenon 401, 342.

[Macchetto(1976)] Macchetto, F. 1976. The International Ultraviolet Explorer (IUE). Memorie della Societa Astronomica Italiana 47, 431.

[Martin and Dubus(2013)] Martin, P., Dubus, G. 2013. Particle acceleration and non-thermal emission during the V407 Cygni nova outburst. Astronomy and Astrophysics 551. doi:10.1051/0004-6361/201220289

[Massey and Hanson(2013)] Massey, P., Hanson, M. M. 2013. Astronomical Spectroscopy. Planets, Stars and Stellar Systems. Volume 2: Astronomical Techniques, Software and Data 35. doi:10.1007/978-94-007-5618-2_2

[Meier et al.(1994)] Meier, S. R., Kafatos, M., Fahey, R. P., Michalitsianos, A. G. 1994. A Far-Ultraviolet Atlas of Symbiotic Stars Observed with IUE. I. The SWP Range. The Astrophysical Journal Supplement Series 94, 183. doi:10.1086/192078

[Merrill and Humason(1932)] Merrill, P. W., Humason, M. L. 1932. A Bright Line of Ionized Helium, λ4686, in Three Stellar Spectra with Titanium Bands. Publications of the Astronomical Society of the Pacific 44, 56. doi:10.1086/124191

[Metzger et al.(2014)] Metzger, B. D. and 6 colleagues 2014. Shocks in nova outflows - I. Thermal emission. Monthly Notices of the Royal Astronomical Society 442, 713–731. doi:10.1093/mnras/stu844

[Mihalas and Mihalas(1984)] Mihalas, D., Mihalas, B. W. 1984. Foundations of radiation hydrodynamics. New York, Oxford University Press, 1984, 731 p..

[Mikolajewska et al.(1999)] Mikolajewska, J. and 6 colleagues 1999. The symbiotic binary system RX Puppis: a possible recurrent nova with a Mira companion. Monthly Notices of the Royal Astronomical Society 305, 190–210. doi:10.1046/j.1365-8711.1999.02449.x

[Mikolajewska(2008)] Mikolajewska, J. 2008. The Place of Recurrent Novae Among the Symbiotic Stars. RS Ophiuchi (2006) and the Recurrent Nova Phenomenon 401, 42.

[Mikolajewska(2010)] Mikolajewska, J. 2010. Symbiotic Novae. arXiv:1011.5657.

[Mikołajewska(2012)] Mikołajewska, J. 2012. Symbiotic Stars: Observations Confront Theory. Baltic Astronomy 21, 5–12. doi:10.1515/astro-2017-0352

[Mikołajewska and Shara(2017)] Mikołajewska, J., Shara, M. M. 2017. The Massive CO White Dwarf in the Symbiotic Recurrent Nova RS Ophiuchi. The Astrophysical Journal 847. doi:10.3847/1538-4357/aa87b6

[Mikołajewska et al.(2021)] Mikołajewska, J. and 6 colleagues 2021. The symbiotic recurrent nova V3890 Sgr: binary parameters and pre-outburst activity. Monthly Notices of the Royal Astronomical Society 504, 2122–2132. doi:10.1093/mnras/stab1058

[Mohamed et al.(2012)] Mohamed, S., Mackey, J., Langer, N. 2012. 3D simulations of Betelgeuse's bow shock. Astronomy and Astrophysics 541. doi:10.1051/0004-6361/201118002

[Mohamed et al.(2013)] Mohamed, S., Booth, R., Podsiadlowski, P. 2013. The Asymmetric Outflow of RS Ophiuchi. Binary Paths to Type Ia Supernovae Explosions 281, 195–198. doi:10.1017/S1743921312014998

[Mondal et al.(2018)] Mondal, A., Anupama, G. C., Kamath, U. S., Das, R., Selvakumar, G., Mondal, S. 2018. Optical spectroscopy of the recurrent nova RS Ophiuchi - from the outburst of 2006 to quiescence. Monthly Notices of the Royal Astronomical Society 474, 4211–4224. doi:10.1093/mnras/stx2988

[Moore and Bildsten(2012)] Moore, K., Bildsten, L. 2012. Circumstellar Shell Formation in Symbiotic Recurrent Novae. The Astrophysical Journal 761. doi:10.1088/0004-637X/761/2/182

[Mróz et al.(2014)] Mróz, P. and 11 colleagues 2014. Recurrent and symbiotic novae in data from the Optical Gravitational Lensing Experiment. Monthly Notices of the Royal Astronomical Society 443, 784–790. doi:10.1093/mnras/stu1181

[Muerset et al.(1991)] Muerset, U., Nussbaumer, H., Schmid, H. M., Vogel, M. 1991. Temperature and luminosity of hot components in symbiotic stars.. Astronomy and Astrophysics 248, 458.

[Mukai(2008)] Mukai, K. 2008. RS Ophiuchi in Quiescence: Why is it X-ray Faint?. RS Ophiuchi (2006) and the Recurrent Nova Phenomenon 401, 84.

[Munari et al.(1990)] Munari, U., Margoni, R., Stagni, R. 1990. The extreme, possible symbiotic Mira V407 CYG and its relevance to the OH/IR sources.. Monthly Notices of the Royal Astronomical Society 242, 653–659. doi:10.1093/mnras/242.4.653

[Munari and Zwitter(2002)] Munari, U., Zwitter, T. 2002. A multi-epoch spectrophotometric atlas of symbiotic stars. Astronomy and Astrophysics 383, 188–196. doi:10.1051/0004-6361:20011724

[Munari et al.(2011)] Munari, U. and 8 colleagues 2011. The 2010 nova outburst of the symbiotic Mira V407 Cyg. Monthly Notices of the Royal Astronomical Society 410, L52–L56. doi:10.1111/j.1745-3933.2010.00979.x

[Munari(2019)] Munari, U. 2019. The Symbiotic Stars. arXiv:1909.01389.

[Nelson et al.(2012)] Nelson, T., Donato, D., Mukai, K., Sokoloski, J., Chomiuk, L. 2012. X-Ray Emission from an Asymmetric Blast Wave and a Massive White Dwarf in the Gamma-Ray Emitting Nova V407 Cyg. The Astrophysical Journal 748. doi:10.1088/0004-637X/748/1/43

[Ness et al.(2008)] Ness, J.-U., Starrfield, S., van Rossum, D. R., Schönrich, R. 2008. The X-ray Spectra from the Shock and the White Dwarf: Two Laboratories in One Spectrum. RS Ophiuchi (2006) and the Recurrent Nova Phenomenon 401, 274.

[Ness et al.(2009)] Ness, J.-U. and 11 colleagues 2009. High-Resolution X-Ray Spectroscopy of the Evolving Shock in the 2006 Outburst of RS Ophiuchi. The Astronomical Journal 137, 3414–3436. doi:10.1088/0004-6256/137/2/3414

[Nishiyama et al.(2010)] Nishiyama, K., Kabashima, F., Guido, E., Sostero, G., Schmeer, P. 2010. V407 Cygni. Central Bureau Electronic Telegrams 2204.

[NIST] National Institute of Standards and Technology (NIST). Atomic Spectra Database. `https://physics.nist.gov/PhysRefData/ASD/linesform.html`

[Nussbaumer and Storey(1978)] Nussbaumer, H., Storey, P. J. 1978. The C III transition probabilities.. Astronomy and Astrophysics 64, 139–144.

[Nussbaumer and Storey(1978)] Nussbaumer, H., Storey, P. J. 1978. The C III transition probabilities.. Astronomy and Astrophysics 64, 139–144.

[Nussbaumer and Schild(1979)] Nussbaumer, H., Schild, H. 1979. C III observable with IUE.. Astronomy and Astrophysics 75, L17–L19.

[Nussbaumer and Schild(1981)] Nussbaumer, H., Schild, H. 1981. A model of V1016 CYG based on the ultraviolet spectrum.. Astronomy and Astrophysics 101, 118–131.

[Nussbaumer(1986)] Nussbaumer, H. 1986. Temperature and density determination from SI III lines. Astronomy and Astrophysics 155, 205–209.

[Nussbaumer and Stencel(1987)] Nussbaumer, H., Stencel, R. E. 1987. Symbiotic Stars. Exploring the Universe with the IUE Satellite 203. doi:10.1007/978-94-009-3753-6_10

[Nussbaumer and Vogel(1987)] Nussbaumer, H., Vogel, M. 1987. A new approach to symbiotic stars.. Astronomy and Astrophysics 182, 51–62.

[Nussbaumer et al.(1989)] Nussbaumer, H., Schmid, H. M., Vogel, M. 1989. Raman scattering as a diagnostic possibility in astrophysics.. Astronomy and Astrophysics 211, L27–L30.

[Nussbaumer and Vogel(1990)] Nussbaumer, H., Vogel, M. 1990. Winds in symbiotic systems.. Astronomische Gesellschaft Abstract Series.

[Nussbaumer et al.(1995)] Nussbaumer, H., Schmutz, W., Vogel, M. 1995. Proof of a fast wind in the symbiotic nova AG Pegasi.. Astronomy and Astrophysics 293, L13–L16.

[O'Brien and Kahn(1987)] O'Brien, T. J., Kahn, F. D. 1987. Models for the remnants of recurrent novae - II. Dynamical effect of radiative heat loss.. Monthly Notices of the Royal Astronomical Society 228, 277–287. doi:10.1093/mnras/228.2.277

[O'Brien et al.(1992)] O'Brien, T. J., Bode, M. F., Kahn, F. D. 1992. Models for the remnants of recurrent novae - III. Comparison with the X-ray observations of RS Ophiuchi (1985).. Monthly Notices of the Royal Astronomical Society 255, 683–693. doi:10.1093/mnras/255.4.683

[O'Brien et al.(2006)] O'Brien, T. J. and 8 colleagues 2006. An asymmetric shock wave in the 2006 outburst of the recurrent nova RS Ophiuchi. Nature 442, 279–281. doi:10.1038/nature04949

[Ojha et al.(1988)] Ojha, P. C., Keenan, F. P., Hibbert, A. 1988. Oscillator strengths for transitions among the $3s^2$ and 3s3p levels of Si III. Journal of Physics B Atomic Molecular Physics 21, L395–L401. doi:10.1088/0953-4075/21/14/002

[Orio et al.(2020)] Orio, M. and 15 colleagues 2020. Chandra High Energy Transmission Gratings Spectra of V3890 Sgr. The Astrophysical Journal 895. doi:10.3847/1538-4357/ab8c4d

[Orlando and Drake(2012)] Orlando, S., Drake, J. J. 2012. Modelling the 2010 blast wave of the symbiotic-like nova V407 Cygni. Monthly Notices of the Royal Astronomical Society 419, 2329–2337. doi:10.1111/j.1365-2966.2011.19880.x

[Orlando et al.(2017)] Orlando, S., Drake, J. J., Miceli, M. 2017. Origin of asymmetries in X-ray emission lines from the blast wave of the 2014 outburst of nova V745 Sco. Monthly Notices of the Royal Astronomical Society 464, 5003–5017. doi:10.1093/mnras/stw2718

[Osborne et al.(2011)] Osborne, J. P. and 15 colleagues 2011. The Supersoft X-ray Phase of Nova RS Ophiuchi 2006. The Astrophysical Journal 727. doi:10.1088/0004-637X/727/2/124

[Osterbrock and Ferland(2006)] Osterbrock, D. E., Ferland, G. J. 2006. Astrophysics of gaseous nebulae and active galactic nuclei. Astrophysics of gaseous nebulae and active galactic nuclei, 2nd. ed. by D.E. Osterbrock and G.J. Ferland. Sausalito, CA: University Science Books, 2006.

[Ostriker and McKee(1988)] Ostriker, J. P., McKee, C. F. 1988. Astrophysical blastwaves. Reviews of Modern Physics 60, 1–68. doi:10.1103/RevModPhys.60.1

[Page et al.(2015)] Page, K. L. and 17 colleagues 2015. Swift detection of the super-swift switch-on of the super-soft phase in nova V745 Sco (2014). Monthly Notices of the Royal Astronomical Society 454, 3108–3120. doi:10.1093/mnras/stv2144

[Page et al.(2020)] Page, K. L. and 8 colleagues 2020. The 2019 eruption of recurrent nova V3890 Sgr: observations by Swift, NICER, and SMARTS. Monthly Notices of the Royal Astronomical Society 499, 4814–4831. doi:10.1093/mnras/staa3083

[Pagnotta(2012)] Pagnotta, A. 2012. Recurrent Novae and Type Ia Supernova Progenitors. Ph.D. Thesis. doi:10.5281/zenodo.51286

[Pan et al.(2015)] Pan, K.-C., Ricker, P. M., Taam, R. E. 2015. Simulations of the Symbiotic Recurrent Nova V407 CYG. I. Accretion and Shock Evolutions. The Astrophysical Journal 806. doi:10.1088/0004-637X/806/1/27

[Pan et al.(2015)] Pan, K.-C., Ricker, P. M., Taam, R. E. 2015. Simulations of the Symbiotic Recurrent Nova V407 CYG. I. Accretion and Shock Evolutions. The Astrophysical Journal 806. doi:10.1088/0004-637X/806/1/27

[Pan et al.(2018)] Pan, Y.-C., Foley, R. J., Filippenko, A. V., Kuin, N. P. M. 2018. Swift UVOT grism observations of nearby Type Ia supernovae - I. Observations and data reduction. Monthly Notices of the Royal Astronomical Society 479, 517–535. doi:10.1093/mnras/sty1420

[Pan et al.(2020)] Pan, Y.-C., Foley, R. J., Jones, D. O., Filippenko, A. V., Kuin, N. P. M. 2020. Swift UVOT grism observations of nearby Type Ia supernovae - II. Probing the progenitor metallicity of SNe Ia with ultraviolet spectra. Monthly Notices of the Royal Astronomical Society 491, 5897–5910. doi:10.1093/mnras/stz3391

[Park and Chamberlin] Park, R. and Chamberlin, A. Solar System Dynamics Group, Horizons On-Line Ephemeris System. `https://ssd.jpl.nasa.gov/horizons.cgi`

[Penston and Lago(1983)] Penston, M. V., Lago, M. T. V. T. 1983. Optical and ultraviolet line profiles and ultraviolet line intensities in the T Tauri star LHα 332-21.. Monthly Notices of the Royal Astronomical Society 202, 77–84. doi:10.1093/mnras/202.1.77

[Raymond(1979)] Raymond, J. C. 1979. Shock waves in the interstellar medium.. The Astrophysical Journal Supplement Series 39, 1–27. doi:10.1086/190562

[Ribeiro et al.(2009)] Ribeiro, V. A. R. M. and 18 colleagues 2009. The Expanding Nebular Remnant of the Recurrent Nova RS Ophiuchi (2006). II. Modeling of Combined Hubble Space Telescope Imaging and Ground-based Spectroscopy. The Astrophysical Journal 703, 1955–1963. doi:10.1088/0004-637X/703/2/1955

[Ribeiro et al.(2013)] Ribeiro, V. A. R. M., Bode, M. F., Williams, R. 2013. Modelling the Late-time Hubble Space Telescope Imaging of the Outburst of the Recurrent Nova RS Ophiuchi (2006). Feeding Compact Objects: Accretion on All Scales 290, 137–140. doi:10.1017/S1743921312019382

[Ribeiro et al.(2014)] Ribeiro, V. A. R. M., Bode, M. F., Williams, R. E. 2014. On the Evolution of the Late-time Hubble Space Telescope Imaging of the Outburst of the Recurrent Nova RS Ophiuchi (2006). Stellar Novae: Past and Future Decades 490, 123.

[Rushton et al.(2010)] Rushton, M. T. and 10 colleagues 2010. Changes in the red giant and dusty environment of the recurrent nova RS Ophiuchi following the 2006 eruption. Monthly Notices of the Royal Astronomical Society 401, 99–104. doi:10.1111/j.1365-2966.2009.15675.x

[Schaefer(2009)] Schaefer, B. E. 2009. Orbital Periods for Three Recurrent Novae. The Astrophysical Journal 697, 721–729. doi:10.1088/0004-637X/697/1/721

[Schaefer(2010)] Schaefer, B. E. 2010. Comprehensive Photometric Histories of All Known Galactic Recurrent Novae. The Astrophysical Journal Supplement Series 187, 275–373. doi:10.1088/0067-0049/187/2/275

[Schwab et al.(2011)] Schwab, C., Spronck, J. F. P., Tokovinin, A., Fischer, D. A., Marcy, G. W. 2011. CHIRON - A new high resolution spectrometer for CTIO. European Physical Journal Web of Conferences 16. doi:10.1051/epjconf/20111607006

[Seaton(1975)] Seaton, M. J. 1975. Collision strengths for [N II], [O III], [Ne II] and [Ne III].. Monthly Notices of the Royal Astronomical Society 170, 475–486. doi:10.1093/mnras/170.3.475

[Sedov(1959)] Sedov, L. I. 1959. Similarity and Dimensional Methods in Mechanics. Similarity and Dimensional Methods in Mechanics, New York: Academic Press, 1959.

[Sekiguchi et al.(1990)] Sekiguchi, K. and 10 colleagues 1990. The 1989 outburst of the recurrent nova V745 Sco.. Monthly Notices of the Royal Astronomical Society 246, 78–83.

[Sekiguchi(1995)] Sekiguchi, K. 1995. Recurrent Novae. Astrophysics and Space Science 230, 75–82. doi:10.1007/BF00658169

[Shore and Aufdenberg(1993)] Shore, S. N., Aufdenberg, J. P. 1993. On the Interpretation of the Ultraviolet Spectra of Symbiotic Stars and Recurrent Novae. I. The Astrophysical Journal 416, 355. doi:10.1086/173239

[Shore et al.(1996)] Shore, S. N., Kenyon, S. J., Starrfield, S., Sonneborn, G. 1996. On the Interpretation of the Ultraviolet Spectra of Symbiotic Stars and Recurrent Novae. II. The 1985 Outburst of RS Ophiuchi. The Astrophysical Journal 456, 717. doi:10.1086/176692

[Shore(2002)] Shore, S. N. 2002. The Tapestry of Modern Astrophysics. The Tapestry of Modern Astrophysics, by Steven N. Shore, pp. 888. ISBN 0-471-16816-5. Wiley-VCH , October 2002. 888.

[Shore(2003)] Shore, S. N. 2003. Binary Stars. Encyclopedia of Physical Science and Technology (Third Edition). Academic Press, New York, 77-92

[Shore(2007)] Shore, S. N. 2007. Astrophysical Hydrodynamics: An Introduction. Astrophysical Hydrodynamics: An Introduction by Steven N. Shore. Wiley, 2007. ISBN: 978-3-527-40669-2.

[Shore(2008)] Shore, S. N. 2008. The 1985 Outburst of RS Ophiuchi: Lessons Learned from the Ultraviolet. RS Ophiuchi (2006) and the Recurrent Nova Phenomenon 401, 19.

[Shore and Wahlgren(2010)] Shore, S. N., Wahlgren, G. M. 2010. The O I] 1641 Å line as a probe of symbiotic star winds. Astronomy and Astrophysics 515. doi:10.1051/0004-6361/201014271

[Shore et al.(2011)] Shore, S. N., Augusteijn, T., Ederoclite, A., Uthas, H. 2011. The spectroscopic evolution of the recurrent nova T Pyxidis during its 2011 outburst. I. The optically thick phase and the origin of moving lines in novae. Astronomy and Astrophysics 533. doi:10.1051/0004-6361/201117721

[Shore et al.(2011)] Shore, S. N. and 9 colleagues 2011. The spectroscopic evolution of the symbiotic-like recurrent nova V407 Cygni during its 2010 outburst. I. The shock and its evolution. Astronomy and Astrophysics 527. doi:10.1051/0004-6361/201015901

[Shore et al.(2012)] Shore, S. N. and 6 colleagues 2012. The spectroscopic evolution of the symbiotic-like recurrent nova V407 Cygni during its 2010 outburst. II. The circumstellar environment and the aftermath. Astronomy and Astrophysics 540. doi:10.1051/0004-6361/201118060

[Shore(2012)] Shore, S. N. 2012. Spectroscopy of novae – a user's manual. Bulletin of the Astronomical Society of India 40, 185.

[Shore(2013)] Shore, S. N. 2013. A unified model for the spectrophotometric development of classical and recurrent novae. The role of asphericity of the ejecta. Astronomy and Astrophysics 559. doi:10.1051/0004-6361/201322470

[Shore(2014)] Shore, S. N. 2014. The Spectroscopic Development of a Nova. Stella Novae: Past and Future Decades 490, 145.

[Singh et al.(2021)] Singh, K. P., Girish, V., Pavana, M., Ness, J.-U., Anupama, G. C., Orio, M. 2021. AstroSat soft X-ray observations of the symbiotic recurrent nova V3890 Sgr during its 2019 outburst. Monthly Notices of the Royal Astronomical Society 501, 36–49. doi:10.1093/mnras/staa3303

[Skopal et al.(2008)] Skopal, A., Vanko, M., Komžík, R., Chochol, D. 2008. Modeling the Composite UV/Optical/IR Continuum of the Recurrent Symbiotic Nova RS Ophiuchi. RS Ophiuchi (2006) and the Recurrent Nova Phenomenon 401, 101.

[Soker(2014)] Soker, N. 2014. What sodium absorption lines tell us about Type Ia supernovae.. Monthly Notices of the Royal Astronomical Society 444, L73–L77. doi:10.1093/mnrasl/slu119

[Sokoloski et al.(2006)] Sokoloski, J. L., Luna, G. J. M., Mukai, K., Kenyon, S. J. 2006. An X-ray-emitting blast wave from the recurrent nova RS Ophiuchi. Nature 442, 276–278. doi:10.1038/nature04893

[Springel(2005)] Springel, V. 2005. The cosmological simulation code GADGET-2. Monthly Notices of the Royal Astronomical Society 364, 1105–1134. doi:10.1111/j.1365-2966.2005.09655.x

[Starrfield(2008)] Starrfield, S. 2008. RS Ophiuchi: The Gift that Keeps on Giving. RS Ophiuchi (2006) and the Recurrent Nova Phenomenon 401, 4.

[Sternberg et al.(2011)] Sternberg, A. and 19 colleagues 2011. Circumstellar Material in Type Ia Supernovae via Sodium Absorption Features. Science 333, 856. doi:10.1126/science.1203836

[Sternberg(2013)] Sternberg, A. 2013. Evidence for Circumstellar Material in Type Ia Supernovae via Sodium Absorption Features. Binary Paths to Type Ia Supernovae Explosions 281, 299–302. doi:10.1017/S1743921312015232

[Szkody et al.(1991)] Szkody, P., Mattei, J. A., Waagen, E. O., Stablein, C. 1991. The Interoutburst Behavior of Cataclysmic Variables. The Astrophysical Journal Supplement Series 76, 359. doi:10.1086/191570

[Suckewer(1967)] Suckewer, S. 1967. Calculation of electron density from the intensity ratio of spectral lines of a given ion. Physics Letters A 25, 284–285. doi:10.1016/0375-9601(67)90908-5

[Tatarnikova et al.(2003)] Tatarnikova, A. A., Marrese, P. M., Munari, U., Tomov, T., Yudin, B. F. 2003. Detection of Lithium in the Spectrum of the Symbiotic Mira Star V407 Cygni. Astronomy Letters 29, 405–408. doi:10.1134/1.1579789

[Tatischeff and Hernanz(2007)] Tatischeff, V., Hernanz, M. 2007. Evidence for Nonlinear Diffusive Shock Acceleration of Cosmic Rays in the 2006 Outburst of the Recurrent Nova RS Ophiuchi. The Astrophysical Journal 663, L101–L104. doi:10.1086/520049

[Taylor(1950)] Taylor, G. 1950. The Formation of a Blast Wave by a Very Intense Explosion. I. Theoretical Discussion. Proceedings of the Royal Society of London Series A 201, 159–174. doi:10.1098/rspa.1950.0049

[Telting et al.(2014)] Telting, J. H. and 8 colleagues 2014. FIES: The high-resolution Fiber-fed Echelle Spectrograph at the Nordic Optical Telescope. Astronomische Nachrichten 335, 41. doi:10.1002/asna.201312007

[Teyssier(2019)] Teyssier, F. 2019. Eruptive stars monitoring and the ARAS database. Contributions of the Astronomical Observatory Skalnate Pleso 49, 217–227.

[Townsley(2008)] Townsley, D. M. 2008. Comparing Thermonuclear Runaway Conditions in Recurrent and Classical Novae. RS Ophiuchi (2006) and the Recurrent Nova Phenomenon 401, 131.

[Truelove and McKee(1999)] Truelove, J. K., McKee, C. F. 1999. Evolution of Nonradiative Supernova Remnants. The Astrophysical Journal Supplement Series 120, 299–326. doi:10.1086/313176

[Vanlandingham et al.(1998)] Vanlandingham, K. M., Schwarz, G. J., Starrfield, S., Shore, S. N. 1998. Determining Turn-off Times for ONeMg Novae in the IUE Archives. American Astronomical Society Meeting Abstracts.

[Vaytet et al.(2007)] Vaytet, N. M. H., O'Brien, T. J., Bode, M. F. 2007. Swift Observations of the 2006 Outburst of the Recurrent Nova RS Ophiuchi. II. One-dimensional Hydrodynamical Models of Wind-driven Shocks. The Astrophysical Journal 665, 654–662. doi:10.1086/519000

[Vaytet et al.(2008)] Vaytet, N. M. H., O'Brien, T. J., Bode, M. F. 2008. 1D Hydrodynamical Models of Wind Driven Shocks in RS Ophiuchi (2006). RS Ophiuchi (2006) and the Recurrent Nova Phenomenon 401, 279.

[Vaytet et al.(2011)] Vaytet, N. M. H., O'Brien, T. J., Page, K. L., Bode, M. F., Lloyd, M., Beardmore, A. P. 2011. Swift Observations of the 2006 Outburst of the Recurrent Nova RS Ophiuchi. III. X-Ray Spectral Modeling. The Astrophysical Journal 740. doi:10.1088/0004-637X/740/1/5

[Wahlgren and Shore(2012)] Wahlgren, G. M., Shore, S. N. 2012. Optical region line list for the early phases of the V407 Cyg outburst. unpublished. manuscript no. v407: 'linelist'

[Walder et al.(2008)] Walder, R., Folini, D., Shore, S. N. 2008. 3D simulations of RS Ophiuchi: from accretion to nova blast. Astronomy and Astrophysics 484, L9–L12. doi:10.1051/0004-6361:200809703

[Wallerstein(2008)] Wallerstein, G. 2008. RS Ophiuchi from 1898 to 2005. RS Ophiuchi (2006) and the Recurrent Nova Phenomenon 401, 14.

[Wang et al.(2002)] Wang, L. and 17 colleagues 2002. The Axisymmetric Ejecta of Supernova 1987A. The Astrophysical Journal 579, 671–677. doi:10.1086/342824

[Warner(1989)] Warner, B. 1989. Properties of novae: an overview.. Classical Novae, 1–16.

[Waxman and Katz(2017)] Waxman, E., Katz, B. 2017. Shock Breakout Theory. Handbook of Supernovae 967. doi:10.1007/978-3-319-21846-5_33

[Webbink et al.(1987)] Webbink, R. F., Livio, M., Truran, J. W., Orio, M. 1987. The Nature of Recurrent Novae. Astrophysics and Space Science 131, 493–495. doi:10.1007/BF00668132

[Williams et al.(1991)] Williams, R. E., Hamuy, M., Phillips, M. M., Heathcote, S. R., Wells, L., Navarrete, M. 1991. The Evolution and Classification of Postoutburst Novae Spectra. The Astrophysical Journal 376, 721. doi:10.1086/170319

[Williams(1992)] Williams, R. E. 1992. The Formation of Novae Spectra. The Astronomical Journal 104, 725. doi:10.1086/116268

[Williams et al.(1994)] Williams, R. E., Phillips, M. M., Hamuy, M. 1994. The Tololo Nova Survey: Spectra of Recent Novae. The Astrophysical Journal Supplement Series 90, 297. doi:10.1086/191864

[Williams(2012)] Williams, R. 2012. Origin of the "He/N" and "Fe II" Spectral Classes of Novae. The Astronomical Journal 144. doi:10.1088/0004-6256/144/4/98

[Williams et al.(2017)] Williams, S. C., Darnley, M. J., Henze, M. 2017. Multiwavelength observations of the 2015 nova in the Local Group irregular dwarf galaxy IC 1613. Monthly Notices of the Royal Astronomical Society 472, 1300–1314. doi:10.1093/mnras/stx1793

[Willson(1976)] Willson, L. A. 1976. Shock-wave interpretation of emission lines in long-period variable stars. I. The velocity of the shock.. The Astrophysical Journal 205, 172–181. doi:10.1086/154261

[Willson and Hill(1979)] Willson, L. A., Hill, S. J. 1979. Shock wave interpretation of emission lines in long period variable stars. II. Periodicity and mass loss.. The Astrophysical Journal 228, 854–869. doi:10.1086/156911

[Wolf et al.(2018)] Wolf, W. M., Townsend, R. H. D., Bildsten, L. 2018. Nonradial Pulsations in Post-outburst Novae. The Astrophysical Journal 855. doi:10.3847/1538-4357/aaad05

[Wood and Linsky(1997)] Wood, B. E., Linsky, J. L. 1997. A New Measurement of the Electron Density in the Local Interstellar Medium. The Astrophysical Journal 474, L39–L42. doi:10.1086/310428

[Wynn(2008)] Wynn, G. 2008. Accretion in RS Ophiuchi. RS Ophiuchi (2006) and the Recurrent Nova Phenomenon 401, 73.

[Yamaguchi et al.(2021)] Yamaguchi, H., Acero, F., Li, C.-J., Chu, Y.-H. 2021. Discovery of Double-ring Structure in the Supernova Remnant N103B: Evidence for Bipolar Winds from a Type Ia Supernova Progenitor. The Astrophysical Journal 910. doi:10.3847/2041-8213/abee8a

[Young] Young, P. Line lists for the IRIS far ultraviolet wavelength bands

[Zajczyk et al.(2008)] Zajczyk, A. and 7 colleagues 2008. RS Ophiuchi – High Velocity Outflows During 1994-2006. RS Ophiuchi (2006) and the Recurrent Nova Phenomenon 401, 106.

[Zamanov et al.(2015)] Zamanov, R. and 9 colleagues 2015. Optical flickering of the recurrent nova RS Ophiuchi: amplitude-flux relation. Monthly Notices of the Royal Astronomical Society 450, 3958–3965. doi:10.1093/mnras/stv873

[Zel'dovich and Raizer(1967)] Zel'dovich, Y. B., Raizer, Y. P. 1967. Physics of shock waves and high-temperature hydrodynamic phenomena. New York: Academic Press, 1966/1967, edited by Hayes, W.D.; Probstein, Ronald F..

Ringraziamenti

Cercare tracce di onde di shock nella radiazione stellare è stato un processo lungo e tortuoso, ma mai quanto riuscire a trovare il modo più giusto per esprimere gratitudine nei confronti di tutti coloro senza i quali questo percorso non sarebbe stato nemmeno possibile. Chiunque mi conosca sa che non sono brava a trasformare in parole ciò che penso e provo, ma alcuni ringraziamenti sono più che doverosi.

Ai miei genitori, per i quali non esiste alcuna espressione verbale umana in grado di spiegare quanto io possa essere fortunata e grata per qualsiasi cosa. Sarebbe impossibile e impensabile anche solo cercare di esprimerlo.

Alla mia intera famiglia, a Olga, Francesca, Federica, Antonio, Gianmarco, Dino, Rita, Angelo, Alessio, Michele, Paola, Giulia e Nicolas per essere sempre stati al mio fianco, anche a distanza e negli anni, a prescindere dalle difficoltà e i terremoti dell'esistenza.

A Casa Bianchi, la mia seconda famiglia: a Camilla, sorella, collega, coinquilina e amica sin dal giorno zero, per aver presto parte ad ogni singolo momento di questa lunga avventura, senza cui nulla sarebbe stato lo stesso; a Francesca, per esserci stata sempre, nella disperazione e nei momenti migliori, per aver condiviso gioie, esaurimenti e follie, per avermi fatto scoprire che anche i figli unici possono avere una sorella su cui contare; a Marta, acquisto più recente dal punto di vista temporale ma non meno fondamentale, grazie per la compagnia, i momenti di solidarietà, sconforto e allegria, per avermi fatto capire che una pandemia può mettere a dura prova le persone, ma affrontandola insieme a quelle giuste diventa tutto più facile.

A Marco, fratello, certezza e presenza costante su cui poter contare sempre e comunque, per avermi sopportata e supportata fin dal primo momento nello studio come nella vita, per non aver mai mollato ed essere stato al mio fianco in qualsiasi istante, dal più buio al più luminoso. Alla restante parte della mia terza famiglia dell'ufficio 60, che considererò per sempre la mia casa, per avermi accompagnata in tutti questi anni, aver creduto in me e avermi aiutata nonostante tutto, essere stati punto di riferimento e ispirazione e avermi dato lezioni sull'astrofisica e la vita con il giusto dosaggio di risate, disperazioni condivise, insulti, scontri e discussioni costruttive, nottate tra le stelle, o fiumi di alcool e montagne di cibo. A Marco, per le mille vicende come Bonnie e Clyde, per essere stato sempre un modello a cui ambire, avermi sempre spronata e non esserti arrabbiato nemmeno per i miei disastri peggiori; a Giovanni, per l'ispirazione, l'incitamento a migliorare, la bravura estrema e la disponibilità di sempre, le giornate di studio, le interrogazioni e le risate infinite; a Giulia, astrofisica d'adozione, per tutti i bei ricordi ed esperienze in giro per Pisa o per il mondo; a Paolo, per avermi sempre spronata ad essere più di sicura di me e i pomeriggi di confronto, sconforto e conforto, per essere punto di riferimento da cui imparare continuamente, con cui paragonare stranezze e caratteri anomali simili, per i tanti bei momenti condivisi; a Tommaso, per le bellissime avventure tra concerti, osservazioni, mangiate e bevute e serate in palestra giusto per non farsi mai mancare niente; a Laura, per esserci stata in tantissime circostanze e aver spartito gioie e dolori, ansie, studio e vacanze; a Sofia, per i consigli e le molte occasioni di svago e angosce in comune; a Paolo, per i tanti preziosi consigli di musica e spettroscopia, per il divertimento e la compagnia in tutti questi anni.

A Steve Shore, per avermi insegnato tutto quel poco che so sull'Astrofisica e l'Universo, per avermi dato fiducia e aver visto in me qualcosa che non riesco ancora a scorgere, ma che lotterò sempre per cercare di trovare. Grazie anche a Paul Kuin, per avermi insegnato i segreti dell'analisi dati con Swift e permesso di scoprire una parte dello spazio nell'ultravioletto.

A Stefano, per aver creduto in me, essermi stato sempre accanto e avermi appoggiata e incoraggiata inconsapevolmente anche quando nient'altro sembrava riuscirci, per avermi insegnato la fisica e la meccanica quantistica ma, soprattutto, che certi legami riescono a sopravvivere anche alla distanza, le poche telefonate e i pochissimi ritrovi. Agli amici della prima ora, Chiara, Andrea, Gloria, Giulia e Alessandro, per le tante avventure passate e l'amicizia nonostante gli anni e i rari incontri.

A tutte le persone che, per un motivo o per un altro, non fanno più parte della mia vita, ognuna ha contribuito a farmi arrivare a questo punto. Alcune le ho sempre con me, e questo traguardo è anche merito loro.

Ultimo, molto patetico ma non meno importante, alla musica, per esserci stata costantemente come sottofondo e protagonista per studio, rabbia, gioia, dolore, per aver riempito i peggiori vuoti e avermi accompagnata nei momenti felici; a tutte le voci e gli strumenti che danno senso e colore alle mie giornate e vita ai miei pensieri, senza i quali letteralmente non sarei nemmeno qui. Perché, come un vecchio *amico* ha detto tempo fa, a volte basta una canzone, anche una stupida canzone, solo una stupida canzone, a ricordarti chi sei.